



UNIVERSITÄT  
ZU KÖLN

---

---

# Rough Surface Conditions for the Turbulent Atmospheric Boundary Layer

---

---

*INAUGURAL-DISSERTATION*

*zur Erlangung des Doktorgrades  
der Mathematisch-Naturwissenschaftlichen Fakultät  
der Universität zu Köln*

*vorgelegt von*

Jonathan Kostelecky

*aus Wilhelmsdorf*

Köln, 2024

**Berichterstatter:**

Dr. Cedrick Ansorge  
Prof.in Dr.in Nikki Vercauteren

**Tag der mündlichen Prüfung:**

19.02.2025

# Abstract

The thesis investigates the effect of surface roughness on the atmospheric boundary layer (ABL) – the lower portion of the atmosphere where humans live. The Earth’s surface is rough at multiple scales (e.g., ice, mud, plant cover). Surface roughness is a ubiquitous feature of the ABL, which modifies the mixing and transport properties of the flow and enhances the drag compared to aerodynamically smooth surfaces. In the ABL, dynamical processes are governed by atmospheric turbulence, the critical agent in surface–atmosphere coupling. At the same time, the state of the ABL is primarily influenced by radiative processes. In the absence of solar irradiation, the surface cools, and the stably stratified boundary layer (SBL) forms, characterized by reduced turbulence intensity. In large-scale climate or numerical weather prediction (NWP) models, unresolved processes, such as turbulence or the effect of surface roughness, are parameterized. In particular, the very stable regime remains poorly understood and challenges these models with drastic implications for weather forecasting. Here, process-level insight is gained through direct numerical simulation (DNS) of turbulent Ekman flow subjected to small-scale surface roughness (ratio of roughness height to boundary layer depth scale is  $\mathcal{O}(1\%)$ ). In DNS, turbulent motions and three-dimensional roughness elements are explicitly, fully resolved.

Performing DNS at scales relevant to geophysical problems requires a highly optimized numerical framework. This is prepared as part of the thesis by implementing and validating an immersed boundary method (IBM) along with a pressure treatment to avoid artificial oscillations. In Study I, the effect of surface roughness under neutral conditions on the bulk properties of the flow is investigated. The bottom of the domain is covered with  $56 \times 56$  homogeneously distributed cuboids of varying mean height. The cases range from the aerodynamically smooth to the verge of the fully rough regime. The total drag increases with roughness height, along with the friction of velocity and scalar, and is measured using an integration approach of the budget equations. The enhanced turbulence intensity results in a deeper logarithmic layer as the friction Reynolds number significantly increases, and an accurate collapse of data onto the rough wall scaling is observed. Further, a pronounced veering of the wind with height from the ground is observed, which considerably outweighs the typical decrease in veering angle with increasing Reynolds number under smooth surface conditions. In Study II, a rough case located at the verge of the fully rough regime is subjected to an incrementally increasing strength of stable density stratification. Roughness efficiently counteracts buoyancy-induced suppression of turbulence. It extends the stability regime, where turbulence is in a continuous state, by inducing flow instabilities and producing detached eddies from sharp edges of roughness elements. Despite maintaining turbulence at much larger stability, global intermittency is observed once stratification becomes strong enough. With increasing stability, an over-veering of the wind appears, with a strong veering already within the roughness. Veering of the wind in the SBL challenges classical atmospheric surface layer (ASL) theory. However, it holds within the known limits and agrees with semi-empirical fits from field observations.

The results demonstrate that–based on modern HPC–an extension of the well-established modelling framework for DNS to rough configurations is possible and allows unveiling dynamics in the rough surface layer based on first principles.





# Contents

<b>1</b>	<b>Introduction</b>	<b>1</b>
1.1	The Stable Boundary Layer . . . . .	2
1.2	The Aerodynamically Rough Boundary Layer . . . . .	4
1.3	Representation of Roughness in DNS . . . . .	5
1.4	Objectives and Research Questions . . . . .	6
<b>2</b>	<b>Theoretical Foundation and Numerics</b>	<b>9</b>
2.1	Governing Equations of Geophysical Fluid Dynamics . . . . .	9
2.2	General Assumptions Underlying the Simulations of Turbulent Flow . . . . .	10
2.2.1	Continuum Hypothesis . . . . .	10
2.2.2	Incompressibility . . . . .	10
2.2.3	Hydrostatic Equilibrium . . . . .	10
2.2.4	Potential Temperature . . . . .	11
2.2.5	Boussinesq Approximation . . . . .	11
2.2.6	Coriolis Acceleration and f-Plane Approximation . . . . .	11
2.2.7	Pressure Decomposition and Geostrophic Balance . . . . .	12
2.2.8	Simplified Set of Equations and Boundary Conditions . . . . .	12
2.3	Non-dimensionalization . . . . .	13
2.3.1	Non-dimensional Parameters . . . . .	13
2.3.2	Parameter Space and Regime Transitions . . . . .	14
2.4	Wall-bounded Turbulent Ekman Flow . . . . .	16
2.4.1	Statistical Analysis . . . . .	16
2.4.2	The Laminar Ekman Solution . . . . .	17
2.4.3	The Scales of Neutrally Stratified Turbulent Ekman Flow . . . . .	18
2.4.4	Viscous Sublayer and Logarithmic Law of the Wall . . . . .	19
2.4.5	Monin–Obukhov Similarity Theory . . . . .	21
2.5	Numerical Framework of the DNS Code . . . . .	22
2.5.1	Temporal and Spatial Discretization Strategy . . . . .	23
2.5.2	Pressure Treatment . . . . .	26
2.5.3	Immersed Boundary Methods . . . . .	29
<b>3</b>	<b>Implementation and Validation of the Immersed Boundary Method</b>	<b>35</b>
3.1	Implementation of the Pressure Grid Staggering and Filtering . . . . .	35
3.2	Implementation of the Alternating Direction Reconstruction Immersed Boundary Method . . . . .	37

3.3	Validation of the Numerical Tools . . . . .	39
3.3.1	Numerical Setup of the Turbulent Channel Flow . . . . .	40
3.3.2	Validation of the Horizontal Pressure Grid Staggering for a Smooth Wall . . . . .	42
3.3.3	Validation of the Horizontal Pressure Grid Staggering for a Rough Wall . . . . .	43
3.3.4	Comparison of Rough Turbulent Channel Flow Data . . . . .	45
3.3.5	Comparison with Wind Tunnel and LES Data . . . . .	48
3.3.6	Effect of the IBM on a Passive Scalar . . . . .	53
<b>4</b>	<b>Study I: The Neutrally Stratified Rough Ekman Layer</b>	<b>57</b>
<b>5</b>	<b>Study II: The Stably Stratified Rough Ekman Layer</b>	<b>93</b>
<b>6</b>	<b>Conclusions and Outlook</b>	<b>131</b>
6.1	Study I: The Neutrally Stratified Rough Ekman Layer . . . . .	132
6.2	Study II: The Stably Stratified Rough Ekman Layer . . . . .	133
6.3	Outlook . . . . .	133
	<b>Bibliography</b>	<b>135</b>
	<b>Nomenclature</b>	<b>151</b>
	<b>Appendix: Channel Flow – Description and Forcing</b>	<b>157</b>

# 1. Introduction

The atmospheric boundary layer (**ABL**) begins directly at the Earth’s surface and, together with the free atmosphere, forms the troposphere, the lowest layer of the Earth’s atmosphere (Stull, 1988). Although a consistent and precise definition of the **ABL** is lacking, Monin (1970) defines the **ABL** in his seminal work as follows:

*“In large-scale air currents, the combined action of turbulent friction and Coriolis force results in the formation, near the surface of a planet, of the atmospheric boundary layer.”*

Three characteristic processes govern the boundary layer dynamics: (i) the direct impact of the Earth’s surface, including friction and exchange processes of mass, heat, moisture and pollutants with the free atmosphere aloft, (ii) the Earth’s rotation, described by the Coriolis force, and (iii) the density stratification of the air (Garratt, 1992). The structure of the **ABL** is heavily influenced by the diurnal cycle and is, thus, highly variable in time and space. Usually, the boundary layer depth ranges from hundreds of meters to the kilometer scale (in the Arctic, **ABL** depths of  $\mathcal{O}(10\text{ m})$  are observed, Petenko et al., 2019). Most of our human activities take place within the **ABL**, such as weather-forming processes and the direct impact of weather on our societal life (e.g. transportation, aviation, shipping, agriculture). An accurate representation of the **ABL** in numerical models is a major challenge for precise predictions, as is the case in climate models, operational numerical weather predictions (**NWPs**) and atmospheric dispersion models of pollutants.

A challenge in earth system models is accurately representing the **ABL**, particularly turbulence, which is the main agent of the dynamical system. In recent decades, the overall forecasting skill significantly increased with the ever-increasing compute power (cf. skill score on page 4, ECMWF, 2024; Vitart, 2014). Nevertheless, challenges persist in these general circulation models (**GCMs**); for example, increasing the total number of vertical levels in the model from 91 to 137, favored by increased computing power, improves the overall forecast skill. However, the 10-meter wind and the 2-meter temperature skill scores degraded, which indicates misrepresenting boundary layer dynamics in the model (cf. figure 2, Haiden et al., 2021). In particular, the representation of the stably stratified planetary boundary layer (**SBL**) during nighttime, polar nights, and evening/morning transitions experiences large errors (Sandu et al., 2013; Holtslag et al., 2013; Mahrt, 2014; Steeneveld, 2014). Turbulence closure schemes and parameterizations based on atmospheric surface layer (**ASL**) similarity theory that rely on Kolmogorov-type turbulence (cf. K41 theory, Kolmogorov, 1941) tend to fail due to the increasing anisotropy and local absence of turbulence with increasing stability in the **SBL** (Jiménez, 2004; Mauritsen and Svensson, 2007; Stiperski and Calaf, 2018; Vercauteren et al., 2019). These challenges are

often tackled in **GCMs** with highly tuned parameterization coefficients, while a profound physical concept of the **SBL** is still lacking.

The direct impact of the surface results in characteristic velocity and temperature (density) gradients throughout the boundary layer, as the near-surface values must match those of the surface and, at the upper boundary, those of the free atmosphere. Frictional forces at the surface decelerate the flow, resulting in wind shear and, thus, a turbulent flow state caused by the high atmospheric Reynolds number (due to the large vertical extent of the **ABL** and the low viscosity of air). In this state, turbulence is mainly generated mechanically by wind shear in vicinity of the surface, provided that buoyancy is neglected. Turbulence plays a pivotal role in dynamic processes in the **ABL**, as it is the primary agent for the surface–atmosphere coupling and mixing within the **ABL**. In a turbulent flow, the transport and mixing properties of heat, momentum, humidity, and pollutants are enhanced by orders of magnitude compared to a non-turbulent flow, where mixing is accomplished only by molecular diffusion.

Temperature gradients in the **ABL** predominantly originate in radiative processes: during the day, solar radiation heats the surface, and plumes of warmer air rise, yielding an overall turbulent mixed layer (**ML**), whereas in the absence of solar radiation (nights, long-lasting polar nights), the surface cools and the **SBL** forms, where buoyant restoring forces damp turbulent motions. With increasing strength of stratification, turbulence intensity in the **ABL** is reduced. A state of reduced continuous turbulence might set in or turbulence might even locally cease (Mahrt, 1998; Van de Wiel et al., 2012b), with an associated decoupling of the **ABL** from the surface. The phenomenon of local cessation of turbulence in an otherwise turbulent flow is called global intermittency (Mahrt, 1999).

Shear and buoyancy determine if a turbulent state of the **ABL** sets in, and the surface structure directly affects the latter. For geophysical flow, the underlying Earth’s surface is always considered rough, whereby surface roughness has a great variability in length scale, ranging from the smallest scale as flow over frozen lakes to larger scales as flow over forests and cities. Roughness is a ubiquitous feature of **ABL** dynamics, as the transport of momentum and energy and the turbulent structures in the flow are significantly altered (Kadivar et al., 2021). Considering surface roughness in idealized **ABL** studies opens up the possibility of more realistic approaches compared to canonical flow problems with smooth walls, but leads to a higher complexity of the considered physical system.

The objective of this dissertation is to examine the wall-bounded rough **ABL** subjected to neutral and stable density stratification to gain insights into boundary layer dynamics. Process-level understanding is based on first principles using the paradigm of direct numerical simulation (**DNS**), which does not rely on turbulence closure assumptions and parameterizations.

## 1.1 The Stable Boundary Layer

During nighttime, longwave radiative cooling of the ground cools the ambient near-surface air, causing the potential temperature to increase with height. Here, stability is meant dynamically; and it refers to the fact that colder and dense air near to the ground hampers velocity perturbations (turbulent motion) to a certain degree by buoyant restoring forces. In the stable regime, shear mainly produces turbulence, particularly turbulent kinetic energy (**TKE**). Depending on the strength of stratification, turbulence is observed to cease locally or even globally (Mahrt, 1999; Van de Wiel et al., 2012a), whereas a full laminarization of the flow in the **ABL** is questionable (Mauritsen and Svensson, 2007). Commonly, the **SBL** is classified into three regimes (Mahrt, 1998; Sun et al., 2012): the weakly stable boundary layer (**WSBL**), the very stable boundary layer (**VSBL**) and the transition in between both, the intermediately stable boundary layer.

The **WSBL** regime is characterized by reduced but still continuous turbulence and is well understood using parameterizations such as the omnipresent Monin–Obukhov Similarity

Theory (**MOST**) in earth system models (cf. the seminal work of Monin and Obukhov, 1954). The validity of **MOST** in the **WSBL** regime is proven based on extensive observational data from large measurement campaigns (Nieuwstadt, 1984; Högström, 1988, 1996; Sorbjan and Grachev, 2010; Grachev et al., 2012). Moreover, the **WSBL** is accurately represented in numerical models, including the large-eddy simulation (**LES**) approach and single-column models (Beare et al., 2006; Svensson et al., 2011; Huang and Bou-Zeid, 2013; Holtslag, 2014).

Meanwhile, the **VSBL**, characterized by weak wind and weak turbulence conditions, remains a significant challenge in numerical models and observations. Observational studies reveal the inability of **MOST** to correctly relate turbulent surface fluxes to mean gradients with universal stability functions. In this regime, turbulence is observed to drastically change and locally collapse in time and space (global intermittency; cf. Ha et al. (2007); Van de Wiel et al. (2012a); Vignon et al. (2017)). Conceptual studies of the **VSBL** exist (Derbyshire, 1999; Van de Wiel et al., 2002, 2012b), although a general framework of the **SBL** still needs to be developed. Covering the **VSBL** in numerical experiments is hard to achieve since intermittent and anisotropic turbulence reduces confidence in the validity of turbulent subgrid closures. Consequently, due to an over-dependence on closure assumptions, the **LES** approach fails to simulate intermittent turbulence in the **VSBL**. The numerical artefact called *runaway cooling* is observed in **LES** and results in unrealistic cooling at the surface (Jiménez and Cuxart, 2005). The **VSBL** is, therefore, assigned to the regime in which classical turbulence closures break down, as the title of Mahrt’s (1998) study emphasizes.

In contrast, the **DNS** approach is free of turbulence closure assumptions. **DNS** was proven to cover the intermittent state of the **VSBL** in simplified canonical flow problems at reduced Reynolds number. The real-world **VSBL** dynamics were investigated by many researchers using either a stably stratified Poiseuille flow in the form of an open or closed turbulent channel flow or a stably stratified Couette flow, i.e. a shear-driven flow between two plates (Zonta and Soldati, 2018). These setups have in common that the effects of the Coriolis force and surface roughness are often neglected. Global intermittency in the **VSBL** was successfully simulated by García-Villalba and del Álamo (2011), Flores and Riley (2011), Brethouwer et al. (2012), Deusebio et al. (2015) and He (2016). Flores and Riley (2011) define a Reynolds number based on the Obukhov length (a measure of stability that describes the available scale separation) as a criterion of turbulence collapse rather than criteria based on Richardson numbers (Garg et al., 2000; García-Villalba and del Álamo, 2011). Furthermore, the computational domain size must be large enough for laminar and turbulent patches to coexist (cf. effect of finite domain size on stable stratified shear layers, Watanabe and Nagata, 2021). Otherwise, an artificial full laminarization of the flow is observed (García-Villalba and del Álamo, 2011). The effect of heterogeneous surface temperature is investigated in closed channel flow by Bon and Meyers (2022) (more recently for the **WSBL**, Bon et al., 2023) and in Couette flow by Mironov and Sullivan (2023). Both studies observe a higher level of turbulence in the presence of heterogeneous surface temperature and, thus, a regime shift from the **VSBL** to the state of continuous turbulence (**WSBL**).

One approach to studying the **ABL** dynamics of higher complexity is turbulent Ekman flow (Ekman, 1905), the flow over a flat plate subjected to steady system rotation and driven by a constant pressure gradient, respectively constant geostrophic wind (free-stream velocity). **DNS** of turbulent Ekman flow was initially studied by Coleman et al. (1990) for neutral density stratification. Ekman flow exhibits, in contrast to channel flow, no symmetry in the spanwise direction due to the rotation of the reference frame. Furthermore, the rotation results in a height-dependent wind turning and a quasi-stationary boundary layer height. **DNS** of stable Ekman flow was studied by Coleman et al. (1992), Ansorge and Mellado (2014, 2016), Deusebio et al. (2014), Shah and Bou-Zeid (2014), Lee et al. (2020)

and Stefanello et al. (2022). Ansonge and Mellado (2014) demonstrated the suitability of Ekman flow for studying the global intermittency of the **VSBL** compared to the channel flow analogue. Moreover, they prove that intermittency is an inherent flow feature and appears without external triggering mechanisms.

In the present study, **DNS** of the turbulent stratified Ekman layer as a canonical flow that resembles the **ABL**. This relatively concise overview is supplemented by a comprehensive and detailed introduction in Study II (chapter 5).

## 1.2 The Aerodynamically Rough Boundary Layer

The **ABL** is exposed to the rough surface of the Earth, e.g. agricultural areas, snow, grass, and forests. The influence of surface roughness on the boundary layer is of crucial importance and affects drag, mixing and transport properties of the flow (Garratt, 1992), and is reviewed by Raupach et al. (1991), Finnigan (2000) and Jiménez (2004) among others (Flack and Schultz, 2010; Piomelli, 2019; Kadivar et al., 2021; Chung et al., 2021).

The relevant roughness length scales in the **ABL** must be considered from two sides. On the one hand, the vertical extent of the **ABL**—the boundary layer thickness—is large, on the order of  $10^2 - 10^3$  m, whereas typical surface roughness is relatively small, on the order of  $10^{-3} - 10^1$  m (e.g. from frozen lake to trees). Hence, the ratio of characteristic roughness length to boundary layer thickness is small, on the order of  $\lesssim 1\%$ . On the other hand, the impact of roughness in the near-wall region depends on the ratio of roughness length to viscous length scale (a roughness Reynolds number), which is relatively large in the **ABL**, due to the low viscosity of air. The latter ratio defines the different regimes of rough wall-bounded flows, ranging from the aerodynamically smooth to the transitionally rough to the fully rough regime, where the **ABL** is commonly located in. Both length scale considerations of the rough **ABL** are contradictory at first sight but result in the necessity of a large scale separation between the small-scale viscous length and the large-scale boundary layer thickness, expressed in terms of a large atmospheric Reynolds number. The requirement for a large scale separation makes **DNS** of the **ABL** with surface roughness challenging.

**DNS** of turbulent channel flow with wall roughness is a widely studied problem in engineering while neglecting the Coriolis force. There are studies with roughness in the form of cubes (Coceal et al., 2006; Leonardi and Castro, 2010), transverse bars (Leonardi et al., 2003; Nagano et al., 2004; Ashraffian et al., 2004), irregular roughness (Ma et al., 2021; Jelly et al., 2022), and studies focussing on secondary motions (Hwang and Lee, 2018; Schäfer et al., 2019; Stroh et al., 2020b; Castro et al., 2021). The roughness setup of the latter ones consist of streamwise aligned ribs to study the occurrence of persistent secondary flows of Prandtl’s second type (Prandtl, 1952) and the influence of the rib geometry on the strength of secondary motions. **DNS** studies of rough turbulent channel flow subject to stable density stratification are scarce. Urban flows are intentionally not considered in this dissertation, as they have a high ratio of roughness height to boundary layer thickness and are understood as flows over obstacles or through canopies rather than surface roughness.

Lee et al. (2020) performed **DNS** of the neutral and very stable **ABL** with periodic smooth bumps on the lower wall of the simulation domain in the transitionally rough regime. They noticed a minor influence of wall roughness on the neutrally stratified flow but a more substantial impact on the very stable **ABL**. Surface roughness efficiently counteracts the suppression of turbulence, and an increase in the thickness of the near-surface layer is observed. Moreover, they observed a regime shift from the **VSBL** to the **WSBL** in the presence of surface roughness. To the author’s knowledge, apart from the study by Lee et al. (2020), there are no other **DNS** studies on the very stable turbulent Ekman flow over roughness elements. The lack of systematic studies on the **VSBL** with heterogeneous surface conditions motivates the current investigation. This overview is supplemented by



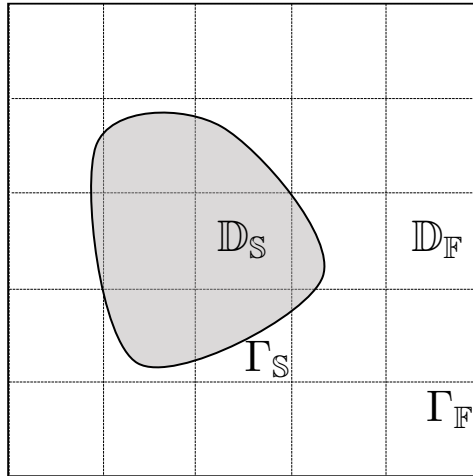


**Fig. 1.1** An object with the solid region  $\mathbb{D}_S$  and the boundary  $\Gamma_S$  is immersed in a Cartesian grid with the fluid region  $\mathbb{D}_F$  and the boundary  $\Gamma_F$ .

a comprehensive and detailed introduction in Studies I & II (chapters 4,5).

### 1.3 Representation of Roughness in DNS

A key research topic in computational fluid dynamics (CFD) is the consideration of complex geometries in the flow, intending to achieve increasingly realistic simulations. Achieving such realism involves the representation of moving bodies and deforming boundaries due to fluid-solid interactions. However, the present dissertation focuses on the flow interactions of fixed objects with rigid boundaries and simple geometric shapes. Nevertheless, the transition from fluid flow over smooth walls to rough flow is challenging: On the one hand, the numerical framework of the used CFD code must be reconsidered to cope with objects in the flow. On the other hand, surface roughness offers a vast parameter space for research (e.g. distribution of roughness elements, roughness type and density, mean height of roughness elements).

**Decomposition of the computational domain and boundary definition.** The computational domain  $\mathbb{D}$  is decomposed into a fluid  $\mathbb{D}_F$  and a solid region  $\mathbb{D}_S$  for methods to represent objects in the flow. Corresponding interfaces of the fluid region are  $\Gamma_F$  and of the solid region  $\Gamma_S$  (Fig. 1.1). The velocity boundary condition of the immersed object is  $\mathbf{u}|_{\Gamma_S} = \mathbf{u}_S$ , where  $\mathbf{u}_S$  denotes the velocity vector of a moving object. Here, the physical velocity boundary condition  $\mathbf{u}_S = 0$  is used for fixed objects and rigid boundaries. It ensures the impermeability of the walls  $\mathbf{u}_n|_{\Gamma_S} = 0$ , where  $\mathbf{u}_n$  is the wall-normal velocity vector and the no-slip boundary condition  $\mathbf{u}_t|_{\Gamma_S} = 0$ , where  $\mathbf{u}_t$  the tangential velocity vector at the interfaces. An indicator function  $\epsilon(x_i)$  is introduced as a descriptive geometry field for the decomposition of the computational domain into a solid and fluid part and is defined as

$$\epsilon(x_i) = \begin{cases} 1, & \text{if } x_i \in \mathbb{D}_S, \\ 0, & \text{if } x_i \in \mathbb{D}_F, \text{ with } x_i = (x, y, z)^T, \end{cases} \quad (1.1)$$

where  $x_i$  are Cartesian coordinates. Grid points on the interface are included in the solid domain since the physical boundary conditions hold here.

**Two different approaches** exist in general to represent solid bodies in the computational domain. The conventional approach (Ferziger et al., 2020; Roy et al., 2020) consists of the following steps: First, a surface mesh of the solid boundary  $\Gamma_S$  is generated, then a body-fitted mesh of the fluid domain  $\mathbb{D}_F$  is created, and finally the governing equations are discretized in the fluid domain  $\mathbb{D}_F$  (Fig. 1.1). It is emphasized that no equations are solved

inside the solid body  $\mathbb{D}_S$  since the geometry information and boundary conditions are directly imposed by the use of a body-conform mesh and thus  $\mathbb{D} = \mathbb{D}_F$ . An example is the **DNS** study by Lee et al. (2020) of a stably stratified Ekman layer over sinusoidal-shaped hills. They used a topography-conforming grid to transform the governing equations to curvilinear coordinates (Gayen and Sarkar, 2011). A major disadvantage of the conventional approach is that it is very time-consuming and expensive to generate the grids. Besides, the geometry cannot be changed once the body-fitted mesh is generated, and sophisticated numerical methods are needed. Certain limitations exist regarding possible roughness types in the case of topography following grids, as sharp edges are barely feasible, and thus, mainly undulating surfaces are possible.

Another promising method for using **DNS** as a modelling paradigm is to represent complex geometries in the flow using grids that do not conform to the solid regions (Fig. 1.1). The associated methods are called immersed boundary methods (**IBMs**), where objects are immersed in the regular grid. These methods are primarily applied to Cartesian grids since grid generation costs are negligible. The review of Mittal and Iaccarino (2005) presents a comprehensive overview of the various existing **IBMs** from the last decades. The essence of an **IBM** is to maintain the existing grid and its associated numerical framework while indirectly introducing the boundary conditions of an immersed object. Usually, the effect of solid boundaries in the Cartesian grid is simulated by adding a new source or sink term to the governing flow equations, which ideally preserves computational efficiency and gives flexibility in positioning the fluid-solid interface concerning the grid nodes. The interface does not necessarily have to match the positions of the grid nodes. In contrast to the conventional approach, the **IBM** solves the equations on the entire computational domain  $\mathbb{D} = \mathbb{D}_F + \mathbb{D}_S$ , including the solid region. The numerical impact of an **IBM** and the correct imposition of boundary conditions are not straightforward (cf. section 2.5).

## 1.4 Objectives and Research Questions

This dissertation aims to investigate the characteristics of the neutral, weakly and very stably stratified **ABL** exposed to heterogeneous surface conditions. As a virtual laboratory to study the **ABL** dynamics by first principles, **DNS** of the rough, turbulent Ekman flow is chosen. The **DNS** approach is as accurate as possible in numerically solving the governing flow equations without a subgrid model for turbulence, apart from the inevitable numerical errors (Moin and Mahesh, 1998). Moreover, previous **DNS** studies of the turbulent Ekman flow with smooth walls have proven the suitability of this setup to capture the **VSBL** dynamics with global intermittency.

The fundamental ingredient to **DNS** is resolving the entire cascade of turbulent motion, from the largest energy-containing eddies to the smallest scales, where energy dissipates. Resolving turbulent motions in their entirety requires fine grid resolution, resulting in a highly demanding computational problem. This effort comes at the price of only low to moderate Reynolds numbers being affordable. In contrast to the engineering context, **DNS** is relatively new in geophysics. With the increasingly powerful high-performance computing (**HPC**) facilities of the last years, a state is now reached where geophysically relevant domain sizes and simulation durations can be attained. Nevertheless, it is nowadays impossible to simulate all scales of a *real-world* **ABL**.

Typical realistic scales are a boundary layer thickness of  $\delta \sim 10^3$  m, wind velocity of  $u \sim 1$  m/s and air viscosity of  $\nu_{\text{air}} \sim 10^{-5}$  m<sup>2</sup>/s (cf. scaling arguments by Mellado et al. (2018) and Dimotakis (2005)). Following Kolmogorov's theory (Kolmogorov, 1941), which states that the largest eddies are of  $\mathcal{O}(1)$  domain scale, leads to a characteristic Reynolds number for the largest motion of  $Re_{\text{ABL}} = \delta u / \nu_{\text{air}} = 10^8$ . The scale separation between smallest (determined by the Kolmogorov length scale  $\eta = (\nu_{\text{air}}^3 / \epsilon_{\text{dis}})^{1/4} = 10^{-3}$  m, with the dissipation rate  $\epsilon_{\text{dis}} = u^3 / \delta$ ) and largest eddies covered by the **DNS** in this case is given with  $\eta / \delta \sim Re_{\text{ABL}}^{-3/4} \sim 10^{-6}$ . Currently, **DNS** of stratified Ekman flow with a Reynolds



number of  $\sim 10^4$  is possible (Anson, 2019), leaving a separation in the Reynolds number between DNS and real-world ABL of four orders of magnitude. Nevertheless, the concept of Reynolds number similarity is routinely employed here, which according to Townsend (1976, p.53–54) states:

*“Perhaps the most significant fact about turbulent flows is that, while geometrically similar flows are expected to be dynamically and structurally similar if their Reynolds numbers are the same, their structures are also very nearly similar for all Reynolds numbers which are large enough to allow turbulent flow.”*

At sufficiently high Reynolds number, certain flow statistics are observed to become independent of the Reynolds number and can be extrapolated to the geophysical limit (cf. section 2.3.2).

The three-dimensional roughness elements on the ground of the computational domain are fully resolved using an IBM, whereby physical boundary conditions are ensured on all rigid walls. Furthermore, the length scale ratio of the roughness and the boundary layer thickness of atmospheric relevance is small, viz. of  $\mathcal{O}(1\%)$ . Hence, the term *small-scale* surface roughness is used throughout this dissertation. Performing these simulations with small-scale, fully resolved surface roughness requires large Reynolds numbers in the DNS context and, thus, a cutting-edge algorithmic framework. As preliminary work, an IBM compatible with the optimized numerics of the DNS code is implemented and validated to pave the way for highly computationally demanding simulations.

The following published studies address open questions in land-atmosphere interactions in the form of turbulent Ekman flow subject to small-scale surface roughness, unveiling for the first time processes within the roughness sublayer. Study I investigates the effects of small-scale surface roughness on bulk properties of the flow with neutral stratification. The following research questions are addressed (cf. introduction of chapter 4):

- What is the impact of a controlled and fully resolved surface roughness on bulk parameters and mean flow properties?
- Do vertical velocity and temperature profiles in the near-wall region follow the expected and widely-used scaling approaches in MOST for neutral conditions? Moreover, can we arrive at meaningful estimates for the corresponding scaling parameters (zero-plane displacement height, roughness length for momentum and scalar) compared to widely accepted values?
- How different is the enhanced mixing of the momentum and the scalar in the presence of surface roughness?

Study II investigates the competing interplay of small-scale surface roughness, turbulence and stable stratification. The following research questions are addressed (cf. introduction of chapter 5):

- Does the presence of roughness affect the transition from the weakly stable regime, in which turbulence is in a continuous state, to the very stable regime, in which global intermittency is observed?
- Does large-scale intermittency occur in the very stable regime, and are its effects comparable to those in aerodynamically smooth flow?
- Are common stability corrections for MOST applicable to our data, and do the associated parameter values (e.g., von Kármán constant, roughness length, displacement thickness) match expectations based on observational data from atmospheric measurement campaigns?

The structure of the current dissertation is as follows. The following chapter 2 gives an overview of the fundamentals needed for the understanding of the conducted ABL analyses, including the governing equations and their assumptions, the theory of wall-bounded flows, and a description of the numerical framework of the used algorithm. Afterwards, chapter 3 presents the implementation and validation of the numerical methods to introduce surface roughness in the DNS. In chapters 4, 5, the rough ABL is studied with neutral and stable density stratification. Both studies are reproduced in the form they were published in the Journal of Fluid Mechanics and Boundary-Layer Meteorology. Hence, minor repetitions in the present and following chapters could not be avoided. Finally, a concluding statement is given in chapter 6.

## 2. Theoretical Foundation and Numerics

This chapter introduces the theoretical framework required for DNS of turbulent Ekman flow over a rough surface. First, the governing equations (section 2.1), underlying assumptions and simplifications (section 2.2), and thereafter the non-dimensionalization (section 2.3) of the flow problem are presented. Section 2.4 describes the characteristics of wall-bounded turbulent Ekman flow. Section 2.5 concludes this chapter with an explanation of the numerical framework of the DNS code.

### 2.1 Governing Equations of Geophysical Fluid Dynamics

The governing equations of fluid motion (section 2.1) and the corresponding derivation of assumptions and boundary conditions (section 2.2) are based on the textbooks of Tritton (1977), Cushman-Roisin and Beckers (2011) and Vallis (2017).

The conservation equation of mass in differential form reads as

$$\frac{1}{\rho} \frac{D\rho}{Dt} = -\frac{\partial u_j}{\partial x_j}, \quad \text{with} \quad \frac{D(\cdot)}{Dt} = \frac{\partial(\cdot)}{\partial t} + u_i \frac{\partial(\cdot)}{\partial x_i} \quad (2.1a,b)$$

the total derivative  $D(\cdot)/Dt$ , while neglecting mass sources or sinks in the system. The continuity equation states that the sum of mass flowing into and out of a control volume equals the mass change within the volume. The spatial coordinates  $x_i = (x, y, z)^T$  are the streamwise, spanwise and wall-normal directions. The corresponding velocity vector field is  $\mathbf{u} = (u, v, w)^T = (u_1, u_2, u_3)^T$  and the fluid density  $\rho$ . The indices  $i, j$  and  $k$  run from one up to three.

Fluid motions are characterized by the chaotic nature of turbulence and described with sufficient accuracy by the non-linear Navier–Stokes equations (NSE) (Batchelor, 1967) while considering the Coriolis force due to a rotation of the reference frame. The conservation equations of momentum can be written as

$$\frac{D\rho u_j}{Dt} = -\frac{\partial p}{\partial x_j} + \frac{\partial}{\partial x_j} \left[ 2\rho\nu \left( e_{ij} - \frac{1}{3} \frac{\partial u_k}{\partial x_k} \delta_{ij} \right) \right] - 2\rho\epsilon_{ijk}\Omega_i u_k - \rho g_{\text{grav}}\delta_{3j}, \quad (2.2)$$

where  $p$  is the pressure scalar field,  $\nu$  the kinematic viscosity,  $g_{\text{grav}}$  the gravitational acceleration in the wall-normal direction,  $\Omega_i$  the rotation vector,  $\delta_{ij}$  the Kronecker delta and  $\epsilon_{ijk}$  the Levi–Civita symbol. The symmetric rate-of-strain tensor is defined as

$$e_{ij} = \frac{1}{2} \left( \frac{\partial u_i}{\partial x_j} + \frac{\partial u_j}{\partial x_i} \right). \quad (2.3)$$

The conservation equation of energy can be written as

$$\frac{D\rho(c_p - R)T}{Dt} = -p\frac{\partial u_i}{\partial x_i} + 2\nu\rho\left[e_{ij}e_{ij} - \frac{1}{3}\left(\frac{\partial u_i}{\partial x_i}\right)^2\right] + \frac{\partial}{\partial x_i}\left(\kappa_d\rho c_p\frac{\partial T}{\partial x_i}\right), \quad (2.4)$$

where  $\kappa_d$  is the thermal diffusivity,  $T$  the temperature,  $c_v$  and  $c_p$  the specific heat capacities at constant volume and pressure, and  $R$  the specific gas constant. The energy equation is complemented with the equation of state for an ideal gas

$$\frac{p}{\rho} = RT, \quad \text{with } R = c_p - c_v. \quad (2.5a,b)$$

## 2.2 General Assumptions Underlying the Simulations of Turbulent Flow

The conservation equations of mass (2.1), momentum (2.2), energy (2.4) and the equation of state (2.5a) form a closed coupled set of partial differential equations (PDEs). General assumptions are required and introduced in the following to solve this set of PDEs numerically.

### 2.2.1 Continuum Hypothesis

The fundamental assumption of geophysical fluid dynamics is the continuum hypothesis, according to which the smallest fluid volume under consideration still consists of many molecules. As a result, the volume dimensions are considerably larger than the mean free path of the molecules. In this finite volume, field variables are defined (i.e. macroscopic quantities such as pressure, density, velocity, and temperature), which are continuous functions in space and time and obtained by averaging the properties of the molecules. The discontinuous nature of such values on the atomic scale is disregarded; thus, the fluid is treated as a continuous medium. Moreover, in the present study, the fluid is considered as a Newtonian fluid with a constant viscosity, which is independent of the strain rate.

### 2.2.2 Incompressibility

The fluid density  $\rho(x_i, t) = \rho_0(z) + \rho'(x_i, t)$  is decomposed into a reference density  $\rho_0$  and a fluctuating part  $\rho'$ , assuming that the density changes in the fluid, which are mainly due to pressure perturbations, are negligible small:

$$\frac{\rho'}{\rho_0} \ll 1. \quad (2.6)$$

Consequently, density changes have no impact on the mass balance since  $\rho \approx \rho_0$  and thus  $D\rho/Dt = 0$ . The continuity equation (2.1a) simplifies to the requirement of a solenoidal velocity field  $\partial u_j/\partial x_j = 0$  (Vallis, 2017). The divergence-free constraint simplifies the viscous term on the right-hand side (RHS) of the NSE (2.2) ( $\partial u_k/\partial x_k = 0$ ) and the energy equation (2.4), where the dissipative heating on the RHS is zero ( $\partial u_i/\partial x_i = 0$ ). Furthermore, the incompressibility assumption implies that the fluid velocity  $c_u$  is far away from the speed of sound  $c_s$  and, therefore, expressed in non-dimensional numbers, a small Mach number  $(Ma)^2 = (c_u/c_s)^2 \ll 1$  is required (Batchelor, 1967; Tritton, 1977).

### 2.2.3 Hydrostatic Equilibrium

In geophysical flows, particularly in the ABL, the pressure field is assumed to be in hydrostatic equilibrium, i.e., the pressure at a certain height equals the weight of the fluid column above it (Holton, 2004). Analogously to the density, the pressure is decomposed into a reference and fluctuating part, with  $p(x_i, t) = p_0(z) + p'(x_i, t)$ . For a statistically steady background state, the hydrostatic balance is

$$\frac{dp_0}{dz} = -\rho_0 g_{\text{grav}}. \quad (2.7)$$

With the concept of hydrostasy, the pressure and gravitational terms on the **RHS** of the vertical component of the **NSE** (2.2) are

$$-\left[\frac{\partial p}{\partial z} + \rho g_{\text{grav}}\right] = -\left[\frac{\partial (p_0 + p')}{\partial z} + (\rho_0 + \rho') g_{\text{grav}}\right] = -\rho_0 \left[\frac{1}{\rho_0} \frac{\partial p'}{\partial z} + \frac{\rho'}{\rho_0} g_{\text{grav}}\right]. \quad (2.8)$$

### 2.2.4 Potential Temperature

The potential temperature  $\Theta$ , is the temperature of a fluid parcel when moved adiabatically to a reference state ( $p_{\text{ref}}$ ,  $T$ ) and is defined as

$$\Theta = T \left(\frac{p_{\text{ref}}}{p}\right)^{\frac{R}{c_p}}, \quad (2.9)$$

with the typical value of the standard pressure of  $p_{\text{ref}} = 10^5$  Pa. The potential temperature is thus a conserved quantity for adiabatic processes  $D\Theta/Dt = 0$  and directly related to the entropy  $s$ , with ( $ds = c_p d \ln \Theta$ ) (Vallis, 2017, p.25).

### 2.2.5 Boussinesq Approximation

The *Boussinesq approximation* is an extension of the incompressible **NSE** (2.2) to take buoyancy effects in the boundary layer due to density changes into account (for a comprehensive derivation, the reader is referred to Spiegel and Veronis (1960)). In the flow system, density perturbations are assumed to be small compared to the reference state, i.e.  $\rho' \ll \rho_0$ . Density perturbations are solely considered in the gravitational term of the vertical momentum equation. Otherwise, a constant reference state is assumed with  $\rho \approx \rho_0$ . In the atmosphere, the density changes drastically between the ground and the troposphere, but this effect is attributed to the hydrostatic equilibrium (2.7). The pressure and gravitational term of the **RHS** of the vertical component of the **NSE** (2.2, 2.8) are

$$-\left[\frac{1}{\rho_0} \frac{\partial p'}{\partial z} + \frac{\rho'}{\rho_0} g_{\text{grav}}\right] = -\frac{\partial \pi^*}{\partial z} + \frac{\Theta'}{\Theta_0} g_{\text{grav}} = -\frac{\partial \pi^*}{\partial z} + b, \quad \text{with } b = \frac{\Theta'}{\Theta_0} g_{\text{grav}}. \quad (2.10a,b)$$

Here,  $\pi^* = p'/\rho_0$  is the modified non-hydrostatic pressure, and  $b$  is the buoyancy variable, while using the relation  $\rho'/\rho_0 \approx -\Theta'/\Theta_0$  from perturbation analysis of the ideal gas law (cf. chapter 3.3.1, Stull, 1988). In the following, the hydrostatic pressure is also subtracted from the pressure in the horizontal components of the **NSE** (2.2) since the reference pressure  $p_0$  is only a function of the wall-normal direction  $z$ .

### 2.2.6 Coriolis Acceleration and f-Plane Approximation

The Earth rotates; therefore, geophysical flow problems are generally analyzed with rotating reference frames. The sphericity of the Earth is neglected by considering a tangential plane on the Earth's surface at a particular latitude  $\phi$  so that the problem is amenable to Cartesian coordinates. The Coriolis acceleration (**RHS** of equations 2.2) is of crucial importance for the dynamics of geophysical flows and is defined as

$$-2\epsilon_{ijk}\Omega_i u_k = -2\Omega \begin{pmatrix} w \cos(\phi) - v \sin(\phi) \\ u \sin(\phi) \\ -u \cos(\phi) \end{pmatrix}, \quad \text{with } \Omega \equiv |\Omega_i| = \left| \begin{pmatrix} 0 \\ \cos(\phi) \\ \sin(\phi) \end{pmatrix} \right|, \quad (2.11a,b)$$

where  $\Omega_i$  is the angular velocity vector of the Earth in the tangential plane. The *thin layer approximation* states that the horizontal extent of geophysical flow problems is significantly larger than the vertical. Hence,  $|u|, |v| > |w|$  and  $w \cos(\phi)$  is neglected in equation (2.11a) (cf. Kundu et al., 2015). The effect of the Coriolis acceleration is confined to the horizontal components of the momentum equations (2.2), a limitation that is valid at high latitudes,

and thus the equation (2.11a) reduces to

$$-2\epsilon_{ijk}\Omega_i u_k = \begin{pmatrix} fv \\ -fu \\ 0 \end{pmatrix}, \quad \text{with } f = 2\Omega \sin(\phi), \quad (2.12a,b)$$

the Coriolis parameter. By choosing  $f = \text{const.}$  (e.g. at the poles, where  $f = 2\Omega$  or at a fixed latitude  $\phi_0$ ), the *f-plane approximation* applies. The associated time scale is the inertial period  $2\pi/f$ .

### 2.2.7 Pressure Decomposition and Geostrophic Balance

The total, non-hydrostatic pressure gradient of the system is decomposed into a large-scale geostrophic and an ageostrophic contribution

$$\frac{\partial \pi^*}{\partial x_k} = \frac{\partial \pi_{\text{geo}}}{\partial x_k} + \frac{\partial \pi}{\partial x_k}, \quad (2.13)$$

where  $\partial \pi_{\text{geo}}/\partial x_k$  is an external parameter of the flow problem. Above the **ABL**, the pressure gradient term is in equilibrium with the Coriolis acceleration, assuming a large-scale flow, which is stationary, inviscid (frictionless) and shear-free. The geostrophic balance in the horizontal direction is defined as

$$fG_j = \epsilon_{jk3} \frac{\partial \pi_{\text{geo}}}{\partial x_k}, \quad (2.14)$$

with the geostrophic wind vector  $\mathbf{G} = (G_1, G_2, 0)^T$ . In this study, the flow is driven by a constant geostrophic wind, e.g., a constant geostrophic pressure gradient perpendicular to the flow. If not stated otherwise, the direction of the geostrophic wind is in the streamwise, and the pressure gradient is in the spanwise direction.

### 2.2.8 Simplified Set of Equations and Boundary Conditions

The conservation equations of mass (2.1), momentum (2.2) and energy (2.4) are simplified, under consideration of the above assumptions, to the divergence-free constraint, the incompressible **NSE** under the Boussinesq approximation on an f-plane and the advection-diffusion equation for buoyancy:

$$\frac{\partial u_j}{\partial x_j} = 0, \quad (2.15a)$$

$$\frac{\partial u_j}{\partial t} + u_i \frac{\partial u_j}{\partial x_i} = -\frac{\partial \pi}{\partial x_j} + \nu \frac{\partial^2 u_j}{\partial x_i^2} + f\epsilon_{jk3}(u_k - G_k) + b\delta_{j3}, \quad (2.15b)$$

$$\frac{\partial b}{\partial t} + u_j \frac{\partial b}{\partial x_j} = \kappa_d \frac{\partial^2 b}{\partial x_j^2}, \quad (2.15c)$$

where  $\pi$  is the ageostrophic and non-hydrostatic modified pressure of the system (2.13) and  $b$  is the buoyancy variable (2.10b). This set of equations is valid for a Newtonian fluid with constant fluid properties. The fluid motion is driven by the external parameter of the flow problem, the constant geostrophic wind. The boundary conditions for the velocity fields are no-slip and impermeability on solid walls, e.g. the lower domain boundary and roughness elements attached to it, with

$$u_i|_{z=\text{wall}} = 0. \quad (2.16)$$

Free-slip boundary conditions are applied on the upper domain boundary such that

$$\left. \frac{\partial u}{\partial z} \right|_{z=\text{top}} = \left. \frac{\partial v}{\partial z} \right|_{z=\text{top}} = 0. \quad (2.17)$$

From the divergence-free condition (2.15a), it follows  $w|_{z=\text{top}} = 0$ . The use of Dirichlet boundary conditions instead of Neumann boundary conditions (2.17) by matching the horizontal velocities with the geostrophic wind at the upper domain boundary would converge to similar results, according to the considerations of Deusebio et al. (2014). Provided that the vertical extent of the domain is sufficiently large. Dirichlet boundary conditions are used for the buoyancy fields on the upper and lower domain boundaries, with a constant difference  $\Delta B = B_0 - 0$ , so:

$$b|_{z=\text{wall}} = 0, \quad b|_{z=\text{top}} = B_0. \quad (2.18a,b)$$

## 2.3 Non-dimensionalization

Dimensional analysis is a powerful tool in fluid dynamics for reducing complexity and developing similarity theories. The underlying physical principles of the flow systems under consideration are independent of units. Therefore, describing flow problems with non-dimensional parameters is mathematically possible, resulting in a reduced set of relevant variables (Kundu et al., 2015). The concept of hydrodynamic similarity can be applied with the Buckingham- $\Pi$  theorem (Buckingham, 1914) when rescaling a real-world flow problem for numerical or laboratory experiments. In the following, the governing equations (2.15) are non-dimensionalized and leading dimensionless parameters are identified (section 2.3.1). The parameter space spanned by the set of non-dimensional numbers of the flow problem is then investigated (section 2.3.2).

### 2.3.1 Non-dimensional Parameters

The set of the governing, dimensional flow equations (2.15) is non-dimensionalized with the following characteristic scales of the flow problem: the geostrophic wind  $G = \sqrt{G_1^2 + G_2^2}$ , the Coriolis parameter  $f$ , the Rossby radius  $\Lambda_{Ro} = G/f$ , the dynamical reduced pressure  $G^2$  and the buoyancy difference between the upper and lower domain boundary  $\Delta B = B_0$  (cf. equations 2.18). Using these characteristic scales, the non-dimensional set of flow equations is as follows

$$\frac{\partial u_j}{\partial x_j} = 0, \quad (2.19a)$$

$$\frac{1}{Ro_\Lambda} \frac{\partial u_j}{\partial t} + u_i \frac{\partial u_j}{\partial x_i} = -Eu_\Lambda \frac{\partial \pi}{\partial x_j} + \frac{1}{Re_\Lambda} \frac{\partial^2 u_j}{\partial x_i^2} + \frac{1}{Ro_\Lambda} \epsilon_{jk3} (u_k - g_k) + Ri_\Lambda b \delta_{j3}, \quad (2.19b)$$

$$\frac{1}{Ro_\Lambda} \frac{\partial b}{\partial t} + u_j \frac{\partial b}{\partial x_j} = \frac{1}{Re_\Lambda Pr} \frac{\partial^2 b}{\partial x_j^2}, \quad (2.19c)$$

with the non-dimensional geostrophic wind vector  $\mathbf{g} = (g_1, g_2, 0)^T$ , with  $\mathbf{g} = \mathbf{G}/G$  (by construction  $g = \|\mathbf{g}\| = 1$ ). Hats over non-dimensional variables are omitted for convenience. Unless otherwise noted, variables are always non-dimensional from this point onwards. Five dimensionless numbers determine the flow problem, including the Prandtl number, which is fixed to unity in this study and is therefore close to the value for air  $Pr_{\text{air}} \approx 0.71$ . The Rossby number  $Ro_\Lambda$  and Euler number  $Eu_\Lambda$  are equal to unity due to the choice of scales since

$$Pr = \frac{\nu}{\kappa_d} = 1, \quad Ro_\Lambda = \frac{G}{\Lambda_{Ro} f} = 1, \quad Eu_\Lambda = \frac{G^2}{G^2} = 1, \quad (2.20a,b,c)$$



and are therefore not considered further. The remaining two relevant non-dimensional numbers are

$$Re_\Lambda = \frac{G\Lambda_{Ro}}{\nu} = \frac{G^2}{f\nu}, \quad Ri_\Lambda = \frac{\Delta B\Lambda_{Ro}}{G^2} = \frac{\Delta B}{Gf}, \quad (2.21a,b)$$

with the Reynolds number  $Re_\Lambda = Ek_\Lambda^{-1}$ , which is the inverse of the Ekman number  $Ek_\Lambda$ , and with the Richardson number  $Ri_\Lambda = Fr_\Lambda^{-2}$ , which is the squared inverse of the Froude number  $Fr_\Lambda$ . In the absence of buoyancy, i.e.  $Ri_\Lambda = 0$ , the buoyancy term in the NSE (2.19b) is omitted and the buoyancy equation (2.19c) becomes an advection-diffusion equation of a passive scalar  $s$  (e.g. tracer gas, pollutant concentration), which is non-dimensionalized with the scalar difference  $\Delta S = S_0$  between the upper and lower domain boundary. The passive scalar conservation equation is

$$\frac{\partial s}{\partial t} + u_j \frac{\partial s}{\partial x_j} = \frac{1}{Re_\Lambda Sc} \frac{\partial^2 s}{\partial x_j^2}, \quad (2.22)$$

where  $Sc \hat{=} Pr$  is the Schmidt number. In that case, the dynamics of the neutrally stratified boundary layer is solely governed by the Reynolds number  $Re_\Lambda$ .

### 2.3.2 Parameter Space and Regime Transitions

The neutral Ekman flow is governed by one single dimensionless number, the Reynolds number, which results from the non-dimensionalization of the governing equations in section 2.3.1. The Richardson or Froude numbers enter the problem as a second parameter if stratification is considered additionally. Surface heterogeneity is introduced by inserting obstacles into the flow domain using suitable boundary conditions. A plethora of parameters exist to describe surface roughnesses (cf. Kadivar et al., 2021). In the present study, the type and statistical properties of the surface roughness are constant, except for the mean height of the roughness elements, which is fixed in time and varies only among obstacles. Since the focus of this study is on the logarithmic region (section 2.4.4) and surface layer similarity (section 2.4.5), the effect of roughness is typically condensed into one single parameter, the aerodynamic or hydraulic roughness length  $z_0^+$  (non-dimensionalized with the viscous scale, which equals to a roughness Reynolds number). Potentially, further roughness parameters exist relating to the roughness pattern, but are ignored consciously in accordance with surface layer similarity. The flow problem is therefore determined by the three-dimensional parameter space spanned by  $Re$ ,  $Ri$  and  $z_0^+$  (cf. Figs. 2.1).

According to Monin and Yaglom (1971), the laminar regime is characterized by a smooth, quiet flow in space and time, whereby some canonical flow problems are amenable to analytical solutions. In contrast, turbulent flow is characterized by irregular fluctuations in all flow quantities. The transition from laminar to turbulent flow—the onset of turbulence—without density stratification is attributed to the seminal work of Reynolds (1895). The laminar flow turns turbulent if the Reynolds number exceeds a critical value  $Re > Re_{\text{crit}}$ . For neutral Ekman flow, it is  $Re_{\text{crit}} = 115$  (Lilly, 1966).

Nevertheless, a Reynolds number close to  $Re_{\text{crit}}$  is undesirable since a fully-developed turbulent flow demands a large enough Reynolds number (cf. discussion: *How high a  $Re$  is high enough?*, Moin and Mahesh, 1998; Dimotakis, 2000). Meanwhile, dynamical similarity, which requires matching the Reynolds numbers of an atmospheric flow and the DNS, is practically impossible (cf. discussion in Mellado et al., 2018). Here, the principle of Reynolds number similarity comes into play despite the mismatch in the Reynolds numbers (several orders of magnitude). The core of the Reynolds number similarity is the assumption that certain statics of the flow become independent of  $Re$  at sufficiently high  $Re$ , i.e. viscous effects are negligible (Monin and Yaglom, 1971; Tennekes and Lumley, 1972; Wyngaard, 2010). Reynolds number similarity is applicable if the scale separation



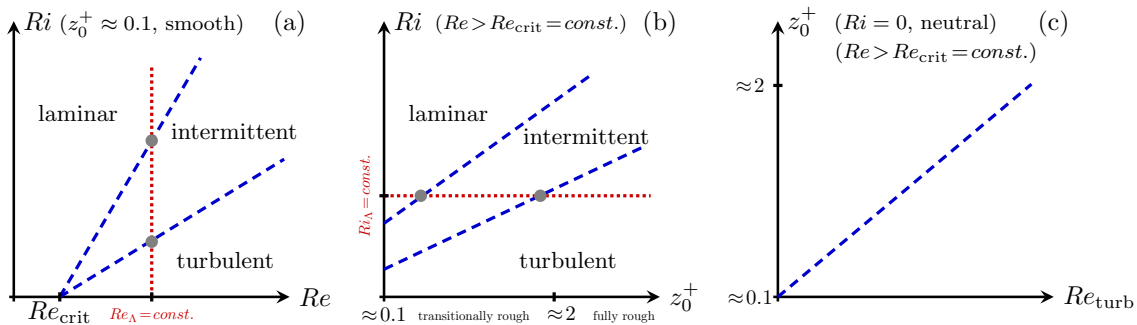


**Fig. 2.1** Schematic of the three-dimensional parameter space of the stratified turbulent Ekman flow over a rough surface. Spanned by the Reynolds number  $Re$ , Richardson number  $Ri$  and the aerodynamic roughness length in viscous units  $z_0^+$ . The red dotted lines exemplify the expected regime changes for (a) fixed external Reynolds number and increasing stability and (b) fixed Richardson number but increasing aerodynamic roughness length. The exact shapes of the regions are unknown and, therefore, depicted with straight dashed lines.

between large and small scales is sufficiently large to exhibit a fully-developed inertial subrange in the theory of Kolmogorov (1941). Moreover, it is a useful concept since the focus of interest is often the asymptotical behavior of  $z_0^+$  of certain statistics with the Reynolds number.

Stable density stratification suppresses turbulence production, and if the latter is strong enough, it leads to a collapse of turbulence and a relaminarization of the flow. Global intermittency is observed in the **VSBL**, a process in time and space where turbulent and quasi-laminar fluid patches coexist (Mahrt, 1999). A flow at constant external Reynolds number, e.g.  $Re_\Lambda = \text{const.}$ , and increasing stability would experience a regime transition from the turbulent (**WSBL**) via the intermittent (**VSBL**) to the laminar regime (cf. red dotted line in Fig. 2.1a). Theoretical and conceptual studies have explored the collapse of turbulence for qualitative understanding of the phenomenon (Derbyshire, 1999; Van de Wiel et al., 2002), alongside the concept of the maximum sustainable heat flux (**MSHF**) (Van de Wiel et al., 2012a,b; Van Hooijdonk et al., 2018). Numerical studies of stably stratified flow discovered the relevance of the Obukhov length (another measure of stability beside  $Ri$ ) either scaled with the boundary layer thickness (Nieuwstadt, 2005) or scaled in viscous units (equal to an Obukhov–Reynolds number) as a criterion for the collapse of turbulence (Flores and Riley, 2011; Deusebio et al., 2015). Coleman et al. (1992) give a critical surface Richardson number for the relaminarization of the flow, whereas Shah and Bou-Zeid (2014) observed a Reynolds number dependence of this criterion. According to Anson and Mellado (2014), global intermittency is an intrinsic feature of the **VSBL** without needing external triggering mechanisms, apart from requiring large-scale structures to be sufficiently represented in the computational domain.

Lee et al. (2020) performed **DNS** of the stably stratified Ekman flow over a smooth and rough wall with a periodic hill. A constant large-scale forcing drives their cases, and the roughness setup is located in the transitionally rough regime. When comparing the smooth and rough case, they observe a regime shift from the **VSBL** with intermittent turbulence to the **WSBL** with continuous turbulence in the near-wall region of the flow. Hence, roughness effectively counteracts buoyancy-induced stability through enhanced mixing and an increased vertical velocity. Similar destabilizing effects are investigated by Mironov and Sullivan (2023), who studied very stable stratified Couette flow (flow between two periodic horizontal plates, one at rest and the other moving at a constant speed, which drives the flow) with a heterogeneous surface temperature. Here, convective instabilities enable

turbulence to survive in contrast to a laminar flow over a surface with a homogeneous temperature. Therefore, a system with constant stratification (and Reynolds number) is expected to experience a regime shift for an increasing aerodynamic roughness length (cf. red dotted line in Fig. 2.1b).

The apparent effect of surface roughness is enhanced mixing and transport of the turbulent flow and an increasing drag (drag-reducing riblets are irrelevant to geophysical flows and thus not considered; Soleimani and Eckels, 2021). It is expected that a turbulent Reynolds number (based on a turbulent velocity scale, e.g. square root of **TKE**) increases with increasing roughness height, respectively  $z_0^+$  (cf. Fig. 2.1c).

## 2.4 Wall-bounded Turbulent Ekman Flow

Most technical and geophysical flows are turbulent flows bounded by at least one solid (impermeable) wall. A condition that also applies to atmospheric flows, which are confined below by the Earth's surface. The wind decelerates towards the lower wall, where it comes to rest due to friction, resulting in vertical wind shear and mixing. Turbulence is mainly mechanically produced in the vicinity of the wall by wind shear and in the presence of unstable stratification by buoyancy. In the near-wall region, the viscosity is essential to enforce the no-slip boundary condition at the wall (cf. chapter 5., Tennekes and Lumley, 1972). Within the **ABL**, the dominant dynamical processes are fluid-wall interactions by drag, rotation of the reference frame (Coriolis force) and stratification caused by a mean temperature gradient in the boundary layer. In this study, the canonical Ekman flow is a surrogate for studying the dynamics of the **ABL**. The statistical tools for analyzing turbulent flow are briefly outlined in the first section (section 2.4.1), followed by the presentation of the analytical solution of the laminar Ekman flow (section 2.4.2). Afterwards, the important scales of turbulent motion (section 2.4.3), the logarithmic law of the wall (section 2.4.4) and the Monin–Obukhov Similarity Theory (section 2.4.5) are presented.

### 2.4.1 Statistical Analysis

The flow is turbulent once the Reynolds number exceeds a critical value,  $Re > Re_{\text{crit}}$  (cf. section 2.3.2), which is generally the case in the **ABL**. The characteristic chaotic, turbulent nature of the atmospheric flow is described by the deterministic, non-linear **NSE**, which are highly sensitive to unavoidable initial perturbations. The exact prediction and reproducibility of a hydrodynamic variable  $\varphi(x_i, t)$  (e.g.  $\mathbf{u}$ ,  $\pi$ ,  $\Theta$ ) at a specific instance in time and space is impossible, even in the best controlled experimental surroundings (Lorenz, 1963, 1969). Thus, hydrodynamic variables in the turbulent flow are treated as random variables. However, turbulent flows behave similarly under the same conditions and are therefore studied in the mean by statistical methods rather than examining individual realizations of the random flow variables. The ensemble mean is the arithmetic average of a large number of samples from experiments with similar external conditions, though hard to achieve in practice. The ergodicity hypothesis circumvents this issue and implies that time averages of a steady flow and space averages of a homogeneous flow converge for sufficient large measurement intervals (in space/time) to the ensemble mean (Monin and Yaglom, 1971; Wyngaard, 2010).

The Reynolds decomposition (Reynolds, 1895) splits the instantaneous random flow variable  $\varphi$  into a mean part  $\bar{\varphi}$  and fluctuating part  $\varphi'$ , the departure from the mean, and

is defined for a statistically stationary flow as

$$\varphi(x_i, t) = \overline{\varphi}(x_i) + \varphi'(x_i, t), \quad \text{with} \quad \overline{\varphi}(x_i) = \lim_{\Delta t \rightarrow \infty} \frac{1}{\Delta t} \int_{t-\Delta t/2}^{t+\Delta t/2} \varphi(x_i, \tilde{t}) d\tilde{t}. \quad (2.23a,b)$$

Throughout this study, periodic boundary conditions are used in the horizontal directions. The mean is considered a space-time estimated mean, given that the simulations are conducted on a discrete Cartesian grid  $[n_x, n_y, n_z]$  for a limited time interval  $\Delta t$ , with  $n_t$  statistically independent samples, under the assumption of a quasi-steady state of the flow. Hence, the computed mean is a function of the vertical grid node positions  $x_k$  and given by

$$\langle \overline{\varphi} \rangle(z_k) = \frac{1}{n_x n_y n_t} \sum_{i=1}^{n_x} \sum_{j=1}^{n_y} \sum_{l=1}^{n_t} \varphi(x_i, y_j, z_k, t_l). \quad (2.24)$$

Here,  $\langle (\cdot) \rangle$  is used for spatial averaging in the horizontal and  $\overline{(\cdot)}$  for temporal averaging.

If roughness is present in the computational domain, intrinsic averaging is applied for first-order and second-order statistical moments of the flow variables. This method excludes any values inside the solid objects from averaging, as the focus of interest is on the statistical properties of the fluid and is based on the framework of conditional averaging (Pope, 2000). Therefore, the computational domain is decomposed into a solid and fluid part according to the indicator function  $\epsilon(x_i)$  (equation 1.1), where  $\epsilon(x_i) = 1$  in the solid and  $\epsilon(x_i) = 0$  in the fluid part of the domain. Taking the horizontal average of  $\epsilon(x_i)$  results in height-dependent volume fractions  $\gamma(z)$ , with the corresponding superscript  $(\cdot)^{0,1}$  for fluid/solid, which reads as

$$1 = \gamma^0(z) + \gamma^1(z) = [1 - \langle \epsilon(x_i) \rangle] + \langle \epsilon(x_i) \rangle. \quad (2.25)$$

The first and second order statistical moments are decomposed as follows

$$\langle \overline{\varphi}_i \rangle^{\text{ex}} = \gamma^0 \langle \overline{\varphi}_i \rangle^0 + \gamma^1 \langle \overline{\varphi}_i \rangle^1, \quad (2.26a)$$

$$\langle \overline{\varphi'_i \varphi'_j} \rangle^{\text{ex}} = \gamma^0 \langle \overline{\varphi'_i \varphi'_j} \rangle^0 + \gamma^1 \langle \overline{\varphi'_i \varphi'_j} \rangle^1 + \gamma^0 \gamma^1 [\langle \overline{\varphi}_i \rangle^0 - \langle \overline{\varphi}_i \rangle^1] [\langle \overline{\varphi}_j \rangle^0 - \langle \overline{\varphi}_j \rangle^1], \quad (2.26b)$$

where  $\langle \overline{(\cdot)} \rangle^{\text{ex}}$  are extrinsic averages. Extrinsic averages consider all values across the domain equally and correspond to equation (2.24) applied to a flow with roughness. Hereby the values of  $\langle \overline{(\cdot)} \rangle^1$  must be known in advance and statistical moments  $\langle \overline{(\cdot)} \rangle^0$  are of interest. The conditional averaging is further advanced in study I (cf. chapter 4).

## 2.4.2 The Laminar Ekman Solution

Inspired by the fact that ice in the Arctic Ocean drifts not in the direction of the mean wind, but rather at an angle of  $20^\circ - 40^\circ$ , Ekman (1905) presented in his seminal work at the beginning of last century an analytical solution of the laminar problem. In his honor, this flow problem is named after him. The flow is considered stationary and horizontal homogeneous, subsidence is neglected, and the flow is in the Boussinesq limit and geostrophic balance. Regarding these assumptions, the horizontal momentum equations (2.15b) of the mean flow by applying Reynolds averaging are as follows:

$$0 = -f(G_2 - \bar{v}) + \nu \frac{\partial^2 \bar{u}}{\partial z^2} - \frac{\partial \overline{u'w'}}{\partial z}, \quad (2.27a)$$

$$0 = f(G_1 - \bar{u}) + \nu \frac{\partial^2 \bar{v}}{\partial z^2} - \frac{\partial \overline{v'w'}}{\partial z}. \quad (2.27b)$$

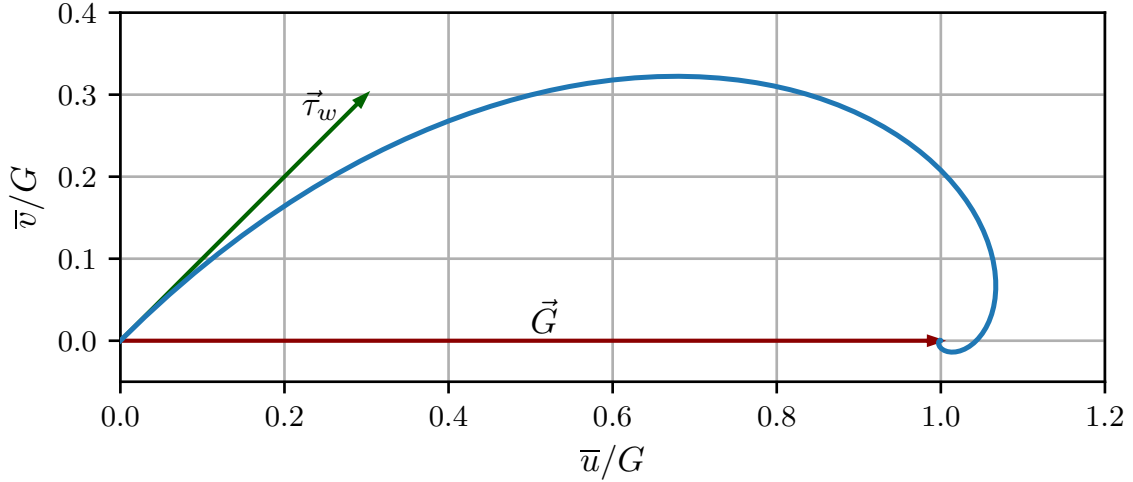


**Fig. 2.2** The laminar Ekman spiral (cf. equations 2.29). The velocities are normalized by the magnitude of the geostrophic wind vector  $G = G_1$  (red arrow). The surface shear stress  $\vec{\tau}_w$  (green arrow) has an angle of  $45^\circ$  with respect to  $\vec{G}$ .

Note that the equations are in dimensional form. The turbulent shear stress is approximated using the eddy-diffusivity approach with a constant eddy viscosity  $\nu_e$ , which was initially mentioned by Boussinesq (cf. § 3.4.1 on p.171, Rotta, 1972) and reads as

$$\frac{\partial}{\partial z} \left( \nu \frac{\partial \bar{u}_i}{\partial z} - \overline{\partial u'_i w'} \right) = \frac{\partial}{\partial z} \left( \nu \frac{\partial \bar{u}_i}{\partial z} + \nu_e \frac{\partial \bar{u}_i}{\partial z} \right) = \nu_{\text{eff}} \frac{\partial^2 \bar{u}_i}{\partial z^2}, \quad (2.28a)$$

$$\text{with } \nu_{\text{eff}} = \nu + \nu_e = \text{const.}, \quad (2.28b)$$

where  $\nu_{\text{eff}}$  is the constant effective viscosity. The boundary conditions are no-slip at the ground  $\bar{u}_i|_{z=\text{wall}} = 0$  and a constant geostrophic wind above the boundary layer  $\bar{u}|_{z \rightarrow \infty} = G_1$  while aligning the geostrophic wind with the  $x$ -axis, viz.  $G = G_1$  and  $\bar{v}|_{z \rightarrow \infty} = 0$ . The solution of the coupled second-order differential equation is the Ekman spiral (Fig. 2.2):

$$\frac{\bar{u}}{G}(\tilde{z}) = 1 - e^{-\tilde{z}} \cos(\tilde{z}), \quad (2.29a)$$

$$\frac{\bar{v}}{G}(\tilde{z}) = e^{-\tilde{z}} \sin(\tilde{z}), \quad (2.29b)$$

where the dimensionless height  $\tilde{z} = z/D$ , is the height normalized by the laminar Ekman layer depth  $D = \sqrt{2\nu_{\text{eff}}/f}$ . The associated Reynolds number is  $Re_D = DG/\nu_{\text{eff}}$  and is commonly used for the comparison of numerical studies, whereby  $Re_D \propto \nu_{\text{eff}}^{-1/2}$ . The height-dependent turning of the wind is  $45^\circ$  between the surface shear stress and the geostrophic wind.

### 2.4.3 The Scales of Neutrally Stratified Turbulent Ekman Flow

Ekman flow is, according to Spalart (1989), the “[...] simplest situations that can produce a boundary layer with three-dimensional statistics”. The author refers to the decisive term in the NSE, the Coriolis term, which renders the turbulent Ekman flow truly three-dimensional with non-zero components of the Reynolds stress tensor  $\overline{u'_i u'_j}$ . In other words, the steady system rotation leads to a loss of symmetry in the spanwise direction compared to turbulent channel flow. After sufficient time for the initial transient phase, when the flow is decorrelated from the initial conditions, the system reaches a statistically steady state. Once the flow is turbulent, the boundary layer thickness  $\delta$  is the relevant length scale rather than the laminar scale  $D$  (cf. equations 2.29). In turbulent Ekman flow, the

boundary layer thickness is  $\delta = u_\tau/f$  (non-dimensional:  $\delta_\star = \delta/\Lambda_{Ro}$ ), with the friction velocity  $u_\tau$  (non-dimensional:  $u_\star = u_\tau/G$ ) and Coriolis parameter  $f$ . The relevant time scale is the eddy-turnover time  $\delta/u_\tau = f^{-1}$ , emerging from the ratio of turbulent scales for the boundary layer thickness  $\delta$  and velocity  $u_\tau$ . The steady system rotation stabilizes the boundary layer thickness, which is constant in contrast to a boundary layer flow over a flat plate, where the boundary layer spatially evolves with  $\delta(x)$ .

In the vicinity of the wall, the relevant parameters are: the viscosity  $\nu$ , the wall shear stress  $\boldsymbol{\tau}_w$  (non-dimensional:  $|\boldsymbol{\tau}_\star| = |\boldsymbol{\tau}_w|/(\rho G^2)$ ) and the density  $\rho$ . With these parameters, the friction velocity  $u_\star$ , the viscous length scale and the friction Reynolds number are defined as

$$u_\star^2 = \frac{1}{Re_\Lambda} \sqrt{\left(\left.\frac{\partial \langle u \rangle}{\partial z}\right|_{z=0}\right)^2 + \left(\left.\frac{\partial \langle v \rangle}{\partial z}\right|_{z=0}\right)^2} = |\boldsymbol{\tau}_\star|, \quad \delta_\nu = \frac{\nu}{u_\tau}, \quad Re_\tau = \frac{u_\tau \delta}{\nu}. \quad (2.30a-c)$$

The friction Reynolds number can be rewritten to  $Re_\tau = \delta/\delta_\nu$ , as the scale separation between the largest and the smallest possible length scale of the flow problem. The angle of the surface wind to the geostrophic wind, respectively, the surface shear stress alignment, is given by

$$\alpha_\star = \sphericalangle(-\boldsymbol{\tau}_\star, \mathbf{g}). \quad (2.31)$$

In turbulent Ekman flow, the scales  $u_\star$ ,  $\alpha_\star$  (and  $\delta_\star$ ) are inherent flow parameters and therefore unknown *a priori*. They are weak functions of the Reynolds number  $Re_D$  according to the higher-order theory of Spalart (1989) and Coleman et al. (1990). In contrast, the friction velocity is an external parameter in turbulent channel flow since the imposed streamwise pressure gradient equals the total shear stress. A dual scaling system is used to consider different dominant processes depending on the wall distance. The viscous scaling  $(\cdot)^+$  is used in the inner layer, with the relevant scales  $u_\tau$  and  $\delta_\nu$ . Moreover, the outer scaling  $(\cdot)^-$  is used in the outer layer, with the relevant scales  $G$  and  $\delta$ . Limits of the flow regions are  $z^- = z/\delta < 0.1$  for the inner layer and  $z^+ = z/\delta_\nu > 50$  for the outer layer according to Pope (2000). The given limits are valid for turbulent channel flow and are also a good approximation for turbulent Ekman flow.

Analogously to the friction velocity, the friction of the buoyancy parameter is

$$b_\star = \frac{q_\star}{u_\star}, \quad \text{with} \quad q_\star = \frac{1}{Re_\Lambda Pr} \left.\frac{\partial \langle b \rangle}{\partial z}\right|_{z=0}, \quad (2.32a,b)$$

where  $b_\star$  is the friction value and  $q_\star$  the buoyancy surface flux. This procedure applies similarly to the passive scalar. The given definitions of  $u_\star$  (equation 2.30a), and  $b_\star$  (equation 2.32a) are valid for smooth walls. In the presence of surface roughness, the friction velocity (buoyancy) is evaluated from the total surface shear stress (total surface buoyancy flux).

#### 2.4.4 Viscous Sublayer and Logarithmic Law of the Wall

The logarithmic *Law of the Wall (log-law)* provides a universal velocity profile in the near-wall region of a turbulent flow and was initially postulated by Von Kármán (1930) and Prandtl (1932) and experimentally measured by Nikuradse (1932). The following derivations for a flow over a smooth and rough surface are based on the books of Monin and Yaglom (1971) and Pope (2000).

The relevant scales for turbulent flow are identified as  $\{\delta, u_\tau, \nu, \rho\}$  (resp.  $\boldsymbol{\tau}_w$  instead of  $u_\tau$ ) and dimensional analysis (e.g. Buckingham II-Theorem, Buckingham, 1914) yields

$$\frac{d \langle \bar{u} \rangle}{dz} = \frac{u_\tau}{z} \Psi \left( \frac{z}{\delta_\nu}, \frac{z}{\delta} \right), \quad (2.33)$$

with the velocity gradient as a universal non-dimensional function  $\Psi$  of the non-dimensional length scales for the inner and outer layer  $z^+ = z/\delta_\nu$ ,  $z^- = z/\delta$  (section 2.4.3). In the near-wall region, viscous effects dominate; thus, the only relevant scale is  $\delta_\nu$  for  $z/\delta \ll 1$  and  $z^+ \gg 1$  (Prandtl, 1925). This necessity implies no contradiction since the ratio of both length scales equals to the friction Reynolds number

$$Re_\tau = \frac{z^+}{z^-} = \frac{u_\tau \delta}{\nu}. \quad (2.34)$$

Hence, a sufficiently large Reynolds number, i.e. a scale separation between the inner and outer length scale, is required for a properly developed logarithmic layer in the flow. The logarithmic layer is commonly assumed to be located at  $z/\delta < 0.1$  and  $z^+ > 50$ , and thus  $Re_\tau > 500$  is necessary. The dimensionless velocity gradient and the velocity are

$$\frac{d\langle \bar{u} \rangle^+}{dz^+} = \frac{1}{z^+} \Psi_w(z^+), \quad (2.35a)$$

$$\langle \bar{u} \rangle^+ = \psi(z^+) = \int_0^{z^+} \frac{1}{z'} \Psi_w(z') dz'. \quad (2.35b)$$

Away from the wall,  $z^+ \gg 1$ , viscosity is negligible and  $\Psi_w = const. = 1/\kappa$ , with the von Kármán constant  $\kappa$ . The logarithmic law of the wall is defined as

$$\langle \bar{u} \rangle^+ = \frac{1}{\kappa} \ln(z^+) + A, \quad (2.36)$$

with the commonly accepted values of the integration constant of  $A \approx 5$  and  $\kappa \approx 0.4$ , although the exact values are under debate. In the close vicinity of the wall, the flow is assumed to be laminar and viscous drag dominates the wall shear stress  $\tau_w$ . Integration of  $\tau_w$  with the no-slip boundary condition  $\psi'|_{z^+=\text{wall}} = 1$  and Taylor-series expansion, gives

$$\langle \bar{u} \rangle^+ = z^+, \quad (2.37)$$

the linear velocity profile in the *viscous sublayer*, valid for  $z^+ < 5$ .

The above derivations are valid for an ideal, smooth wall. In contrast, roughness in turbulent flows appears at a characteristic length scale  $h_R$  (e.g. mean height of the roughness) and is an omnipresent feature of real-world applications. In his pioneering work, Nikuradse (1933) studied wall roughness by measuring the friction of rough pipe flow. The pipe walls were covered with uniform sandpaper roughness, specified by the sand grain diameter  $k_s$ . In general, the roughness scale  $h_R/\delta_\nu = h_R^+$  is identified as a relevant length scale for the effect of roughness on the law of the wall, and with  $z \ll \delta$  the velocity gradient is a non-dimensional universal function  $\Psi_I(z/\delta_\nu, h_R/\delta_\nu)$ . Roughness impacts the flow dependent on the scale  $h_R^+$ , provided that the Reynolds number of the flow is sufficiently high; (i) if  $h_R \ll \delta_\nu$  is small, the log-law (equation 2.36) is retained; (ii) if the roughness Reynolds number  $u_\tau h_R/\nu = h_R^+ \gg 1$  is large, momentum transport is dominated by pressure drag. Hence,  $\nu$  and  $\delta_\nu$ , are not relevant and the function  $\Psi_I$  is rewritten to  $\Psi_R(z/h_R)$ . The influence of roughness vanishes for  $z \gg h_R$ , and a constant asymptotic is reached with  $\Psi_R = const. = 1/\kappa$ . The velocity profile in this regime is

$$\langle \bar{u} \rangle^+ = \frac{1}{\kappa} \ln\left(\frac{z}{h_R}\right) + A_R, \quad (2.38)$$

where  $A_R$  is a universal constant. (iii) If  $h_R$  is  $\mathcal{O}(\delta_\nu)$ , the integration constant is a function of the roughness scale

$$\langle \bar{u} \rangle^+ = \frac{1}{\kappa} \ln\left(\frac{z}{h_R}\right) + \tilde{A}_R(h_R^+). \quad (2.39)$$



The associated roughness regimes are: (i) hydraulically (aerodynamically) smooth for  $k_s^+ \leq 5$ , with  $\tilde{A}_R(h_R^+) = A + \kappa^{-1} \ln(h_R^+)$ ; (ii) fully rough for  $k_s^+ \geq 70$ , with  $\tilde{A}_R(\infty) = B_2 = 8.5$ ; (iii) transitionally rough, with  $\tilde{A}_R(h_R^+)$  and  $5 < k_s^+ < 70$  (cf. Monin and Yaglom, 1971, Fig. 28). Roughness shifts the logarithmic region of the velocity profile downwards by the roughness function  $\Delta \langle \bar{U} \rangle^+$  (Hama, 1954; Clauser, 1954), which can be interpreted as a momentum loss due to deceleration of the flow by roughness. An alternative way to write the rough log-law (equation 2.39) is

$$\langle \bar{u} \rangle^+ = \frac{1}{\kappa} \ln(z^+) + A - \Delta \langle \bar{U} \rangle^+, \quad \text{with} \quad \Delta \langle \bar{U} \rangle^+ = \frac{1}{\kappa} \ln(h_R^+) + A - \tilde{A}_R(h_R^+). \quad (2.40a,b)$$

In the meteorological context, the rough log-law is commonly formulated as

$$\langle \bar{u} \rangle^+ = \frac{1}{\kappa} \ln\left(\frac{z}{z_0}\right), \quad \text{with} \quad z_0^+ = e^{\kappa(\Delta \langle \bar{U} \rangle^+ - A)}, \quad (2.41a,b)$$

where  $z_0$  is the aerodynamic roughness length, which is not a physical length scale but instead describes the dynamical impact of roughness on the logarithmic region with one single parameter. The roughness length for an aerodynamically smooth flow is  $z_0^+ \approx 0.1$ , for a fully rough flow  $z_0^+ \gtrsim 2$  and the transitionally rough flow at  $0.1 < z_0^+ < 2$ .

So far, the reference level  $z = 0$  was used equally for the smooth and rough surfaces. Surface roughness leads to a shift in the origin of the vertical axis by the zero-plane displacement height  $d_R$ , introduced by (Paeschke, 1937). Therefore, the rough log-laws derived above are extended using  $(z - d_R)$  instead of  $z$ . The displacement thickness  $0 \leq d_R \leq h_R$  depends on the roughness type and configuration, but a common estimate is given with  $d_R \approx \frac{2}{3}h_R$ . Height-dependent veering of the wind (Ekman spiral, cf. section 2.4.2) is an intrinsic feature of Ekman flow, which results in the use of the total horizontal wind  $\langle \bar{u}_h \rangle = \sqrt{\langle \bar{u} \rangle^2 + \langle \bar{v} \rangle^2}$  instead of  $\langle \bar{u} \rangle$  in the log-law.

Analogously to the above derivation for the velocity, the viscous sublayer and logarithmic layer are present for the non-dimensional temperature  $\Theta^+$  (Kader and Yaglom, 1972) with the universal profiles

$$\langle \bar{\Theta} \rangle^+ = Pr z^+, \quad \text{and} \quad \langle \bar{\Theta} \rangle^+ = \frac{1}{\kappa} \ln(z^+) + B(Pr), \quad (2.42a,b)$$

accordingly for the passive scalar  $s$  with Schmidt number  $Sc$ , instead of the Prandtl number  $Pr$ . The derivation of the rough log-law for the temperature (passive scalar) follows the above-described steps.

### 2.4.5 Monin–Obukhov Similarity Theory

The Monin–Obukhov Similarity Theory (Obukhov, 1946; reprinted in the Boundary-Layer Meteorology journal: Obukhov, 1971; Monin and Obukhov, 1954; Foken, 2006) provides a natural extension of the log-law by considering buoyancy effects in the surface layer. The underlying assumptions of the **MOST** are a steady, horizontally homogeneous flow in the Boussinesq limit over a flat surface (cf. discussion in Monin and Yaglom, 1971). The theory is valid in the surface layer, representing the lower part of the **ABL** near the ground, in which turbulent fluxes vary less than 10 % of their peak value. Therefore, this layer is commonly referred to as the constant flux or Prandtl layer, where  $\tau_* = q_* = \text{const.}$  (Garratt, 1992). In the constant flux layer, the effect of the Coriolis force and, thus, the veering of the wind with height is neglected ( $v = 0$ ). Consequently, the channel flow analogy is typically used to study the surface layer.

The parameters governing the dynamics of the surface layer are identified as (cf. Wyngaard, 2010): the distance from the wall  $z$ , the friction velocity  $u_\tau$ , the buoyancy parameter

$g_{\text{grav}}/\Theta_{\text{sfc}}$ , and the heat flux  $\langle w'\Theta' \rangle$ . Under consideration of these parameters, the dimensionless parameter  $z/L_O$  is formed with a new length scale, the Obukhov length<sup>1</sup>, which is defined as

$$L_O = -\frac{u_*^3}{\frac{g_{\text{grav}}}{\Theta_{\text{sfc}}} \langle w'\Theta' \rangle|_{z=\text{sfc}}} = \frac{u_*^2}{b_*}. \quad (2.43)$$

Here,  $\langle w'\Theta' \rangle|_{z=\text{sfc}}$  is the surface heat flux and  $\Theta_{\text{sfc}}$  the reference temperature in the surface layer. Physically,  $L_O$  is the height where the **TKE** production by shear equals the buoyant production (destruction) of **TKE** (Wyngaard, 2010). Flores and Riley (2011) proposed the Obukhov length scaled in wall units  $L_O^+ = L_O/\delta_\nu = Re_L$  as the relevant scale in a stably stratified flow over a smooth surface.  $L_O^+$  is a buoyancy Reynolds number  $Re_L$  (Obukhov–Reynolds number), describing the scale separation between the largest and smallest possible turbulent structures. Furthermore, they suggest  $L_O/h_R$  as the relevant scale in the presence of surface roughness.

By using the Buckingham  $\Pi$ -theorem, the non-dimensional gradient of a flow variable  $\mathcal{F}$  (e.g. the streamwise velocity  $u$ , temperature  $\Theta$ , respectively buoyancy  $b$ ) is described exclusively by a function of the non-dimensional stability parameter  $\zeta_{\mathcal{F}}$ , and thus

$$\Phi_{\mathcal{F}}(\zeta_{\mathcal{F}}) = \frac{\kappa_{\mathcal{F}}(z - d_R)}{\mathcal{F}_*} \frac{\partial \mathcal{F}}{\partial z}, \quad \text{with} \quad \zeta_{\mathcal{F}} = \frac{\kappa_{\mathcal{F}}(z - d_R)}{L_O}, \quad (2.44a,b)$$

where  $d_R$  is the zero-plane displacement thickness (smooth surface  $d_R = 0$ ),  $\kappa_{\mathcal{F}}$  the von Kármán constant of the log-layer of the variable  $\mathcal{F}$ , and  $\mathcal{F}_*$  the friction value of  $\mathcal{F}$ . The stability parameter is  $\zeta_{\mathcal{F}} < 0$  for unstable,  $\zeta_{\mathcal{F}} > 0$  for stable, and  $|\zeta_{\mathcal{F}}| \rightarrow 0$  for neutral conditions. Without density stratification, the log-law is recovered with  $\Phi_{\mathcal{F}}(\zeta_{\mathcal{F}} = 0) = 1$ . If stratification is present, the universal stability correction function  $\Phi_{\mathcal{F}}$  is used, which is determined experimentally. For stable conditions, the linear Businger–Dyer relation (Businger et al., 1971; Dyer, 1974) are widely accepted, with

$$\Phi_{\mathcal{F}}(\zeta_{\mathcal{F}}) = \alpha_{\mathcal{F}} + \beta_{\mathcal{F}}\zeta_{\mathcal{F}}. \quad (2.45)$$

The empirical parameters for the velocity profile are  $\alpha_m = 1$  and  $\beta_m \approx 5$  (Högström, 1988).

## 2.5 Numerical Framework of the DNS Code

**DNS** is the approach of numerically solving the **NSE** (2.2) by resolving all turbulent scales without parameterization for unrepresented processes. Hence, the size of the computational domain must be sufficient to capture the large energy-containing eddies, and the grid resolution must be fine enough to resolve the smallest scales for dissipation to represent the entire turbulent energy cascade. The fundamental flow equations with the four primitive variables pressure  $p$  and the three velocity components  $\mathbf{u} = (u, v, w)^T$  are abbreviated as

$$\frac{\partial \mathbf{u}}{\partial t} = F(\mathbf{u}, p), \quad \text{with} \quad F \in \mathbb{R}^4 \quad \text{and} \quad \mathbf{u} \in \mathbb{R}^3, \quad (2.46)$$

where the temporal evolution of the flow is described by  $\partial_t \mathbf{u}$  with the physical time  $t$  and a function  $F$ , representing the **RHS** of the **NSE** (2.2). This term includes the advection, diffusion, pressure gradient and other source or sink terms. Moreover, it can be decomposed into a function  $\tilde{F}$ , with  $F(\mathbf{u}, p) = \tilde{F}(\mathbf{u}) + \nabla p$ , which solely acts on the velocity vector field  $\mathbf{u}$ .

<sup>1</sup>By tradition, the Obukhov length includes the von Kármán constant  $\kappa$ , which is omitted here. The conversion is  $L_O^{46} = \kappa^{-1}L_O$ , where  $L_O^{46}$  is the original Obukhov length defined in Obukhov (1946).



The first step of numerically solving the continuous PDEs (2.46) is discretizing the fundamental flow problem in space and time with appropriate schemes (section 2.5.1). The focus of the next section 2.5.2 is on an adequate pressure treatment to avoid spurious numerical oscillations in the resulting flow fields efficiently. The last section 2.5.3 describes the IBM for inserting flow obstacles in the computational domain.

### 2.5.1 Temporal and Spatial Discretization Strategy

Temporal and spatial discretization strategies for numerically solving the governing flow equations are inevitable since no analytical solution for turbulent flow is known yet. With the underlying objective of accessing moderate to high Reynolds numbers, DNS of turbulent flow is computationally highly demanding with the need for massively parallel computation on HPC infrastructures. The discretization schemes need close attention to accuracy, stability, and efficiency to keep the simulation expenses within feasible limits and precisely represent small-scale processes.

**Spatial discretization with compact finite difference schemes.** Realizations of the three-dimensional flow are computed on a Cartesian mesh with an orthogonal coordinate system  $x_i = (x, y, z)^T$  throughout the present work. The grid is uniformly spaced in the horizontal directions and only stretched in the vertical direction. A one-dimensional uniform distribution of  $n_x$  grid nodes in the periodic domain of  $[0, L_x]$  is considered here. Grid node positions are given by  $x_i = (i - 1) \Delta x$  with  $1 \leq i \leq n_x$  and a uniform spacing between two neighboring grid nodes of  $\Delta x = L_x / (n_x - 1)$ . A continuous function  $f$ , representing any flow variable, is discretized as  $f_i = f(x_i)$ , with the approximate first and second derivatives  $f'_i, f''_i$  on the grid nodes.

The present DNS code uses compact Padé schemes of sixth-order accuracy for the evaluation of the spatial derivatives, first described in the seminal work of Lele (1992). They are written for the first derivative in general form as follows:

$$c_{11}f'_{i+2} + c_{21}f'_{i+1} + f'_i + c_{21}f'_{i-1} + c_{11}f'_{i-2} = c_{31} \frac{f_{i+1} - f_{i-1}}{2\Delta x} + c_{41} \frac{f_{i+2} - f_{i-2}}{4\Delta x} + c_{51} \frac{f_{i+3} - f_{i-3}}{6\Delta x}. \quad (2.47)$$

By choosing the prefactors to  $c_{11} = 0$ ,  $c_{21} = 1/3$ ,  $c_{31} = 14/9$ ,  $c_{41} = 1/9$  and  $c_{51} = 0$  a sixth-order accurate scheme is defined. Analogously, the second-order derivative is given by

$$c_{12}f''_{i+2} + c_{22}f''_{i+1} + f''_i + c_{22}f''_{i-1} + c_{12}f''_{i-2} = c_{32} \frac{f_{i+1} - 2f_i + f_{i-1}}{\Delta x^2} + c_{42} \frac{f_{i+2} - 2f_i + f_{i-2}}{4\Delta x^2} + c_{52} \frac{f_{i+3} - 2f_i + f_{i-3}}{9\Delta x^2}. \quad (2.48)$$

Again, choosing the prefactors to  $c_{12} = 0$ ,  $c_{22} = 2/11$ ,  $c_{32} = 12/11$ ,  $c_{42} = 3/11$  and  $c_{52} = 0$  results in a sixth-order accurate scheme. The unknown derivative values of neighboring grid nodes are located on the left-hand side (LHS), and known function values are on the RHS of the equations (2.47, 2.48). The linear equation systems of the compact schemes (2.47, 2.48) are written as

$$\mathbf{A}_x f' = \frac{1}{\Delta x} \mathbf{B}_x f, \quad \mathbf{C}_x f'' = \frac{1}{(\Delta x)^2} \mathbf{D}_x f, \quad (2.49a,b)$$

with the square matrices  $\mathbf{A}_x$ ,  $\mathbf{B}_x$ ,  $\mathbf{C}_x$  and  $\mathbf{D}_x$ , which are narrow banded, but circulant for periodic problems. The matrix  $\mathbf{A}_x$  ( $\mathbf{C}_x$ ) on the LHS couples all grid points needed to solve for  $f'$  ( $f''$ ) based on  $f$ . Hence, these schemes are considered as non-local or

global operators, which act on complete lines of data in every single direction in which the derivative of a field is evaluated. For that purpose, costly global transpositions of data between computational cores are necessary to solve the linear equation systems of the compact schemes. For solving these equations, the computationally efficient Thomas algorithm (solving tridiagonal equation systems on the basis of Gaussian elimination, cf. Thomas, 1949) with an operation count of  $\mathcal{O}(n)$  in contrast to the pseudo-spectral codes with  $\mathcal{O}(n \log n)$  is applied.

Up to here, uniformly spaced grids with periodic boundary conditions are considered. For non-periodic boundary conditions, biased schemes of lower order are used at the two boundary points closest to the wall (Carpenter et al., 1993). If a non-uniform grid in the vertical direction is used, the physical coordinate needs to be mapped first on a computational coordinate, which is uniformly spaced (Laizet and Lamballais, 2009).

On the one hand, second-order (central difference) schemes are computationally very cheap but suffer from significant errors at small scales; on the other hand, spectral schemes are considered exact, with the drawback of unfavorable computational costs and low flexibility concerning the choice of grids and compatibility of implementing an **IBM**. Compact schemes combine the benefits of both approaches: higher accuracy at small scales, affordable computational costs, high flexibility in terms of possible domain configurations and the ability to use **IBMs**. However, this comes at the price of costly global data transpositions.

Modified wavenumber analysis is applied to assess the resolution properties of a spatial discretization scheme (Lele, 1992). Here, the modified wavenumbers for the first  $k'(k)$  and second derivatives  $k''(k)$  of a specific differencing scheme are compared to the exact wavenumbers  $k$  of the spectral scheme (Figs. 2.3) and read as

$$k'(k) = \frac{c_{31} \sin(k) + (c_{41}/2) \sin(2k) + (c_{51}/3) \sin(3k)}{1 + 2c_{21} \cos(k) + 2c_{11} \cos(2k)}, \quad (2.50a)$$

$$k''(k) = \frac{2c_{32} [1 - \cos(k)] + (c_{42}/2) [1 - \cos(2k)] + (2c_{52}/9) [1 - \cos(3k)]}{1 + 2c_{22} \cos(k) + 2c_{12} \cos(2k)}. \quad (2.50b)$$

Coefficients for the second-order and tenth-order schemes can be found in Lele (1992). If a sixth-order compact scheme (equation 2.47) is used instead of a second-order central difference scheme (with  $f'_i = (f_{i+1} - f_{i-1})/(2\Delta x)$ ) for a fixed physical problem size and a 90% accurate resolution of the first derivative at small scale, only approximately 36% (0.25/0.7) of the grid nodes are required in one direction to obtain a similar resolution (cf. Fig. 2.3b).

**Temporal advancement with an explicit low-storage Runge-Kutta scheme.** With the endeavor of reaching the high Reynolds number regime with **DNS**, the need for preferably stable, efficient and accurate time-marching schemes arises due to limited computing resources. These requirements translate into a large time increment  $\tau$ , a memory-efficient computation and a small discretization error. Therefore, an explicit low-storage Runge-Kutta scheme (**RK**) is taken to integrate the set of **PDEs** (2.46) in time, starting from the state  $\mathbf{u}_n = \mathbf{u}(t_n)$  to  $\mathbf{u}_{n+1} = \mathbf{u}(t_n + \tau)$  with  $M$  intermediate stages. Low-storage **RK** schemes demand only  $2N$  memory per grid node, with  $N$  being the number of flow variables. The underlying idea is to leave valuable data in the memory and gradually overwrite it at the sub-stages. First, schemes up to third-order accuracy with three-stages were introduced by Williamson (1980), which read in general form as

$$\mathbf{u}_{n+1} = \mathbf{u}_n + \tau \sum_{j=1}^M b_j k_j, \quad \text{with} \quad (2.51a)$$

$$k_1 = F(t_n, \mathbf{u}_n), \quad (2.51b)$$

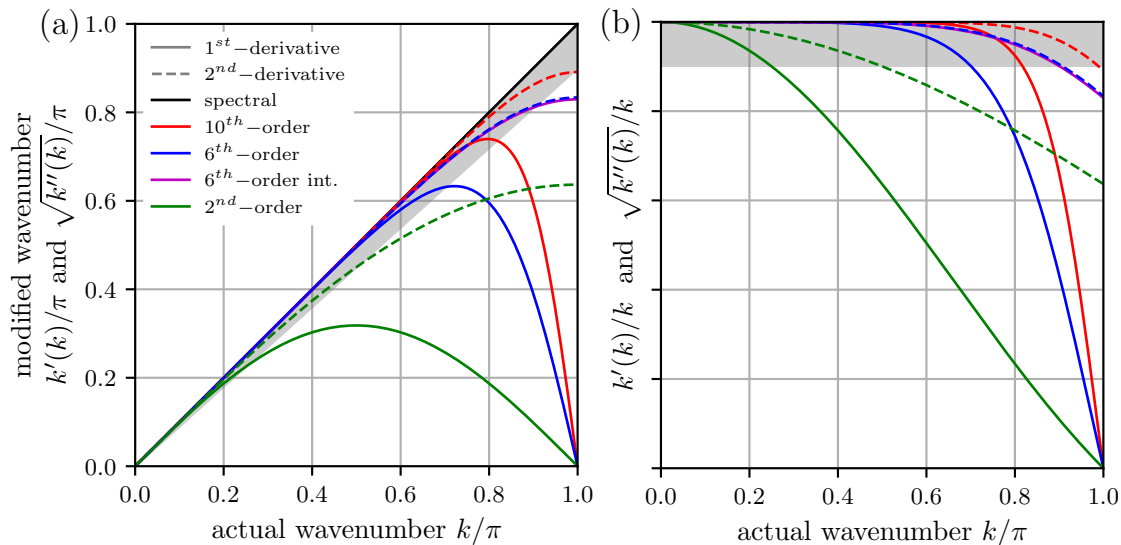


**Fig. 2.3** (a) Modified wavenumber analysis for second-order central differences and sixth-/tenth-order compact scheme, plotted against the actual wavenumber. (b) Relative deviation from the exact solution. The grey shaded area depicts the 90% resolution range.

$$k_j = F \left( t_n + c_i \tau, \mathbf{u}_n + \tau \sum_{j=1}^{i-1} a_{ij} k_j \right) \text{ and } i \in \{2, \dots, M\} \subset \mathbb{N}, \quad (2.51c)$$

with the set of **RK** coefficients  $a_{ij}, b_j, c_j \in \mathbb{R}$ . The sub-stages  $c_i$ , with  $i \in \{1, \dots, M\} \subset \mathbb{N}$ , are defined as  $c_i = \sum_{j=1}^M a_{ij}$ , with  $c_1 = 0$ , where  $a_{ij}$  represents the weights of the sub-stages. The coefficients  $b_j$ , with  $j \in \{1, \dots, M\} \subset \mathbb{N}$ , are the weights of the final sub-stage. Here, a low-storage fourth-order **RK** scheme is used with five sub-stages (**RK45**), introduced by Carpenter and Kennedy (1994). Compared to the conventional **RK4** scheme, one additional stage is needed to maintain storage efficiency and gain a better stability envelope.

The criterion based on the Courant–Friedrichs–Lewy number (**CFL**, Courant et al., 1928) gives the maximum stable time step size for an advection problem, which is discretized with an explicit time marching scheme. The idea is that the numerical velocity  $(\Delta x_i)/\tau$  should not exceed the advection velocity  $|u_i|$  by far. Nevertheless, implicit schemes as well as some **RK** schemes, can have larger values than  $CFL_{\max} = 1$ . The advection Courant–Friedrichs–Lewy number (**CFL**) number reads as

$$CFL_a = \tau \left\| \frac{u_i}{\Delta x_i} \right\|_{\infty}, \quad (2.52)$$

where  $\|\cdot\|_{\infty}$  is the infinity norm, representing the maximum ratio between the velocity component  $u_i$  and the corresponding grid spacing  $\Delta x_i$ . Similar to the advection problem, a diffusion **CFL** number is given by

$$CFL_d = \tau \left\| \frac{\nu}{(\Delta x_i)^2} \right\|_{\infty}, \quad (2.53)$$

with the viscosity  $\nu$ . Wilson et al. (1998) provides values for the advection and diffusion constraints, with values of  $CFL_{a,\max} \approx 1.7$  and  $CFL_{d,\max} \approx 0.7$  for a **RK45** temporal scheme and a sixth-order compact scheme. To retain numerical stability and also keeping numerical errors small,  $CFL_a \approx 1.2$  with a safety factor of 30% and  $CFL_d = 0.25 \times$

$CFL_a \approx 0.3$  (with this choice of  $CFL_d$ , dissipative and diffusive errors are of  $\mathcal{O}(1\%)$ , cf. Ansonge (2017)) are used in this study. The simulation time step  $\tau$  is adapted according to both constraints.

### 2.5.2 Pressure Treatment

**The pressure problem and the fractional-step method.** The fundamental equations for an unsteady and incompressible flow without a scalar are a set of four equations (three momentum equations (2.19b), one continuity equation 2.19a) with the same number of unknown variables ( $p, \mathbf{u}$ ), but without an explicit evolution equation for the pressure. In the primitive variable formulation, pressure implicitly couples the continuity and momentum equations. Here, the pressure projects the velocity fields onto a divergence-free space. The implicit coupling is circumvented by taking the divergence of the momentum equations and thereby obtaining an explicit Poisson-type equation for the pressure, which is time-consuming and numerically challenging to solve. (In contrast, the implicit coupling of pressure and velocities does not occur in the compressible formulation of flow problems, where the continuity equation contains the time-derivative of the fluid density. In this case, the pressure is directly calculated with the equation of state (equation 2.5a).)

The discretized equations in time and space are solved via the fractional-step (also known as time-splitting) method, which was introduced by Chorin (1968) and Témam (1969) and in the context of DNS described by Kim and Moin (1985) and Wilson et al. (1998). A significant drawback of this method is first-order accuracy in terms of time for pressure (Perot, 1993). Brown et al. (2001) studied the interplay of boundary conditions on the intermediate velocity vector and the approximation of the pressure gradient term. With a change in the pressure-update step, a second-order accuracy in the pressure is achieved.

In principle, the fractional-step method splits the time advancement of the discretized equations into three steps:

$$\mathbf{u}^* = \tau \tilde{F} + \mathbf{u}_n, \quad (2.54a)$$

$$\phi_{n+1} = \frac{1}{\tau} \Delta^{-1} (\nabla \mathbf{u}^*), \quad (2.54b)$$

$$\begin{aligned} \frac{\mathbf{u}_{n+1} - \mathbf{u}^*}{\tau} &= -\nabla \phi_{n+1} \\ &= -\nabla \left\{ \frac{1}{\tau} \Delta^{-1} \left[ \nabla \left( \tau \tilde{F} + \mathbf{u}_n \right) \right] \right\}, \text{ with } \nabla \mathbf{u}_{n+1} = 0, \end{aligned} \quad (2.54c)$$

where the subscript  $n$  denotes the previous sub-step,  $n+1$  respectively the next unknown one and  $\tau$  the time increment in between. The procedure presented here is performed at every sub-stage of the temporal discretization scheme and holds in the fluid region  $\Omega_{\mathbb{F}}$  of the computational domain (cf. section 1.3). In the first step (equation 2.54a), an intermediate velocity  $\mathbf{u}^*$  is computed without the pressure gradient term, where  $\tilde{F}$  contains the convective, diffusive terms and potential sources and sinks of the flow (equations 2.46). In the second step (equation 2.54b), the pressure  $\phi_{n+1}$  is computed by solving a Poisson equation with Neumann boundary conditions. In the last step (equation 2.54c), the new and divergence-free velocity  $\mathbf{u}_{n+1}$  is computed and  $\mathbf{u}^*$  discarded afterwards.

Numerically solving the pressure Poisson equation (equation 2.54b) for an incompressible flow can be avoided by taking the curl of the momentum equations, which yields a non-primitive formulation (of  $\Delta w$  and the wall-normal vorticity  $\omega_z$ ) of the incompressible flow problem through eliminating the pressure term since  $\nabla \times \nabla p = 0$  (Kim et al., 1987). Hence, the pressure is only computed if needed for statistics containing the pressure.

**Solving the Poisson equation and pressure grid staggering.** The current **DNS** code solves the pressure Poisson equation in the horizontal directions in Fourier space with periodic boundary conditions and in the non-periodic vertical direction with an inverse-compact approach (Mellado and Ansonge, 2012). The applied Poisson solver is consistent with the higher-order compact discretization kernel since it uses the corresponding modified wavenumbers of the spatial scheme in the frequency space. Up to this point, the pressure and velocity values were computed in a collocated arrangement, where all variables were computed on the same grid.

Since the analogue of an integration in physical space is a simple division of the Fourier modes by the wavenumbers, the calculus in the horizontal directions consists of a division of the pressure modes by the modified wavenumbers  $(k_x'^2 + k_y'^2)$ , which are for the first derivative (equation 2.50a) zero at  $k_i = [0, \pi]$ . As a result, four possible combinations of a zero division in the two-dimensional case appear and, therefore, must be excluded from the division and treated separately. Nevertheless, a division by very small wavenumbers in the vicinity of these singular pressure modes causes and exaggerates spurious pressure oscillations that may propagate to the velocity fields, due to the inherent coupling (Laizet and Lamballais, 2009). One can observe these oscillations for higher wavenumbers as an accumulation of energy in the spectral energy density of the pressure and spanwise velocity, analyzed in detail in the section 3.3.2 for a smooth and rough turbulent channel flow. So far, this numerical artefact was acceptable for simulations with smooth walls since it does not severely affect the data quality. Implementing an **IBM** intensifies these pressure oscillations as the **IBM** imposes a forcing at the smallest scales and severely degrades the pressure and velocity fields. Furthermore, this mechanism is observed to be amplified with increasing grid resolution.

The numerical strategy implemented in this work provides a partially staggered pressure mesh in the horizontal directions, where the Fourier transformation is performed, and an additional pressure filter in the vertical to avoid the prescribed numerical artefacts in all three dimensions. With this strategy, the velocities are always on the same grid, and the pressure Poisson equation is solved on a staggered pressure grid by half a grid spacing ( $\Delta x_i/2$ ) in the horizontal directions. Partially staggered pressure grids were introduced by Fortin et al. (1971), further applied by Almgren et al. (1996) and George et al. (2000) and used with compact schemes of sixth-order and an **IBM** by Laizet and Lamballais (2009). In the first step, the **LHS** terms of the pressure Poisson equation are interpolated to the pressure grid. The Poisson equation is solved in the next step, and the pressure is filtered in the vertical. The pressure gradients are evaluated back on the velocity mesh in the last step.

An interpolatory compact scheme (Lele, 1992) for the first derivative on midpoints is used to preserve the consistency of the sixth-order compact spatial discretization scheme in the code. The interpolatory schemes read as

$$c_{13}f_{i+5/2}^{\prime I} + c_{23}f_{i+3/2}^{\prime I} + f_{i+1/2}^{\prime I} + c_{23}f_{i-1/2}^{\prime I} + c_{13}f_{i-3/2}^{\prime I} = c_{33}\frac{f_{i+1} - f_i}{\Delta x} + c_{43}\frac{f_{i+2} - f_{i-1}}{3\Delta x} + c_{53}\frac{f_{i+3} - f_{i-2}}{5\Delta x}. \quad (2.55)$$

The prefactors are  $c_{13} = 0$ ,  $c_{23} = 9/62$ ,  $c_{33} = 63/62$ ,  $c_{43} = 17/62$  and  $c_{53} = 0$  to get a sixth-order accurate scheme. This scheme offers beneficial properties since it combines a derivative and an interpolation operator in a single step, which saves computational effort and possesses better resolution characteristics in the modified wavenumber space (Fig. 2.3a) as its non-interpolatory counterpart (equation 2.47). The compact midpoint

interpolation scheme from Lele (1992) is given by

$$c_{14}f_{i+5/2}^I + c_{24}f_{i+3/2}^I + f_{i+1/2}^I + c_{24}f_{i-1/2}^I + c_{14}f_{i-3/2}^I = c_{34}\frac{f_{i+1} - f_i}{2} + c_{44}\frac{f_{i+2} - f_{i-1}}{2} + c_{54}\frac{f_{i+3} - f_{i-2}}{2}, \quad (2.56)$$

with choosing the prefactors to  $c_{14} = 0$ ,  $c_{24} = 3/10$ ,  $c_{34} = 3/4$ ,  $c_{44} = 1/20$  and  $c_{54} = 0$  again a sixth-order accurate scheme is obtained. The modified wavenumbers  $k^I$  of the interpolatory compact scheme of sixth-order for the first derivative (equation 2.55) and the transfer function  $T^I$  of the interpolation scheme (equation 2.56) associated with the actual wavenumbers  $k$  are given by (Laizet and Lamballais, 2009)

$$k^I(k) = \frac{2c_{33} \sin(k/2) + (2c_{43}/3) \sin(3k/2)}{1 + 2c_{23} \cos(k)}, \quad (2.57a)$$

$$T^I(k) = \frac{2c_{33} \cos(k/2) + (2c_{43}/3) \cos(3k/2)}{1 + 2c_{23} \cos(k)}. \quad (2.57b)$$

The modified wavenumber analysis  $k^I$  reveals that when an interpolatory first-order derivative scheme (equation 2.55) is used, only one singular pressure mode at  $k_i = 0$  remains instead of the previous four. Nevertheless, using the sixth-order midpoint interpolation scheme (equation 2.56) introduces new singular modes, where  $T^I = 0$  at  $k_i = \pi$ . Fortunately, Laizet and Lamballais (2009) discovered that the singular pressure modes associated with the pure interpolation do not exaggerate spurious oscillations.

In the vertical direction, two different pressure filters are considered, a spectral and a compact filter, to eliminate spurious pressure oscillations in all spatial directions while being consistent with the existing algorithm. The spectral filter has the following transfer function (Fig. 2.4a):

$$T^{sf}(k_{\text{rel}}) = \frac{\text{erf}[8(1 - k_{\text{rel}})] + 1}{2}, \quad \text{with } k_{\text{rel}} = \frac{k_z}{k_{\text{ref}}}, \quad k_{\text{ref}} = \frac{n_z}{l_{\text{cut}}}, \quad (2.58a-c)$$

and the relative and reference wavenumber  $k_{\text{rel}}$ ,  $k_{\text{ref}}$  to map the filter on a specific relative position of the vertical pressure spectra. At this location, the expected energy accumulation at the highest wavenumbers in the pressure spectra is smoothly cut off with the error function. The filter parameter  $l_{\text{cut}}$  determines the strength of the filter, respectively the relative position of the cut-off and should be in the range of  $l_{\text{cut}} = [2, 4]$ . This filtering approach is, by construction, limited to periodic signals. Therefore, the filter only applies for simulation setups with symmetric boundary conditions on the vertical domain boundaries, such as closed channel flow, where a quasi-periodic pressure signal in the vertical is assumed.

This assumption is invalid for boundary layer flows like Ekman flows due to the lack of symmetry in the vertical boundary conditions, resulting in a non-periodic vertical pressure signal. In that case, a compact filter (Lele, 1992) is applied in the vertical direction to the pressure, which reads

$$c_{15}\hat{f}_{i-2} + c_{25}\hat{f}_{i-1} + \hat{f}_i + c_{25}\hat{f}_{i+1} + c_{15}\hat{f}_{i+2} = c_{35}f_i + c_{45}\frac{f_{i+1} - f_{i-1}}{2} + c_{55}\frac{f_{i+2} - f_{i-2}}{2} + c_{65}\frac{f_{i+3} - f_{i-3}}{2}, \quad (2.59)$$



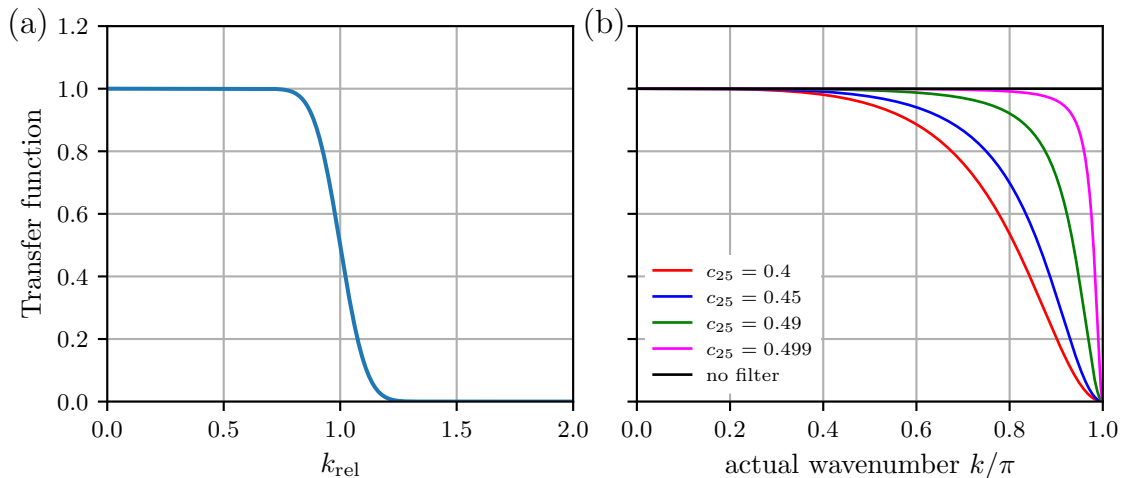


**Fig. 2.4** Transfer functions of the (a) spectral error function filter (equations 2.58) for filtering the spectral pressure, and (b) the compact filter (equation 2.59) for filtering the pressure in the vertical direction as a function of the filter parameter  $c_{25}$ .

with the approximate filtered flow variable  $\hat{f}_i$  on the grid nodes. This representation is valid for interior points, and biased schemes are needed on the boundaries, as can be found in Lele (1992). The transfer function of the compact filter (equation 2.59, Fig. 2.4b) is given by

$$T^{cf}(k) = \frac{c_{35} + c_{45}\cos(k) + c_{55}\cos(2k) + c_{65}\cos(3k)}{1 + 2c_{25}\cos(k) + 2c_{15}\cos(2k)}. \quad (2.60)$$

Choosing the prefactors  $c_{15} = c_{65} = 0$  and  $c_{35} = \frac{1}{8}(5 + 6c_{25})$ ,  $c_{45} = \frac{1}{2}(1 + 2c_{25})$ ,  $c_{55} = -\frac{1}{8}(1 - 2c_{25})$  a fourth-order tridiagonal filter scheme is derived. The parameter  $c_{25}$  defines the strength of the filter and is observed to be strong enough by choosing  $c_{25} = 0.49$  (Fig. 2.4b).

With the proposed pressure treatment, consisting of a partially staggered pressure grid in the horizontal directions and a pressure filter in the vertical, artificial pressure oscillations can be avoided while being entirely consistent with the accuracy of the spatial discretization schemes. This paves the way for representing complex boundaries in the computational domain and ensuring high-resolution data of all flow variables.

### 2.5.3 Immersed Boundary Methods

Immersed boundary methods were first introduced by the seminal work of Peskin (1972) (later: Peskin, 1977, 2002), who simulated the two-dimensional movement of a heart valve with elastic boundaries at low Reynolds number by applying a forcing term to the **NSE** based on Hooke's law (describes the elastic body deformation). Later, this method was adjusted by a feedback forcing approach of Goldstein et al. (1993) for application to objects with rigid boundaries to study the effect of riblets in turbulent channel flow. The **IBM** volume force  $\mathbf{f}^{\text{IBM}}(x_i, t) = (f_x, f_y, f_z)^T$  added to the **RHS** of the **NSE** (equation 2.46) is given by

$$\mathbf{f}^{\text{IBM}}(x_i, t) = \underbrace{\epsilon(x_i)\beta_1 \int_0^t \mathbf{u}(x_i, \tilde{t}) d\tilde{t}}_{f_{i,\beta_1}} + \underbrace{\epsilon(x_i)\beta_2 \mathbf{u}(x_i, t)}_{f_{i,\beta_2}}, \quad (2.61)$$

with the negative constants  $\beta_1, \beta_2$  (Lamballais and Silvestrini, 2002). The feedback forcing term  $\mathbf{f}^{\text{IBM}}$  can be interpreted as a proportional-integral controller with two heuristic param-

eters and therefore behaves like a damped oscillator (Mittal and Iaccarino, 2005). In the case of rigid boundaries at high Reynolds numbers, this leads to large oscillator frequencies, damping coefficients and turns the modified **NSE** stiff. Hence, severe stability issues are faced with the need for very small time increments and carefully tuned parameters of the forcing function (Mittal and Iaccarino, 2005).

**The Gibbs phenomenon and spurious force oscillations (SFOs)**<sup>2</sup> are common artefacts when simulating moving and rigid bodies with **IBMs** (Lee et al., 2011a; Li et al., 2016). **SFOs** are unphysical, numerical artefacts in the velocity and pressure fields that appear near solid boundaries at high frequencies. They are closely related to the Gibbs phenomenon in spectral space (Fornberg, 1996, p. 11) when an expansion of continuous trigonometric functions expresses a discontinuous function. The deterioration of the flow fields by **SFOs** is often not limited to instantaneous realizations but also contaminates time-averaged statistics of the flow and is, therefore, non-negligible as the overall data quality may deteriorate significantly. When using **IBMs**, the origin of **SFOs** traces back to the discontinuous behavior of the **IBM** forcing term at the interface between the fluid and solid regions. Higher-order discretization schemes with spectral-like resolution, such as compact schemes (section 2.5.1), excite Gibbs oscillations at the interface, which propagate into the fluid region owing to the non-local behavior of these schemes. The spectral derivatives show the most pronounced oscillation in the far field, followed by sixth-order compact schemes (Figs. 2.5). Local schemes, such as central finite differencing schemes of second or higher order, do not transport the differentiation error far from the wall. Saiki and Biringen (1996) observed this behavior with a fourth-order central finite difference scheme, and also Fadlun et al. (2000) did not observe the oscillations in combination with a second-order scheme.

In introducing the feedback forcing approach, Goldstein et al. (1993) described a procedure to reduce the **SFOs** in the flow fields as they use a pseudo-spectral **DNS** code. The proposed procedure comprises a smearing of the forcing term at the interfaces with a Gaussian weight function to distribute the forcing over neighboring grid points. Furthermore, the non-linear convective term is low-pass filtered. Lamballais and Silvestrini (2002) followed a similar treatment with sixth-order compact schemes. In recent years, different filtering and smoothing procedures in physical and frequency space were discussed to reduce and control **SFOs**. Fang et al. (2011) proposed a smoothing with a radial basis function and Tseng et al. (2006) a Laplacian smoothing function, both in combination with pseudo-spectral schemes and an **IBM**. Another possibility is adding a source or sink term to the **NSE** (Kim et al., 2001). The methods to deal with **SFOs** have symptomatic treatment in common, which does not entirely solve the problem and, therefore, does not lead to oscillation-free **IBM** approaches. They alter the velocity fields by filtering them and blurring the interface’s location between fluid and solid regions. The boundaries of the objects are no longer precisely represented on the grid, which is inconsistent from a physical point of view, and the impact on turbulent wall interactions is non-negligible. Moving away from pseudo-spectral and non-local, higher-order schemes towards second-order schemes is not desirable: Parnaudeau et al. (2004) showed the improvement of the solution when sixth-order compact schemes are used. The same holds from the modelling perspective if high-resolution **DNS** of high Reynolds number flows with large computational domains are planned. A possibility to avoid **SFOs** was initially proposed by Fadlun et al. (2000) for a direct forcing approach, with an internal treatment of the solid regions to reduce discontinuities at the interface for the derivative schemes.

<sup>2</sup>The following paragraph about the Gibbs phenomenon corresponds contentwise to section 2.4. in Kostecky and Ansgore (2024a) (cf. chapter 4) and is reproduced here for convenience. The paragraph is adapted in parts and complemented with figures.



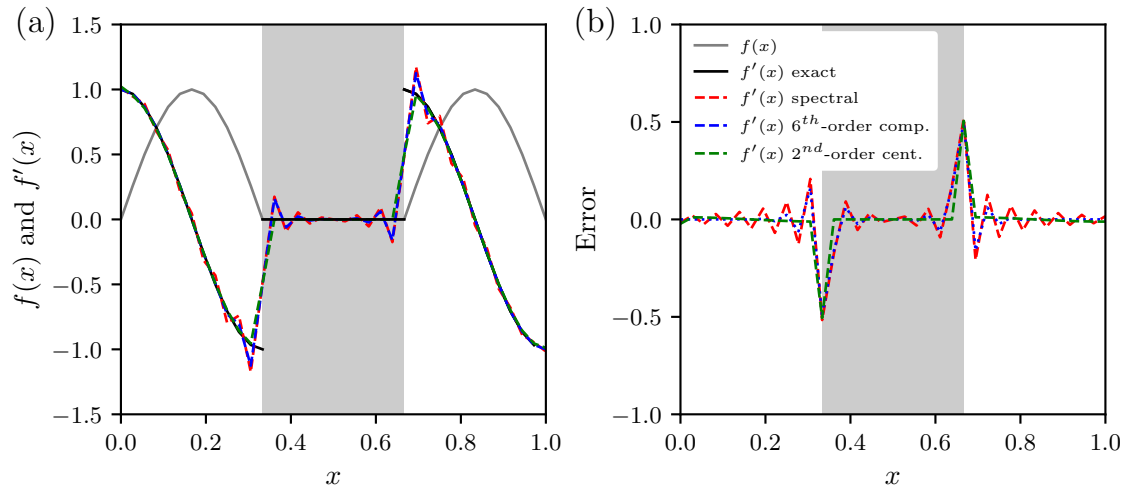


**Fig. 2.5** Gibbs phenomenon for different spatial discretization schemes. (a) Derivatives of the sinusoidal test function  $f(x)$ , with  $n_x = 36$  and a discontinuity in the center. (b) Absolute error of the approximate and the exact solution. Grey shaded area depicts the region where  $f(x) = 0$  and  $f'_{exact}(x) = 0$ .

**The direct forcing IBM approach** was first introduced by Mohd-Yusof (1997) and Fadlun et al. (2000) to directly impose the immersed boundary conditions to the discretized governing equations without dynamical processes, tuning parameters (cf.  $\beta_1, \beta_2$  in equation 2.61) or blurring of boundaries to obtain a sharp representation of the interface. The conceptual idea of the direct forcing approach (Giannenas and Laizet (2021) use the term “No-Reconstruction IBM”, without an internal treatment of the solid body) is to add an IBM force to the RHS of equation 2.54a in each sub-stage  $t_n$  of the RK45 scheme. The IBM force is given by

$$\mathbf{f}_n^{\text{IBM}} = \epsilon \left( \frac{\mathbf{u}_b - \mathbf{u}_n}{\tau} - \tilde{F} \right), \quad (2.62)$$

with  $\mathbf{u}^* = \epsilon \mathbf{u}_b$  and  $\mathbf{u}_b = 0$  for a fixed body with rigid boundaries. The provisional velocity  $\mathbf{u}^*$  is not divergence-free; hence, the pressure Poisson equation (equation 2.54b) is adjusted as follows

$$\phi_{n+1} = \frac{1}{\tau} \Delta^{-1} \{ \nabla \cdot [(1 - \epsilon) \mathbf{u}^*] \}. \quad (2.63)$$

It is important to note that the IBM boundary conditions are applied to  $\mathbf{u}^*$  before computing the gradient, resulting in a first-order accurate approximation. The pressure Poisson equation is a global operation solved for the whole computational domain with pressure values inside the solid body. Moreover, the continuity equation (equation 2.54c) is modified to  $\nabla \cdot [(1 - \epsilon) \mathbf{u}_{n+1}] = 0$ .

Using a simple no-reconstruction IBM leads to the Gibbs phenomenon, and so to SFOs in the presence of higher-order schemes. To reduce the discontinuity at the interface for the derivative schemes, Mohd-Yusof (1997) and Fadlun et al. (2000) proposed a reversed flow at the first solid grid point adjacent to the interface while ensuring valid boundary conditions at the interface (no-slip and impermeability). Besides the control of SFOs, a vital feature of this treatment is that the external flow is unaffected by the internal flow (Fadlun et al., 2000), allowing the use of more sophisticated methods for flow control inside the solid region. Parnaudeau et al. (2004) and Parnaudeau et al. (2008) refined the velocity mirroring approach for investigating flow around a cylinder with sixth-order

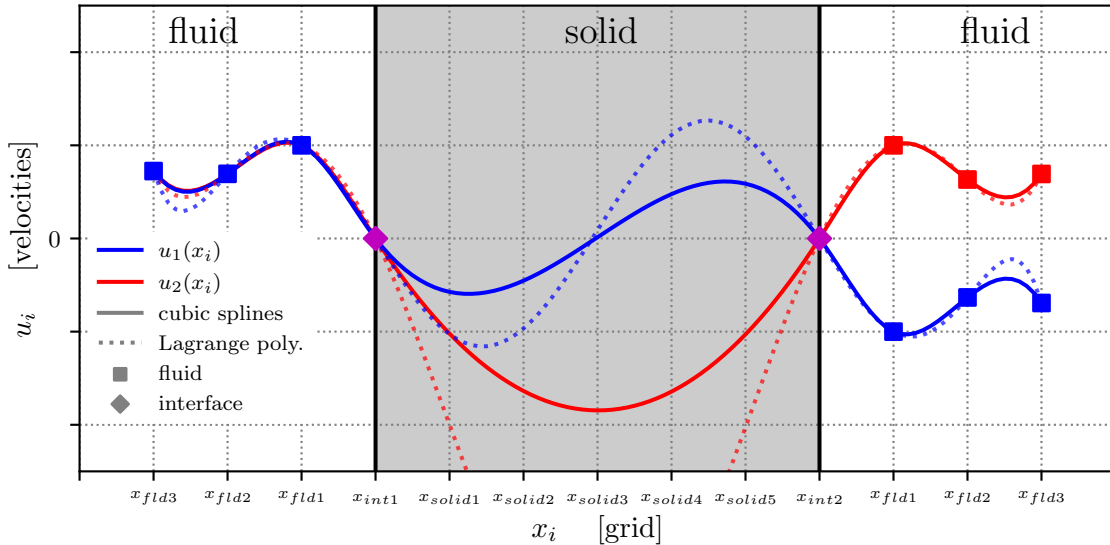


**Fig. 2.6** Schematic of the **ADR IBM** with cubic splines (solid lines) and Lagrangian polynomials (dotted lines) for two exemplary velocity distributions  $u_1(x_i)$  (blue),  $u_2(x_i)$  (red) and interfaces with  $u_i|_{x_i=\text{interface}} = 0$  located on grid nodes. The grey shaded area depicts the solid region, including the interfaces.

compact schemes. Nonetheless, this approach is limited to simple geometries like cylinders but problematic for objects with sharp edges (Giannenas and Laizet, 2021, Fig. 2 on p. 610).

**The alternating direction reconstruction (ADR) IBM<sup>3</sup>** was initially introduced by Gautier et al. (2014) and is based on the velocity mirroring procedure for a flow around cylinders (Parnaudeau et al., 2008). The core idea is to preserve the homogeneity of spatial operators to simulate more complex geometries. While preserving the physical boundary conditions at the interface of the solid object (no-slip and impermeability), an artificial flow field is generated inside the solid region to smooth the resulting field. This is achieved by interpolation with one-dimensional Lagrangian polynomials in the direction of the subsequent derivative evaluation. This procedure is repeated before each spatial derivation in the respective spatial direction. Hence, the values in the solid region are continuously updated and only used to evaluate one single spatial derivative, after which they are discarded.

The Lagrangian polynomial function is created by taking the interface points with velocity values of zero and three adjacent fluid points on either side, resulting in a set of eight points and, therefore, an eighth-order polynomial function (Fig. 2.6). This method comes with restrictions regarding the number of required grid nodes. In general, the interface can be located anywhere between two grid nodes. The first grid point in the fluid is always skipped to avoid numerical instabilities if the interface is close to a grid node, and the following three nodes are then taken for reconstruction. Moreover, sufficient grid points between and inside the objects are essential. In a rough turbulent channel flow study with mixed convection, Schäfer et al. (2022a) adapted the **ADR IBM** also for the spatial derivatives in the energy balance with constant temperature boundary conditions at the interface. To the author's knowledge, the **ADR IBM** was so far only used for Dirichlet boundary conditions.

Lagrangian polynomials tend to produce signals with large amplitudes close to the interface as the solid regions get wider with increasing polynomial degrees. This dis-

<sup>3</sup>The following paragraph about the **ADR IBM** corresponds contentwise to section 2.4. in Kostecky and Ansoerge (2024a) (cf. chapter 4), and is reproduced here for convenience. The paragraph is adapted in parts and complemented with figures.

advantageous characteristic is attributed to the Runge's phenomenon (Runge, 1901) that concerns polynomials of higher order on equidistant grids (Fig. 2.6). Consequently, large derivative values are created close to the interface with significant pressure signals in the solid regions, which might lead to numerical instabilities. Instead of Lagrangian polynomials, Giannenas and Laizet (2021) used cubic splines, piecewise and smooth third-order polynomial functions with reduced amplitudes, in the solid region to avoid Runge's phenomenon at boundary nodes (Fig. 2.6). In a comprehensive error convergence study, Giannenas and Laizet (2021) showed that the **ADR IBM** with cubic splines is well-suited for sixth-order compact schemes and will not degrade the overall error convergence of the **DNS** code. From the numerical perspective, the method is robust since no additional stability constraints are added. Moreover, the **ADR IBM** is beneficial from the computational perspective, as the communication overhead is not increased between computational cores, and the method fits accordingly to the two-dimensional parallelization strategy of **DNS** codes with compact schemes. Furthermore, Giannenas and Laizet (2021) presented a high scalability of this method on **HPC** systems.

The **ADR IBM** is validated successfully in-depth for a flow around a cylinder with experimental and modelling databases (Giannenas and Laizet, 2021; Gautier et al., 2014, 2013; Parnaudeau et al., 2008) and across different **DNS** codes (Theobald et al., 2021; Schäfer et al., 2020) to ensure high data quality and physically reasoned results. The method has been used in several recent studies, showing its high implementation capability. The **ADR IBM** was applied for moving objects (Giannenas and Laizet, 2021), upon wavy channel turbulence (Khan and Jayaraman, 2019; Jayaraman and Khan, 2020), control a turbulent jet (Gautier et al., 2014), **LES** of a circular cylinder wake flow (Resseguier et al., 2017; Chandramouli et al., 2018), flow over periodic hill (Xiao et al., 2020) and on channel flow over streamwise-aligned ridges (Schäfer et al., 2019) and with free convection (Schäfer et al., 2022b).



## 3. Implementation and Validation of the Immersed Boundary Method

This chapter describes the implementation and validation of the previously described **ADR IBM** (section 2.5.3) in the open source **DNS** code `t1ab`<sup>1</sup>, which is used to generate the results for Study I & II (chapters 4, 5). The technical implementation of the pressure treatment and the **ADR IBM** are presented in section 3.1 and section 3.2, respectively. The validation of the numerical tools with literature data is presented in section 3.3. Note the change of the coordinate system in the present chapter<sup>2</sup>.

### 3.1 Implementation of the Pressure Grid Staggering and Filtering

The implementation of the horizontal pressure grid staggering with the vertical pressure filters in the **DNS** code is described for the flow fields in the pseudo-code in Fig. 3.1. The tendencies of the flow evolution equation for the **RK45** sub-step are stored in the arrays `h[1-3]`. Additional memory for computation is guaranteed by the auxiliary arrays `tmp[1-6]`. Coriolis and buoyancy forces are added to the tendencies already before entering the displayed **RK45** sub-time loop.

After computing the convection and diffusion terms (line 4), the pressure forcing terms are prepared with the aim of solving the pressure Poisson equation (line 26) on the horizontally staggered pressure grid. The derivatives in the horizontal `tmp1`, `tmp3` (lines 16,18) are evaluated in one direction with combined interpolatory derivative schemes (equation 2.55) and, subsequently, in the other direction with pure interpolation schemes (equation 2.56). Since the vertical levels of the pressure and velocity grid coincide, the vertical derivative (line 17) is computed on the velocity grid and interpolated in the horizontal directions. Note that there is no significant difference in the order of the pure interpolation and the combined operators. The same applies to the order of operators in line 17 and for the interpolation back on the velocity grid (lines 32 – 34), respectively. The total pressure forcing term `tmp1` in line 21 is on the pressure grid.

The pressure field itself is computed in the pressure Poisson solver (lines 26, 45f.) considering one singular pressure mode at  $k_i = 0$  for the combined interpolatory derivative schemes. In addition to the pressure, the Poisson solver outputs the vertical derivative

---

<sup>1</sup><https://github.com/turbulencia/t1ab>

<sup>2</sup>In contrast to the rest of the thesis, this chapter swaps the vertical axis with the spanwise axis. Thus,  $x$  is the streamwise,  $y$  is the vertical, and  $z$  is the spanwise direction. For the following reasons: (i) consistency with the conventions of the research community of wall-bounded turbulence (especially for channel flows), and (ii) convenience in using a consistent coordinate system throughout the code implementation and validation.

```

! Time loop for RHS terms (flow + scalar) with the RK45 scheme
2 do i=1,rk_endstep ! RK45 sub-steps
! buoyancy + Coriolis terms already added, tendencies in h1,h2,h3
4 ! compute convection + diffusion terms with burgers operator
...
6 ! compute pressure (remove residual divergence)
! (dte = time step of each RK45 sub-step)
8 tmp1 = h1 + u/dte; tmp2 = h2 + v/dte; tmp3 = h3 + w/dte

10 ! apply IBM boundary conditions on tmp arrays
call IBM_bcs(tmp1,tmp2,tmp3)
12
! compute derivatives for the pressure forcing
14 ! (der1 = 1st deriv.; der1_int = 1st int.-deriv.; int = interp.)
! (on pressure grid, no IBM reconstruction here!)
16 tmp5=der1_int_x(tmp1); tmp4=int_z(tmp5) ! d()/dx
tmp6=int_x(tmp2); tmp2=der1_y(tmp6); tmp5=int_z(tmp2) ! d()/dy
18 tmp1=int_x(tmp3); tmp6=der1_int_z(tmp1) ! d()/dz

20 ! pressure forcing term
tmp1 = tmp4 + tmp5 + tmp6
22
! Neumann boundary conditions (for pressure Poisson solver)
24 ...
! pressure Poisson solver (pressure in tmp1, dpdy in tmp6)
26 call pressure_poisson(tmp1,tmp6)

28 ! compact pressure filter in the vertical (filter p and dpdy)
if vfilter_p_compact: call compact_filter_vertical_p(tmp1, tmp6)
30
! compute pressure gradients (dp/dy already there)
! (on velocity grid, no IBM reconstruction here!)
32 tmp3 = der1_int_x(tmp1); tmp2 = int_z(tmp3) ! dp/dx
34 tmp4 = int_x(tmp6); tmp3 = int_z(tmp4) ! dp/dy
tmp5 = int_x(tmp1); tmp4 = der1_int_z(tmp5) ! dp/dz
36
! add pressure gradients to tendencies
38 h1 = h1 - tmp2; h2 = h2 - tmp3; h3 = h3 - tmp4;

40 ! apply BCs on tendencies again (zero velocities in solid)
end do
42
contains
44 ! -----
subroutine pressure_poisson(tmp1, tmp6)
46 ! forward Fourier transform in horizontal directions
...
48 ! solve Laplace equation for pressure
! (spectral in horizontal + compact inverse in vertical)
50 ! (only one singular pressure mode at (kx,kz)=(0,0))
...
52 ! spectral vertical pressure filter (filter p and dpdy)
if vfilter_p_spectral: call spectral_filter_vertical_p(tmp1, tmp6)
54
! backward Fourier transform in horizontal directions
56 end subroutine

```

**Fig. 3.1** Pseudo-code for the pressure treatment implementation in the DNS code.

of the pressure. In the case of the spectral filter, the pressure and its vertical derivative are filtered in the vertical within this routine in their native Fourier space representation, whereas, if the compact pressure filter is used, they are filtered on the pressure grid after leaving the pressure Poisson solver (line 29). After the vertical filtering, the pressure gradients are evaluated backwards on the velocity grid (lines 33 – 35) and added to the tendencies (line 38) to remove the residual divergence. Since the pressure is computed globally in the computational domain with non-zero values in the solid regions, boundary conditions are applied again at the end of the sub-step.

### 3.2 Implementation of the Alternating Direction Reconstruction Immersed Boundary Method

The implementation of the **ADR IBM** in the **DNS** code, which is accomplished as part of this work, is described in the pseudo-code in Fig. 3.2. An indicator field  $\epsilon(x_i)$  (equation 1.1) is used to fully describe the spatial properties of the immersed roughness geometry in the computational domain. This field is prepared in the initialization phase of the **IBM** (line 6), with a similar shape and size as the computational domain. Grid node positions are filled with zeros in fluid regions and ones in solid regions, where the interfaces between the two are attributed to the solid regions since physical boundary conditions are valid here. Therefore, in the present implementation, the geometry of the roughness elements is bound to the positions of the grid nodes. The indicator field is either read from an existing file (line 38) or generated by an intrinsic routine (line 41). To efficiently write the field to disk, three different format options are implemented: (i) the double-precision floating point format (64-bit), comparable with the I/O of complete three-dimensional fields of the code, (ii) the integer format (8-bit), (iii) the most efficient bitwise representation (1-bit), which only needs 1/64 storage compared to option (i).

The **IBM** algorithm requires further information about the roughness geometry besides the indicator field  $\epsilon(x_i)$  to perform the one-dimensional alternating direction reconstruction with cubic splines (section 2.5.3). Since the cubic spline reconstruction in the solid regions is a line-by-line operator executed independently before each spatial derivative, the algorithm must know the number of objects and their exact positions in each line. For example, in the  $x$ -direction, the two-dimensional field  $\epsilon_{x,\text{noobj}}(y, z)$  of size  $n_y \times n_z$  with the normal  $x$ -vector stores the number of objects in each line. The reduced three-dimensional fields  $\epsilon_{x,\text{start}}(y, z, \text{noobj})$ ,  $\epsilon_{x,\text{end}}(y, z, \text{noobj})$  of sizes  $n_y \times n_z \times \max\{\epsilon_{x,\text{noobj}}(y, z)\}$  contain the indices of the left and right interfaces of the solid objects, respectively, when moving along the  $x$ -axis with increasing indices. Each time the code is started, nine descriptive geometry fields of reduced sizes are created for a three-dimensional flow based on the indicator field  $\epsilon(x_i)$  (line 43).

A self-written library is implemented to evaluate cubic splines between left and right interfaces while ensuring physical boundary conditions for velocities  $\mathbf{u}|_{x_i=\text{interface}} = 0$ . The splines are evaluated with the help of a predefined number of solid points and fluid grid points on each side of the object (Fig. 2.6). In addition to the interface points, at least two points are needed on each side to construct the cubic splines, which sets the limit for spline construction. Moreover, the outermost fluid points can already serve as interface points of the neighboring elements. Theoretically, one liquid point on each side of the object is sufficient. However, the intended setting consists of three fluid points and a minimum of two solid points. These limits reduce the risk of numerical instabilities, especially for high Reynolds number when local gradients are expected to be large. Clamped-type boundary conditions are taken to match the first derivative values at the endpoints. In the non-periodic vertical direction, the values of the fluid points are mirrored at the lower domain boundary. Furthermore, the **ADR IBM** is implemented for scalar fields (passive scalar, buoyancy) with Dirichlet boundary conditions, with the restriction that the objects on the ground and the lower domain boundary have identical boundary values (section 2.2.8).



```

program DNS
2
  ! initialization part of the DNS code (IO, memory, MPI, FFTW, ...)
4  ...
  ! initialization of the IBM module
6  ! (create descriptive geometry fields)
  call IBM_initialize(geometry_fields_xyz)
8  ! apply boundary conditions on restart fields (flow + scalar)
  call IBM_bcs(u,v,w,s)      ! important if geometry changes
10 ! enter time loop of the RK45 scheme
  do i=it_start , it_stop
12   if (DNS_filter = true) then
     call DNS_filter(u,v,w,s)
14     call IBM_bcs(u,v,w,s)  ! if filtering is active enforce BCs
   end if
16   ! compute advection + diffusion with modified burgers operator
   ! (modified fields with cubic splines in solid regions)
18   call opr_burgers_IBM_xyz()
   ! compute pressure projection step (tmp contains pre. forcing)
20   tmp = ...
   call pressure_poisson(tmp)
22   ! add pressure x-/y-/z-derivatives to flow tendencies (no IBM!)
   ...
24   ! apply BCs on tendencies again (zero velocities in solid)
   ...
26 end do
  ! finalize program (IO of fields/averages ... , ...)
28 call DNS_finalize()

30 contains

32 ! -----
  subroutine IBM_initialize(geometry_fields_xyz)
34   ! read IBM parameters from dns.ini with consistency check
   call IBM_read_parameters(inifile)
36   ! read / generate eps field
   if (ibm_eps_exist = true) then
38     call IBM_read_eps(eps)
   else
40     call IBM_generate_eps(eps)
   end if
42   ! generate descriptive geometry fields (nobi, nobi_b, nobi_e)
   call IBM_generate_geo()
44   ! verify the used geometry field
   call IBM_verify_geo()
46   ! stagger eps on the pressure grid
   call IBM_stagger()
48   ! compute solid/fluid fractions for conditional averaging
   call IBM_gamma()
50   ! define which MPI threads are active/idle for the IBM
   call IBM_check_procs()
52 end subroutine
  ! -----
54
end program DNS

```

**Fig. 3.2** Pseudo-code for the ADR IBM implementation in the DNS code.

Objects on the upper domain boundary are not supported if the **IBM** is applied to scalar fields.

The initialization part contains the following steps: (i) the descriptive geometry fields are verified (line 45), (ii) the indicator field  $\epsilon(x_i)$  is horizontally staggered on the pressure grid to  $\epsilon_p(x_i)$  (line 47), (iii) the solid and fluid fractions are computed from  $\epsilon(x_i)$  for conditional averaging (line 49), (iv) and both active and idle threads for the **IBM** module are identified (line 51). The last step (iv) may lead to a load imbalance of the threads but was observed to speed up the implementation.

Before entering the time-integration of the code (line 11), boundary conditions are applied in line 9 to flow and scalar fields, with

$$\mathbf{u}(x_i) \mapsto \mathbf{u}(x_i)[1 - \epsilon(x_i)], \quad \text{respectively} \quad s(x_i) \mapsto s(x_i)[1 - \epsilon(x_i)] + s_{BCs}\epsilon(x_i), \quad (3.1a,b)$$

where  $s_{BCs}$  describes the fixed scalar boundary values. When filtering is applied to flow fields, boundary conditions are enforced again at the beginning of the time-integration loop (line 14) since global filter operations can deteriorate boundary values. The crucial part of the **ADR IBM**, namely the cubic spline interpolation, is performed within the low-level Burgers-operator (line 18), where first and second derivatives are evaluated for the advection and diffusion terms of the **NSE**. The Burgers operator in the direction  $i$  is defined as

$$\mathcal{B}_i(\varphi) = \mathbf{u}D'_i(\varphi) + \frac{1}{Re_\Lambda}D''_i(\varphi), \quad (3.2)$$

where  $\varphi$  is either a velocity or scalar field and  $D'_i$ ,  $D''_i$  are the discrete first and second derivatives. Before passing  $\varphi$  to the discrete derivative operators inside the Burgers kernel, the one-dimensional reconstruction is carried out in the solid regions. Afterwards, the pressure forcing term for the Poisson solver (line 21) is computed without using the **ADR** since the pressure grid staggering (section 2.5.2) acts already as a filter. Solving the pressure Poisson equation is a global operator, i.e. the pressure is defined in the entire computational domain and pressure gradients are thus evaluated without the **ADR**. Again, the **IBM** boundary conditions are enforced on the tendencies.

For reasons of clarity and in order to transfer the implementation on further flow problems, the **ADR IBM** is written in modular form complying to an object-orientated software development strategy. Moreover, the implementation is fully compatible with the code's parallelization strategy. The computation for the reconstruction is active on a low-level code basis, which increases the serial part for each thread slightly but is significantly dependent on the simulation setup. A three-dimensional flow problem with one scalar (four prognostic variables) results in a total random-access memory (**RAM**) demand of 15 three-dimensional fields. They are needed for the prognostic variables, tendencies and temporal working arrays. When using the **ADR IBM**, two additional fields  $\epsilon(x_i)$ ,  $\epsilon_p(x_i)$  are stored with an overall memory increase of approximately 13%.

### 3.3 Validation of the Numerical Tools

Newly implemented numerical methods (sections 3.1, 3.2) in a **DNS** code require validation. An overview of existing strategies and recommendations for validating a **DNS** code is described in Coleman and Sandberg (2010). In line with that study, there is no need in the present dissertation to validate the **DNS** code with comprehensive convergence studies or comparisons of analytical laminar flow problems since the core of the numerical solver is well-tested (Mellado and Ansonge, 2012; Ansonge and Mellado, 2014, 2016) and unchanged by the current implementation.

Well-established literature databases were chosen for validation since no analytical solutions for a three-dimensional, fully-developed turbulent flow are known. By neglecting the rotation of the reference frame (Coriolis force) and density stratification (buoyancy), the flow simplifies to the canonical turbulent channel flow problem (cf. Kim et al., 1987).

This section first describes the numerical setup of a fully-developed turbulent channel flow (section 3.3.1), followed by the validation of the implemented horizontal pressure grid staggering and the **ADR IBM** in four stages:

- Validating the horizontal pressure grid staggering with a vertical pressure filter using data from a smooth and a rough, turbulent channel flow (sections 3.3.2, 3.3.3).
- Comparing rough turbulent channel flow with streamwise aligned bars on the upper and lower boundary with data from another **DNS** code (section 3.3.4).
- Comparing street canyon air flow using a suitable **DNS** setup with wind tunnel experiments and **LES** data (section 3.3.5).
- Investigating the effect of the **IBM** on scalar fields (section 3.3.6).

### 3.3.1 Numerical Setup of the Turbulent Channel Flow

**General setup and dimensions.** The simulations in this chapter cover a fully-developed, three-dimensional turbulent channel flow driven by a constant streamwise pressure gradient. All simulations are conducted on a Cartesian mesh  $x_i = (x, y, z)^T$ , representing the streamwise, wall-normal and spanwise directions. The computational domain size is  $[L_x \times L_y \times L_z] = [8\delta \times 2\delta \times 4\delta]$  with the half-channel height<sup>3</sup>  $\delta \equiv 1$ , except for the open channel flow configuration in section 3.3.5, where  $L_y = \delta$ . The computational mesh is stretched only in the vertical direction with a hyperbolic tangent function and a maximum grid stretching of  $d(\Delta y) / dy \lesssim 4.5\%$  to keep the spatial discretization scheme on non-uniform grids stable (Shukla and Zhong, 2005). In the absence of surface roughness, the grid stretching starts far above the viscous sublayer at  $y^+ \gtrsim 20$ , and in the case of surface roughness, it starts on top of the obstacles. A fine resolution is required in the vicinity of the wall to resolve the viscous sublayer. In contrast, a coarser resolution is sufficient in the center region of the channel where large-scale turbulent motions reside, and velocity gradients are expected to be small. A uniform grid spacing is used in the horizontal directions.

**Domain configuration.** The validation involves three different domain configurations of turbulent channel flow. First, a closed channel flow is considered with smooth walls (case without an **IBM**). Second, a closed channel flow with four evenly distributed streamwise aligned bars is considered (Fig. 3.3a). The bars are located in phase on the upper and lower wall of the channel with the following dimensions: width and height  $W = H = 0.1\delta$  and a uniform spacing  $S = 1\delta$  (center to center). Third, an open channel flow is considered to mimic the wind tunnel and **LES** domain of the study by Llaguno-Munitxa et al. (2017) (Fig. 3.3b) in the sense of geometric similarity. In this setup, seven housing blocks of equal height, width and spacing (center to center)  $W = H = S/2 = 1/8\delta$  are located perpendicular to the main flow direction. In the reference case, this complies with a housing block size of  $W = H = S/2 = 0.076$  m.

**Boundary conditions.** Periodic boundary conditions are applied to velocity and temperature fields in the streamwise and spanwise directions, resulting in infinitely extended walls in horizontal directions. No-slip and impermeability boundary conditions are applied to the flow fields at rigid boundaries. Free-slip boundary conditions are used at the upper boundary for open channel flows. Isothermal boundary conditions are chosen for temperature fields with a constant value on the upper and lower wall and inside the roughness elements. For validation purposes, temperature is treated as a passive scalar.

<sup>3</sup>In this chapter only,  $\delta$  is the (half) channel height for a (closed) open channel flow, which otherwise refers to the turbulent boundary layer thickness (section 2.4.2).

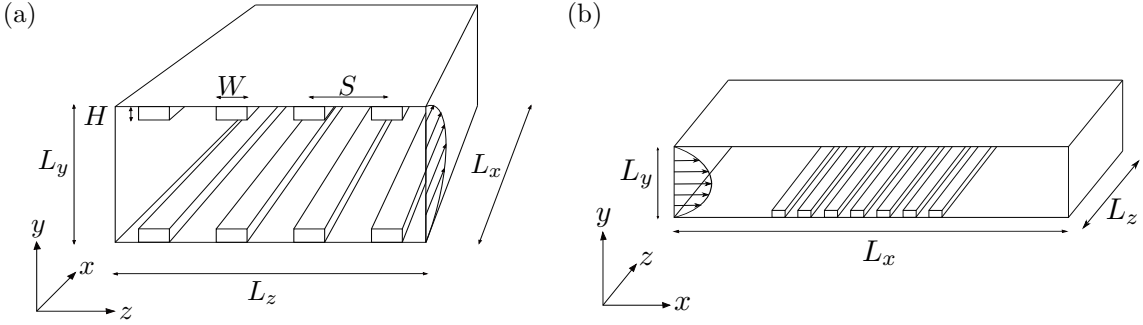


**Fig. 3.3** Schematic of the domain configurations of turbulent flows. (a) Closed channel flow with streamwise aligned bars, the flow is into the plane, and (b) open channel flow with spanwise housing blocks, the flow is from left to right, imitating the setup in the reference study of Llaguno-Munitxa et al. (2017) with geometric similarity.

**Forcing of the simulations.** In principle, turbulent channel flow is forced either with a constant pressure gradient (CPG) in the streamwise direction or with a constant flow rate (CFR). These options translate for the CPG strategy to a constant forcing term and a fluctuating bulk velocity and for the CFR strategy to the opposite – a fluctuating forcing term and a constant bulk velocity. During the simulations, the time-varying bulk velocity  $\tilde{u}_b(t)$ , which is defined as

$$\tilde{u}_b(t) = \frac{1}{L_y} \int_0^{L_y} \langle u \rangle (y, t) dy, \quad (3.3)$$

is tracked for the smooth channel flow with the CPG strategy. These fluctuations are small and unbiased and serve as a measure for bulk convergence of the flow if a stable long-term average  $u_b$  has formed. Combining both forcing strategies leads to the constant power input (CPI) forcing, as described in Quadrio et al. (2016). Here, the CPG approach is chosen for the current channel flow simulations<sup>4</sup>, and the forcing strategy is briefly outlined below; a more detailed derivation can be found in the Appendix.

The following set of fundamental equations (Kim et al., 1987; Kim and Moin, 1987) in non-dimensional form describes the turbulent channel flow:

$$\frac{\partial u_j}{\partial x_j} = 0, \quad (3.4a)$$

$$\frac{\partial u_j}{\partial t} + u_i \frac{\partial u_j}{\partial x_i} = -\frac{\partial p}{\partial x_j} + \frac{1}{Re} \frac{\partial^2 u_j}{\partial x_i \partial x_i} + \delta_{1j} F_{CPG}, \quad (3.4b)$$

$$\frac{\partial s}{\partial t} + u_j \frac{\partial s}{\partial x_j} = \frac{1}{ReSc} \frac{\partial^2 s}{\partial x_j \partial x_j}, \quad (3.4c)$$

consisting of the conservation equations for mass, momentum, and passive scalar. Depending on the choice of the characteristic scales, different formulations of the Reynolds number  $Re$  exist (equations A.1). Here, the centerline velocity  $u_{cl} = \langle \bar{u} \rangle|_{y=\delta}$  and the half channel height  $\delta$  are taken, which results in the centerline Reynolds number  $Re \triangleq Re_{cl} = \delta u_{cl} / \nu$  as the governing parameter of the turbulent channel flow (and  $Sc$ ). For comparison with other studies, the friction Reynolds number  $Re_\tau$  (equation 2.34) is given. Both Reynolds numbers are linked with a semi-empirical power law (Dean, 1978; Pope, 2000)

<sup>4</sup>Quadrio et al. (2016) showed in their study that the choice of a certain forcing has no significant effect on the flow statistics.

and combined to the forcing term  $F_{\text{CPG}}$  as follows:

$$Re_{cl} = \left( \frac{Re_\tau}{0.116} \right)^{\frac{1}{0.88}}, \quad F_{\text{CPG}} = \left( \frac{Re_\tau}{Re_{cl}} \right)^2, \quad (3.5a,b)$$

where the **CPG** forcing term  $F_{\text{CPG}} = \tau_w/\delta$  compensates for the wall shear stress  $\tau_w$ .

Applying these relations directly to a rough channel flow yields a friction Reynolds number that is too low as the total shear stress increases. Therefore, a correction of  $F_{\text{CPG}}$  is required. Roughness elements in the flow domain reduce the cross-sectional area of the channel, which is expressed in terms of the effective half-channel height  $\delta_{\text{eff}} = \delta - \delta_{\text{melt}}$ . The meltdown height  $\delta_{\text{melt}}$  of the obstacles is defined as

$$\delta_{\text{melt}} = \frac{1}{2} \frac{\sum_{i=1}^{n_{\text{obj}}} V_{\text{obj},i}}{L_x L_z}, \quad \text{with } i = 1, \dots, n_{\text{obj}}, \quad (3.6)$$

half of the sum of all  $n_{\text{obj}}$  obstacle volumes  $V_{\text{obj}}$  divided by the horizontal plane of the computational domain. If objects are present on both walls of the closed channel, the equation (3.6) is valid; otherwise, the factor 1/2 is skipped for an (open) channel flow with objects on only one wall. Since the wall is not smooth, the wall shear stress is evaluated at a virtual height  $\delta_{\text{melt}}$ , which avoids evaluating the wall shear stress on oblique surfaces by a simple bulk formulation (Chan-Braun et al., 2011). The **CPG** forcing term for the rough turbulent channel flow is corrected by

$$\frac{F_{\text{CPG,rough}}}{F_{\text{CPG,smooth}}} = \left( \frac{\delta}{\delta_{\text{eff}}} \right)^3. \quad (3.7)$$

The detailed derivation of the presented relations is presented in the [Appendix](#).

**Data sampling.** A sufficient simulation duration and exclusion of the initial transient of the simulations guarantee statistical convergence of the presented cases. Convergence improves further by exploiting the centerline symmetry of the closed channel configurations by averaging over the half-channel height. A phase averaging operator of the flow variable  $\varphi$  is introduced by Stroh et al. (2016) for the closed channel flow setup (Fig. 3.3a) with streamwise aligned bars, given by

$$\left[ \overline{\varphi(y_j, z_k)} \right] = \frac{1}{n_p n_t n_x} \sum_{m=1}^{n_p} \sum_{i=1}^{n_x} \sum_{l=1}^{n_t} \varphi(x_i, y_j, z_k + mS, t_l), \quad (3.8)$$

where  $n_t$ ,  $n_p$ , and  $n_x$  are the numbers of samples, phases and grid nodes in the streamwise direction, and  $S$  is the spacing of the bars.

### 3.3.2 Validation of the Horizontal Pressure Grid Staggering for a Smooth Wall

The horizontal pressure grid staggering combined with a pressure filter in the vertical direction (section 2.5.2) is validated using a smooth turbulent channel flow with a friction Reynolds number of  $Re_\tau \approx 180$  and a rough channel flow at  $Re_\tau \approx 360$  (Fig. 3.3a). Relevant simulation parameters are displayed in Table 3.1. Available reference data from the literature is computed on different computational domains:  $[L_x \times L_y \times L_z] = [8\pi \times 2 \times 3\pi]$  for Lee and Moser (2015) and  $[L_x \times L_y \times L_z] = [4\pi \times 2 \times 4/3\pi]$  for Vreman and Kuerten (2014).

In the first step, mean statistics of the implemented pressure grid staggering (case **SC180**) are compared with smooth channel flow data from Lee and Moser (2015) and the **DNS** code **Xcompact3d** (Lazet and Lamballais, 2009). Lee and Moser (2015) use a spectral **DNS** code (Lee et al., 2013) by solving the **NSE** in the vorticity formulation (Kim et al., 1987). In contrast, the **Xcompact3d** code is equipped with compact schemes of sixth-order and a

Case	Type	$Re_\tau$	$n_x \times n_y \times n_z$	$\Delta x^+$	$\Delta y_{\min}^+$	$\Delta y_{\max}^+$	$\Delta z^+$	$Sc$	$t^+$
SC180	S	179.48	$256 \times 194 \times 128$	5.625	1.008	3.571	5.625	0.71	20
Xcompact3d	S	179.79	$256 \times 193 \times 128$	5.625	1.000	3.515	5.625	0.71	143
Moser <sup>5</sup>	S	182.09	$1024 \times 192 \times 512$	4.500	0.074	3.400	3.100	-	32
Vreman <sup>6</sup>	S	180.00	$512 \times 256 \times 256$	4.400	0.240	2.230	2.900	-	200
RC360	R	359.43	$512 \times 384 \times 320$	5.623	0.997	3.622	4.500	1.00	62
Xcompact3d	R	360.28	$512 \times 321 \times 384$	5.625	1.000	5.063	3.750	1.00	31

**Table 3.1** Simulation parameters of the smooth (S) and rough (R) turbulent channel flow. The grid spacing  $\Delta x_i^+$  is normalized with the viscous length scale  $\nu/u_\tau$ , and the simulation duration  $t^+$  is normalized with the viscous time scale  $\delta/u_\tau$ . Results from cases SC180 & RC360 are part of this work.

partial pressure grid staggering in all spatial directions. Overall, an excellent agreement is observed between the first-order and second-order mean statistics with the reference data (Figs. 3.4). Minor deviations are found in the root-mean-square (rms) of the mean passive scalar variance (Fig. 3.4d) for  $y/\delta > 0.2$ , where the maximum deviation of approximately  $-2.2\%$  is found at  $y/\delta \approx 0.6$ . Nevertheless, the newly implemented pressure treatment does not affect the statistics' quality.

Spurious pressure oscillations occur if pressure and velocities are computed on collocated grids (Laizet and Lamballais, 2009). In turn, the numerical noise in the pressure fields will degrade the quality of the velocity fields because of the inherent coupling resulting from the incompressibility assumption. It is important to note that this phenomenon is not caused by insufficient grid resolution but rather by the Poisson solver amplifying energy in the near-singular wavenumber range. At higher grid resolution, the spectral energy density decreases even further, and the tail of the spectra returns to a certain level at the highest wavenumbers, which seems to be independent of grid resolution. Furthermore, the phenomenon is intensified in the presence of an IBM, as finer grid resolution is required to resolve the viscous sublayer around the objects sufficiently. At the same time, the IBM adds energy at the small scales by the locality of forcing. Oscillations in the non-staggered simulations can be observed in the one-dimensional energy density spectra of the pressure fluctuations in Figs. 3.5 as a cusp in the high wavenumber tails of the spectra. The pressure fluctuation spectra are compared with Vreman and Kuerten's (2014) data, which is generated with a staggered finite difference code.

The staggering acts like a filter by removing energy from the pressure fluctuations at the largest wavenumbers (smallest scales) in both horizontal directions (Figs. 3.5a,b). As proposed (section 2.5.2), large scales in the pressure and velocity spectra are not affected by the pressure treatment; only the tail of the spectra decreases towards zero values. An accumulation of energy at the smallest scales in the velocity fluctuations is only observed in the spanwise direction for the spanwise velocity component (Fig. 3.5d). This numerical artefact in the non-staggered arrangement is assumed to be closely linked to the Poisson solver for the pressure since the unphysical behavior at the tail of the spectra disappears when staggering is applied.

### 3.3.3 Validation of the Horizontal Pressure Grid Staggering for a Rough Wall

In the second step, the effect of the proposed pressure treatment (section 2.5.2) is investigated on a rough flow with an active ADR IBM. The pressure is staggered in the horizontal directions and filtered in the vertical direction with a spectral pressure filter, with the filter strengths  $l_{cut} = [3, 4]$  (equations 2.58). Fig. 3.6a displays the phase-averaged pressure field

<sup>5</sup>Reference data from Lee and Moser (2015).

<sup>6</sup>Reference data from Vreman and Kuerten (2014).



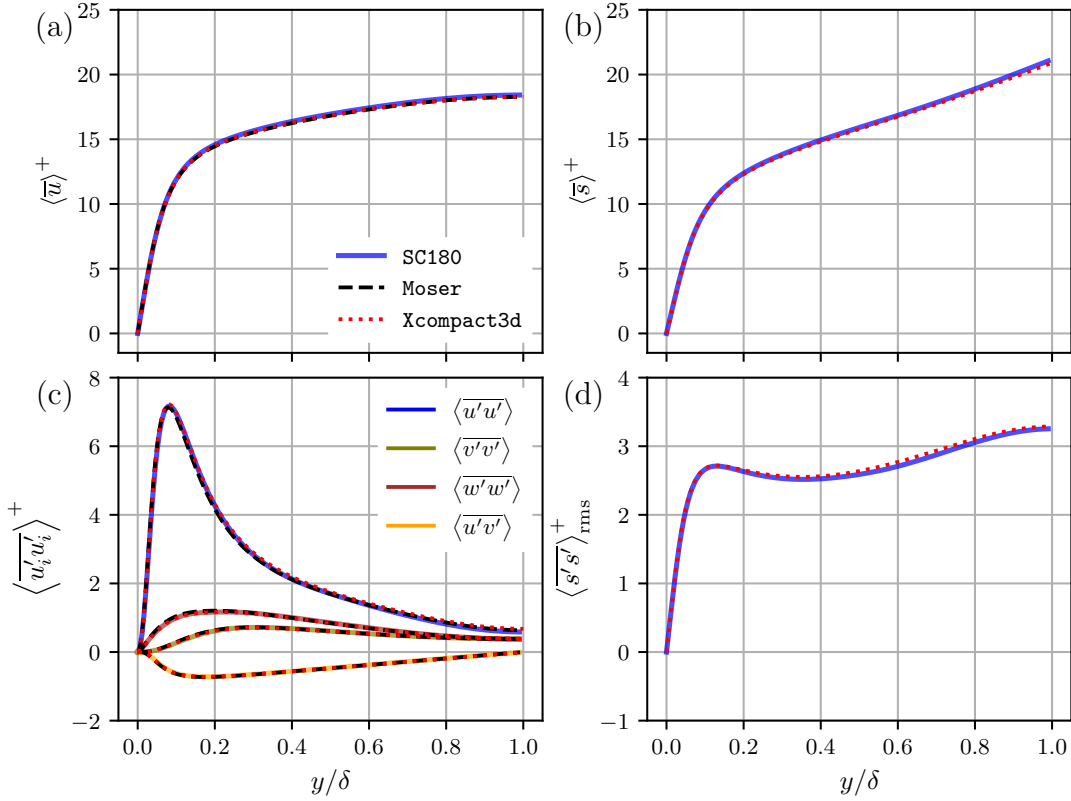


**Fig. 3.4** Comparison of mean vertical profiles of smooth channel flow in viscous units. (a) Mean streamwise velocity, (b) mean passive scalar, (c) mean Reynolds stresses, and (d) mean passive scalar variance.

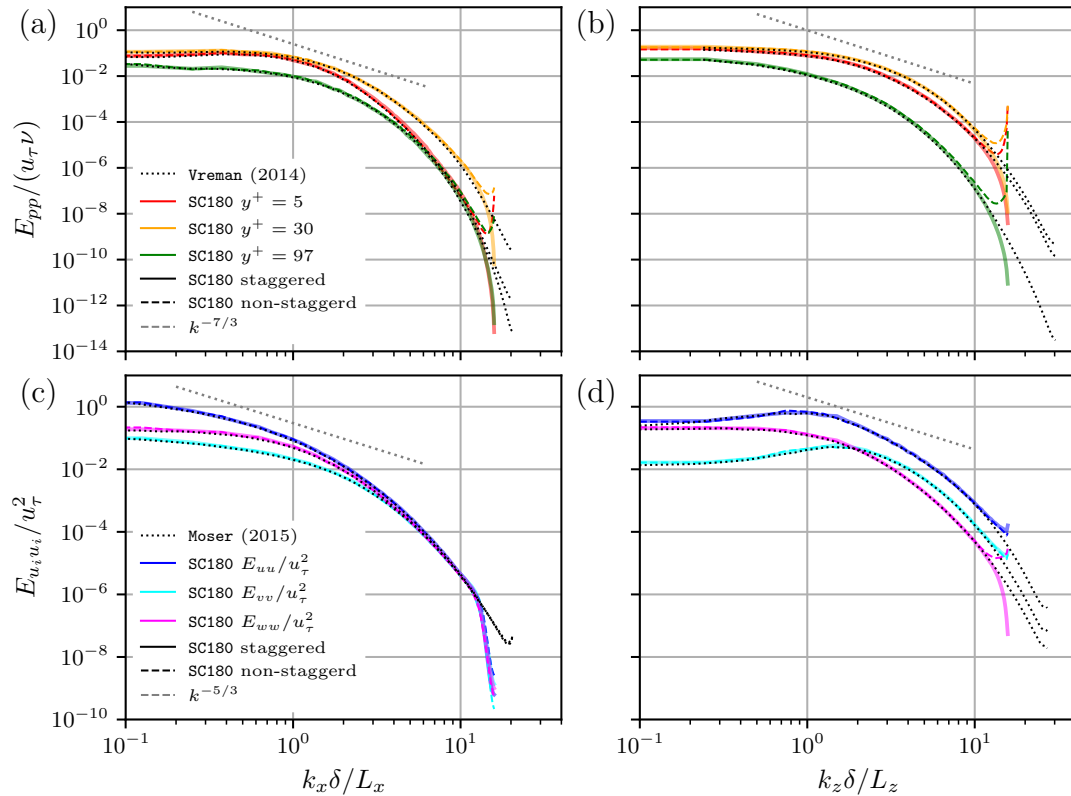


**Fig. 3.5** Comparison of spectral energy densities of (non-)staggered arrangements in streamwise and spanwise direction with literature data. (a,b) Pressure fluctuations at various vertical levels, and (c,d) velocity fluctuations at  $y^+ = 30$ .



surrounding one streamwise aligned bar, with different vertical and horizontal positions of the pressure slices. The solution of the pressure Poisson solver is a pressure field with values in the entire simulation domain, including the solid regions. One-dimensional pressure signals in the horizontal and vertical directions are not perfectly aligned (cf. Figs. 3.6b,c) since pressure fields are not perfectly converged after each 4000 computational iteration steps.

The spanwise pressure distribution (Fig. 3.6c) reveals the advantage of applying a horizontal pressure grid staggering. Spurious pressure oscillations in the collocated arrangement are smoothed by solving the pressure on a horizontally staggered grid. Eliminating pressure oscillations in the vertical is not as efficient as in the spanwise direction. Nevertheless, the applied vertical pressure filters (section 2.5.2) remove energy from the tail of the spectra by smoothly truncating the spectra at a specific wavenumber defined by the parameters  $l_{cut}$  and  $c_{25}$ . Noticeable oscillations in the vertical pressure signal are still present at  $z/\delta = 0.45$  after applying the filter (Fig. 3.6d). This spanwise location coincides with the interface, respectively, the vertical wall of the bar. To further investigate the behaviour of vertical pressure oscillations at this particular interface, an additional simulation is performed with parameters similar to RC360 but with a finer vertical grid resolution of  $n_y = 1024$ . In viscous units, the fine resolution corresponds to  $y_{min}^+ \approx 0.4$  at the bottom and up to the height of the bars, and  $y_{max}^+ \approx 1.4$  in the center of the channel. The appearance of spurious pressure oscillations is clearly linked to the vertical grid resolution and vanishes at higher resolution (Fig. 3.6d).

A similar behavior of the pressure treatment is observed not only in the mean fields but also for the distributions of spectral energy densities of pressure fluctuations at various vertical levels and velocity fluctuations at  $y^+ = 30$ , which lies within the height of the roughness elements  $H^+ = 36$  (Figs. 3.7). Here, considering only the spanwise direction is sufficient due to the one-dimensional roughness structure of the streamwise aligned bars. Reoccurring peaks in the velocity spectra in Fig. 3.7b are not related to spurious oscillation. They are a signature that the spectra is computed from three-dimensional velocity fields with zero velocities in the solid regions.

The elimination of artificial spurious pressure oscillations from the numerical solution by using a horizontally staggered pressure grid in combination with a filter in the vertical does not impact the large and intermediate scales (Fig. 3.7a). The velocity spectra is solely changed at the smallest scales for the spanwise velocity in the spanwise direction (Fig. 3.7b). This provides a stable and consistent algorithm for the representation of geometrically complex horizontal boundaries that maintain the advantages of the code, namely modular implementation, high scalability, and flexibility concerning the choice of the wall-normal grid. The next step validates the proposed algorithm against an existing DNS code (section 3.3.4) and wind tunnel measurements in combination with LES data (section 3.3.5).

### 3.3.4 Comparison of Rough Turbulent Channel Flow Data

The implementation is tested against the Xcompact3d algorithm, which is well-validated against literature data (Parnaudeau et al., 2008; Gautier et al., 2013, 2014; Giannenas and Laizet, 2021). Besides similar spatial discretization schemes and order of accuracy, Xcompact3d uses the ADR IBM described in section 2.5.3, with a distinct difference in the interpolation strategy used for the artificial flow inside the solid regions. In Xcompact3d, Lagrangian polynomials are applied instead of cubic splines as in the present code. Cubic splines efficiently avoid the well-known problem of Runge's phenomenon (Runge, 1901) for polynomial interpolation of high-order on equidistant grids, where large errors are observed at the boundaries of an interval. This phenomenon is analogous to the Gibbs phenomenon in spectral space for periodic functions with discontinuities.

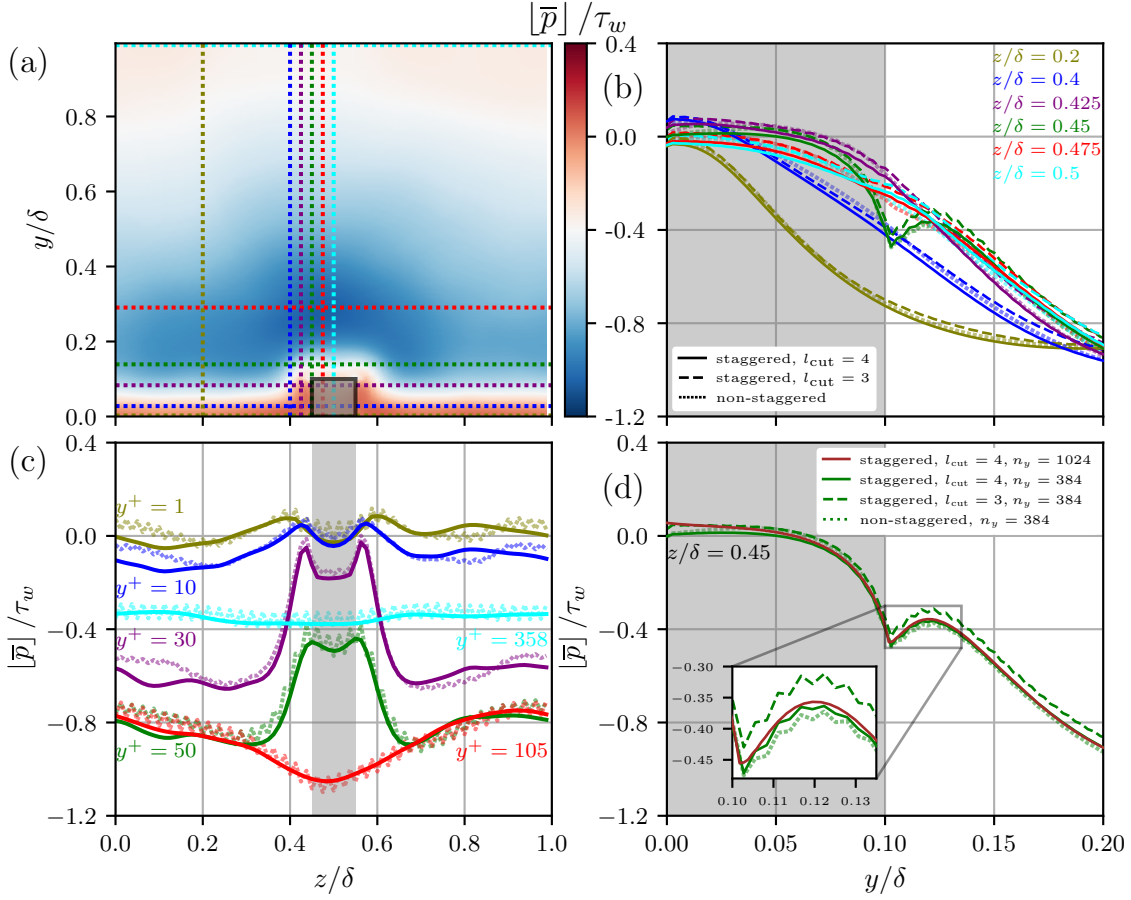


**Fig. 3.6** (a) Phase-averaged mean pressure field, with horizontal pressure grid staggering and vertical filter strength  $l_{\text{cut}} = 4$ , dotted colored lines depict positions of slices at  $z/\delta = [0.2, 0.4, 0.45, 0.5]$  and  $y^+ = [1, 10, 30, 50, 105, 358]$ . (b) Vertical pressure slices, the ordinate is identical to the colorbar range of (a). (c) Horizontal pressure slices. (d) Vertical pressure slice at the interface of fluid and solid at  $z/\delta = 0.45$  with an additional staggered simulation with  $n_y = 1024$  and  $l_{\text{cut}} = 4$  (brown line). Grey shaded areas depict the solid region, and the colors of the line plots correspond to positions in (a).

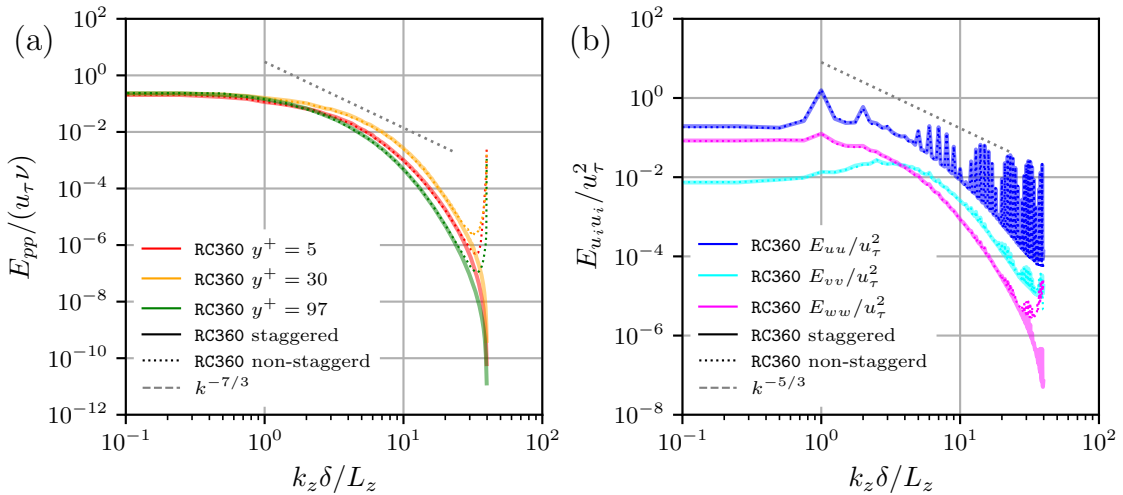


**Fig. 3.7** Comparison of spectral energy densities with staggered and non-staggered arrangements in the spanwise direction. (a) Pressure fluctuations at various vertical levels and (c) velocity fluctuations at  $y^+ = 30$ .

Case	$Re_{\tau,\text{eff}}$	$Re_{b,\text{eff}}$	$u_{b,\text{eff}}^+$	$C_{f,\text{eff}}$	$Nu_{\text{eff}}$
RC360	359.43	5741.77	15.97	$7.84 \cdot 10^{-3}$	15.21
Xcompact3d	360.28	5671.62	15.74	$8.07 \cdot 10^{-3}$	15.28

**Table 3.2** Global flow properties for rough channel flow with streamwise aligned bars. Reynolds numbers and bulk velocity according to equations (A.1a,b,e), skin friction coefficient  $C_{f,\text{eff}} = 2(u_{\tau,\text{eff}}/u_{b,\text{eff}})^2$  and Nusselt number according to Stroh et al. (2020a), cf. their equations 4-8. Results from case R360 as part of this work.

Both rough turbulent channel flow simulations are computed with a similar friction Reynolds number of  $Re_{\tau,\text{eff}} \approx 360$ . The grid resolution and dimensionless numbers can be found in Table 3.1, and a sketch of the domain configuration is shown in Fig. 3.3a. This simulation setup with streamwise aligned bars generates a secondary motion of Prandtl's second kind (Prandtl, 1952) orientated perpendicular to the main flow direction (Vanderwel et al., 2019; Schäfer et al., 2019).

Effective integral flow properties in Table 3.2 (denoted with the subscript  $(\cdot)_{\text{eff}}$ ) are evaluated with the effective half-channel height  $\delta_{\text{eff}}$  respectively at the virtual mean roughness height  $y_0 = \delta_{\text{melt}}$  (section 3.3.1). A closer look reveals a slightly lower friction Reynolds number by 1.6‰ than the initially intended  $Re_{\tau} = 360$ . Therefore, the friction velocity is also slightly reduced by 1.1‰ compared to the Xcompact3d data. The friction coefficient between both codes decreases by 3‰, resulting from the enhanced bulk velocity of 1.4‰ due to a lower wall shear stress. The deviations between both codes are in an acceptable range. They can be explained with the difference of the IBM interpolation schemes and differences in the total simulation time  $t^+$ .

The vertical mean profiles of first and second-order statistics are derived by applying conditional averaging (section 2.4.1) to compute the mean values within the roughness  $y/\delta \leq 0.1\delta$  (Figs. 3.8). The mean velocity and passive scalar profiles agree well with the reference data for the inner layer scaled in viscous units and the outer layer scaled in bulk units (Figs. 3.8a,b). Minor deviations appear at  $y/\delta \approx 0.2$  scaled in viscous units, where a reduced streamwise velocity is observed (Fig.3.8a), emerging from the lower friction Reynolds number. In the case of outer scaling with bulk properties of the flow, the mean profiles match perfectly (Fig.3.8b). This alleged discrepancy underlines the importance of correct scaling corresponding to the flow region in which the data is compared. The variances for the mean streamwise velocity  $\langle u'u' \rangle$  and the passive scalar  $\langle s's' \rangle$  agree well with the reference data in the range of  $y/\delta \geq 0.15$ , whereas deviations occur in the vicinity of the bars for  $y/\delta < 0.15$  (Figs. 3.8c,d). Both variances are increased by up to 10‰ between roughness elements. Differences in the implementations of the ADR IBMs in the codes may explain this behavior: Lagrangian polynomials in Xcompact3d instead of cubic splines in the present algorithm. Furthermore, fluid-solid interfaces can be located anywhere between grid points in Xcompact3d. The first fluid grid point next to an interface is skipped to avoid numerical instabilities in the interpolation procedure. This could affect turbulent properties in the IBM's operating range because of a filtering effect. For clarity, the other non-zero mean vertical Reynolds stress profiles ( $\langle v'v' \rangle$ ,  $\langle w'w' \rangle$ ,  $\langle u'v' \rangle$ ) are not displayed here but show a good agreement for  $y/\delta \geq 0.15$  with the reference data and slightly reduced values for  $y/\delta < 0.15$  with a maximum reduction in  $\langle w'w' \rangle^+$  of 5‰.

In summary, the present comparison of rough channel flow with reference data from a well-tested DNS code Xcompact3d and the current IBM implementation present an excellent overall agreement between integral flow properties and first-order and second-order statistics above roughness elements. In the reach of roughness elements, where the ADR IBM is mainly impacting the flow, deviations in the Reynolds stresses are observed

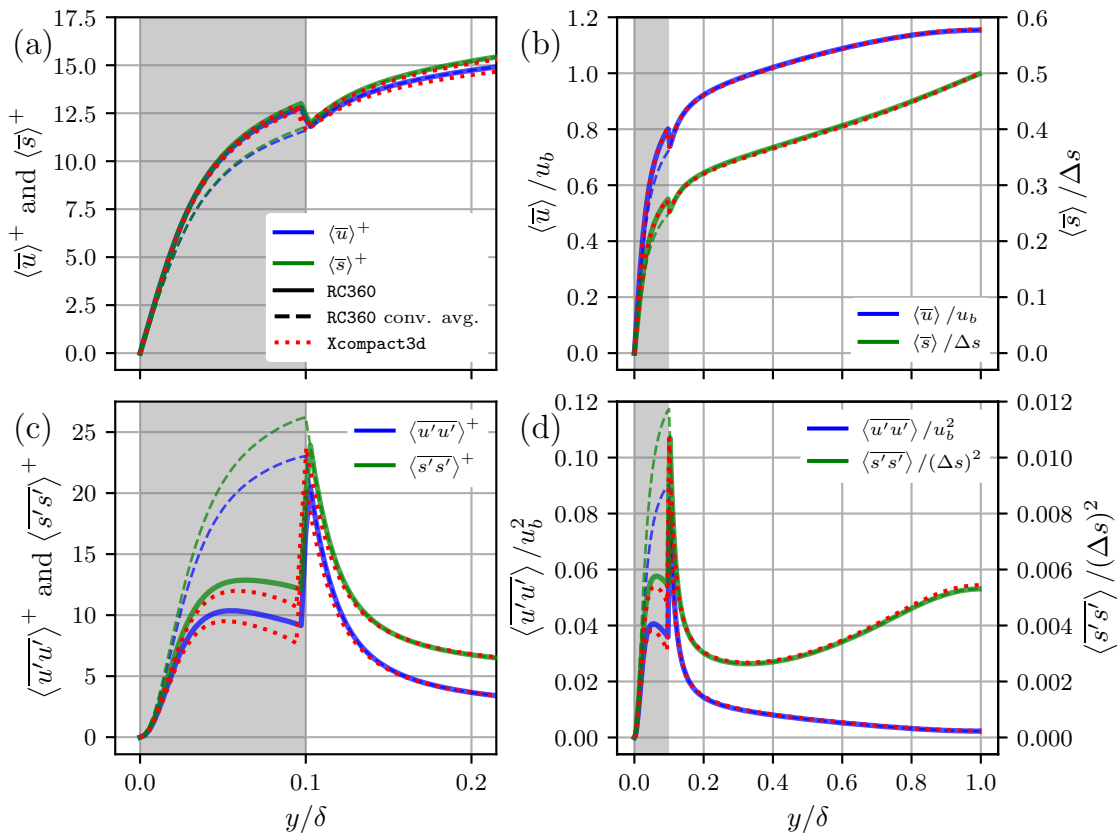


**Fig. 3.8** Comparison of mean vertical profiles of rough channel flow, non-dimensionalized in inner and outer units. (a) Mean streamwise velocity and mean passive scalar in viscous units, and (b) in bulk units; (c) mean streamwise velocity and passive scalar variance in viscous units, and (d) in bulk units. Dashed lines are conventional averages, and grey shaded areas depict the height of the bars.

between both codes and are related to implementation differences. Previous comparison studies of codes using body-conforming grids and IBM codes show similar magnitudes of deviations in second-order statistics (Theobald et al., 2021; Schäfer et al., 2020, pp. 91-96). Besides the consistency of the results of both codes, the following validation step shows the physical consistency of the ADR IBM implementation.

### 3.3.5 Comparison with Wind Tunnel and LES Data

The second part of the IBM validation is a comparison between the reference study of Llaguno-Munitxa et al. (2017) and a current DNS setup with geometric similarity. In the reference study, air flows in street canyons were investigated in LES and wind tunnel experiments with different roof geometries. This validation step aims to ensure physically reasonable results of the implemented IBM. All vertical profiles of DNS, LES and wind tunnel data presented in the following correspond to measurements in the middle of the last street canyon – the center between two housing blocks with flat roofs (Fig. 3.3b). Assuming that the flow at this position is in equilibrium with the new rough boundary conditions, respectively, the flow is fully developed here.

**Setup and scale considerations.** The simulation setup is described in section 3.3.1 and depicted in Fig. 3.3b with the simulation parameters in Table 3.3. Three simulations were carried out with an identical viscosity, roughly constant friction Reynolds number of  $Re_\tau \approx 400$ , but with increasing buffer strengths of  $\alpha_{\text{buf}} = [0.25, 0.5, 1.0]$  (cf. equations 3.9). The numerical (LES) and wind tunnel experiments exhibit geometric similarity with a

Case	$Re_\tau$	$\alpha_{\text{buf}}$	$n_x \times n_y \times n_z$	$\Delta x^+$	$\Delta y_{\text{min}}^+$	$\Delta y_{\text{max}}^+$	$\Delta z^+$
WT025	441.21	0.25	$1024 \times 256 \times 1024$	3.45	0.886	3.416	1.72
WT050	415.21	0.50	$1024 \times 256 \times 1024$	3.24	0.834	3.215	1.62
WT100	406.87	1.00	$1024 \times 256 \times 1024$	3.18	0.817	3.150	1.59

**Table 3.3** Simulation parameters of rough open channel flows with the buffer strength  $\alpha_{\text{buf}}$ .

test section of  $[L_x \times L_y \times L_z] = [49H \times 8H \times 12H]$ , where  $H = 0.076$  m is the building height, and a grid size of  $[n_x \times n_y \times n_z] = [490 \times 80 \times 120]$ . The Reynolds numbers for the wind tunnel experiments, based on the building height and viscosity of air  $\nu_{\text{air}} \approx 1.5 \cdot 10^{-5}$  m<sup>2</sup>/s, are estimated as  $Re_{H,\text{WT}} \approx [1.8, 3.8] \cdot 10^4$  for the inlet velocities of  $u_{r,\text{WT}} = [3.5, 7.5]$  m/s. Analogously to this definition, the present DNS cases have a Reynolds number of  $Re_{H,\text{DNS}} = 1.14 \cdot 10^3$  ( $Re_\tau \approx 400$ ,  $u_{r,\text{DNS}} \approx 0.48$ ), which leads to a Reynolds number disparity between wind tunnel and DNS by the factors 16, respectively 33.

Assuming the existence of a viscous sublayer in the vicinity of the housing blocks, the grid resolution selected in Table 3.3 in the horizontal directions does not meet the requirement of  $\Delta x_i^+ \approx 1$  in the vicinity of vertical walls. Consequently, oscillations appear in the velocity fields in the horizontal directions, which are most pronounced at the upper edge of the first housing block. Further investigations showed a distinct dependence between a grid resolution that is too coarse and the occurrence of these velocity oscillations. A spectral filter comparable to the one described in section 2.5.2 is applied to reduce the oscillations while ensuring a feasible simulation expense.

**Buffer zone.** Periodic boundary conditions are applied in the horizontal directions. This assumption is reasonable in the spanwise direction, as wall effects from lateral boundaries of the test section in the wind tunnel should be avoided during measurements. However, a periodic boundary condition in the streamwise direction is not appropriate to match the quasi-laminar inflow condition of the reference study. Therefore, a Rayleigh-damping layer (sponge region) is located at the first and last eighth of the domain length to suppress the wake of the flow and turbulence enhanced by the roughness. A relaxation term modulated by the coefficient  $\sigma(x)$  is added to the RHS of the NSE (3.4b) and reads as

$$\left( \frac{\partial u_j}{\partial t} \right)_{\text{buf}} = -\sigma(x) (u_j - u_{j,\text{buf}}), \quad (3.9a)$$

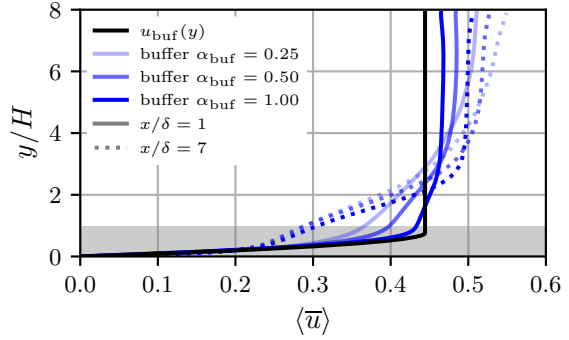
$$\text{where } \sigma(x) = \begin{cases} x_{b,1} \leq x \leq x_{e,1} & : \alpha_{\text{buf}} \left( \frac{x_{e,1}-x}{\Delta x_{\text{buf},1}} \right)^{\beta_{\text{buf}}} \\ x_{e,1} < x < x_{b,2} & : 0 \\ x_{b,2} \leq x \leq x_{e,2} & : \alpha_{\text{buf}} \left( \frac{x-x_{b,2}}{\Delta x_{\text{buf},2}} \right)^{\beta_{\text{buf}}}, \end{cases} \quad (3.9b)$$

with  $\Delta x_{\text{buf},i} = x_{e,i} - x_{b,i}$  and  $i \in \{1, 2\} \subset \mathbb{N}$  (Hu, 1996). The buffer regions start and end in the streamwise direction at  $x_{b,i} \in \{0, 7\delta\} \subset \mathbb{R}$ ,  $x_{e,i} \in \{\delta, 8\delta\} \subset \mathbb{R}$ , each buffer with a length of  $\Delta x_{\text{buf},i} = \delta$ . The buffer parameters are set to  $\alpha_{\text{buf}} = [0.25, 0.5, 1.0]$  and  $\beta_{\text{buf}} = 2$ . With this buffer area, the flow is damped to a certain extent to the quasi-laminar velocity profile  $u_{\text{buf}}(y)$  with vanishing vertical and spanwise velocities  $u_{j,\text{buf}} = (u_{\text{buf}}(y), 0, 0)^T$ , which is given by

$$u_{\text{buf}}(y) = \begin{cases} y < y_{tr} & : -\frac{u_{tr}}{y_{tr}^2} (y - y_{tr})^2 + u_{tr} \\ y_{tr} \leq y \leq L_y & : u_{tr}, \end{cases} \quad (3.10a)$$

$$\text{where } u_{tr} = u_{b,\text{buf}} \left( 1 - \frac{y_{tr}}{3\delta} \right)^{-1}, \text{ with } u_{b,\text{buf}} = \frac{1}{\delta} \int_0^\delta u_{\text{buf}} dy. \quad (3.10b,c)$$

**Fig. 3.9** Mean velocity profiles of the inflow at  $x/\delta = 1$  (solid) and the outflow at  $x/\delta = 7$  (dotted) for the three simulations (WT025, WT050, WT100) with their corresponding buffer strengths  $\alpha_{\text{buf}}$ . The buffer velocity profile  $u_{\text{buf}}(y)$  is displayed in black. The wall-normal direction  $y$  is normalized with the building height  $H$ , as depicted by the grey shaded area.



The profile  $u_{\text{buf}}(y)$  consists of a lower parabolic velocity profile and an upper constant transition velocity  $u_{tr}$ , both smoothly blended at the transition height  $y_{tr}$ . Therefore, the transition height and the bulk velocity of the profile  $u_{b,\text{buf}}$  must be estimated in advance. For this purpose, a simulation without buffer zones is conducted to measure the bulk velocity  $u_b$  and the friction Reynolds number  $Re_\tau$ . Afterwards, the bulk velocity and the velocity gradient at the wall  $d_y u_{\text{buf}}|_{y=0}$  of the buffer velocity profile are matched with the previous measurements. The transition height is determined with the following quadratic relation

$$y_{tr}^2 - 3\delta y_{tr} + 6 \frac{u_b \delta^3}{Re_\tau^2 \nu} = 0. \quad (3.11)$$

An unbuffered flow with  $Re_\tau \approx 400$  would have a transition height of  $y_{tr}/\delta \approx 1/10$ , close to the building height  $H/\delta = 1/8$ . Inflow and outflow conditions are shown in Fig. 3.9. The shape of the mean inflow velocity profiles at  $x/\delta = 1$  resembles the target buffer velocity to a higher degree with increasing buffer strength. As the buffer strength increases, the remaining turbulence reduces more and more. This does not lead to physically reasonable results since a certain level of inflow turbulence always exists in the wind tunnel. Nevertheless, the profile with  $\alpha_{\text{buf}} = 1.0$  is a good representation of the **LES Inlet#1**-condition (cf. Llaguno-Munitxa et al., 2017, their Fig. 4d). The exact inflow profile of the wind tunnel in the near-wall region is not documented.

**Instantaneous velocity fields.** The effect of the applied buffer zone on the flow in the streamwise direction is not only observable in the mean inflow and outflow profiles in Fig. 3.9 but also in the instantaneous snapshots of the velocity fields. These velocity snapshots are normalized with the free stream velocity  $u_r$  (Figs. 3.10a,b). Vertical and spanwise (not shown) velocities vanish when passing the buffer region. In the instantaneous velocity snapshot (Fig. 3.10a), very little turbulence activity and a quasi-laminar inflow are observed between the buffer and the first housing block. The streamwise distribution of turbulence activity in the flow can be analyzed by the vertical component of enstrophy  $\xi_y$  of the flow, which is given by

$$\xi_y = \frac{1}{L_y L_z} \int_0^{L_z} \int_0^{\tilde{y}} \omega_y^2 \, dy \, dz, \quad (3.12)$$

where the squared vertical vorticity  $\omega_y = (\partial_z u - \partial_x w)$  is integrated vertically from the lower boundary up to  $\tilde{y} = H$  or over the entire domain  $\tilde{y} = \delta$ . As shearing effects are excluded from this analysis, the streamwise and spanwise enstrophy components are not considered. Laminar inflow conditions with a vanishing enstrophy are observable before the first housing block (Fig. 3.11). The flow is abruptly deflected upwards at the first housing block, creating a stagnation point near the wall. This initially triggers turbulence and hence growth of a roughness sublayer (cf. peak in  $\xi_y$  at the first vertical



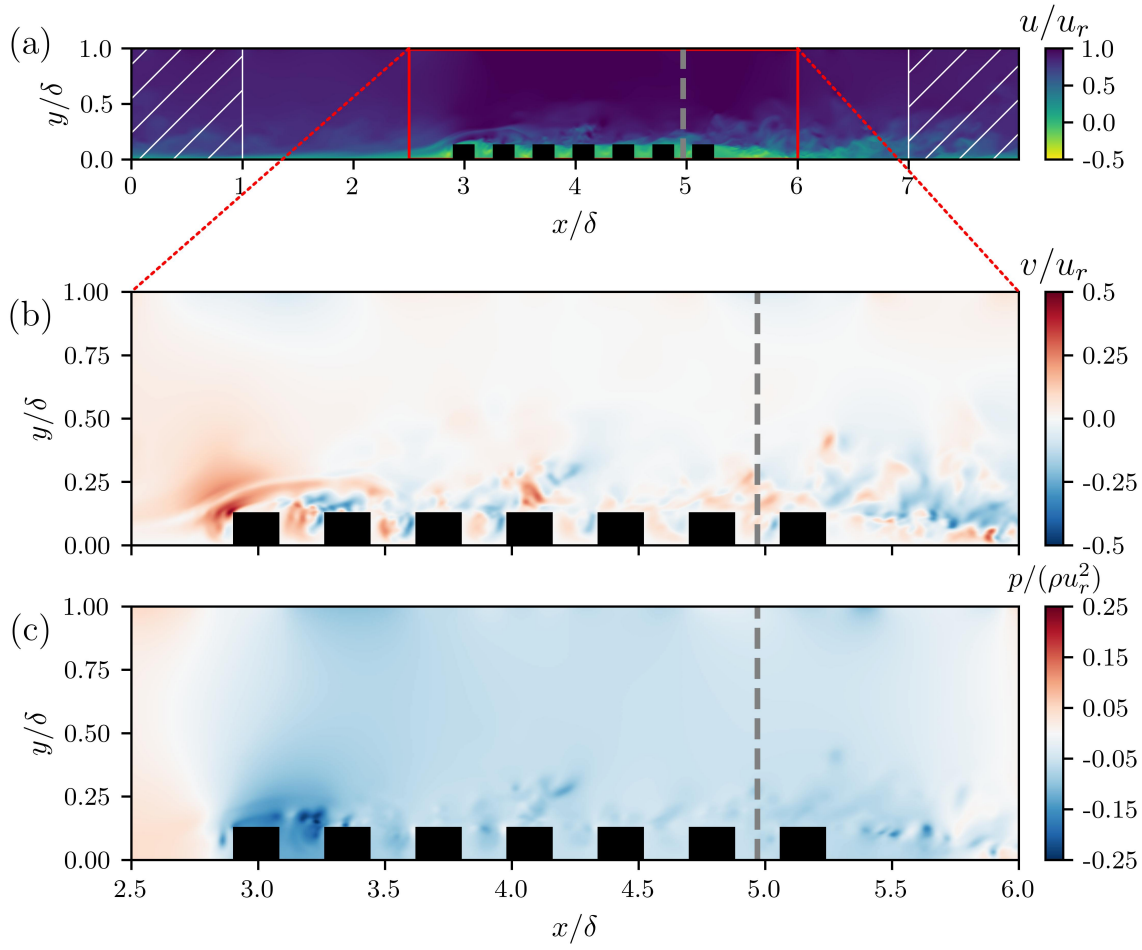


**Fig. 3.10** Instantaneous snapshots of the simulation WT050 at the spanwise location  $z/\delta = L_z/2$ . The positions of housing blocks are depicted as black squares, the measurement location for vertical profiles as grey dashed lines, and the buffer regions as white hatched areas. (a) Streamwise, (b) vertical velocity components, and (c) pressure, all normalized with the free stream velocity  $u_r$ . The close-up views of (b,c) are depicted as the red area in (a). The flow direction is from left to right.

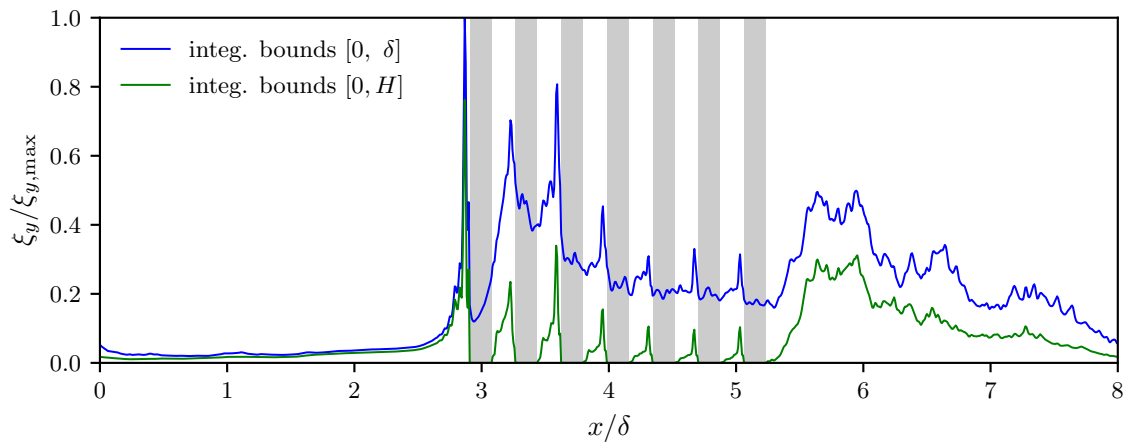


**Fig. 3.11** Streamwise distributions of the vertically integrated enstrophy  $\xi_y$ , based on the three-dimensional snapshots in Fig. 3.10. Upper integration bounds are  $[H, \delta]$  and normalization with the maximum of  $\xi_y$ , when integrated over the full domain height  $[0, \delta]$ . The grey shaded areas show the position of housing blocks.



wall in Fig. 3.11). Since the horizontal grid resolution is too coarse to fully resolve the viscous sublayer at the vertical boundary, slight residual oscillations are visible in the vertical velocity component, originating at the sharp edge of the first housing block and propagating diagonally outwards. This effect disappears at the edges of the subsequent housing blocks, and the roughness sublayer grows as the flow passes over the roughness elements. Moreover, recirculation areas inside the street canyons and a larger vortex after the buildings are formed. The streamwise distribution of  $\xi_y$  reveals that the flow adapts to the new boundary conditions from the fourth street canyon, located at  $x/\delta \approx 4.2$ .

In reality, such laminar inflow conditions (Figs. 3.10, 3.11) are questionable, as turbulent motion is always present to a certain extent. Therefore, the oscillations emerging from the quasi-laminar inflow conditions at the first housing block are neither physical nor important since they disappear at the following blocks.

The present flow configuration with solid bodies perpendicular to the streamwise direction is numerically more challenging than the simulation setup with streamwise aligned bars (section 3.3.4). Potential instabilities in the flow field might occur due to an abrupt forcing of the flow to rest at a vertical wall. Nevertheless, the instantaneous pressure field (Fig. 3.10c) is free of spurious oscillations. These findings confirm the effectiveness of the implemented numerical framework with the pressure treatment and the **ADR IBM**, resulting in high-resolution data of excellent quality.

**Vertical profiles** (Figs. 3.12). In the last street canyon, the flow over the housing blocks is assumed to be fully developed. The vertical direction is normalized with the building height  $H$  and the mean vertical profiles are normalized with the free stream velocity  $u_r$ , measured at  $y/H = 7$ , where the mean streamwise velocity is constant. Since the spanwise velocity is not measurable with the spanwise aligned hot wires in the wind tunnel experiments, this component is dropped from the mean variance (Fig. 3.12c).

The total mean velocity of the simulation WT100 agrees very well with the experimental data from the wind tunnel (Fig. 3.12a). Above the housing block, for  $y/H > 1$ , a weaker streamwise velocity gradient can be observed in Fig. 3.12b, due to the lower Reynolds number in the **DNS**. The recirculation flow inside the street canyon ( $y/H < 1$ ) is weaker and almost laminar. Within the recirculation region (between two housing blocks), the mean velocities of the standing recirculation and variances are substantially reduced compared to the reference case. This can be attributed to the difference in the scale separation on the order of one for the **DNS** setup. A test simulation was conducted to confirm that this difference vanishes with increasing Reynolds number. Given that the objective is not to reproduce this particular case but rather to confirm the consistency of the numerical and algorithmic approaches, no attempt is made here to further investigate the  $Re$ -dependence of this problem. As expected, flow statistics inside the street canyons are unaffected by varying buffer strengths since they are primarily governed by the Reynolds number.

The peaks of the mean variance profiles (Fig. 3.12c) aloft the housing blocks are a signature of an elevated buffer layer. In smooth channel flow, the buffer layer is between the viscous sublayer and the log-law region (Pope, 2000). In this setup of densely arranged roughness elements, the flow above the housing blocks can be compared to a flow over a porous medium with a roughness sublayer and a buffer layer above. The buffer zones affect the shape of variance profiles above the housing blocks (Figs. 3.12c,d). In the case of a weaker buffer, the variance is larger in the outer region, whereas in the experimental data, the variance is vanishing for  $y/H > 3$ . Considering the mean velocity profiles leads to the conclusion of an appropriate buffer strength close to unity to mimic the wind tunnel measurements. The plateau in the variance profile at  $y/H \approx 1.5$  for case WT100 is less pronounced in the **LES** data. In contrast, observing the plateau in the experimental data is impossible due to the measurement uncertainties and large vertical spacing of samples. Moreover, the buffer layer in the **LES** is either absent or not adequately resolved. It is

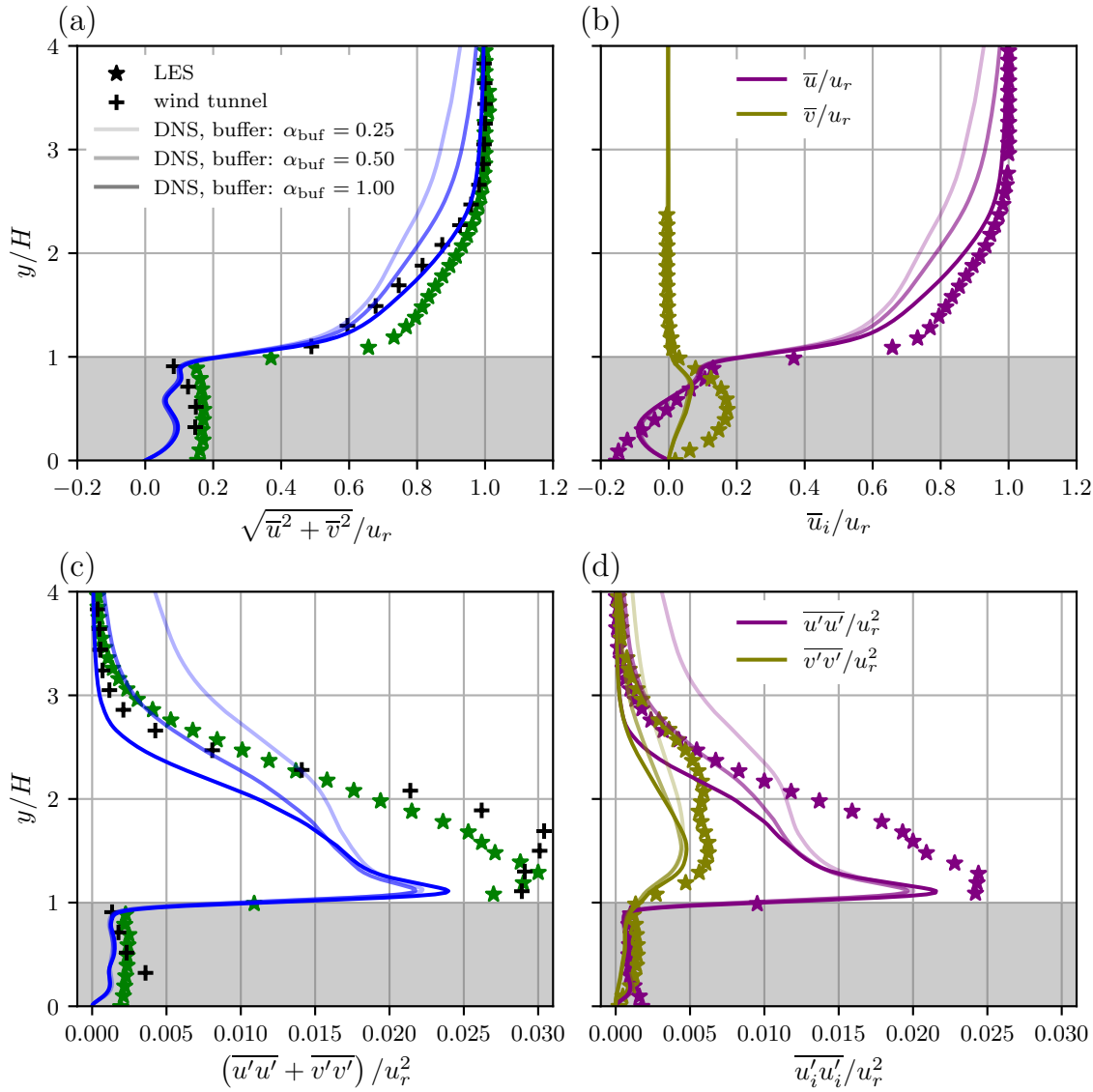


**Fig. 3.12** Comparison of mean vertical profiles of wind tunnel measurements (plus symbol), **LES** data (star symbol) and **DNS** data (solid lines, cases WT025, WT050, WT100). (a,b) Mean velocities, (c,d) mean velocity variances. All profiles are normalized with the free stream velocity  $u_r$  and the building height  $H$ . Grey shaded areas depict the height of the housing blocks.

known from previous **DNS** studies of channel flow at very high Reynolds numbers that the velocity variance peak values increase, the peak positions on the vertical axis decrease, and the plateau becomes more pronounced with increasing friction Reynolds numbers (Lee and Moser, 2015). Overall, the vertical profiles agree well with the reference data, and this comparison shows that the numerical approach is consistent. Another **DNS** at higher friction Reynolds number of  $\mathcal{O}(10^3)$  would be interesting to access the tendency of mean profiles even further compared to the wind tunnel and **LES** data.

### 3.3.6 Effect of the IBM on a Passive Scalar

To avoid spurious oscillations in the flow field, the **ADR IBM** is used in an implementation that avoids the Gibbs phenomenon. Oscillations appear due to the interplay of discontinuous functions for the higher-order derivative operators and the redistributive nature of the pressure. In the absence of the pressure gradient term in the passive scalar equation (3.4c), the question is whether the oscillations occur or not in the scalar fields if no **IBM** is used

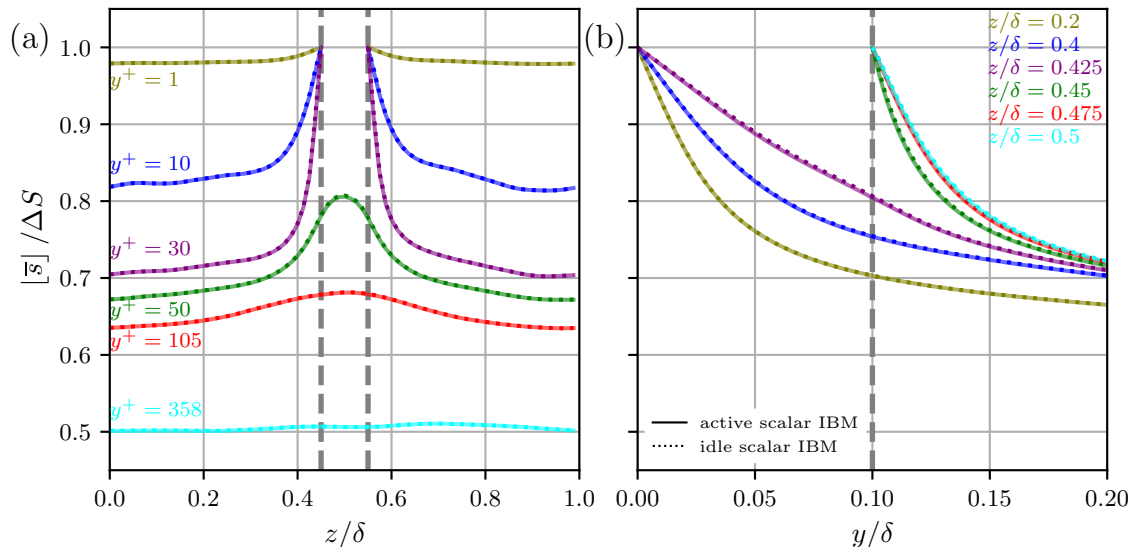


**Fig. 3.13** Line plots of the phase-averaged mean passive scalar field. (a) Horizontal and (b) Vertical passive scalar slices. Colors correspond to positions in Fig. 3.6a with slices at  $z/\delta = [0.2, 0.4, 0.425, 0.45, 0.475, 0.5]$  and  $y^+ = [1, 10, 30, 50, 105, 358]$ . Grey dashed lines depict the region of the streamwise aligned bar.

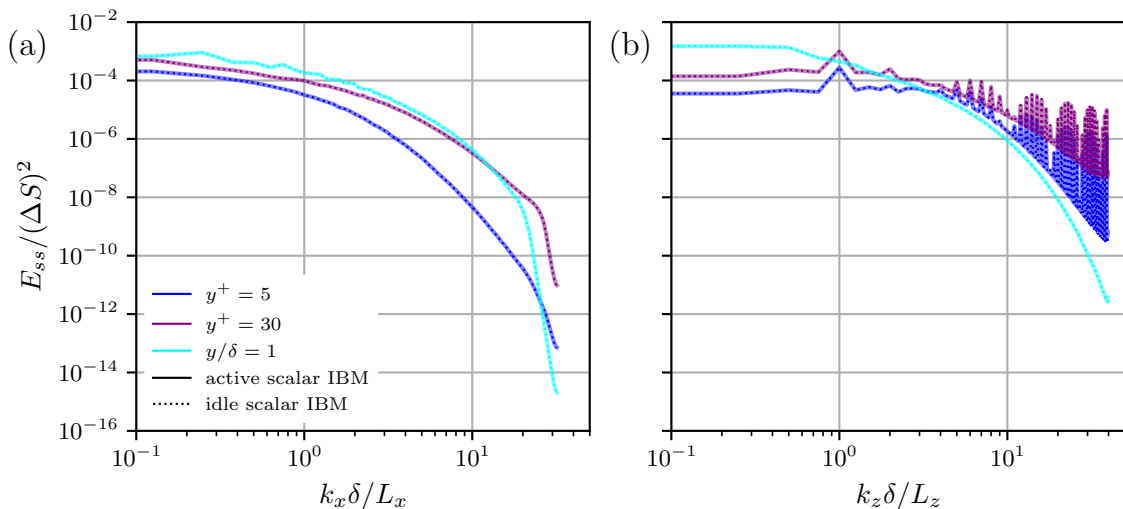


**Fig. 3.14** Comparison of spectral energy densities of scalar fluctuations with an active and idle IBM for scalar fields in (a) streamwise and (b) spanwise direction.

to compute derivatives of scalars.

The effect of an active or idle IBM on spurious oscillations in the scalar fields is tested with a slightly different simulation setup: In contrast to case RC360 (cf. Table 3.1), there are no streamwise aligned bars on the upper domain boundary. The scalar boundary values at the bottom wall and inside the solid regions have a value of one, and on the upper smooth boundary, the value is zero.

Vertical and horizontal slices of the phase-averaged mean scalar field in Figs. 3.13 reveal no significant difference if the IBM is turned on or off for the scalar transport equation. These findings are confirmed by observing the spectral energy density of scalar fluctuations in horizontal directions, depicted in Figs. 3.14. The spectral energy distribution of both settings shows very similar results, concluding that there is no significant difference in the scalar fields concerning an active or idle IBM. This observed insensitivity of scalar fields concerning the use of the ADR IBM signifies the physical consistency of the implemented

method. Hence, the present **IBM** avoids the deterioration of flow fields through oscillations and ensures a physically correct representation of the flow. The pressure term in the momentum transport equations is assumed to be closely linked to amplifying spurious numerical oscillations.



## 4. Study I: The Neutrally Stratified Rough Ekman Layer

This study deals with the effects of small-scale surface roughness in the turbulent boundary layer with neutral stratification on the bulk and transport properties of the flow. This is addressed using three rough cases with varying mean heights of roughness elements, covering the whole regime from the smooth to the transitionally rough to the verge of the fully rough regime. A method to estimate the friction of the velocity and passive scalar is presented with a focus on the logarithmic region of the flow and the corresponding parameters, such as von Kármán constants, zero-plane displacement heights and aerodynamic roughness lengths.

The following study has been published:

**Kostelecky J., Anson C. (2024): Simulation and scaling analysis of periodic surfaces with small-scale roughness in turbulent Ekman flow**, *Journal of Fluid Mechanics*, 992, pp. A8, <https://doi.org/10.1017/jfm.2024.542>.

The article is reproduced here using its original layout of the journal, where it was published under the terms of the Creative Commons Attribution 4.0 licence.

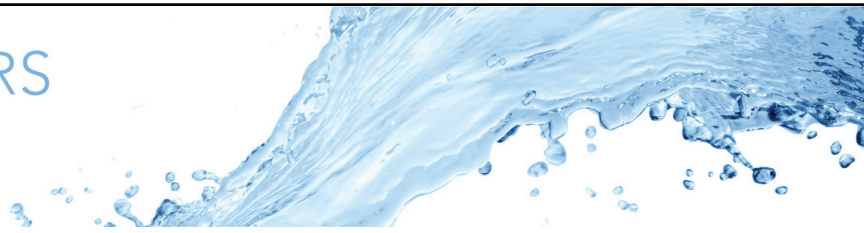
### **Author contributions:**

*Jonathan Kostelecky:* Code implementation, numerical simulations, post-processing of the data, visualization and interpretation of results, writing of the original draft, conceptualization of the study.

*Cedrick Anson:* Supervising of the research, discussion and interpretation of results, reviewing and editing the original draft, acquisition of funding, conceptualization of the study.







# Simulation and scaling analysis of periodic surfaces with small-scale roughness in turbulent Ekman flow

Jonathan Kostelecky<sup>1,2,†</sup> and Cedrick Ansorge<sup>1</sup>

<sup>1</sup>Institut für Meteorologie, Freie Universität Berlin, Carl-Heinrich-Becker-Weg 6-10, 12165 Berlin, Germany

<sup>2</sup>Institut für Geophysik und Meteorologie, Universität zu Köln, Pohligr. 3, 50969 Cologne, Germany

(Received 20 December 2023; revised 14 May 2024; accepted 30 May 2024)

Roughness of the surface underlying the atmospheric boundary layer causes departures of the near-surface scalar and momentum transport in comparison with aerodynamically smooth surfaces. Here, we investigate the effect of  $56 \times 56$  homogeneously distributed roughness elements on bulk properties of a turbulent Ekman flow. Direct numerical simulation in combination with an immersed boundary method is performed for fully resolved, three-dimensional roughness elements. The packing density is approximately 10% and the roughness elements have a mean height in wall units of  $10 \lesssim H^+ \lesssim 40$ . According to their roughness Reynolds numbers, the cases are transitionally rough, although the roughest case is on the verge of being fully rough. We derive the friction of velocity and of the passive scalar through vertical integration of the respective balances. Thereby, we quantify the enhancement of turbulent activity with increasing roughness height and find a scaling for the friction Reynolds number that is verified up to  $Re_\tau \approx 2700$ . The higher level of turbulent activity results in a deeper logarithmic layer for the rough cases and an increase of the near-surface wind veer in spite of higher  $Re_\tau$ . We estimate the von Kármán constant for the horizontal velocity  $\kappa_m = 0.42$  (offset  $A = 5.44$ ) and for the passive scalar  $\kappa_h = 0.35$  (offset  $\mathbb{A} = 4.2$ ). We find an accurate collapse of the data under the rough-wall scaling in the logarithmic layer, which also yields a scaling for the roughness parameters  $z$ -nought for momentum ( $z_{0m}$ ) and the passive scalar ( $z_{0h}$ ).

**Key words:** topographic effects, turbulent boundary layers, meteorology

† Email address for correspondence: [j.kostelecky@posteo.de](mailto:j.kostelecky@posteo.de)

© The Author(s), 2024. Published by Cambridge University Press. This is an Open Access article, distributed under the terms of the Creative Commons Attribution licence (<http://creativecommons.org/licenses/by/4.0>), which permits unrestricted re-use, distribution and reproduction, provided the original article is properly cited.

## 1. Introduction

Roughness characterizes a plethora of turbulent flows at various scales – from the smallest scales encountered in geophysical flow (such as the roughness of individual surfaces, tree leaves, etc.) via the bulk roughness of real surfaces to the largest scales in the Earth system, where topographic undulations present a roughness for synoptic-scale systems. While under strong conditions on the surface properties, a flow can be considered hydraulically smooth (Pope 2000), atmospheric flows are virtually always rough due to the small-scale heterogeneity of the underlying Earth's surface in combination with the low viscosity of air. The atmospheric boundary layer (ABL) is the lowest part of the Earth's atmosphere with a thickness of 0.1 to 2 km (Garratt 1992) and a prototype rough ABL is the objective of this study.

Rotation of the Earth is a unique feature of the ABL; despite the small Rossby number, it causes significant departures in comparison with simpler canonical flows (e.g. closed channel or pipe flow). It is commonly considered by background rotation around the vertical axis – giving rise to Ekman flow (Ekman 1905). For a statistical two-point description of the flow, such rotation breaks the symmetry in the spanwise direction. Near the ground, surface friction comes into play and decelerates the flow, and the mean wind rotates in favour of the pressure gradient force, forming the Ekman spiral. Given the friction velocity  $u_\tau$  and the Coriolis parameter  $f$ , the outer scale of the Ekman flow  $\delta = u_\tau/f$ , a scale for the boundary-layer thickness, forms as a consequence of shear growth and rotational suppression of the boundary layer; though unknown *a priori*, it is a constant for neutrally stratified flow and depends on the Reynolds number only – in stark contrast to spatially evolving boundary layers. Further, the turbulent boundary layer is complemented by an infinite reservoir of non-turbulent fluid aloft, which can be entrained into the boundary layer, causing departures of mean-flow statistics with respect to non-external canonical flows.

Direct numerical simulation (DNS) of Ekman flow is a viable model for ABL turbulence. Following the seminal work of Coleman, Ferziger & Spalart (1990), it was studied for hydraulically smooth configurations (Coleman 1999; Shingai & Kawamura 2004; Miyashita, Iwamoto & Kawamura 2006; Spalart, Coleman & Johnstone 2008, 2009; Anson & Mellado 2014, 2016; Deusebio *et al.* 2014; Shah & Bou-Zeid 2014; Anson 2019). Considerations over non-smooth surfaces are scarce: to the authors' knowledge, Lee, Gohari & Sarkar (2020), who conduct DNS of the Ekman flow for sinusoidal surface topography under neutral and stable density stratification, is the only example. They investigate two-dimensional periodic bumps with  $H^+ = 15$  at  $Re_\tau = 700$ , where  $H^+$  is the height of the bumps in viscous units and  $Re_\tau$  the friction Reynolds number, i.e. in the transitionally rough regime and find increased turbulent kinetic energy (TKE) production with an increasing slope of the bumps – counteracting buoyancy-induced suppression of turbulence. Limitations of the study are the absence of sharp edges, thus limiting flow instability and flow turbulence enhancement, the two-dimensional shape of their roughness elements and limited scale separation ( $Re_\tau$ ). Here, we complement this approach by (i) adding square surface elements to represent the small-scale roughness over homogeneous surfaces encountered frequently underneath the ABL and (ii) by an increased scale separation.

The effect of a rough boundary in turbulent flow is reviewed by Raupach, Antonia & Rajagopalan (1991), Finnigan (2000), Jiménez (2004), Kadivar, Tormey & McGranaghan (2021) and Chung *et al.* (2021). Homogeneously rough flow, i.e. flow with a statistically homogeneous description of the roughness elements, is governed by two dimensionless

parameters: (i) a roughness Reynolds number

$$H^+ = \frac{H}{\delta_v}, \quad (1.1)$$

where  $H$  is the height of roughness,  $\delta_v = \nu/u_\tau$  the viscous length scale with  $u_\tau$  the friction velocity and  $\nu$  the kinematic viscosity, and (ii) the blocking ratio  $H/\delta$ , where  $\delta$  is the boundary-layer thickness. Different roughness regimes are encountered for increasing  $H^+$ , ranging from hydraulically smooth – where no roughness effects are found in the flow statistics above the viscous layer – via transitionally rough to fully rough – where pressure drag outweighs the skin frictional drag and the buffer layer is replaced by a roughness sublayer. Values for the regime transitions are reported based on experiments (cf. table 2 in Kadivar *et al.* 2021). These are based on the pioneering work of Nikuradse (1933), who studied pipe flow with uniform sand-grain roughness and on the later work by Schlichting (1936), who introduced the equivalent sand-grain roughness with the aim of transferring Nikuradse’s theory to other roughness geometries. In essence, the latter work suggests there exists an approximate scale  $z_{0m}$  representing roughness effects also for less ideal configurations. This equivalent parameter, the aerodynamic roughness length for momentum  $z_{0m}$ , defines an empirical roughness Reynolds number  $z_{0m}^+$  which is commonly used in studies of rough configurations. The ABL flow is considered hydraulically smooth flow for  $z_{0m}^+ \lesssim 0.135$  and fully rough for  $z_{0m}^+ \gtrsim 2 - 2.5$  with the transitionally rough regime in between (Brutsaert 1982; Andreas 1987). The zero-plane displacement height  $d$  reflects a virtual shift of the effective underlying surface for high packing densities when fitting the logarithmic law. In the essence of classical scaling theory, the logarithmic law of the wall for the mean velocity  $\bar{u}(z)$  under neutral conditions is

$$\bar{u}(z) = \frac{u_\tau}{\kappa} \ln \left( \frac{z}{z_0} \right), \quad (1.2)$$

following the notation of Monin (1970) (cf. their equation 9a), with the von Kármán constant  $\kappa$ . For flow over rough surfaces,  $z$  is substituted by  $z - d$  (in 1.2), for consideration of the zero-plane displacement height  $d$ . This form of the logarithmic law – with the roughness parameter  $z_0$  – forms the cornerstone of the Monin–Obukhov similarity theory (MOST, cf. Monin 1970; Foken 2006).

The second parameter of the roughness, the blocking ratio  $H/\delta$ , can be used to describe the influence of roughness on the logarithmic layer and wall similarity (based on Townsend 1961, 1976, and elaborated by Raupach *et al.* 1991). Jiménez (2004) found that wall similarity holds if  $\delta/H > \delta_{crit}/H$  for  $\delta_{crit}/H \approx 40-80$ . Notably, for the friction Reynolds number  $Re_\tau = \delta^+$ , it is

$$Re_\tau = \frac{\delta}{H} H^+ = \delta^+. \quad (1.3)$$

However, this suggests that the total turbulent scale separation measured in terms of  $Re_\tau$  is to be considered as geometrically composed of, first, a separation between large eddies and the roughness scale and, second, a separation between the roughness scale and viscosity. The scale separation between the inner viscous scale  $\delta_{inner}$  and the outer scale  $\delta_{outer}$  of the problem in a general formulation is given as

$$Re_{gen} = \frac{\delta_{outer}}{\delta_{inner}} = \frac{\delta}{F(\delta_v, H)}, \quad (1.4)$$

in the form of the general-Reynolds number  $Re_{gen}$ . In the smooth limit, it is  $\delta_{inner} \sim \delta_v$ ,  $Re_{gen}$  is the friction Reynolds number  $Re_\tau$ . However, in the fully rough limit  $\delta_{inner} \sim H$

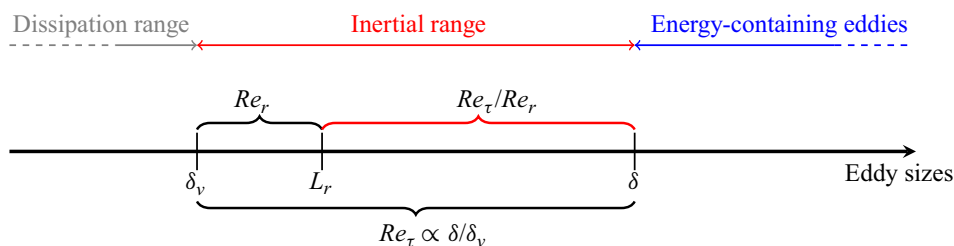


Figure 1. Schematic of the scale separation in a turbulent flow as a function of the eddy sizes, with roughness acting at a range of scale  $O(L_r)$ . The energy-containing eddies are  $O(\delta)$  for a turbulent Ekman layer and the onset of the dissipation range is located at  $O(\delta_v)$ , with the viscous scale  $\delta_v = \nu/u_\tau$ . The Reynolds numbers  $Re_\tau$  and  $Re_r$  in this schematic give rise to a reduced Reynolds number  $Re_\tau \propto Re_\tau/Re_r$ , capturing the scale separation available for large-scale eddies until they hit the effects of bulk roughness.

and  $Re_{gen}$  is the blockage ratio  $\delta/H$ . An overlap and logarithmic layer is only present if the scale separation in terms of  $Re_{gen}$  is sufficiently large.

When interpreting turbulent Ekman flow as an idealized representation of the ABL, a DNS approach inevitably resorts to the concept of Reynolds-number similarity: the scale separation necessary for a direct representation of geophysical problems at scale is out of reach, even using the most modern computational approaches. The common representation of a prototype turbulent flow shows a cascade of motions from large-scale energy-containing eddies to the dissipation range (figure 1). If there is sufficient scale separation in between the two, the inertial range develops a self-similar scaling. In this regime of fully developed turbulence, i.e. when a sufficiently large inertial range exists (Dimotakis 2005), the spectral properties are well described by the seminal theory put forward by Kolmogorov (1941) and Obukhov (1941). Further, some statistics of the flow – in particular low-order statistics, such as dissipation (Dimotakis 2005) and mean velocity profiles (Barenblatt 1993) – will cease to depend on the separation of scales, viz. Reynolds number. While these scales, and thus also  $Re_\tau$ , exist and bear a physical meaning in the rough configuration, the roughness parameter  $L_r$  (characteristic roughness length scale) defines a new length scale. For all problems of relevance, it is  $L \gg L_r$ , with  $L$  the scale of the largest eddies and in our specific problem we identify  $L \sim O(\delta)$  with the boundary-layer thickness, and  $L_r \gtrsim O(\delta_v)$  (if  $L_r \ll \delta_v$ , the surface must be aerodynamically smooth; and if  $L_r$  reaches  $O(\delta)$ , an obstacle is no longer considered a roughness element). In analogy to the decomposition of the Reynolds number  $Re_\tau$  proposed above (1.3), this gives rise to a roughness Reynolds number  $Re_r \propto L_r/\delta_v$  which can be interpreted as a range of eddy sizes locally ‘occupied’ by roughness. This range is not available for an undisturbed continuation of the inertial range as roughness alters the scales of turbulent production, as measured by  $u_\tau$ , and local dissipation of turbulence kinetic energy (Davidson & Krogstad 2014). From the perspective of large-scale motions, this limitation is similar to reducing the Reynolds number by  $O(Re_r^{-1})$ . In our study we will hence resort to cases with  $Re_r = O(1)$  such that the turbulence instability of the large-scale eddies is retained despite the intermediate Reynolds number achieved in our DNS. While this limits us to relatively small roughness elements, we retain a proper turbulent interaction between the inner and outer scales as is observed in the real-world ABL.

The investigation of roughness gives rise to a huge parameter space, as the geometry, distribution and arrangement of roughness elements impact on the turbulent flow (Kadivar *et al.* 2021). Cubical roughness elements are one preferred set-up for studying the effect of three-dimensional roughness on wall-bounded turbulent flow in vegetation and urban canopies, and we choose them also here as the building blocks of the rough surface.



There are several numerical studies with staggered or aligned arrays, varying the roughness density and the size of roughness elements. The problem is investigated through DNS for channel flow (Coceal *et al.* 2006; Leonardi & Castro 2010), and for a turbulent boundary layer (Lee, Sung & Krogstad 2011*b*). It was also assessed by large-eddy simulation (LES) (Stoesser *et al.* 2003; Kanda, Moriwaki & Kasamatsu 2004; Cheng & Porté-Agel 2015) and through wind tunnel measurements (Castro 2007; Cheng *et al.* 2007; Perret *et al.* 2019). Coceal *et al.* (2006) emphasize the difference between two- and three-dimensional roughness: mixing and transport are different for a two-dimensional setting. For flow orthogonal to the elements, there are unrealistically large sheltering effects; for flow parallel to elements, secondary motions become unrealistically large. Furthermore, their findings imply that a variable height of the roughness elements is needed to capture real-world conditions. Indeed, LES studies of Xie, Coceal & Castro (2008) and Yang *et al.* (2016), investigated flows over blocks with a Gaussian height distribution. In this study, we chose blocks with a uniform height and width distribution to represent the randomness of individual roughness elements. Individual roughness elements are randomly offset from an equidistant, regular grid to also break symmetry due their positioning. The height of roughness elements can be considered with respect to the outer scale  $\delta$  (giving rise to the blocking ratio) and the inner scale  $\nu/u_\tau$  (yielding the roughness Reynolds number  $H^+$ ; cf. (1.3)). The present work is limited to rectangular roughness blocks with a small blocking ratio ( $H/\delta \lesssim 1.5\%$ ) such that sufficient scale separation exists for a logarithmic layer to form.

The packing density of roughness elements – and hence the mutual sheltering– gives rise to three different flow regimes: isolated roughness, wake interference and skimming flow (Hussain & Lee 1980; Grimmond & Oke 1999). In the skimming regime, the packing density is sufficiently high such that the flow ‘slides’ over the roughness crests. In the other extreme case, the isolated roughness, the flow interaction between roughness elements is negligible and roughness elements can be considered as individual bluff bodies. Leonardi & Castro (2010) found the drag maximum for a packing density of 15%, which is in agreement with Kanda *et al.* (2013), whereas Ahn, Lee & Sung (2013) measured a value of 11.1% to 12.5% and Cheng & Porté-Agel (2015) a value of 10%. In the present study, we use a packing density of approximately 10%, which falls in between isolated and wake interference roughness according to Grimmond & Oke (1999) (cf. their figure 1).

In the current work, we aim to answer the following research questions regarding the quantitative effects of surface roughness on a prototype ABL: (i) What is the impact of a controlled and fully resolved surface roughness on bulk parameters and mean flow properties in the inner and outer layer? (ii) Do the rough-wall scaling and log-layer scaling follow the expected and widely used approaches in MOST for neutral conditions? (iii) Can we arrive at meaningful estimates for the zero-plane displacement and roughness length for momentum and scalar? (iv) How different is the enhanced mixing of the momentum and of the scalar in the presence of surface roughness? To do so, we extend a well-established modelling set-up for turbulent Ekman flow by an immersed boundary method (IBM) and deploy the problem on the supercomputing system Hawk at Höchstleistungsrechenzentrum Stuttgart (HLRS, Germany) to reach scale separation of up to  $Re_\tau \approx 2700$ .

## 2. Methodology

We consider Ekman flow of an incompressible fluid over a horizontal plate on the  $f$ -plane, that is, the Coriolis force only affects the horizontal velocity components and is constant. Far away from the wall, shear effects vanish and the flow is in geostrophic equilibrium, i.e. the pressure gradient is balanced by the Coriolis force.

2.1. Governing equations and parameters

The three-dimensional Navier–Stokes equations are numerically solved for an incompressible, Newtonian fluid with constant fluid properties (density  $\rho$ , viscosity  $\nu$ ) subject to steady system rotation about the vertical axis. The problem is discretized on the Cartesian coordinate system  $X_i = (X, Y, Z)^T$ , where  $X, Y$  is the streamwise, spanwise and  $Z$  the wall-normal coordinate, and we solve it on a cubic domain of size  $[0, 0, 0] \leq [X, Y, Z] \leq [L_x, L_y, L_z]$ . The streamwise direction is defined with respect to the smooth-wall flow; the flow direction deviates with increasing height and surface roughness. The dynamical system is governed by the following parameters: (i) the geostrophic wind vector  $\mathbf{G} = (G_1, G_2, 0)^T$  and force  $G = \sqrt{G_1^2 + G_2^2}$ , and (ii) the Coriolis parameter  $f$ . Both scales yield the Rossby radius  $\Lambda_{Ro} = G/f$  as a length scale. Thus, the governing flow equations are non-dimensionalized with the characteristic scales  $G, f, \Lambda_{Ro}$  and read

$$\frac{\partial u_i}{\partial x_i} = 0, \quad \frac{\partial u_i}{\partial t} + u_j \frac{\partial u_i}{\partial x_j} = -\frac{\partial \pi}{\partial x_i} + \frac{1}{Re_\Lambda} \frac{\partial^2 u_i}{\partial x_j^2} + f \epsilon_{ijk} (u_k - g_k). \tag{2.1a,b}$$

Here,  $t$  is the non-dimensional time,  $\mathbf{u} = (u, v, w)^T = (u_1, u_2, u_3)^T$  is the non-dimensional velocity vector,  $x_i = (x, y, z)^T$  the non-dimensional coordinates and  $\partial \pi / \partial x_i$  the non-dimensional, non-hydrostatic, ageostrophic pressure gradient. Further,  $\mathbf{g} = (g_1, g_2, 0)^T$  with  $g_j = G_j/G$  is the normalized geostrophic wind (by construction  $g = \|\mathbf{g}\| = 1$ ) and  $\epsilon_{ijk}$  is the alternating unit tensor. The boundary conditions for the velocities are no slip at the bottom and free slip at the top boundary; periodic boundary conditions are applied in the horizontal directions. Equations (2.1b) solely depend on the Reynolds number  $Re_\Lambda = \Lambda_{Ro}G/\nu$ . For comparison with other studies, we refer to the Reynolds number

$$Re_D = \frac{GD}{\nu} = \sqrt{2Re_\Lambda}, \tag{2.2}$$

with  $D = \sqrt{2\nu f^{-1}}$  the laminar Ekman layer thickness. Both Rossby and Ekman scalings lose their relevance once the system is in a fully turbulent state. Then, the system is scaled by the friction velocity  $u_\tau$  (non-dimensionalized form  $u_\star = u_\tau/G$ ), the turbulent boundary-layer thickness  $\delta = u_\tau/f$  (non-dimensionalized form  $\delta_\star = \delta/\Lambda_{Ro} = u_\star$ ) and the eddy-turnover scale  $f^{-1}$ . These turbulent scales result in the friction Reynolds number  $Re_\tau = u_\tau \delta / \nu$  with

$$u_\star^2 = \frac{1}{Re_\Lambda} \sqrt{\left(\frac{\partial \langle u \rangle}{\partial z} \Big|_{z=0}\right)^2 + \left(\frac{\partial \langle v \rangle}{\partial z} \Big|_{z=0}\right)^2}, \tag{2.3}$$

such that  $Re_\tau$  equals the non-dimensional wind-speed gradient at the surface. The definition (2.3) of  $u_\star$  is valid for a smooth wall located at  $z = 0$ . Over a non-flat surface, it is  $u_\star^2 = \|\boldsymbol{\tau}_w\| / (\rho G^2) = \|\boldsymbol{\tau}_\star\|$ , where  $\boldsymbol{\tau}_w$  is the total surface shear stress (non-dimensional form  $\boldsymbol{\tau}_\star$ ) and  $\rho$  the constant fluid density. As a consequence of rotation, the surface shear stress is not aligned with the geostrophic wind vector and the wind veers towards the surface as

$$\alpha(z) \triangleleft (\langle \bar{\mathbf{u}}(z) \rangle, \mathbf{g}) \quad \text{and} \quad \alpha_\star \triangleleft (-\boldsymbol{\tau}_\star, \mathbf{g}). \tag{2.4a,b}$$

The values  $u_\star, \alpha_\star$  and  $\delta_\star$  are unknown *a priori* but can be approximated as functions of  $Re_D$  (Spalart 1989). In external flow, there is a duality of scales, where the inner layer scales in inner units and the corresponding normalized quantities are denoted by  $(\cdot)^+$ , while the

## Small-scale roughness in Ekman flow

outer layer scales in outer units, denoted by  $(\cdot)^-$ . The non-dimensional length and velocity scales are defined as

$$x_i^+ = x_i u_\star Re_\Lambda = \frac{X_i}{\delta_v}, \quad u_i^+ = \frac{u_i}{u_\star}, \quad x_i^- = \frac{x_i}{u_\star} = \frac{X_i}{\delta}, \quad u_i^- = u_i. \quad (2.5a-d)$$

The scalings are mapped by  $x_i^+ = Re_\tau x_i^-$  and  $u_i^- = u_\star u_i^+$ . Spatial averaging of flow variables in the horizontal is denoted by  $\langle(\cdot)\rangle$  and temporal averaging by  $\overline{(\cdot)}$ .

Along with the conservation equation of momentum, we solve the transport equation of a passive scalar  $s$ . Boundary conditions for the passive scalar are of Dirichlet type, with a constant difference between the lower and upper walls  $\Delta s = s|_{z=L_z} - s|_{z=w}$ , with  $s|_{z=L_z} = 1$  and  $s|_{z=w} = 0$ . The conservation equation of the scalar is non-dimensionalized with the additional characteristic scale  $\Delta s$ , and it reads as

$$\frac{\partial s}{\partial t} + u_j \frac{\partial s}{\partial x_j} = \frac{1}{Re_\Lambda Sc} \frac{\partial^2 s}{\partial x_j^2}, \quad (2.6a)$$

with

$$Sc = \frac{\nu}{\kappa_d}, \quad (2.6b)$$

where  $Sc$  is the Schmidt number and  $\kappa_d$  the constant molecular diffusivity for the scalar. Analogously to the friction velocity we define a non-dimensional reference friction value for the scalar with

$$s_\star = \frac{q_\star}{u_\star} \quad \text{and} \quad q_\star = \frac{1}{Re_\Lambda Sc} \left. \frac{\partial s}{\partial z} \right|_{z=0}, \quad (2.7a,b)$$

where  $q_\star$  is the surface flux of the scalar for a smooth surface at  $z = 0$ . The scalar in inner units is given by  $s^+ = s/s_\star$  and in outer units by  $s^- = s$ , since  $s$  is scaled by  $\Delta s$ .

Following Ansgore (2017), a Rayleigh-damping layer is introduced on the uppermost 20 grid points to suppress spurious boundary effects, that may occur as a consequence of a finite domain height.

### 2.2. Intrinsic averaging

Intrinsic averaging implies that only values inside the fluid domain are considered for averaging, in contrast to extrinsic averaging, where all values in the whole domain are taken into account. Since there is a mismatch between the volume share covered by roughness elements (figure 2a, red and blue shaded area) and the corresponding share of grid points, a volume approach (figure 2b) yielding a fluid fraction for the volume in the box around each grid point is used and described in detail in Appendix A. In this study, we apply intrinsic averaging to all mean vertical profiles and global flow parameters, within the roughness layer  $z \leq H_{max}$ , where  $H_{max}$  is the height of the largest roughness element.

### 2.3. Numerical approach of the DNS code

Simulations in this study use the open source DNS code `tlab` (<https://github.com/turbulencia/tlab>). The governing equations are advanced in time with a fourth-order five-stage low-storage Runge–Kutta scheme (Williamson 1980). Spatial derivatives are computed with finite differences of sixth-order accuracy (Lele 1992). Biased compact schemes of reduced order are used at the vertical (non-periodic) boundaries. The applied discretization results in an overall fourth-order accuracy of the code. Incompressibility



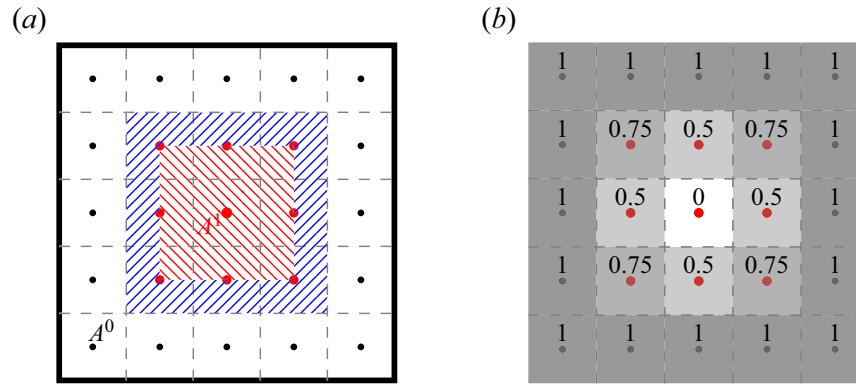


Figure 2. (a) Two-dimensional schematic of a solid object (red points) covering the area  $A^1$  immersed in a fluid domain (black points) covering the area  $A^0$ . The blue-shaded area belongs to the fluid, but field values in the area would be represented by the value on the solid surface. (b) Corresponding indicator field with volume fractions of the fluid  $\epsilon^F(x_i) = [1 - \epsilon^S(x_i)]$ .

is enforced with the fractional step method (Chorin 1968; Témam 1969) to ensure divergence-free velocity fields up to machine accuracy. The Poisson solver uses a Fourier-spectral approach in the periodic horizontal directions, and an inverse-compact approach along the vertical (Mellado & Ansorge 2012). Originally, pressure and velocities are computed on the same grid in `tlab`. This collocated arrangement is well known to cause spurious pressure oscillations (Lazet & Lamballais 2009) in combination with an IBM. Hence, the existing code was extended by a partially staggered pressure grid in the horizontal and a compact filter (Lele 1992) for the pressure in the vertical to circumvent the deterioration of the data by numerical artefacts in the pressure.

#### 2.4. Immersed boundary method

The representation of flow obstacles with vertical walls and rigid boundaries challenges DNS codes of high-order accuracy and may cause numerical artefacts, referred to as spurious force oscillations (SFOs). With the aim of using Cartesian grids, an IBM is implemented in `tlab` and tested against reference data to ensure sufficient resolution and absence of SFOs that deteriorate the flow statistics.

The Gibbs phenomenon and SFOs are known artefacts to occur in moving-body problems (Lee *et al.* 2011a), but also for non-moving bodies represented through an IBM (Li, Bou-Zeid & Anderson 2016). The SFOs appear as high-frequency oscillations near a solid boundary (Fornberg 1996, p. 11). They can severely deteriorate the numerical solution. Not only may this impact instantaneous realizations of the flow, but also the long-time averages of flow quantities. In our case of rigid bodies represented by an IBM, SFOs are caused by a stepwise signal of the IBM forcing at the solid boundary in combination with a spectral-like compact differencing scheme. The oscillations may contaminate the flow field due to the non-local character of these schemes. Filtering and smoothing procedures in physical and frequency space can be used to reduce or control SFOs (Goldstein, Handler & Sirovich 1993; Kim, Kim & Choi 2001; Lamballais & Silvestrini 2002; Tseng, Meneveau & Parlange 2006; Fang *et al.* 2011).

The direct forcing IBM approach was introduced by Mohd-Yusof (1997) and Fadlun *et al.* (2000). It tries to avoid SFOs through an artificial flow in the solid regions that reduces discontinuities at the interface while fulfilling the boundary conditions. This leaves the external flow unaffected by the artificial flow (Fadlun *et al.* 2000). While the method was extended towards higher-order derivative schemes (Parnaudeau *et al.* 2004, 2008),

it remains limited to simple geometries like cylinders, and is problematic for objects with sharp edges (Giannenas & Laizet 2021, figure 2 on p. 610).

The alternating direction reconstruction (ADR) IBM, proposed by Gautier, Laizet & Lamballais (2014), allows simulations with more complex geometries while preserving the homogeneity of spatial operators. The flow is artificially expanded into solid regions to ensure the smoothness of fields across the interface, while the boundary conditions  $u_i|_{interface} = 0$  are met. Gautier *et al.* (2014) used one-dimensional Lagrangian polynomials for interpolation, which are evaluated in the respective direction before a spatial derivative of the governing equations is evaluated in this direction. This procedure is repeated anew for each derivative and the values within the solid regions are not considered for subsequent calculations.

Lagrangian polynomials suffer from Runge's phenomenon (Runge 1901), where large amplitudes occur at the boundaries for equidistant grids. As objects get wider, numerical instabilities can occur due to unphysically large derivatives at the interface and corresponding large pressure signals inside the solid. Giannenas & Laizet (2021) use cubic splines, avoiding the Runge phenomenon at boundary nodes, which results in reduced amplitudes of the auxiliary field within the solid. They demonstrate that the ADR IBM with cubic splines is well suited for sixth-order compact schemes and does not degrade the overall convergence order of the DNS code. Further, no additional stability constraints emerge and the computational overhead is marginal. Finally, the ADR IBM is highly scalable on high-performance computing systems, as the communication overhead of the parallel algorithm does not increase.

The ADR IBM is well tested for flow around a cylinder against both experimental and simulation data (Parnaudeau *et al.* 2008; Gautier, Biau & Lamballais 2013; Gautier *et al.* 2014; Giannenas & Laizet 2021) and across different DNS codes (Schäfer *et al.* 2020; Theobald *et al.* 2021). More recently, the ADR IBM was also applied for moving objects (Giannenas & Laizet 2021), to wavy channel turbulence (Khan & Jayaraman 2019; Jayaraman & Khan 2020), jet control with microjets (Gautier *et al.* 2014), LES of a circular cylinder wake flow (Resseguier *et al.* 2017; Chandramouli *et al.* 2018), flow over periodic hill (Xiao *et al.* 2020) and to channel flow over streamwise-aligned ridges (Schäfer *et al.* 2019) and with free convection (Schäfer *et al.* 2022b).

The implementation of the ADR IBM based on cubic splines in `tlab` enables DNS of Ekman flow with fully resolved roughness. An indicator field  $\epsilon(x_i)$  is used to fully describe the spatial properties of the immersed roughness geometry in the computational domain  $\Omega$ , which is decomposed into the solid and interface  $\Omega_S$  and fluid  $\Omega_F$  regions (figure 2), given by

$$\epsilon(x_i) = \begin{cases} 1, & \text{if } x_i \in \Omega_S, \\ 0, & \text{if } x_i \in \Omega_F. \end{cases} \quad (2.8)$$

Objects are bound to the location of the grid node positions, where the outer grid nodes labelled as solid represent the exterior of the solid. Hence, a minimum of two solid points is required for the solid to have a finite size; further, three fluid points at each side are used to define the cubic spline. The ADR IBM is used to compute the derivatives (advection, diffusion) for the provisional velocity in the fractional step method, which is not divergence free. Next, the Poisson equation

$$\Delta \pi = \nabla \{ [1 - \epsilon(x_i)] f_\pi \}, \quad (2.9)$$

is solved for  $\pi$  on the staggered grid where no reconstruction is applied when calculating the pressure forcing  $\nabla f_\pi$ . The continuity equation in the presence of the IBM is now

$[1 - \epsilon(x_i)]\partial u_i/\partial x_i = 0$  and the Dirichlet boundary conditions of the velocity fields are  $[1 - \epsilon(x_i)]u_i(x_i) = 0$ . In addition, the ADR IBM is also implemented for a passive scalar, with the following boundary conditions  $s(x_i) = [1 - \epsilon(x_i)]s(x_i) + s_{BCs}\epsilon(x_i)$ , where  $s_{BCs}$  describes the fixed boundary values of the scalar. Here, the reconstruction is used for the derivatives in the advection and diffusion terms of (2.6a).

### 3. Surface roughness configuration

The targeted examination of small-scale roughness requires a small blocking ratio  $H/\delta$  (Jiménez 2004), and is in contrast to urban-like geometries or other canopy flows where obstacles may cover a considerable portion of the boundary layer. This necessitates sufficient scale separation to yield values of  $H$  of the order of tens of wall units while keeping the blocking ratio limited below  $\approx 1/100$ . In comparison with simulations over aerodynamically smooth surfaces, the grid resolution needs consideration in all three directions: first, the viscous sublayer is not restricted to  $z^+ \lesssim 5$  (Pope 2000) but forms around the obstacles, also on top of the elements such that we may expect a viscous sublayer up to  $z^+ < H^+ + 5$ . Second, the flow is also forced to rest at vertical walls, accompanied by sharp velocity gradients in the spanwise direction and an upward deflection in the streamwise direction. Hence, the horizontal grid must be sufficient for resolution of viscous sublayers at the vertical walls, which imposes additional constraints on the horizontal resolution.

We consider four simulations, one smooth and three rough cases with labels [s, r1, r2, r3]. The roughness properties are defined *a priori* in terms of the inner scaling of the smooth case (subscript  $(\cdot)_s$ ), since the drag over the rough surface is unknown. The roughness consists of  $56^2$  elements of horizontally squared shape. The centroids of these elements are slightly displaced according to the roughness grid by up to  $\pm 2$  grid points in the horizontal directions, to break the symmetry (figure 3a). Heights and widths of the elements are uniformly distributed in the range of  $\Delta H_s^+ \approx 10$  and  $\Delta W_s^+ \approx 20$ , that is  $H_s \in [H_s^+ - \Delta H_s^+/2, H_s^+ + \Delta H_s^+/2]$  and similar for  $W_s$ , with mean heights of  $H_s^+ = [9.9, 19.8, 29.5]$  and a uniform width of  $W_s^+ = [39.8, 39.8, 39.9]$ . The volume fraction covered by the roughness (A3d) at the ground is  $\gamma^S = 1 - \gamma^F = 0.099$  and equals the plan area density  $\lambda_p \hat{=} \gamma^S$ . The frontal solidities of the three rough cases are  $\lambda_f = [0.023, 0.047, 0.071]$ . The surface area increases with respect to the horizontal  $L_{xy}$ -plane for the rough cases by  $\Delta A_{eff} = 4\lambda_f$ , since the roughness elements have a square base.

For consistency, we use the same computational grid and forcing parameters at  $Re_D = 1000$  (note that simulation parameters are listed in table 1) for all four cases. The large-scale forcing is such that the mean velocity of the smooth case on the ground is approximately shear aligned, thus  $\tau_{*s} = \tau_{*s,x}$ . In the vertical, the grid spacing is  $\Delta z_s^+ \approx 1$  up to the top of the roughness elements with  $z_s^+ \geq 35$ , where stretching begins. In the horizontal it is  $[\Delta x_s^+, \Delta y_s^+] \approx 2.3$ . Obstacles increase the drag, therefore the resolution in terms of wall units is expected to be coarser, which results in slight oscillations in velocities close to the roughness elements. Preliminary simulations showed that this effect is resolution dependent and is suppressed by a spectral cutoff filter at highest frequencies.

Interpolated turbulent fields from precursor simulations are used as initial conditions for the smooth simulation. In rotating systems, disturbances from the equilibrium state cause pervasive inertial oscillations with a period  $2\pi/f$  (Appendix B, figure 17). We reduce those by replacing the mean in the three-dimensional velocity fields by a time and horizontal average over one inertial period. Once the smooth case has converged, we use velocity and passive scalar fields to initialize the rough simulations. The insertion of

## Small-scale roughness in Ekman flow

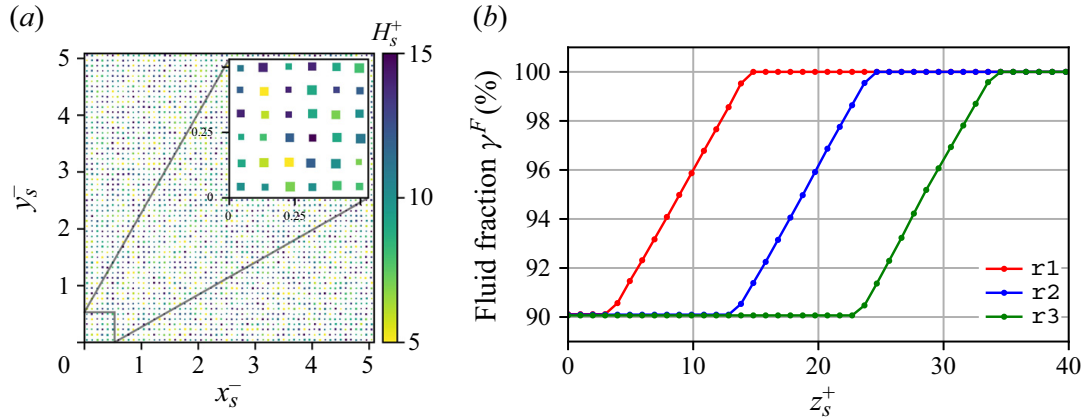


Figure 3. (a) Top view of the horizontal distribution of elements for case r1 and close-up view, colour coded according to their height; the horizontal axes are scaled by outer units of the smooth case. (b) Fluid fraction  $\gamma^F(z_s^+)$  as a function of the distance from the wall for the rough cases r1, r2, r3 to illustrate the uniform height distribution of the elements; the vertical distance is scaled in smooth inner units. Round markers indicate the vertical position of grid nodes.

$Re_\Lambda$	$Re_D$	$Sc$	$N_{xy} \times N_z$	$(L_{xy} \times L_z)/\delta_s^3$	$\Delta x y_s^+ \times \Delta z_{s,min}^+$			
$5 \times 10^5$	$10^3$	1.0	$3072^2 \times 656$	$5.1^2 \times 4.9$	$2.3^2 \times 1.0$			
Case	(ID)	$H_s^+$	$W_s^+$	$\Delta H_s^+$	$\Delta W_s^+$	$\lambda_p$ [%]	$\lambda_f$ [%]	$\Delta A_{eff}$ [%]
Rough	(r1)	10	40	10	20	10	2.3	9.2
Rough	(r2)	20	40	10	20	10	4.7	18.8
Rough	(r3)	30	40	10	20	10	7.1	28.4

Table 1. Upper table: grid, domain parameters and external Reynolds number for all cases presented in this study (subscript  $(\cdot)_s$  relates to the smooth case), and the computational domain size normalized with the Rossby radius is  $(L_{xy} \times L_z)/\Lambda_{Ro}^3 = 0.27^2 \times 0.26$ . Lower table: average height  $H_s^+$  and width  $W_s^+$  of the roughness elements for the rough cases, and their range of heights  $\Delta H_s^+$  and widths  $\Delta W_s^+$ . Also given are the plan area density  $\lambda_p$ , frontal solidity  $\lambda_f$  and the effective increase of the surface area  $\Delta A_{eff}$ .

roughness elements in fully turbulent fields is possible since the numerical methods are stable and robust. Statistics of rough simulations are collected once the flow has adapted to the new boundary conditions. In eddy-turnover times,  $f^{-1}$ , flow statistics are collected for a timespan of [6.8, 2.3, 1.9, 6.3] (Appendix B); scalar statistics are considered over the final eddy-turnover time (§ 4.7).

The data used for statistical analyses in the remainder of this study are available for download at Kostecky & Ansoerge (2024) (<http://dx.doi.org/10.17169/refubium-43215>).

## 4. Results

### 4.1. Momentum budget and wall shear stress

For our configuration, roughness enhances the drag in comparison with smooth flow. However, the quantitative impact of our roughness arrangement (§ 3) on scalar and momentum transfer is unknown *a priori*. Total surface drag is the sum of pressure drag (also called ‘form’ drag), acting normal to the vertical walls of the cuboids, and of skin

friction drag, acting tangentially. The frictional drag may further be decomposed into ground-surface drag at  $z = 0$  and roughness-element-surface drag (Shao & Yang 2008). The vertical component of the frictional drag on the roughness elements, the lift, is not of interest here.

Accurate quantification of horizontal drag exerted by roughness is essential for the subsequent analysis. A key feature of the Ekman flow is the veering of the wind with greater distance from the ground, due to the triadic balance of Coriolis, pressure gradient and frictional forces. This manifests in a non-zero spanwise component  $\tau_{zy}$  such that

$$\langle \bar{\tau} \rangle(z) = \sqrt{\langle \bar{\tau} \rangle_{zx}^2 + \langle \bar{\tau} \rangle_{zy}^2}. \tag{4.1}$$

Over smooth surfaces, the wall shear stress  $\tau_{\star s} = \langle \bar{\tau} \rangle|_{z=0}$  reduces to the streamwise component  $\tau_{\star s} = \langle \bar{\tau} \rangle_{zx} \equiv 1/Re_\Lambda \partial \langle \bar{u} \rangle / \partial z|_{z=0}$ , since we align the streamwise direction of the computational grid with  $\tau_{\star s}$  (§ 3 and figure 4, dashed lines). Over rough surfaces, we determine the total drag from the vertically integrated momentum equations (2.1b) in the streamwise and spanwise directions

$$\langle \bar{\tau} \rangle_{zi}(z) = \underbrace{- \int_0^z \frac{\partial \langle \bar{u} \rangle_i}{\partial t} dz}_{\mathcal{T}} + \underbrace{f \int_0^z \epsilon_{ik3} (\langle \bar{u} \rangle_k - g_k) dz}_{\mathcal{C}} + \underbrace{\frac{1}{Re_\Lambda} \frac{\partial \langle \bar{u} \rangle_i}{\partial z}}_{\mathcal{V}} - \underbrace{\langle \bar{u}'_i w' \rangle}_{\mathcal{R}}. \tag{4.2}$$

The total surface drag is composed of the temporal tendency ( $\mathcal{T}$ ), Coriolis ( $\mathcal{C}$ ), viscous ( $\mathcal{V}$ ) and turbulent stress contributions ( $\mathcal{R}$ ) (figure 4). Here, we define the turbulent contribution as the sum of turbulent (Reynolds) and dispersive stresses, since we study small-scale roughness.

The integrated temporal tendency is a measure of the convergence of a simulation towards its statistically steady equilibrium, and indeed cases *s* and *r3* appear as statistically converged ( $\partial_t(\cdot)/\partial t \approx 0$ ). For the rough cases *r1*, *r2*, we observe that they have not fully converged towards equilibrium in the outer layer, whereas in the near-wall region  $z^+ < 300$  the integrated tendency is negligible. This behaviour is attributed to the different averaging times of the cases (Appendix B). Disturbances from the ground, i.e. the introduction of roughness elements into the flow, slowly progress to the outer layer, starting at  $z^- \gtrsim 0.12$  and the relatively slower process of equilibration in the outer layer is apparently not converged after approximately 2–3 eddy-turnover periods.

Viscous friction dominates the momentum budget close to the wall (figure 4a), where the largest velocity gradient for the smooth case appears at  $z = 0$ , followed by a rapid decrease. With increasing roughness height a second peak develops for the cases *r2*, *r3*, linked to large velocity gradients at the top of the roughness elements. The turbulent stress dominates in the near-wall region away from the wall, with a maximum located above the roughness elements and a share of up to 80%. Turbulent stress increases with the roughness height in absolute values, pointing to enhanced turbulent mixing. The contribution of the Coriolis term is non-negligible within the roughness layer. At the top of the elements its contribution reaches up to 10%. With increasing roughness height, the veering of the wind inside the roughness layer is enhanced, underpinning the importance of the term  $\mathcal{C}$  to close the momentum budget in the roughness sublayer. Above the boundary-layer height, (4.2) is a balance between the Coriolis term, the total friction term, and for the non-converged cases the temporal tendency term.

The total surface drag of the smooth case is  $\tau_{\star s} = 2.82 \times 10^{-3}$ , as estimated from the velocity gradient at  $z = 0$ . For the rough cases,  $\tau$  reaches its maximum at the crest height of the highest elements, and it is  $\|\tau_\star\| = [3.36, 4.39, 5.38] \times 10^{-3}$ .



Small-scale roughness in Ekman flow

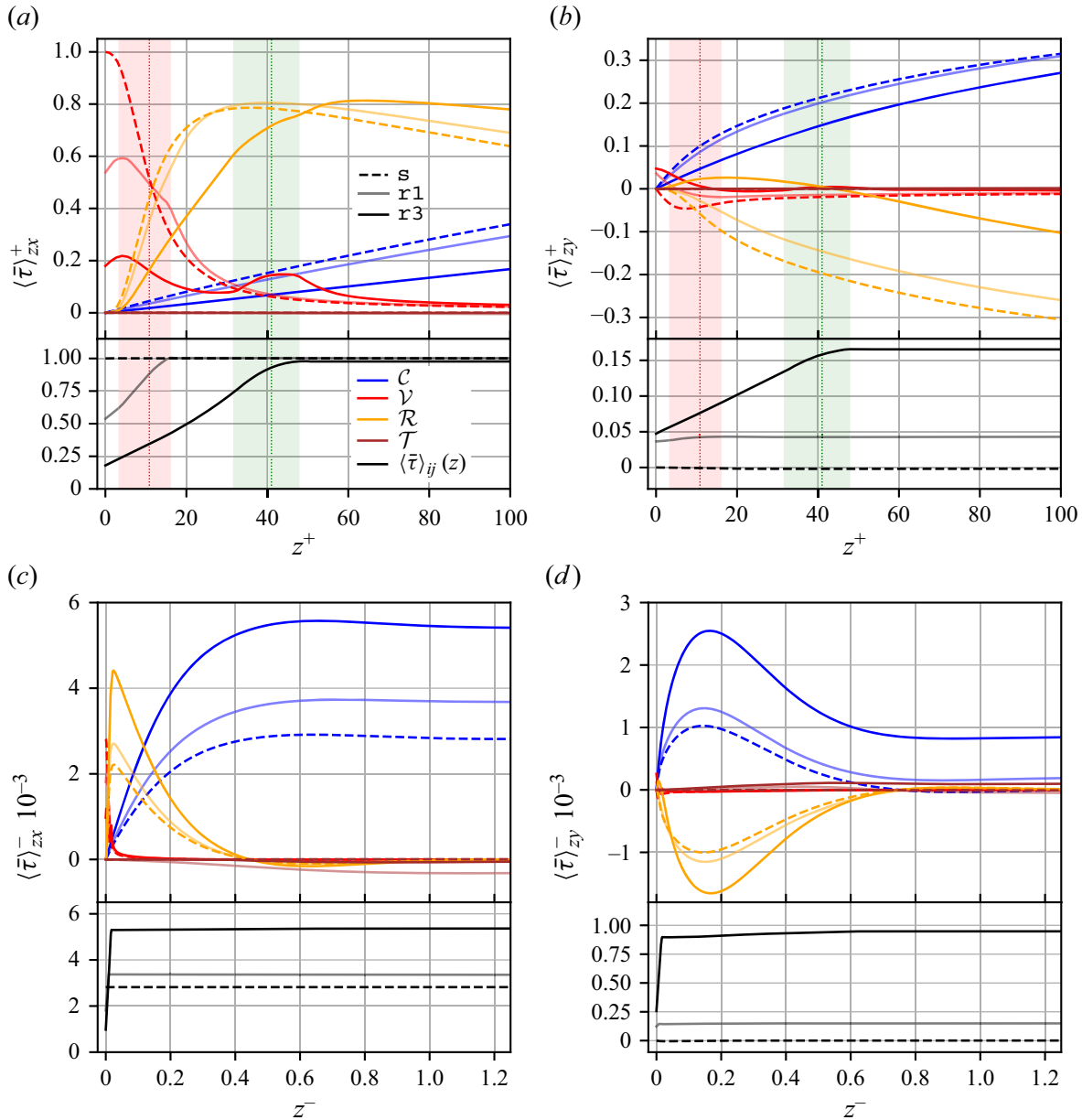


Figure 4. Integration of the mean momentum conservation in the streamwise (*a,c*) and spanwise directions (*b,d*), the terms according to (4.2). For clarity case  $r_2$  is not shown and the total drag  $\langle \bar{\tau} \rangle_{zi}(z)$  is moved to the lower panels of the plots. Colour shaded areas in the near-wall region in (*a,b*) correspond to the range of top heights of the roughness elements (cf. colour coding figure 3*b*), mean heights are displayed by vertical dotted lines. Shear stress components of the cases in the near-wall region (*a,b*) are scaled with the respective  $1/u_*^2$  and in the outer region in (*c,d*) with  $10^{-3}/G^2$ .

This gives a relative increase of the drag with respect to the smooth case of  $\Delta_{rel} \|\boldsymbol{\tau}_*\| = [19.1\%, 55.7\%, 90.8\%]$ ; this corresponds to an increase of geostrophic drag of approximately 10%–40% (table 2). Notably, when the surface stress is determined from the values of the maximum turbulent stress in the constant-flux layer (where turbulent fluxes vary less than 10%, Stull 1988; Garratt 1992), approximately 20%–30% of the total stress is neglected (cf. figure 4*a*) for the configurations considered here. While this figure is likely on the upper end of expected outcomes for atmospheric conditions at higher Reynolds number, this illustrates that estimates of skin friction from inner-layer stress may experience considerable bias over rough surfaces.

Case (ID)	Smooth (s)	Rough (r1)	Rough (r2)	Rough (r3)
$H^+$	—	10.8	24.7	40.8
$u_\star$	0.0531	0.0580	0.0663	0.0733
$\alpha_\star$	18.6	22.3	28.4	33.2
$\delta_{95}/\delta_\star$	0.612	0.621	0.594	0.578
$\delta_{CF}^+$	[39, 91, 52]	[42, 101, 59]	[51, 121, 70]	[65, 147, 82]
$Re_\tau = \delta^+$	1408	1680	2196	2688
$Re_t = \max_z \{ \frac{e^2}{\nu \epsilon} \}$	764	895	1049	1254
$Re_k = \frac{\sqrt{K} \delta}{\nu}$	316	389	528	676

Table 2. Integral flow properties of the cases. The boundary-layer thickness  $\delta_{95}$  refers to the height, where the total vertical flux is  $\sqrt{\langle u'w' \rangle^2 + \langle v'w' \rangle^2} = 0.05u_\star^2$ . The constant-flux layer  $\delta_{CF}^+$  refers to the layer between the maximum of the total vertical flux and the height where it is reduced by 10% of the maximum, and given as [start, end, extend] in inner units. The maximum for the Reynolds number of isotropic turbulence  $Re_t$  (defined in Ansorge & Mellado 2014, table 2, equation 5b) is always located above the highest roughness elements, and the Reynolds number for turbulence intensity  $Re_k$  is defined according to Schäfer, Frohnäpfel & Mellado (2022a), where  $K = \int_0^\delta e \, dz$  is the integrated TKE  $e \equiv 0.5 \langle u_i' u_i' \rangle$  within the boundary layer.

#### 4.2. Scalar budget and scalar wall stress

The scalar flux is determined by the vertical integration of the scalar budget (2.6a)

$$\overline{\langle q \rangle(z)} = - \underbrace{\int_0^z \frac{\partial \langle s \rangle}{\partial t} \, dz}_{\mathcal{T}_s} + \underbrace{\frac{1}{Re_\Lambda Sc} \frac{\partial \langle s \rangle}{\partial z}}_{\mathcal{V}_s} - \underbrace{\langle w' s' \rangle}_{\mathcal{R}_s}, \quad (4.3)$$

with the temporal tendency  $\mathcal{T}_s$ , the viscous term  $\mathcal{V}_s$  and the scalar flux term  $\mathcal{R}_s$  (cf. their behaviour in figure 5), which incorporates again the Reynolds and dispersive stresses. Unlike the momentum budget, the passive scalar concentration in the boundary layer evolves in time. Hence, the vertical integration (4.3) precedes time averaging. Near the wall, again the tendency  $\mathcal{T}_s$  is small and the viscous contribution is relevant. For increasing roughness, the viscous stress is smeared out over the height of the roughness sublayer and a second peak similar to the one discussed for the momentum budget forms. This second peak becomes more dominant for increasing roughness and will eventually govern the viscous stress for large roughness elements or skimming flow. While the share of the turbulent contribution  $\mathcal{R}$  was limited to  $\approx 80\%$  for momentum, mixing of the scalar is by far turbulence dominated, with a share of  $\gtrsim 90\%$ . In the outer region, the balance – in the absence of a rotational term – is governed by the turbulent scalar flux  $\mathcal{R}_s$  and the integrated tendency  $\mathcal{T}_s$ .

The surface flux of the scalar  $q_{\star s}$  is estimated for the smooth case at  $z = 0$  and for the rough cases,  $q$  reaches its maximum and at the same time constant value at the height of the highest elements, where  $q_\star$  is estimated. If temporal averaging of (4.3) is omitted, the development of  $q_\star(t)$  and the friction of the scalar  $s_\star(t) = q_\star(t)/u_\star(t)$  with the respective friction velocity  $u_\star(t)$  are estimated (§ 4.7 and figure 14).

#### 4.3. Global flow properties

The most prominent features when the turbulent flow is exposed to a rough surface are an increase in turbulence production associated with increased bulk shear stress  $\|\boldsymbol{\tau}_\star\|$ , a deeper boundary layer and higher turbulent Reynolds numbers (table 2). As  $\delta^+ = Re_\tau$



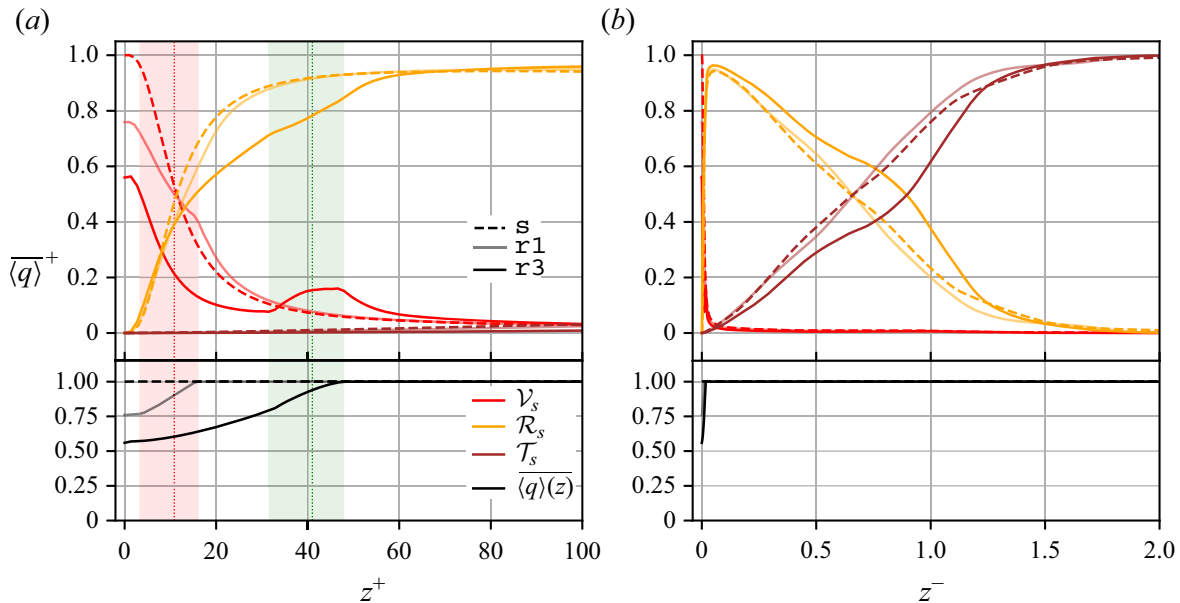


Figure 5. Integration of the mean passive scalar conservation (4.3). For clarity  $r2$  is not shown and the scalar flux  $\overline{\langle q \rangle}(z)$  is moved to the lower panels of the plots. (a) Terms in the near-wall region and (b) terms in the outer region are scaled with the respective  $1/q_\star$  and temporal averaging over the final eddy-turnover time (cf. colour coding and shaded areas in figure 4).

and  $\|\tau_\star\|$  are linearly related, also  $Re_\tau$  grows by up to 91 % (for the case  $r3$ ). For the range of blocking ratios considered here,  $Re_\tau$  appears to be a linear function of the height of the roughness elements; with  $Re_D = \text{const.} = 1000$ , this implies  $u_\star \propto (H^+)^{1/2}$ . As a consequence of increased  $u_\star$ , the grid resolution of case  $r3$  in wall units is  $\Delta xy^+ \times \Delta z_{min}^+ = 3.2^2 \times 1.4$  (compared with  $2.3^2 \times 1.0$  for the smooth case). In inviscid units, i.e. normalized with  $\Lambda_{Ro}$ , the boundary-layer thickness  $\delta_\Lambda = u_\tau / (f \Lambda_{Ro})$  also increases with  $H^+$  (not shown in table 2). This illustrates an enhanced level of turbulence in the rough cases, quantifiable by an increase of  $Re_t$  and  $Re_k$  (table 2). Changes in global flow properties of case  $r1$  are comparatively small, underpinning that the set-up is close to the aerodynamically smooth case  $s$ .

#### 4.4. Wind veer in the surface layer

Due to surface friction, the wind veers in favour of the pressure gradient force as it approaches the surface (figure 6), giving rise to the Ekman spiral. While  $\alpha_\star$ , the veer of the near-surface wind with respect to the outer layer is commonly taken into account by a rotation of the reference frame for surface-layer similarity (Ansorge 2019), wind veer within the atmospheric surface (Prandtl) layer, is commonly neglected (Monin 1970). Under this neglect, the surface layer becomes a componentwise ‘constant’-flux layer, i.e. the total vertical turbulent flux and its partitioning to the components is constant with height (commonly, a deviation of less than 10 % from the maximum value, usually measured close to the ground, is accepted). For the rough cases, the position of the constant-flux layer shifts upwards with  $H^+$ , and it grows in extent when measured in inner units. Consistently with the increased scale separation, manifest in larger  $Re_\tau$ ,  $Re_k$  and  $Re_t$ , the constant-flux layer’s thickness increases both when expressed relative to  $\Lambda_{Ro}$  and when expressed in wall units by approximately 15 %.

Within the roughness sublayer, the direct effect of surface friction is strong, and we observe a veer of up to approximately  $33^\circ$  for case  $r3$ , nearly twice the veer of the smooth

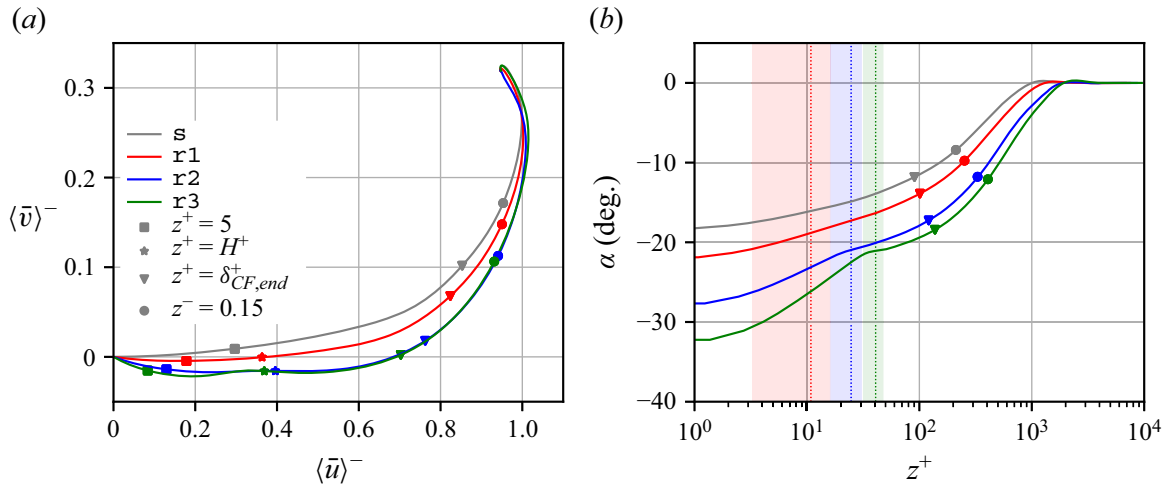


Figure 6. (a) Hodograph and (b) veering of the wind shown by means of the turning angle  $\alpha$  (2.4a) of the surface shear stress to the geostrophic wind. Symbols in panel (b) correspond to the heights as labelled in panel (a), i.e. the end of the constant-flux layer as defined by a 10% stress reduction and the upper bound of the inner layer  $z^- = 0.15$  are marked.

case ( $18^\circ$ ). Close to the ground, for  $z^+ < H^+$ , both streamwise and spanwise velocity are slower compared with the smooth case (figure 6a), but the reduction of streamwise velocity is relatively stronger – manifest in the increased veer. In reach of the roughness tops, the turning angle  $\alpha$  stays constant for r3, visible in the kink of the green curve in figure 6(b), which occurs for cases r2 and r3. As a consequence of the different wind veers within the surface roughness, the roughness field is approached at different angles for the cases presented here.

We find here that wind veer within the surface layer is not negligible for the current rough cases – and this effect appears to become stronger with increasing roughness. From previous studies on smooth Ekman flow and scaling arguments (Rossby & Montgomery 1935; Coleman *et al.* 1990), it is known that  $u_\star$  and  $\alpha_\star$  decrease with higher  $Re$  (Shingai & Kawamura 2004) and increases for stably stratified conditions (Ansorge & Mellado 2014). Roughness, which acts to increase the scale separation in terms of  $Re_\tau$  counteracts this relation by an increase in  $u_\star$  and  $\alpha_\star$ ; that means, the dependence of  $\alpha$  on the Reynolds number is outweighed by a stronger coupling of the outer and inner layers in the case of a rough surface such that overall the veering decreases. Roughness apparently comes into play as another important factor in real-world conditions for the strong dependence of both  $\alpha$  and  $u_\star$  on the height of the roughness elements (figure 6). In fact, our simulations suggest that the dependence of wind veer on both roughness and surface friction is stronger than the effects of intermediate Reynolds number (a change of  $u_\star$  and  $\alpha$  by 50% due to variation of the Reynolds number requires a change of  $Re$  by several orders of magnitude while we have only varied the roughness height by approximately a factor three).

#### 4.5. Aerodynamic parameters of the momentum

For the subsequent estimation of aerodynamic parameters, we use the total magnitude of the horizontal wind, defined as

$$\langle \bar{u}_h \rangle^+ = \sqrt{(\langle \bar{u} \rangle^+)^2 + (\langle \bar{v} \rangle^+)^2}. \quad (4.4)$$

This choice is in accordance both with atmospheric observations, where the wind magnitude is measured at different heights, and with previous numerical studies of Ekman

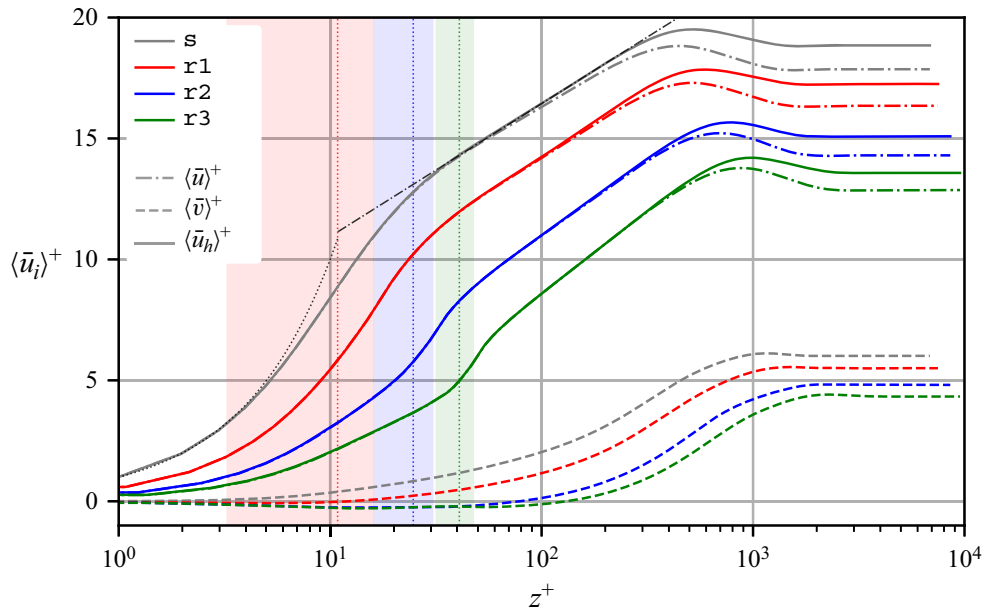


Figure 7. Intrinsically averaged velocity profiles in inner units. Displayed are the mean streamwise ( $\langle \bar{u} \rangle^+$ , dash-dotted lines), spanwise ( $\langle \bar{v} \rangle^+$ , dashed lines) and total horizontal velocity magnitudes ( $\langle \bar{u}_h \rangle^+$ , solid lines). For reference, the logarithmic and viscous laws are shown for the smooth case by thin dash-dotted and dotted lines, respectively. Parameters of the smooth logarithmic law are  $\kappa_m = 0.42$ ,  $A = 5.44$ .

flow (Shingai & Kawamura 2004; Deusebio *et al.* 2014; Jiang, Wang & Sullivan 2018). For reference, we commence by consideration of the mean velocity profile for the smooth case *s* (figure 7) in inner and outer units. This profile agrees well with previous work (Spalart *et al.* 2008, 2009; Ansorge & Mellado 2014; Ansorge 2019): in the vicinity of the ground ( $0 < z^+ \lesssim 5$ ), the viscous sublayer has a linear velocity profile  $\langle \bar{u}_h \rangle^+ = z^+$ . Above the viscous sublayer and the adjacent buffer layer, where turbulent production peaks, the logarithmic layer is found (Von Kármán 1930; Prandtl 1961; Zanoun, Durst & Nagib 2003)

$$\frac{\partial \langle \bar{u}_h \rangle^+}{\partial z^+} = \frac{1}{\kappa_m z^+} \quad \text{or in the integrated form} \quad \langle \bar{u}_h \rangle^+ = \frac{1}{\kappa_m} \ln(z^+) + A. \quad (4.5a,b)$$

Here,  $\kappa_m$  is the von Kármán constant and  $A$  an integration constant encoding the lower boundary condition, i.e. the integrated velocity profile of the viscous and buffer layers. The exact vertical bounds of the logarithmic layer are a matter of debate; following Marusic *et al.* (2013), the logarithmic region for the streamwise turbulent intensity is located at  $3\sqrt{Re_\tau} < z^+ < 0.15Re_\tau$ . For the smooth case, we choose  $z^+ > 30$  as a common value for the lower boundary (Tennekes & Lumley 1972) and  $z^+ < 0.15Re_\tau$  as the upper boundary. Within this region, we estimate  $\kappa_m = 0.42$  and  $A = 5.44$  from a least squares fit.

Over rough surfaces, the logarithmic law is expressed as

$$\langle \bar{u}_h \rangle^+ = \frac{1}{\kappa_m} \ln(z - d_m)^+ + A - \Delta \langle \bar{u}_h \rangle^+ = \frac{1}{\kappa_m} \ln\left(\frac{z - d_m}{z_{0m}}\right), \quad (4.6)$$

where  $d_m$  is the zero-plane displacement height, a function of the packing density of roughness elements (Placidi & Ganapathisubramani 2015), and  $\Delta \langle \bar{u}_h \rangle^+ = A + \kappa_m^{-1} \ln(z_{0m}^+)$  is the roughness function (Clauser 1954; Hama 1954), which describes the additional momentum loss due to roughness. Also,  $A$  is an integration constant. The roughness function measures the deceleration of the velocity with respect to smooth flow within the logarithmic region (figure 8a). If the surface is smooth, the parameters

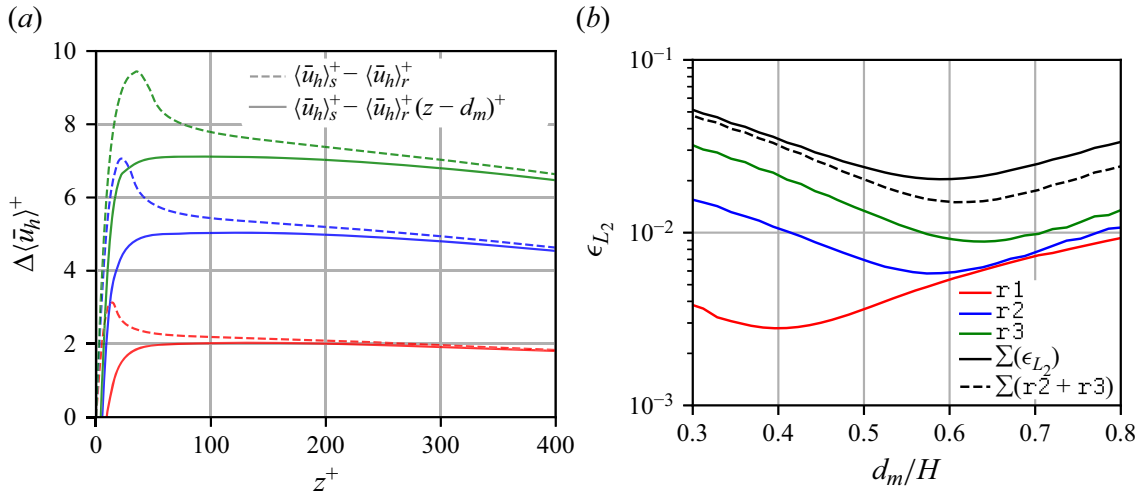


Figure 8. (a) Roughness function for the horizontal velocity magnitude. (b) Relative error  $\epsilon_{L_2}$  of the present velocity profiles and the logarithmic law fit for an optimal  $z_{0m}$  as a function of the normalized displacement height  $d_m/H$ .

$d_m$ ,  $\Delta \langle \bar{u}_h \rangle^+$  are zero. The aerodynamic roughness length  $z_{0m}$  for the smooth case is  $z_{0m}^+ = e^{-\kappa_m A} \approx 0.1$ . Traditionally, the equivalent sand-grain roughness Reynolds number  $k_s^+ = k_s u_* / \nu$  is used to compare different roughness set-ups. The roughness function follows, in the fully rough regime, a logarithmic law  $\Delta \langle \bar{u}_h \rangle^+ = \kappa_m^{-1} \ln(k_s^+) + A - A'_{FR}$  (cf. equation 2.2 in Squire *et al.* 2016). With the constant  $A'_{FR} = 8.5$  (Nikuradse 1933) the relation  $k_s^+ \approx 35.5 z_{0m}^+$  directly appears and is valid under fully rough conditions. Both forms of the rough log law (4.6) are interchangeable, whereas the first expression is preferably used in an engineering context and the second in a meteorological context.

In the quest for a universal scaling for the mean velocity profiles in the logarithmic region, an optimization problem over the set of parameters  $\{\kappa_m, z_{0m}, d_m\}$  arises, which is challenging to solve. Therefore, the following assumptions are drawn. First, the von Kármán constant is universal in this study, since the only difference in the simulation set-ups of the cases are in the surface conditions. The observed dependence of the von Kármán constant on the roughness Reynolds number  $\kappa_m = f(z_0^+)$  in atmospheric measurement data in the fully rough regime (Frenzen & Vogel 1995a,b) is according to Andreas *et al.* (2006) an artificial consequence of correlation when calculating the parameters. We follow the notion of  $\kappa_m$  as a universal constant for canonical flows over smooth (Nagib & Chauhan 2008) and rough surfaces (Castro & Leonardi 2010). As shown below, the roughness Reynolds number varies by approximately one decade in the current cases. The increase of roughness heights among cases r1–r3 is considered via an adjusted fitting interval for the logarithmic law (4.6). That is, second, we assume the logarithmic layer is located in the range  $z_{\log,m}^+ < z^+ < 0.15 Re_\tau$ , where we use  $z_{\log,m}^+ = 30 + d_m^+$ . (Due to the small value of  $H$ , the choice of  $z_{\log,m}^+$  fits the data, and should not be interpreted as predictive or general; great care should be taken with respect to higher-order statistics.) The subsequent analysis shows that we are still well within the logarithmic range of the flow with the choice of the lower limit  $z_{\log,m}^+$ . Third, the normalized displacement height  $d_m/H$  is assumed to be constant for all rough cases. In fact, this ratio is known to be mainly governed by the roughness density  $\lambda_p$  and an unclear relation of  $\lambda_f$  for  $\lambda_f < 0.1$  (Placidi & Ganapathisubramani 2015, figure 11).

### Small-scale roughness in Ekman flow

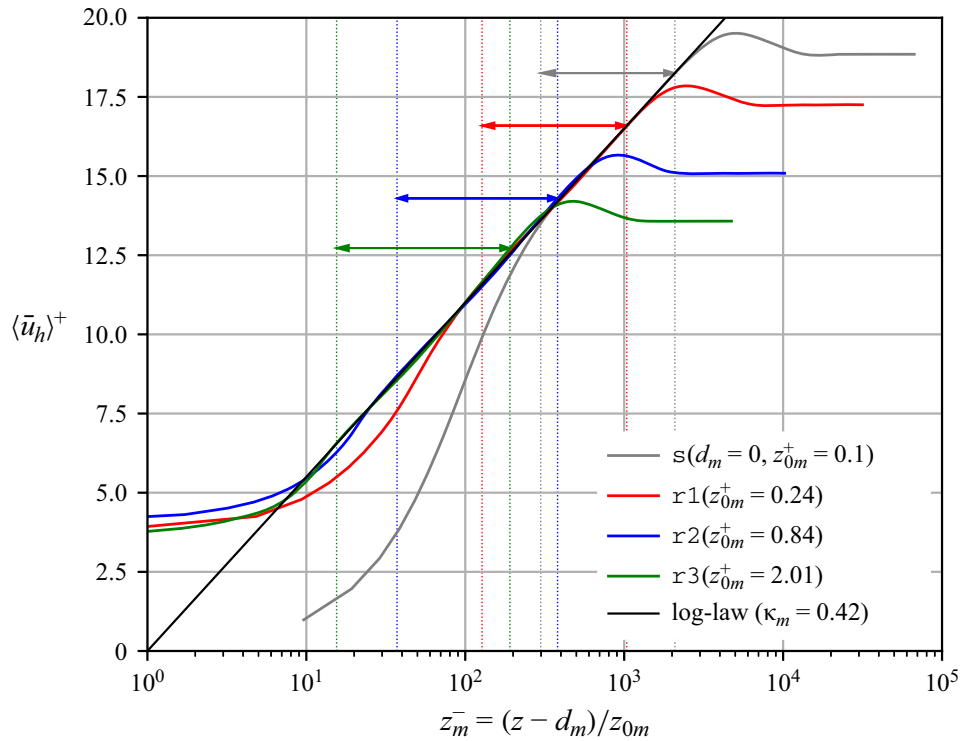


Figure 9. Collapse of the mean horizontal velocity profiles onto the logarithmic law of the wall, with the zero-plane displacement height  $d_m/H = 0.59$ . Coloured arrows and vertical dotted lines indicate the fitting interval for the logarithmic law of each case.

To determine the optimal value of  $d_m/H$ , an error norm  $\epsilon_{L_2}$  is defined for each of the corresponding intervals in (figure 8b)

$$\epsilon_{L_2}(\langle \bar{u}_h \rangle^+) |_{d_m, z_{0m}} = \frac{1}{n} \sqrt{\sum_{i \in \{z^+ | z_{\log, m}^+ < z^+ < 0.15 Re_\tau\}}^n \left[ \langle \bar{u}_h \rangle_i^+ - \frac{1}{\kappa_m} \ln \left( \frac{z_i - d_m}{z_{0m}} \right) \right]^2}. \quad (4.7)$$

The optimum value of  $d_m/H$  minimizes the expression  $\{\sum_{k \in \{r1, r2, r3\}}^n \epsilon_{L_2}\}$ . We find the optimal value of  $d_m/H \approx 0.59$  (cf. black curve in figure 8b) in accordance with literature data for  $\lambda_p = 0.1$  (Kanda *et al.* (2004) with LESs over cube roughness  $d_m/H \approx 0.65$ , Leonardi & Castro (2010) with DNS over staggered cube roughness with  $d_m/H \approx 0.6$  and Brutsaert (1982) for crop covered surfaces  $d_m/H \approx 2/3$ ). Excluding case  $r1$  (which is almost aerodynamically smooth) from the sum would result in a negligible change of the optimal value of  $d_m/H \approx 0.61$ .

The mean velocity profiles collapse onto the proposed rough log law (4.6) when scaled with  $u_\star$  and the vertical distance with  $z_m^- = (z - d_m)/z_{0m}$  (figure 9). We obtain values of the normalized aerodynamic roughness length of  $z_{0m}/H = [0.022, 0.034, 0.049]$  and scaled in inner units  $z_{0m}^+ = Re_{z_{0m}} = [0.24, 0.84, 2.01]$ . In the ABL, the onset of the fully rough regime is assumed for  $z_{0m}^+ \gtrsim 2-2.5$ , and the transitionally rough regime for  $0.135 \lesssim z_{0m}^+ \lesssim 2-2.5$  (Brutsaert 1982; Andreas 1987). By this definition, cases  $r1, r2$  are transitionally rough and  $r3$  is on the edge of being fully rough when considered in terms of  $z_{0m}^+$ . Taking into account that the transition between roughness regimes is highly dependent on the type of roughness, we conclude that case  $r3$  is fully rough for (i) its sharp-edged geometry, (ii) the occurrence of a dual peak in the viscous stress and (iii) the strong signature of roughness in all turbulent statistics. Figure 9 illustrates that the increase

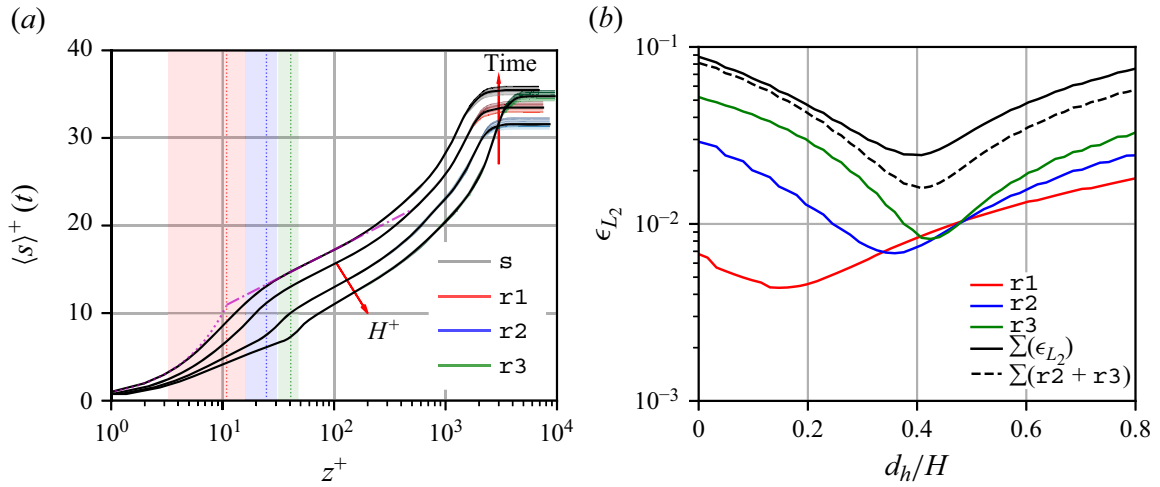


Figure 10. (a) Temporal evolution of the horizontally averaged scalar profile in inner units, shown together with the temporal mean (solid black lines). The viscous law (magenta dotted line) with  $\langle \bar{s} \rangle^+ = z^+ Sc$  and the logarithmic law (magenta dashed-dotted line)  $\langle \bar{s} \rangle^+ = \kappa_h^{-1} \ln(z^+) + \mathbb{A}$  with  $\kappa_h = 0.35$ ,  $\mathbb{A} = 4.2$  are shown for case s. (b) Relative error  $\epsilon_{L_2}$  of the present scalar profiles and the logarithmic law fit for an optimal  $z_{0h}$  as a function of the normalized displacement height  $d_h/H$ .

of  $Re_\tau$  for the rough cases also manifests in a deeper logarithmic layer, i.e. the common bounds of the logarithmic region also hold over the rough surface. In fact, the previous lower limit of  $z^+ > z_{\log,m}^+$  can be adjusted downward to  $z^+ > 25 + d_m^+$  or to  $z^+ > 0.8\sqrt{Re_\tau}$  as a function of the Reynolds number, without  $z_{0m}^+$  differing by more than  $\pm 5\%$  from the above values. The proposed procedure of estimating the aerodynamic properties of the flow is robust to the choice of the displacement height, since changing  $d_m/H = 0.6 \pm 0.1$  results in maximum deviation of the presented  $z_{0m}^+$  values of  $\pm 4.5\%$  (cf. small variation of  $\epsilon_{L_2}$  vs  $d_m/H$  in figure 8b).

#### 4.6. Aerodynamic parameters of the passive scalar

Despite the temporal evolution of mean scalar profiles  $\langle s \rangle^-$  (figure 10a),  $\langle \bar{s} \rangle^+$  is statistically steady in the logarithmic layer: the inner layer is in quasi-equilibrium with the scalar evolution in the outer layer. In the immediate vicinity of a smooth wall (case s) we resolve the conductive sublayer with  $\langle \bar{s} \rangle^+ = z^+ Sc$ . In analogy with the momentum logarithmic layer (4.6), the scalar one reads as

$$\langle \bar{s} \rangle^+ = \frac{1}{\kappa_h} \ln(z - d_h)^+ + \mathbb{A}(Sc) - \Delta \langle \bar{s} \rangle^+ = \frac{1}{\kappa_h} \ln\left(\frac{z - d_h}{z_{0h}}\right), \quad (4.8)$$

where  $\kappa_h$  is the von Kármán constant and the constant of integration  $\mathbb{A}(Sc)$  encodes the surface information. For (aerodynamically) smooth surfaces, it is  $d_h = 0$  and  $\Delta \langle \bar{s} \rangle^+ = 0$ ; for rough surfaces, the displacement height  $d_h > 0$ , the roughness function  $\Delta \langle \bar{s} \rangle^+ \neq 0$  and an aerodynamic roughness length  $z_{0h}$  emerges. We determine the parameters from our simulation data following the procedure described above and find the von Kármán constant  $\kappa_h \approx 0.35$ . While existing data of experiments appear to agree on  $\kappa_h \approx 0.47$ , DNS data yield a large spread in the range  $0.28 \lesssim \kappa_h \lesssim 0.46$  (table 3). The experimental data available (table 3) do, however, not consider external flow while externality of the flow is known to impact estimates of  $\kappa$  and can explain a substantial share of the variation in  $\kappa$  from simulation data (Ansorge & Mellado 2016).



Reference	Type (BCs)	$Re_\tau$	$Sc$	$\kappa_h$	$\mathbb{A}(Sc)$
Kader (1981)	exp. data (collection)	multiple	1.0	0.47	6.5
Subramanian & Antonia (1981)	exp. boundary layer	multiple	—	$0.48 \pm 0.02$	$2.0 \pm 0.02$
Kasagi, Tomita & Kuroda (1992)	DNS channel (v)	150	0.71	0.36	2.09
Kawamura, Abe & Matsuo (1999)	DNS channel (f)	180, 395	0.025–0.71	0.4–0.42	—
Johansson & Wikström (2000)	DNS channel (v)	265	0.71	0.33	0.95
Kawamura, Abe & Shingai (2000)	DNS channel (f/v)	180, 395	0.025–1.0	0.28 (v), 0.41 (f)	—
Pirozzoli, Bernardini & Orlandi (2016)	DNS channel	548–4088	0.2–1.0	0.46	—
Pirozzoli <i>et al.</i> (2022)	DNS pipe flow (v)	6000	1.00	0.459	5.78
Cases of this study (s, r1, r2, r3)	DNS Ekman flow (v)	1408–2688	1.00	0.35	4.2

Table 3. Parameters  $\{\kappa_h, \mathbb{A}(Sc)\}$  for the logarithmic law of the passive scalar. If known, boundary conditions (BCs) for the scalar are indicated with (v) for constant value or (f) for constant flux. All DNS of turbulent channel flow are closed channels. Kader (1981) gives a function for the integration constant with  $\mathbb{A}(Sc) = (3.85Sc^{1/3} - 1.3)^2 + 2.12 \ln Sc$ .

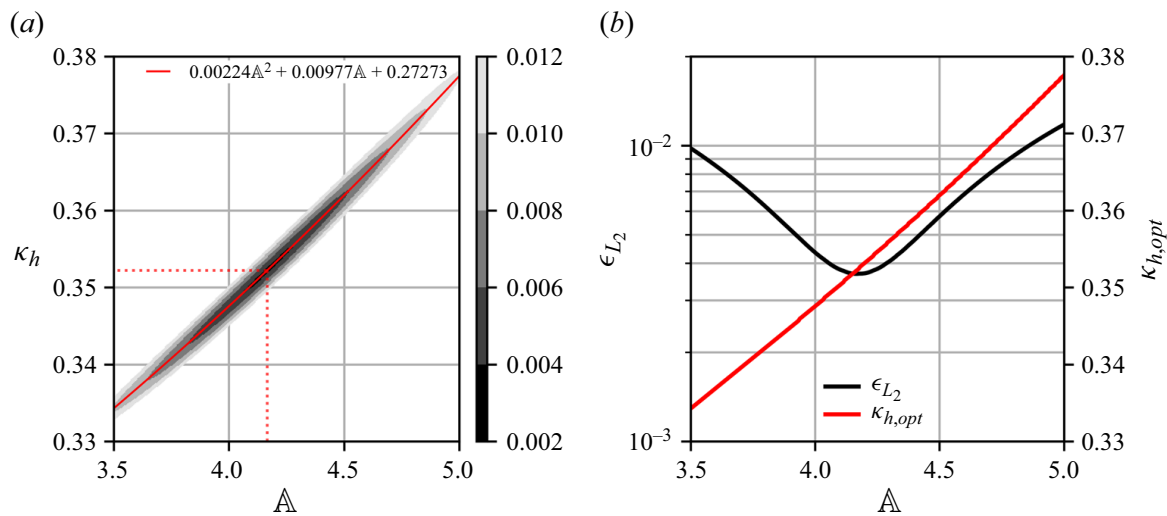


Figure 11. (a) Shading of the error norm  $\epsilon_{L_2}$  (according to (4.7)) for the least squares fit of  $\{\kappa_h, \mathbb{A}\}$  of the passive scalar of the smooth case s. The red line indicates a polynomial fit to the minimum error norm and the best fit is marked with red dotted lines. (b) The error norm  $\epsilon_{L_2}$  as a function of  $\mathbb{A}$  for an optimal value of  $\kappa_{h,opt}$  in black and  $\kappa_{h,opt}$  as function of  $\mathbb{A}$  in red.

The constants  $\kappa_m$  and  $A$  of the logarithmic law for the mean velocity are known to be strongly correlated for the momentum log law (4.5; Ansgore & Mellado 2016; Ansgore 2017), which also holds for the scalar and is quantified in figure 11(a). For the smooth case s, the rather flat curve of the error norm  $\epsilon_{L_2}$  (evaluated similar to (4.7)) for the scalar allows values of the von Kármán constant  $\kappa_h$  in the range of  $0.34 \lesssim \kappa_h \lesssim 0.37$  (figure 11b). For the rough cases, we again pose universality of  $\kappa_h = 0.35$  and minimize the error norm analogous to (4.7), which is shown in figure 10(b), to estimate the scalar displacement



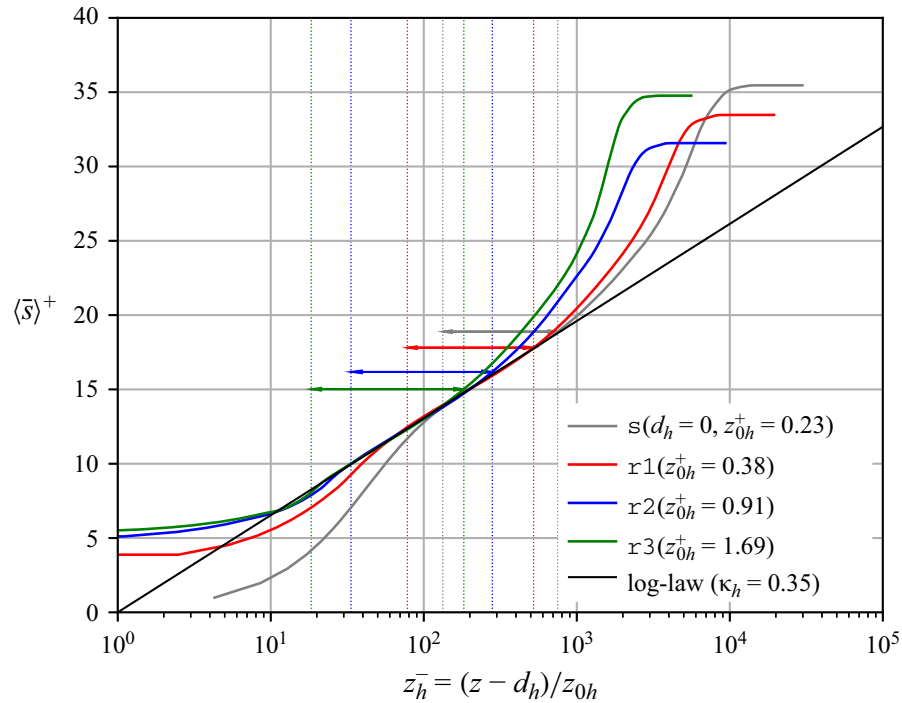


Figure 12. Collapse of the mean scalar profiles onto the logarithmic law of the wall, with the zero-plane displacement height  $d_h/H = 0.41$ . Coloured arrows and vertical dotted lines indicate the fitting interval for the logarithmic law of each case.

height  $(d_h/H)_{opt} = 0.41$  for all rough cases; as expected, this height is substantially lower than that of the momentum, which illustrates the absence of pressure-blocking effects for the scalar exchange in comparison with momentum exchange.

The collapse of profiles to the proposed logarithmic law is shown in figure 12 with  $z_{log,h}^+ < z^+ < 0.12Re_\tau$  for rough cases, where  $z_{log,h}^+ = 30 + d_h^+$ . (Due to the small value of  $H$ , the choice of  $z_{log,h}^+$  fits the data, and should not be interpreted as predictive or general. Great care should be taken with respect to higher-order statistics.) For the smooth case, we find  $z_{0h}^+ = e^{-\kappa_h \Delta} = 0.23$ , more than twice the momentum roughness length  $z_{0m}$ . And for the rough cases, it is  $z_{0h}/H = [0.035, 0.037, 0.040]$  or, in inner units,  $z_{0h}^+ = [0.38, 0.91, 1.69]$ . In contrast to the momentum roughness length  $z_{0m}/H$ , which increases by more than a factor two, the normalized scalar roughness length  $z_{0h}/H$  depends only weakly on the blocking ratio. This difference is due to the absence of pressure-blocking effects in the scalar budgets that hamper vertical momentum exchange in the viscous region.

#### 4.7. Scaling behaviour of aerodynamic parameters

The  $z$ -nought concept with parameters  $z_{0m}$ ,  $z_{0h}$  lumps the roughness effects for the near-surface transport of scalar and momentum (in addition to their displacement heights  $d_m$  and  $d_h$  commonly considered to be related to the covered volume only). These  $z$ -nought parameters are key for the modelling of surface momentum and scalar exchange (Monin 1970; Foken 2006). The mixing of momentum is determined by both pressure drag and viscous drag over rough surfaces, while scalar mixing lacks the pressure-blocking effect and is therefore described by molecular diffusion alone (Cebeci & Bradshaw 1984, p.168), as already discussed when determining  $z_{0h}$  (§ 4.6; cf. also Brutsaert 1982, § 5; Garratt 1992, § 4). In the ABL  $z_{0m} > z_{0h}$ , since mixing of momentum is more efficient than scalar

## Small-scale roughness in Ekman flow

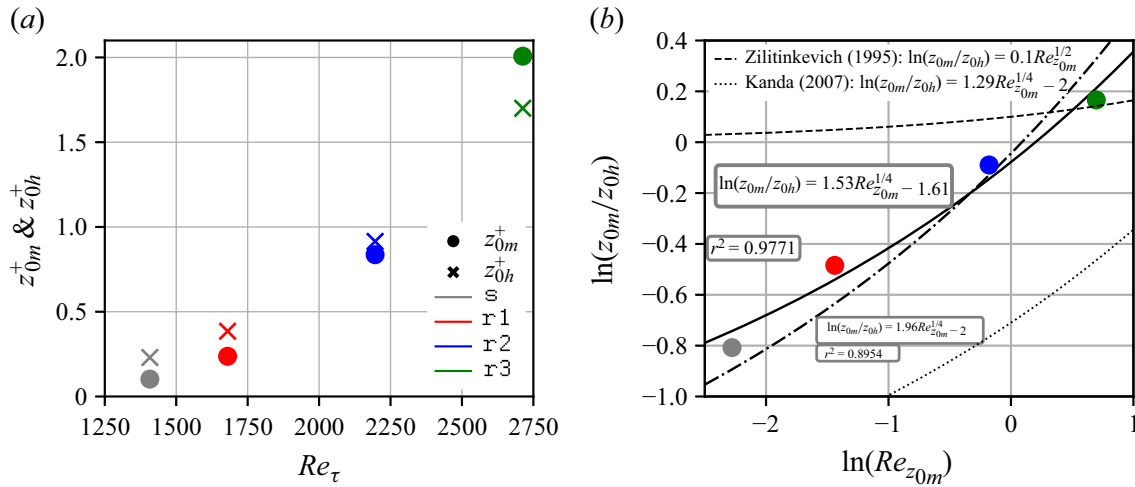


Figure 13. (a) Aerodynamic roughness lengths of momentum  $z_{0m}^+$  and scalar  $z_{0h}^+$  as a function of the friction Reynolds number. (b) Log ratio of the momentum and scalar roughness length plotted as a function of the logarithm of the roughness Reynolds number  $\ln(Re_{z_{0m}})$ , with exponential fitting functions (solid and dotted black lines) and the corresponding values of  $r^2$  (coefficient of determination). The dashed and dotted lines are according to Zilitinkevich (1995) and Kanda *et al.* (2007).

mixing due to pressure gradients in the roughness sublayer (cf. also LES studies with cubical roughness by Li & Bou-Zeid 2019 and Li *et al.* 2020).

Commonly,  $z_{0m}$  is determined as a site-specific parameter from wind profiles, with due regard of roughness geometry and arrangement. Different approaches exist to parametrize  $z_{0h}$  based on  $z_{0m}$ . Conventionally,  $\ln(z_{0m}/z_{0h}) \propto Re_{z_{0m}}^n$  is assumed for constant Schmidt number. A review of classical theories is given by Li *et al.* (2017). Zilitinkevich (1995) proposed an exponent  $n = 1/2$  and Brutsaert (1975a,b) an exponent of  $n = 1/4$ . For the roughest case r3 we observe the proposed behaviour of  $z_{0m} > z_{0h}$  (figure 13a), which supports our assertion that case r3 is in between the transitionally and fully rough regimes, where pressure drag dominates. For the other cases, the scalar roughness length exceeds the aerodynamic one. Following the scalings of Brutsaert (1982) and Kanda *et al.* (2007), we estimate the scaling for the log ratio of roughness lengths as  $\ln(z_{0m}/z_{0h}) = 1.96Re_{z_{0m}}^{1/4} - 2$ , whereas the best fit collapses on  $\ln(z_{0m}/z_{0h}) = 1.53Re_{z_{0m}}^{1/4} - 1.61$ . An extrapolation to the fully rough regime  $z_{0m}^+ > 2$  is, however, delicate due to the lack of data.

We observe a linear relation of  $u_\star$  as a function of the height of roughness elements expressed in external units  $\Lambda_{Ro}$  (figure 14a) in the transitionally rough regime. This scaling appears despite the change in wind direction with which the roughness field is approached for the cases (cf. figure 6b). The scaling behaviour of the friction values of the passive scalar is not as conclusive as for  $u_\star$ , since the scalar is evolving in time (figure 14b) and processes act on different time scales. The imposed initial state of the passive scalar adapts to the imposed boundary conditions on the shortest possible, namely the viscous, time scale (cf. near-sudden increase for the rough cases at  $tf = 0$ , and strong increase for the smooth case at  $tf \approx -2.7$ , figure 14b). Following this initial transition, the scalar gets mixed vertically across the boundary layer by turbulence at the turbulent time scale  $f^{-1}$ . If time is allowed to get sufficiently large, processes at the largest time scale  $\propto Re_\Lambda$  become relevant. Here, the scalar is mixed by laminar diffusion between the top of the boundary layer and the top of the computational domain at a time scale  $\nu/G^2$  (here,  $\sim Re_\Lambda$ ). This separation of time scales is indeed supported by the process of scalar mixing across the ABL (figure 15): after the initial transient, disturbances propagate upwards through the

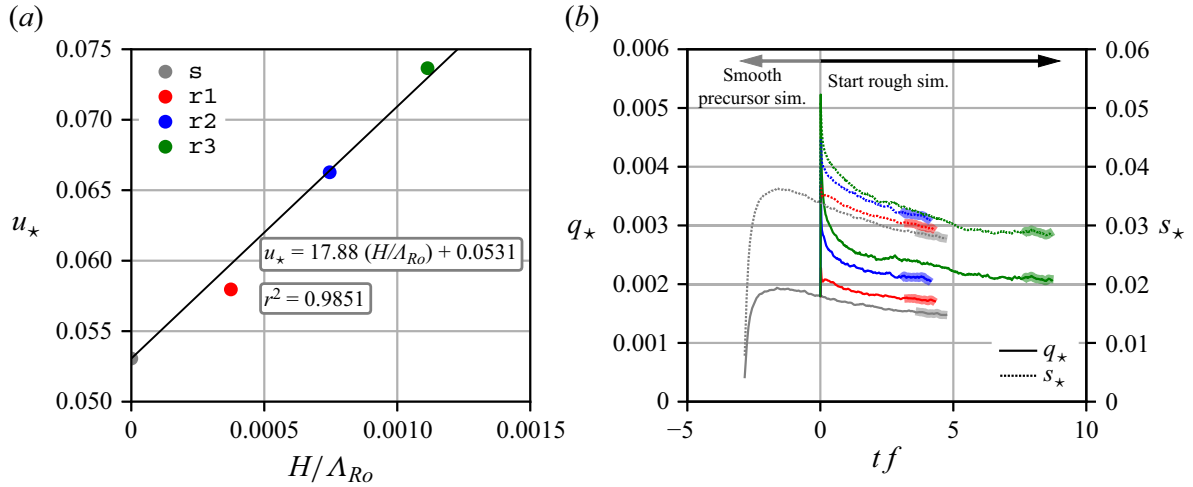


Figure 14. (a) Scaling of the friction velocity  $u_*$  as function of the mean height  $H/\Lambda_{Ro}$  of the roughness elements, normalized with the Rossby radius  $\Lambda_{Ro}$ . The linear function is derived by fitting the slope parameter, whereby the vertical offset parameter is equal to the value of the smooth case  $s$ . With the corresponding  $r^2$  value of the linear fit. (b) Temporal evolution of the friction scalar  $s_*(t)$  and the surface flux  $q_*(t)$ . Time is scaled with eddy-turnover times  $f^{-1}$  (cf. Appendix B for  $u_*(t)$ ).

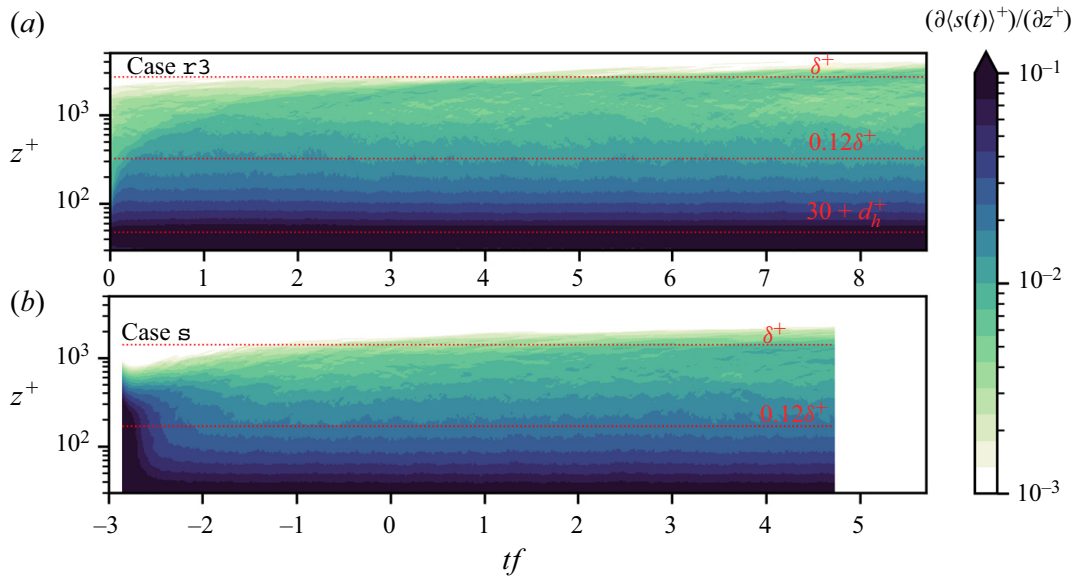


Figure 15. Temporal evolution of the horizontally averaged gradient of the passive scalar for (a) case  $r3$  and (b) case  $s$ , scaled in inner units. The upper boundary of the logarithmic layer is indicated with  $z^+ = 0.12\delta^+$ , the lower boundary with  $z^+ = z_{\log,h}^+$  ( $d_h^+ = 0$  for case  $s$ ) and the boundary-layer thickness with  $\delta^+$ . The lowest part  $0 \leq z^+ < 30$  of the boundary layer is not shown.

logarithmic layer and above. Mixing in the upper part of the boundary layer is visible for case  $r3$  (figure 15a) at time  $tf \gtrsim 6.5$ . This is also seen in figure 14(b) in terms of a decreased rate in  $q_*$  and  $u_*$  for  $tf \gtrsim 6.5$ . The less rough cases have not reached this quasi-steady regime, which points to enhanced turbulent mixing for the roughest case. Nevertheless, mean passive scalar statistics are sufficiently converged in the logarithmic layer so they have reached a quasi-equilibrium, and they are analysed for the period of the final eddy-turnover time of each case.

Based on figure 14(b), we find that the change of  $s_*$  with respect to  $H/\Lambda_{Ro}$  in equilibrium is small in comparison with the change of  $u_*$ . From the data available it is, however,

not clear whether  $s_\star$  becomes a constant or changes weakly with respect to  $H/\Lambda_{Ro}$ . The key difference between the conservation equations for momentum (2.1b) and passive scalar (2.6a) is the pressure gradient term  $-\partial\pi/\partial x_i$ . The friction velocity  $u_\star$  changes by up to 38 % while the change of  $q_\star$  is largely explained by a change of  $u_\star$  such that  $s_\star$  remain approximately constants. This behaviour underlines the strong link between roughness effects on the momentum conservation and the pressure drag.

## 5. Discussion and conclusions

Direct numerical simulations of turbulent Ekman flow with a passive scalar are carried out for a rough surface resembling a typical ABL configuration over homogeneous roughness. The roughness is fully resolved and considered through an ADR IBM, which allows us to maintain a high order of spatial discretization while avoiding SFOs. The fully resolved small-scale roughness (blocking ratio  $H/\delta$  of the order of  $O(1\%)$ ) has the form of  $56^2$  rectangular blocks on the surface; these blocks feature a uniform height and width distribution. In total, four simulations with identical large-scale forcing are performed: one smooth case  $s$  at  $Re_\tau = 1408$  and three rough cases  $r1, r2, r3$  with increasing roughness heights  $H^+ = [10.8, 24.7, 40.8]$ . Regarding our research questions posed in § 1, we find the following:

- (i) For a controlled and fully resolved surface roughness, friction velocity  $u_\star$  and scalar  $s_\star$  can be determined by integration of the scalar and momentum budgets. The increase for  $u_\star$  is up to 38 % and for  $Re_\tau$  up to 91 %. The results of the passive scalar indicate the importance of the pressure drag on the momentum, especially for the fully rough case  $r3$ , in which momentum transfer is dominated by pressure drag and scalar transfer by molecular diffusion (Cebeci & Bradshaw 1984, p. 168). With increasing roughness height the turbulent activity and therefore mixing is enhanced. The influence of roughness on the turning of the wind and hence the Ekman spiral manifests in an enhanced turning angle  $\alpha$ . This is despite an increasing scale separation in viscous units, and it illustrates that, in terms of outer scaling, roughness acts to reduce the Reynolds number; i.e. the scale separation for large eddies is governed by  $Re_\tau/Re_{z_0}$  rather than by  $Re_\tau$ . This means that – from the perspective of large eddies – the ABL has a lower Reynolds number than is usually assumed by a factor  $Re_{z_0}$ .
- (ii) The DNS data collapse onto the rough-wall scaling in the logarithmic layer for the mean horizontal velocity and passive scalar. The estimated von Kármán constants and offset parameters are  $\kappa_m = 0.42, A = 5.44$  and  $\kappa_h = 0.35, \mathbb{A} = 4.2$ . A strong correlation between the von Kármán constant  $\kappa$  and the offset parameter  $A$  is quantified. In the presence of roughness, the extent of the logarithmic layer in inner units grows with increasing roughness height and therefore scale separation. We, however, find that the commonly assumed representation of the total drag by the maximum of the turbulent drag in the lower part of the surface layer may constitute a substantial bias in rough boundary layers as a substantial fraction of up to 20 % of the drag is neglected when considering the turbulent drag only. The substantial variation of drag in the inner layer (below  $z^- \approx 0.15$ ) comes with rotational effects (due to the triadic balance between the Coriolis force, pressure gradient and viscous drag) in the roughness sublayer that manifest in a wind veer across the lowest part of the ABL, even below the logarithmic layer.
- (iii) Based on our data, we estimate the zero-plane displacement height for momentum to  $d_m/H \approx 0.6$  and for the scalar to  $d_h/H \approx 0.4$  and roughness Reynolds numbers

of  $z_{0m}^+ = [0.1, 0.24, 0.84, 2.01]$  and  $z_{0h}^+ = [0.23, 0.38, 0.91, 1.69]$ . This leaves the cases  $r1$ ,  $r2$  in the transitionally rough regime and the roughest case  $r3$  at the edge of the fully rough regime.

- (iv) The log ratios of the roughness lengths  $\ln(z_{0m}/z_{0h})$  exhibit a clear scaling  $\propto Re^{1/4}$ , which fits the known exponent of Brutsaert (1975a,b). For the smooth and transitionally rough regime scalar mixing is enhanced  $z_{0m} < z_{0h}$ , whereas in the fully rough regime  $z_{0m} > z_{0h}$  is recovered, due to the importance of the pressure.

With the framework prescribed in this study, we are now able to study the impact of roughness on the ABL at meaningful scale separations. The extension of these results to the fully rough regime for the scaling of aerodynamic parameters outside the transitionally rough regime as well as the effects of heterogeneous surface conditions on the stably stratified flow are interesting aspects for future work.

**Acknowledgements.** We are grateful for the comments of the anonymous reviewers who helped shape this article. Simulations were performed on the resources of the High-Performance Computing Center Stuttgart (HLRS) on the Hawk cluster, founded by the Baden–Württemberg Ministry for Science, Research, and the Arts and the German Federal Ministry of Education and Research through the Gauss Centre for Supercomputing. The computing time and storage facilities were provided by the project trainABL with the project number 44187.

**Funding.** The authors acknowledge financial support through the ERC grant trainABL with the project number 851374; DOI: <https://doi.org/10.3030/851374>.

**Declaration of interests.** The authors report no conflict of interest.

**Data availability statement.** The data supporting the findings of this study are published in Kostelecky & Ansonge (2024).

**Author ORCIDs.**

Jonathan Kostelecky <https://orcid.org/0000-0002-9983-9310>;

Cedrick Ansonge <https://orcid.org/0000-0001-9913-3759>.

**Author contributions.** J.K. performed the code implementation, carried out the numerical simulations, performed the post-processing of the data, worked on visualization and interpretation of results and wrote the original draft. Both authors contributed to the conceptualization of the study. C.A. supervised the research, contributed with discussion and interpretation of results, reviewed and edited the original draft and was responsible for acquisition of funding.

## Appendix A. Intrinsic averaging in an inhomogeneous domain

Let us consider a square object immersed in a fluid domain (cf. figure 2a, red shaded area), which covers a normalized solid area of  $A^1 = 4$  and fluid area of  $A^0 = 21$  and  $N^1 = 9$ ,  $N^0 = 16$  grid points (superscripts  $(\cdot)^{0,1}$  are used according to (2.8)). The mean of any flow variable  $\varphi_i$  in the solid and fluid region is defined as follows:

$$\langle \varphi_i \rangle^0 = \frac{1}{N^0} \sum_{i \in A^0} \varphi_i, \quad \text{and} \quad \langle \varphi_i \rangle^1 = \frac{1}{N^1} \sum_{i \in A^1} \varphi_i. \quad (\text{A1a,b})$$

Evidently, this approach neglects contributions to the fluid, because of the mismatch in  $A^0/(A^0 + A^1) \neq N^0/(N^0 + N^1)$  (red, blue shaded area), therefore a volume-based approach (for the three-dimensional case) is needed to take precisely the covered space into account. Depending on the location of a certain grid point, the distinction between solid and fluid is augmented by grid points on corners, edges and plane interfaces (cf. figure 2b)



with

$$\epsilon^S(x_j) = \begin{cases} 1, & \text{if } x_i \in \text{fluid,} \\ \frac{1}{2}, & \text{if } x_i \in \text{plane interface,} \\ \frac{1}{4}, & \text{if } x_i \in \text{edge,} \\ \frac{1}{8}, & \text{if } x_i \in \text{corner,} \\ 0, & \text{if } x_i \in \text{solid,} \end{cases} \quad \text{and } \epsilon^F(x_i) = [1 - \epsilon^S(x_i)]. \quad (\text{A2a,b})$$

Expanding the approach to the three-dimensional case leads to height-dependent volume fractions

$$\gamma^0(z) = \langle 1 - \epsilon(x_i) \rangle, \quad \gamma^F(z) = \langle 1 - \epsilon^S(x_i) \rangle, \quad (\text{A3a,b})$$

$$\gamma^1(z) = 1 - \gamma^0(z), \quad \gamma^S(z) = 1 - \gamma^F(z), \quad (\text{A3c,d})$$

$$\gamma^{rel}(z) = \frac{\gamma^0(z)}{\gamma^1(z)}, \quad (\text{A3e})$$

which are easily validated by  $\gamma^F(z) - \gamma^0(z) = \gamma^1(z) - \gamma^S(z)$ . We are interested in the mean conditional statistical moments in the fluid region, since any statistics inside the solid regions are irrelevant. The statistical output of the DNS code provides only the unconditional mean  $\langle \varphi_i \rangle^{code}$  and (co-)variances  $\langle \varphi'_i \varphi'_j \rangle^{code}$  of the flow variables. Following the conditional averaging approach in Pope (2000, p. 169f), the mean can be easily conditioned to the fluid region with

$$\langle \varphi \rangle_i^F = \frac{1}{\gamma^F} (\langle \varphi_i \rangle^{code} - \gamma^S \langle \varphi_i \rangle^S), \quad (\text{A4a})$$

with

$$\langle \varphi_i \rangle^S = \begin{cases} \text{const.}, & \text{if } \varphi_i \text{ is passive scalar,} \\ 0, & \text{if } \varphi_i \text{ is velocity.} \end{cases} \quad (\text{A4b})$$

Advancing this approach for the (co-)variances gives

$$\langle \varphi'_i \varphi'_j \rangle^F = \gamma^{rel} [\langle \varphi'_i \varphi'_j \rangle^0 + (1 - \gamma^{rel})(\langle \varphi_i \rangle^0 - \langle \varphi_i \rangle^S)(\langle \varphi_j \rangle^0 - \langle \varphi_j \rangle^S)], \quad (\text{A5})$$

with

$$\langle \varphi'_i \varphi'_j \rangle^0 = \frac{\langle \varphi'_i \varphi'_j \rangle^{code}}{\gamma^0} - \gamma^1 (\langle \varphi_i \rangle^1 - \langle \varphi_i \rangle^0)(\langle \varphi_j \rangle^1 - \langle \varphi_j \rangle^0), \quad (\text{A6})$$

$$\langle \varphi_i \rangle^0 = \frac{1}{\gamma^0} (\langle \varphi_i \rangle^{code} - \gamma^1 \langle \varphi_i \rangle^1), \quad (\text{A7})$$

$$\langle \varphi_i \rangle^1 = \begin{cases} \text{const.}, & \text{if } \varphi_i \text{ is passive scalar,} \\ 0, & \text{if } \varphi_i \text{ is velocity.} \end{cases} \quad (\text{A8})$$

The values of  $\langle \varphi_i \rangle^S$  and  $\langle \varphi_i \rangle^1$  have to be known in advance and the (co-)variances  $\langle \varphi'_i \varphi'_j \rangle^S \equiv 0$  and  $\langle \varphi'_i \varphi'_j \rangle^1 \equiv 0$  are always zero.

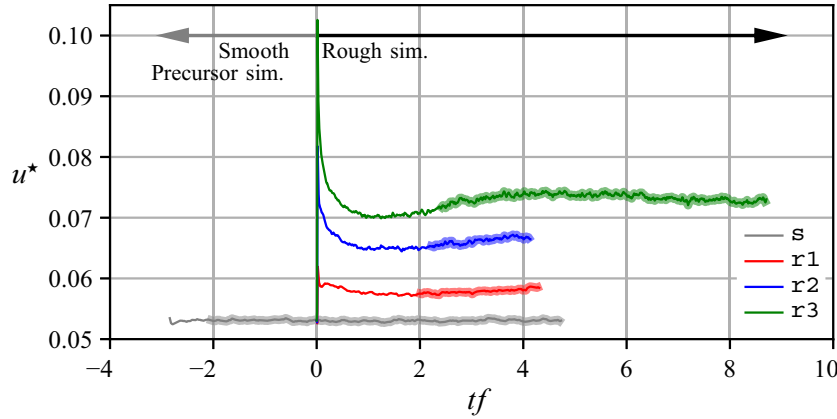


Figure 16. Temporal evolution of the friction velocity  $u_*$  for the smooth (grey) and the three rough cases (red, blue, green), with  $tf = 0$  for the start of the rough cases. Thick transparent lines denote the intervals for time integration of the flow variables. Time is scaled in eddy-turnover times  $f^{-1}$ . The averaging time of cases  $s$  and  $r3$  is a full inertial cycle.

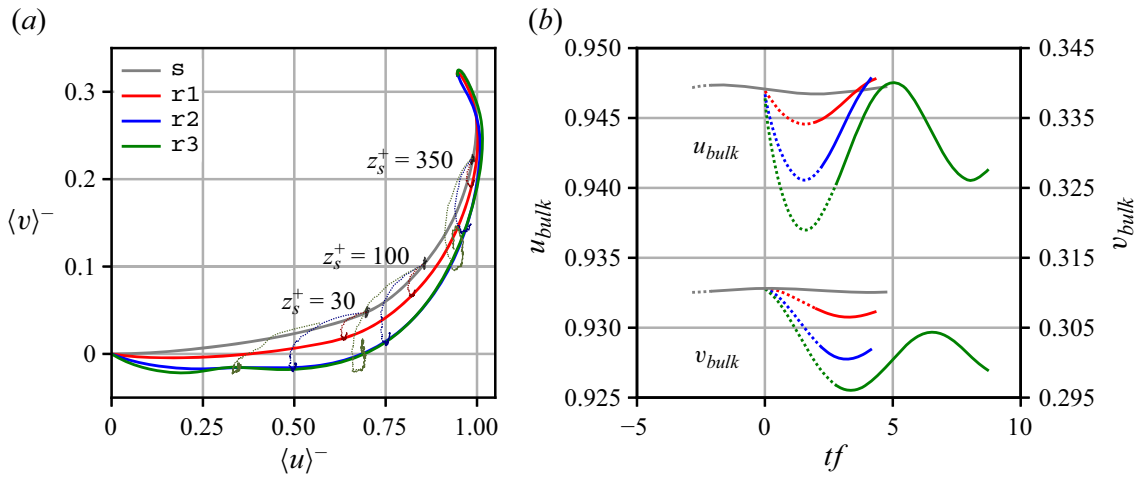


Figure 17. Inertial oscillations of the conducted cases. (a) Mean hodographs are shown with thick solid lines, and the thin lines show the temporal evolution of  $\langle u \rangle^-$ ,  $\langle v \rangle^-$  at specific heights (scaled in inner smooth units). (b) Temporal streamwise (top half) and spanwise (bottom half) bulk velocities  $u_{i,bulk}(t) = L_z^{-1} \int_0^{L_z} \langle u_i(t, z) \rangle dz$ , with time in eddy-turnover times  $f^{-1}$ . Dotted lines in (a) and (b) depict the initial transient of the cases, which is excluded from time averaging.

### Appendix B. Time integration for statistical analysis and inertial oscillations

For initialization of the smooth case  $s$  we take the fully turbulent velocity fields of a previous simulation, which was in a statistically converged state of similar Reynolds number. Those original fields are interpolated to the current computational grid (table 1). The passive scalar of the smooth case is introduced with an initial exponentially decaying profile. The rough cases are initialized to the time instance  $t = 0$  with fully turbulent, three-dimensional fields (velocities and passive scalar) from the smooth case  $s$ , and were already in a statistically converged state.

A measurement for determining statistical convergence of the cases is the temporal evolution of the friction velocity  $u_*(t)$  (figure 16), following the method described in § 4.1. After an initial transient (adaptation phase of new boundary conditions),  $u_*(t)$  reaches a quasi-steady state, which is determined by visual inspection, and from which flow statistics are collected for temporal integration.



Another helpful tool for diagnosing statistical convergence and gradual adaptation of the simulations to the new boundary conditions is the visualizations of inertial oscillations with the period of  $2\pi/f$ , which are visible in the hodographs and horizontal bulk velocities (figure 17). The smooth case  $s$  is statistically converged and therefore the amplitude of the inertial oscillation is negligible. This is also valid in the near-wall region (figure 17a). Adjusting the boundary conditions by introducing surface roughness increases inertial oscillations, which then slowly decay over time. Cases  $s$  and  $r3$  are averaged over approximately one full inertial period, whereas  $r1$ ,  $r2$  are averaged over 0.4, 0.3 inertial periods.

#### REFERENCES

- AHN, J., LEE, J.H. & SUNG, H.J. 2013 Statistics of the turbulent boundary layers over 3D cube-roughened walls. *Intl J. Heat Fluid Flow* **44**, 394–402.
- ANDREAS, E.L. 1987 A theory for the scalar roughness and the scalar transfer coefficients over snow and sea ice. *Boundary-Layer Meteorol.* **38** (1), 159–184.
- ANDREAS, E.L., CLAFFEY, K.J., JORDAN, R.E., FAIRALL, C.W., GUEST, P.S., PERSSON, P.O.G. & GRACHEV, A.A. 2006 Evaluations of the von Kármán constant in the atmospheric surface layer. *J. Fluid Mech.* **559**, 117–149.
- ANSORGE, C. 2017 Analyses of turbulence in the neutrally and stably stratified planetary boundary layer. Springer theses, Springer International.
- ANSORGE, C. 2019 Scale dependence of atmosphere–surface coupling through similarity theory. *Boundary-Layer Meteorol.* **170** (1), 1–27.
- ANSORGE, C. & MELLADO, J.P. 2014 Global intermittency and collapsing turbulence in the stratified planetary boundary layer. *Boundary-Layer Meteorol.* **153** (1), 89–116.
- ANSORGE, C. & MELLADO, J.P. 2016 Analyses of external and global intermittency in the logarithmic layer of Ekman flow. *J. Fluid Mech.* **805** (1), 611–635.
- BARENBLATT, G.I. 1993 Scaling laws for fully developed turbulent shear flows. Part 1. Basic hypotheses and analysis. *J. Fluid Mech.* **248**, 513–520.
- BRUTSAERT, W. 1975a The roughness length for water vapor sensible heat, and other scalars. *J. Atmos. Sci.* **32** (10), 2028–2031.
- BRUTSAERT, W. 1975b A theory for local evaporation (or heat transfer) from rough and smooth surfaces at ground level. *Water Resour. Res.* **11** (4), 543–550.
- BRUTSAERT, W. 1982 *Evaporation into the Atmosphere*. Springer Netherlands.
- CASTRO, I.P. 2007 Rough-wall boundary layers: mean flow universality. *J. Fluid Mech.* **585**, 469–485.
- CASTRO, I.P. & LEONARDI, S. 2010 Very-rough-wall channel flows: a DNS study. In *IUTAM Symposium on The Physics of Wall-Bounded Turbulent Flows on Rough Walls* (ed. T. B. Nickels), IUTAM Bookseries, pp. 175–181. Springer Netherlands.
- CEBECI, T. & BRADSHAW, P. 1984 *Physical and Computational Aspects of Convective Heat Transfer. H: Hauptband*. Springer.
- CHANDRAMOULI, P., HEITZ, D., LAIZET, S. & MÉMIN, E. 2018 Coarse large-eddy simulations in a transitional wake flow with flow models under location uncertainty. *Comput. Fluids* **168**, 170–189.
- CHENG, H., HAYDEN, P., ROBINS, A.G. & CASTRO, I.P. 2007 Flow over cube arrays of different packing densities. *J. Wind Engng Ind. Aerodyn.* **95** (8), 715–740.
- CHENG, W.-C. & PORTÉ-AGEL, F. 2015 Adjustment of turbulent boundary-layer flow to idealized urban surfaces: a large-eddy simulation study. *Boundary-Layer Meteorol.* **155** (2), 249–270.
- CHORIN, A.J. 1968 Numerical solution of the Navier–Stokes equations. *Math. Comput.* **22** (104), 745–762.
- CHUNG, D., HUTCHINS, N., SCHULTZ, M.P. & FLACK, K.A. 2021 Predicting the drag of rough surfaces. *Annu. Rev. Fluid Mech.* **53** (1), 439–471.
- CLAUSER, F.H. 1954 Turbulent boundary layers in adverse pressure gradients. *J. Aeronaut. Sci.* **21** (2), 91–108.
- COCEAL, O., THOMAS, T.G., CASTRO, I.P. & BELCHER, S.E. 2006 Mean flow and turbulence statistics over groups of urban-like cubical obstacles. *Boundary-Layer Meteorol.* **121** (3), 491–519.
- COLEMAN, G.N. 1999 Similarity statistics from a direct numerical simulation of the neutrally stratified planetary boundary layer. *J. Atmos. Sci.* **56** (6), 891–900.
- COLEMAN, G.N., FERZIGER, J.H. & SPALART, P.R. 1990 A numerical study of the turbulent Ekman layer. *J. Fluid Mech.* **213**, 313–348.

- DAVIDSON, P.A. & KROGSTAD, P.-Å. 2014 A universal scaling for low-order structure functions in the log-law region of smooth- and rough-wall boundary layers. *J. Fluid Mech.* **752**, 140–156.
- DEUSEBIO, E., BRETTHOUWER, G., SCHLATTER, P. & LINDBORG, E. 2014 A numerical study of the unstratified and stratified Ekman layer. *J. Fluid Mech.* **755**, 672–704.
- DIMOTAKIS, P.E. 2005 Turbulent mixing. *Annu. Rev. Fluid Mech.* **37** (1), 329–356.
- EKMANN, V.W. 1905 On the influence of the earth's rotation on ocean-currents. *Ark. Mat. Astron. Fys.* **2**, 1–53.
- FADLUN, E.A., VERZICCO, R., ORLANDI, P. & MOHD-YUSOF, J. 2000 Combined immersed-boundary finite-difference methods for three-dimensional complex flow simulations. *J. Comput. Phys.* **161** (1), 35–60.
- FANG, J., DIEBOLD, M., HIGGINS, C. & PARLANGE, M.B. 2011 Towards oscillation-free implementation of the immersed boundary method with spectral-like methods. *J. Comput. Phys.* **230** (22), 8179–8191.
- FINNIGAN, J. 2000 Turbulence in plant canopies. *Annu. Rev. Fluid Mech.* **32** (1), 519–571.
- FOKEN, T. 2006 50 years of the Monin–Obukhov similarity theory. *Boundary-Layer Meteorol.* **119** (3), 431–447.
- FORNBERG, B. 1996 *A Practical Guide to Pseudospectral Methods*. Cambridge Monographs on Applied and Computational Mathematics. Cambridge University Press.
- FRENZEN, P. & VOGEL, C.A. 1995a A further note 'on the magnitude and apparent range of variation of the von Kármán constant'. *Boundary-Layer Meteorol.* **75** (3), 315–317.
- FRENZEN, P. & VOGEL, C.A. 1995b On the magnitude and apparent range of variation of the von Kármán constant in the atmospheric surface layer. *Boundary-Layer Meteorol.* **72** (4), 371–392.
- GARRATT, J.R. 1992 *The Atmospheric Boundary Layer*. Cambridge Atmospheric and Space Science Series. Cambridge University Press.
- GAUTIER, R., BIAU, D. & LAMBALLAIS, E. 2013 A reference solution of the flow over a circular cylinder at  $Re = 40$ . *Comput. Fluids* **75**, 103–111.
- GAUTIER, R., LAIZET, S. & LAMBALLAIS, E. 2014 A DNS study of jet control with microjets using an immersed boundary method. *Int. J. Comput. Fluid Dyn.* **28** (6–10), 393–410.
- GIANNENAS, A.E. & LAIZET, S. 2021 A simple and scalable immersed boundary method for high-fidelity simulations of fixed and moving objects on a Cartesian mesh. *Appl. Math. Model.* **99**, 606–627.
- GOLDSTEIN, D., HANDLER, R. & SIROVICH, L. 1993 Modeling a no-slip flow boundary with an external force field. *J. Comput. Phys.* **105** (2), 354–366.
- GRIMMOND, C.S.B. & OKE, T.R. 1999 Aerodynamic properties of urban areas derived from analysis of surface form. *J. Appl. Meteorol. Climatol.* **38** (9), 1262–1292.
- HAMA, F.R. 1954 Boundary layer characteristics for smooth and rough surfaces. *Trans. Soc. Nav. Archit. Mar. Engrs* **62**, 333–358.
- HUSSAIN, M. & LEE, B.E. 1980 A wind tunnel study of the mean pressure forces acting on large groups of low-rise buildings. *J. Wind Engng Ind. Aerodyn.* **6** (3–4), 207–225.
- JAYARAMAN, B. & KHAN, S. 2020 Direct numerical simulation of turbulence over two-dimensional waves. *AIP Adv.* **10** (2), 025034.
- JIANG, Q., WANG, S. & SULLIVAN, P. 2018 Large-eddy simulation study of log laws in a neutral Ekman boundary layer. *J. Atmos. Sci.* **75** (6), 1873–1889.
- JIMÉNEZ, J. 2004 Turbulent flows over rough walls. *Annu. Rev. Fluid Mech.* **36** (1), 173–196.
- JOHANSSON, A.V. & WIKSTRÖM, P.M. 2000 DNS and modelling of passive scalar transport in turbulent channel flow with a focus on scalar dissipation rate modelling. *Flow Turbul. Combust.* **63** (1), 223–245.
- KADER, B.A. 1981 Temperature and concentration profiles in fully turbulent boundary layers. *Int. J. Heat Mass Transfer* **24** (9), 1541–1544.
- KADIVAR, M., TORMEY, D. & MCGRANAGHAN, G. 2021 A review on turbulent flow over rough surfaces: fundamentals and theories. *Int. J. Thermofluids* **10**, 100077.
- KANDA, M., INAGAKI, A., MIYAMOTO, T., GRYSCHKA, M. & RAASCH, S. 2013 A new aerodynamic parametrization for real urban surfaces. *Boundary-Layer Meteorol.* **148** (2), 357–377.
- KANDA, M., KANEGA, M., KAWAI, T., MORIWAKI, R. & SUGAWARA, H. 2007 Roughness lengths for momentum and heat derived from outdoor urban scale models. *J. Appl. Meteorol. Climatol.* **46** (7), 1067–1079.
- KANDA, M., MORIWAKI, R. & KASAMATSU, F. 2004 Large-eddy simulation of turbulent organized structures within and above explicitly resolved cube arrays. *Boundary-Layer Meteorol.* **112** (2), 343–368.
- KASAGI, N., TOMITA, Y. & KURODA, A. 1992 Direct numerical simulation of passive scalar field in a turbulent channel flow. *J. Heat Transfer* **114** (3), 598–606.
- KAWAMURA, H., ABE, H. & MATSUO, Y. 1999 DNS of turbulent heat transfer in channel flow with respect to Reynolds and Prandtl number effects. *Int. J. Heat Fluid Flow* **20** (3), 196–207.

## Small-scale roughness in Ekman flow

- KAWAMURA, H., ABE, H. & SHINGAI, K. 2000 DNS of turbulence and heat transport in a channel flow with different Reynolds and Prandtl numbers and boundary conditions. *Proceedings of the 3rd International Symposium on Turbulence, Heat and Mass Transfer* (ed. Y. Nagano), pp. 15–32. Engineering Foundation.
- KHAN, S. & JAYARAMAN, B. 2019 Statistical structure and deviations from equilibrium in wavy channel turbulence. *Fluids* **4** (3), 161.
- KIM, J., KIM, D. & CHOI, H. 2001 An immersed-boundary finite-volume method for simulations of flow in complex geometries. *J. Comput. Phys.* **171** (1), 132–150.
- KOLMOGOROV, A.N. 1941 Dissipation of energy in locally isotropic turbulence. *Dokl Akad. Nauk SSSR* **434** (1890), 15–17.
- KOSTECKY, J. & ANSORGE, C. 2024 Direct numerical simulation of turbulent Ekman flow with cubic small-scale surface roughness ( $Re = 1000$ ). <http://dx.doi.org/10.17169/refubium-43215>.
- LAIZET, S. & LAMBALLAIS, E. 2009 High-order compact schemes for incompressible flows: a simple and efficient method with quasi-spectral accuracy. *J. Comput. Phys.* **228** (16), 5989–6015.
- LAMBALLAIS, É. & SILVESTRINI, J. 2002 Direct numerical simulation of interactions between a mixing layer and a wake around a cylinder. *J. Turbul.* **3**, 28.
- LEE, J., KIM, J., CHOI, H. & YANG, K.-S. 2011a Sources of spurious force oscillations from an immersed boundary method for moving-body problems. *J. Comput. Phys.* **230** (7), 2677–2695.
- LEE, J.H., SUNG, H.J. & KROGSTAD, P.-Å. 2011b Direct numerical simulation of the turbulent boundary layer over a cube-roughened wall. *J. Fluid Mech.* **669**, 397–431.
- LEE, S., GOHARI, S.M.I. & SARKAR, S. 2020 Direct numerical simulation of stratified Ekman layers over a periodic rough surface. *J. Fluid Mech.* **902**, A25.
- LELE, S.K. 1992 Compact finite difference schemes with spectral-like resolution. *J. Comput. Phys.* **103** (1), 16–42.
- LEONARDI, S. & CASTRO, I.P. 2010 Channel flow over large cube roughness: a direct numerical simulation study. *J. Fluid Mech.* **651**, 519–539.
- LI, D., RIGDEN, A., SALVUCCI, G. & LIU, H. 2017 Reconciling the Reynolds number dependence of scalar roughness length and laminar resistance. *Geophys. Res. Lett.* **44** (7), 3193–3200.
- LI, Q. & BOU-ZEID, E. 2019 Contrasts between momentum and scalar transport over very rough surfaces. *J. Fluid Mech.* **880**, 32–58.
- LI, Q., BOU-ZEID, E. & ANDERSON, W. 2016 The impact and treatment of the Gibbs phenomenon in immersed boundary method simulations of momentum and scalar transport. *J. Comput. Phys.* **310**, 237–251.
- LI, Q., BOU-ZEID, E., GRIMMOND, S., ZILITINKEVICH, S. & KATUL, G. 2020 Revisiting the relation between momentum and scalar roughness lengths of urban surfaces. *Q. J. R. Meteorol. Soc.* **146** (732), 3144–3164.
- MARUSIC, I., MONTY, J.P., HULTMARK, M. & SMITS, A.J. 2013 On the logarithmic region in wall turbulence. *J. Fluid Mech.* **716**, R3.
- MELLADO, J.P. & ANSORGE, C. 2012 Factorization of the Fourier transform of the pressure-Poisson equation using finite differences in collocated grids. *Z. Angew. Math. Mech.* **92** (5), 380–392.
- MIYASHITA, K., IWAMOTO, K. & KAWAMURA, H. 2006 Direct numerical simulation of the neutrally stratified turbulent Ekman boundary layer. *J. Earth Simul.* **6**, 3–15.
- MOHD-YUSOF, J. 1997 Combined immersed boundaries/B-splines methods for simulations of flows in complex geometries. *Center for Turbulence Research*, pp. 317–327.
- MONIN, A.S. 1970 The atmospheric boundary layer. *Annu. Rev. Fluid Mech.* **2**, 225–250.
- NAGIB, H.M. & CHAUHAN, K.A. 2008 Variations of von Kármán coefficient in canonical flows. *Phys. Fluids* **20** (10), 101518.
- NIKURADSE, J. 1933 Laws of flow in rough pipes. *NACA Tech. Memorandum* 1295, 1–62.
- OBUKHOV, A.M. 1941 O Raspredelenie energii w spektre turbulentnowo potoka. *Isv. Akad. Nauk SSSR* **1941** (4–5), 453–466.
- PARNAUDEAU, P., CARLIER, J., HEITZ, D. & LAMBALLAIS, E. 2008 Experimental and numerical studies of the flow over a circular cylinder at Reynolds number 3900. *Phys. Fluids* **20** (8), 085101.
- PARNAUDEAU, P., LAMBALLAIS, E., HEITZ, D. & SILVESTRINI, J.H. 2004 Combination of the immersed boundary method with compact schemes for DNS of flows in complex geometry. In *Direct and Large-Eddy Simulation V* (ed. R. Friedrich, B.J. Geurts & O. Métais), ERCOFTAC Series, pp. 581–590. Springer Netherlands.
- PERRET, L., BASLEY, J., MATHIS, R. & PIQUET, T. 2019 The atmospheric boundary layer over urban-like terrain: influence of the plan density on roughness sublayer dynamics. *Boundary-Layer Meteorol.* **170** (2), 205–234.

- PIROZZOLI, S., BERNARDINI, M. & ORLANDI, P. 2016 Passive scalars in turbulent channel flow at high Reynolds number. *J. Fluid Mech.* **788**, 614–639.
- PIROZZOLI, S., ROMERO, J., FATICA, M., VERZICCO, R. & ORLANDI, P. 2022 DNS of passive scalars in turbulent pipe flow. *J. Fluid Mech.* **940**, A45.
- PLACIDI, M. & GANAPATHISUBRAMANI, B. 2015 Effects of frontal and plan solidities on aerodynamic parameters and the roughness sublayer in turbulent boundary layers. *J. Fluid Mech.* **782**, 541–566.
- POPE, S.B. 2000 *Turbulent Flows*. Cambridge University Press.
- PRANDTL, L. 1961 Zur turbulenten Strömung in Röhren und längs Platten. In *Ludwig Prandtl Gesammelte Abhandlungen* (ed. W. Tollmien, H. Schlichting, H. Görtler & F.W. Riegels). Springer Berlin Heidelberg.
- RAUPACH, M.R., ANTONIA, R.A. & RAJAGOPALAN, S. 1991 Rough-wall turbulent boundary layers. *Appl. Mech. Rev.* **44** (1), 1–25.
- RESSEGUIER, V., MÉMIN, E., HEITZ, D. & CHAPRON, B. 2017 Stochastic modelling and diffusion modes for proper orthogonal decomposition models and small-scale flow analysis. *J. Fluid Mech.* **826**, 888–917.
- ROSSBY, C.-G. & MONTGOMERY, R.B. 1935 The layer of frictional influence in wind and ocean currents. *Pap. Phys. Oceanogr. Meteorol.* **III** (3), 1–101.
- RUNGE, C. 1901 Über empirische Funktionen und die Interpolation zwischen äquidistanten Ordinaten. *Z. Math. Phys.* **46**, 224–243.
- SCHÄFER, K., FOROOGHI, P., STRAUB, S., FROHNAPFEL, B. & STROH, A. 2020 Direct numerical simulations of a turbulent flow over wall-mounted obstacles – a comparison of different numerical approaches. In *Direct and Large Eddy Simulation XII* (ed. M. García-Villalba, H. Kuerten & M.V. Salvetti), vol. 27, pp. 91–96. Springer International.
- SCHÄFER, K., FROHNAPFEL, B. & MELLADO, J.P. 2022a The effect of spanwise heterogeneous surfaces on mixed convection in turbulent channels. *J. Fluid Mech.* **950**, A22.
- SCHÄFER, K., STROH, A., FOROOGHI, P. & FROHNAPFEL, B. 2022b Modelling spanwise heterogeneous roughness through a parametric forcing approach. *J. Fluid Mech.* **930**, A7.
- SCHÄFER, K., STROH, A., FROHNAPFEL, B. & GATTI, D. 2019 Investigation of turbulent budgets in channels with secondary motions induced by streamwise-aligned ridges. In *11th International Symposium on Turbulence and Shear Flow Phenomena (TSFP11)*, Southampton, UK, July 30–August 2, 2019.
- SCHLICHTING, H. 1936 Experimentelle Untersuchungen zum Rauigkeitsproblem. *Ingenieur-Archiv* **7** (1), 1–34.
- SHAH, S.K. & BOU-ZEID, E. 2014 Direct numerical simulations of turbulent Ekman layers with increasing static stability: modifications to the bulk structure and second-order statistics. *J. Fluid Mech.* **760**, 494–539.
- SHAO, Y. & YANG, Y. 2008 A theory for drag partition over rough surfaces. *J. Geophys. Res.* **113** (F2), F02S05.
- SHINGAI, K. & KAWAMURA, H. 2004 A study of turbulence structure and large-scale motion in the Ekman layer through direct numerical simulations. *J. Turbul.* **5** (1), 013.
- SPALART, P.R. 1989 Theoretical and numerical study of a three-dimensional turbulent boundary layer. *J. Fluid Mech.* **205**, 319.
- SPALART, P.R., COLEMAN, G.N. & JOHNSTONE, R. 2008 Direct numerical simulation of the Ekman layer: a step in Reynolds number, and cautious support for a log law with a shifted origin. *Phys. Fluids* **20** (10), 101507.
- SPALART, P.R., COLEMAN, G.N. & JOHNSTONE, R. 2009 Retraction: ‘Direct numerical simulation of the Ekman layer: a step in Reynolds number, and cautious support for a log law with a shifted origin’ [*Phys. Fluids* 20, 101507 (2008)]. *Phys. Fluids* **21** (10), 109901.
- SQUIRE, D.T., MORRILL-WINTER, C., HUTCHINS, N., SCHULTZ, M.P., KLEWICKI, J.C. & MARUSIC, I. 2016 Comparison of turbulent boundary layers over smooth and rough surfaces up to high Reynolds numbers. *J. Fluid Mech.* **795**, 210–240.
- STOESSER, T., MATHEY, F., FRÖHLICH, J. & RODI, W. 2003 LES of flow over multiple cubes. *ERCOFTAC Bulletin* no. 56, 15–19.
- STULL, R.B. 1988 *An Introduction to Boundary Layer Meteorology*. Atmospheric Sciences Library. Kluwer Academic Publishers.
- SUBRAMANIAN, C.S. & ANTONIA, R.A. 1981 Effect of Reynolds number on a slightly heated turbulent boundary layer. *Intl J. Heat Mass Transfer* **24** (11), 1833–1846.
- TÉMAM, R. 1969 Sur l’approximation de la solution des équations de Navier–Stokes par la méthode des pas fractionnaires (II). *Arch. Ration Mech. Anal.* **33** (5), 377–385.
- TENNEKES, H. & LUMLEY, J.L. 1972 *A First Course in Turbulence*. MIT Press.
- THEOBALD, F., SCHÄFER, K., YANG, J., FROHNAPFEL, B., STRIPF, M., FOROOGHI, P. & STROH, A. 2021 Comparison of different solvers and geometry representation strategies for DNS of rough wall channel flow. In *14th WCCM-ECCOMAS Congress*. CIMNE.



### *Small-scale roughness in Ekman flow*

- TOWNSEND, A.A. 1961 Equilibrium layers and wall turbulence. *J. Fluid Mech.* **11** (1), 97–120.
- TOWNSEND, A.A. 1976 *The Structure of Turbulent Shear Flow*, 2nd edn. Cambridge University Press.
- TSENG, Y.-H., MENEVEAU, C. & PARLANGE, M.B. 2006 Modeling flow around bluff bodies and predicting urban dispersion using large eddy simulation. *Environ. Sci. Technol.* **40** (8), 2653–2662.
- VON KÁRMÁN, T. 1930 Mechanische Ähnlichkeit und turbulenz. *Nachr. Ges. Wiss. Göttingen* **1930**, 58–76.
- WILLIAMSON, J.H. 1980 Low-storage Runge–Kutta schemes. *J. Comput. Phys.* **35** (1), 48–56.
- XIAO, H., WU, J.-L., LAIZET, S. & DUAN, L. 2020 Flows over periodic hills of parameterized geometries: a dataset for data-driven turbulence modeling from direct simulations. *Comput. Fluids* **200**, 104431.
- XIE, Z.-T., COCEAL, O. & CASTRO, I.P. 2008 Large-eddy simulation of flows over random urban-like obstacles. *Boundary-Layer Meteorol.* **129** (1), 1–23.
- YANG, X.I.A., SADIQUE, J., MITTAL, R. & MENEVEAU, C. 2016 Exponential roughness layer and analytical model for turbulent boundary layer flow over rectangular-prism roughness elements. *J. Fluid Mech.* **789**, 127–165.
- ZANOUN, E.-S., DURST, F. & NAGIB, H. 2003 Evaluating the law of the wall in two-dimensional fully developed turbulent channel flows. *Phys. Fluids* **15** (10), 3079–3089.
- ZILITINKEVICH, S. 1995 Non-local turbulent transport: pollution dispersion aspects of coherent structure of connective flows. In *Air Pollution 1995*, pp. 53–60. Porto Carras.



## 5. Study II: The Stably Stratified Rough Ekman Layer

This study addresses the interplay of surface roughness and the stably stratified turbulent Ekman layer. The mean height of the surface roughness is constant and corresponds to the roughest case **r3** of Study I (cf. chapter 4) while incrementally increasing the strength of the stable density stratification. The entire span of stability regimes is covered from the **WSBL** to the **VSBL**, where intermittency occurs. This study focusses on the flow topology and regime shifts due to the presence of roughness and surface layer similarity (**MOST**).

The following study has been published:

**Kostelecky J.**, Anson C. (2025): **Surface Roughness in Stratified Turbulent Ekman Flow**, *Boundary-Layer Meteorology*, 191, pp. 5, <https://doi.org/10.1007/s10546-024-00895-5>.

The article is reproduced here using its original layout of the journal, where it was published under the terms of the Creative Commons Attribution 4.0 licence.

### **Author contributions:**

*Jonathan Kostelecky:* Code implementation, numerical simulations, post-processing of the data, visualization and interpretation of results, writing of the original draft, conceptualization of the study.

*Cedrick Anson:* Supervising of the research, discussion and interpretation of results, reviewing and editing the original draft, acquisition of funding, conceptualization of the study.







# Surface Roughness in Stratified Turbulent Ekman Flow

Jonathan Kostelecky<sup>1,2</sup> · Cedrick Ansorge<sup>1</sup>

Received: 2 October 2024 / Accepted: 20 December 2024 / Published online: 8 January 2025  
© The Author(s) 2024

## Abstract

The interplay of surface roughness and stable stratification is investigated by direct numerical simulation of Ekman flow. Our setup is well within the turbulent regime, reaching a friction Reynolds number of  $Re_\tau \approx 2700$ . Further, we reach the verge of the fully rough regime under neutral conditions with a non-dimensional obstacle height  $H^+ \approx 40$ , corresponding to a z-nought parameter in viscous units  $z_0^+ \approx 2$ . Stability is imposed via a gradual decrease of surface buoyancy from neutral (no stratification) to very strong stratification. The reduced Reynolds number ( $Re_\tau$ ) in comparison to atmospheric problems warrants consideration of viscous effects on our results, and we demonstrate a correction method that consistently incorporates viscous effects, thus reducing the spread of data from our numerical results. The weakly stable regime is maintained at higher stability due to efficient production of turbulence kinetic energy which counteracts buoyant restoring forces in the presence of roughness. When scaled according to Monin–Obukhov similarity theory (MOST) our results for weak stability compares excellent to known formulations based on atmospheric observations. The coefficients of the stability correction functions for momentum and heat are estimated as  $\beta_m = 3.45$ ,  $\beta_h = 5.21$  respectively, and we observe a slight but significant increase of the turbulent Prandtl number with stability. In the very stable regime, global flow properties (e.g. friction velocity, Obukhov length) oscillate with a decaying amplitude and global intermittency, i.e. the co-occurrence of turbulent/laminar fluid at large scale, is observed in the presence of roughness. In such very stable conditions, a strong veering of the surface wind with respect to the large-scale forcing ( $< 90^\circ$ ) is observed.

**Keywords** Boundary-layer turbulence · Direct numerical simulation · Monin–Obukhov similarity theory · Stable boundary layer · Surface roughness

## 1 Introduction

Static stability is ubiquitous in the atmospheric boundary layer (ABL) as radiative processes in vicinity of and at the underneath surface cause vertical temperature gradients at various time scales. In the mid-latitudes, the static stability primarily governs the ABL's diurnal cycle (cf. Figure 1.7 on p. 11, Stull 1988, ): During the day, the sun heats the Earth surface,

---

Jonathan Kostelecky  
j.kostelecky@posteo.de

<sup>1</sup> Institut für Meteorologie, Freie Universität Berlin, Carl-Heinrich-Becker-Weg 6-10, 12165 Berlin, Germany

<sup>2</sup> Institut für Geophysik und Meteorologie, Universität zu Köln, Pohligstr. 3, 50969 Cologne, Germany

plumes of warmer air rise from the ground, resulting in the well-mixed and turbulence-rich convective boundary layer. In absence of solar irradiation – during night or polar night – the surface cools and the stable boundary layer (SBL) forms, characterized by an upward increase of potential air temperature (Mahrt 2014).

Static stability makes the buoyancy conversion term a sink in the budget of turbulence kinetic energy (TKE), such that turbulence is exclusively generated by shear – a stark contrast to convective conditions where both buoyancy and shear generation are a source of TKE. The SBL is commonly classified according to the relative strength of stratification and the impact of stratification on turbulent transport and mixing. This gives rise to classification approaches, suggested, for instance, by Mahrt (1998); Howell and Sun (1999); Grachev et al. (2013); Stopa et al. (2022). Mahrt (1998) distinguishes the *weakly stratified* boundary layer (WSBL), where surface-layer similarity works very well, the temperature behaves like a passive scalar, and the interaction of stratification with the turbulence structure is weak, from the *very stable* boundary layer (VSBL), where buoyancy destruction of turbulence substantially changes the surface-layer flow. Windy conditions (when shear-generation of turbulence is strong), or moderate surface cooling give rise to the WSBL, characterized by a state of continuous turbulence at reduced intensity. For large surface-cooling or weak wind, in the VSBL, turbulence is suppressed, but a complete laminarization is not found in the atmospheric measurements for its high Reynolds number. In such intermittently turbulent flow (Businger 1973; Mahrt 1999; Ansonge and Mellado 2014; Shah and Bou-Zeid 2014; Deusebio et al. 2015) the upper part of the VSBL decouples from the surface layer.

The WSBL is amenable by Monin–Obukhov Similarity theory (MOST) for the atmospheric surface layer (ASL, Monin 1970; Högström 1988; Grachev et al. 2013) and by local similarity aloft (Nieuwstadt 1984). On the contrary, the VSBL is intricate and despite intense efforts over past decades, a number of issues remain unsolved (Holtslag et al. 2013; Sandu et al. 2013; Steeneveld 2014; LeMone et al. 2019; Edwards et al. 2020). Global intermittency plays a pivotal role in the VSBL, and it results in spatio-temporally complex organized turbulence, characterized by anisotropy and wave-like/non-turbulent interaction between laminar and turbulent flow (cf. gravity waves on p. 87, Businger 1973; Vercauteren et al. 2019; Van der Linden et al. 2020; Gucci et al. 2023, ). Most prominently, large-eddy simulation (LES) faces severe challenges in the VSBL for the locality, anisotropy, and inhomogeneity of turbulence (Jiménez and Cuxart 2005). A common problem is the local laminarization of the flow and the associated *runaway cooling* (Jiménez and Cuxart 2005; Van de Wiel et al. 2012a). These problems reflect a conceptual lack models of the VSBL and challenge classical modelling approaches, calling for new avenues in turbulence parameterization (e.g. Stiperski and Calaf 2018; Maroneze et al. 2023; Boyko and Vercauteren 2024, ). Here, we use direct numerical simulation (DNS) of the SBL to circumvent dependencies on turbulence closure models at the cost of (i) a simplified setup, (ii) high computational expense, and (iii) a reduced scale separation.

Neglecting the background rotation of the mean wind in the ASL, which is in accordance with MOST, the ASL can be studied by virtue of the channel-flow analogy. DNS of stratified channel flow (Garg et al. 2000; Nieuwstadt 2005; Flores and Riley 2011; García-Villalba and del Álamo 2011; Donda et al. 2015, 2016, among others), commonly focuses on the collapse of turbulence and associated laminarization in the intermittently turbulent regime. The Obukhov length scaled in viscous units (later defined as  $L_O^+$  and sometimes termed buoyancy Reynolds number) for its appropriate characterization of turbulence instability in a stratified flow—is identified as relevant scaling parameter for the turbulence collapse (Flores and Riley 2011). Over a smooth surface, the flow laminarizes below  $L_O^+ \approx 100$ . For heterogeneous surface conditions, they speculate  $L_O/L_R$ , where  $L_R$  is a characteristic roughness length scale,

is the appropriate parameter. This would suggest that roughness shifts the stability threshold for transition to a laminar or intermittently turbulent flow to higher stability. More recently, Mironov and Sullivan (2023) investigate the turbulence structure in a stratified Couette flow for a thermally heterogeneous bottom boundary. They indeed demonstrate maintenance of turbulence in very stable conditions over thermally heterogeneous surfaces due to the presence of local convective instability as a consequence of the thermal heterogeneity.

When the ABL is considered in its vertical entirety, Earth rotation, i.e. the Coriolis force, manifests in a wind veer. This veer gives rise to the Ekman spiral (Ekman 1905) and a loss of the lateral (spanwise) flow symmetry in comparison with channel flow. Rotational effects are adequately represented in Ekman flow, the flow over a flat, rotating plate. The boundary layer depth scale (outer scale) of the Ekman flow  $\delta = u_\tau / f$ , with the friction velocity  $u_\tau$  and the Coriolis parameter  $f$ , is constant under neutral stratification, but unknown *a priori* to the simulation. The total turbulent scale separation of the outer  $\delta$  (largest eddies of the size of the boundary layer scale) and inner scale  $\delta_\nu$  (smallest eddy size, where dissipation becomes relevant) of the flow problem is expressed as the friction Reynolds number  $Re_\tau$ , defined as:

$$Re_\tau = \frac{\delta}{\delta_\nu} = \frac{u_\tau \delta}{\nu}, \quad (1)$$

where  $\delta_\nu$  is the viscous unit and  $\nu$  the kinematic viscosity.

The neutrally stratified problem was studied by Coleman et al. (1990); Coleman (1999); Shingai and Kawamura (2004); Miyashita et al. (2006); Spalart et al. (2008, 2009); Marlatt et al. (2012); Anson (2019). Different regimes of density stratification are explored in Coleman et al. (1992); Anson and Mellado (2014, 2016); Shah and Bou-Zeid (2014); Deusebio et al. (2014); Stefanello et al. (2022). The turning angle of the wind increases with stability, while a drastic decrease of the boundary layer height is observed. The studies by Anson and Mellado (2014, 2016) enabled a qualitative representation of the turbulence regimes only by varying the strength of stability, measured by an external bulk Richardson number. At sufficient stability, global intermittency is intrinsic to the VSBL and does not require external trigger mechanisms. This intermittency occurs in space and time rather than as an on-off processes in time which calls for conditional analysis and at the same time emphasizes the importance of the laminar patches in the flow's surface layer. As previous studies have indicated, DNS of very stable Ekman flow with global intermittency are demanding for various reasons: (i) the scale separation in terms of the friction Reynolds number  $Re_\tau$  has to be large enough, (ii) fine grid resolution is necessary to resolve the occurrence of large gradients in turbulent patches, (iii) large domain sizes are required to accommodate large-scale flow structures and laminar/turbulent patches.

The aforementioned studies of Ekman flow cover a broad range of stratification, but they are mainly constrained to aerodynamically smooth surfaces. At the same time, surface roughness is an omnipresent and multiscale feature in the ABL. More importantly, the effect of roughness is pronounced in the SBL, since the ABL thickness decreases by up to an order of magnitude in contrast to neutral stratification, from  $\mathcal{O}(1 \text{ km})$  to  $\mathcal{O}(10 - 100 \text{ m})$  (cf. semi-empirical boundary layer depth scheme for neutral and stable stratification by Zilitinkevich et al. 2012, based on LES and observational data). An exception is Lee et al. (2020), who study stratified Ekman flow over a periodic cosine-shaped hill. Their roughness setup is located in the transitionally rough regime with  $H^+ = 15$ , where  $H^+$  is the height  $H$  of the bumps expressed in viscous units. A regime shift from the VSBL to the WSBL is observed, since roughness is a triggering mechanism of turbulence and therefore counteracts the stability-induced suppression of turbulence. More recently, Bhimireddy et al. (2024) describe the effect of roughness on the SBL based on tower measurement from field observations and find

that the increase in the turbulent velocity scale  $V_{TKE}$  (equal to the square root of the TKE) with the wind speed increases with the roughness length.

In a preliminary study (Kostelecky and Ansonge 2024a, hereafter KA24), we investigated the effect of small-scale surface roughness on bulk properties of the neutrally stratified ABL—based on first principles, i.e. using DNS. The cases in KA24 only differ with respect to the mean height of the roughness, and they cover the transitionally rough regime up to the verge of the fully rough regime. From the DNS perspective, the setup exhibits a relatively large scale separation in terms of the friction Reynolds number  $Re_\tau$  (up to  $Re_\tau \approx 2700$ ). In fact, this scale separation is sufficient to explore the rough-wall scaling of the logarithmic layer for velocity and a passive scalar, which allows extrapolation of our results to the high-Reynolds-number regime in which the ABL is generally found. Here, we extend the setup introduced by KA24 to stable stratification, and investigate four research questions: (1) Does the presence of roughness extend the stability regime in which turbulence is maintained, and how is the regime transition from weak to very stable s roughness? (2) Does large-scale intermittency occur in the very stable regime and are its effects comparable to those in aerodynamically smooth flow? (3) How does the flow topology change? (4) Are common stability corrections for MOST applicable to our data and do the associated values of the von Kármán constant  $\kappa$ , aerodynamic roughness length  $z_0$  and the zero-plane displacement height  $d$  match expectations based on observational data from atmospheric measurement campaigns?

## 2 Methodology

We approach the problem by DNS. The governing equations and their non-dimensionalization are described in Sect. 2.1 followed by the algorithm used to solve the equations (Sect. 2.3). The treatment of a rough surface and introduction of stable density stratification are described in Sect. 2.4 and Sect. 2.5 before we introduce the set of simulation cases in Sect. 2.6.

### 2.1 Governing Equations

We solve the incompressible Navier–Stokes equations numerically under the Boussinesq approximation in a horizontally doubly-periodic domain. Stratification effects are represented by buoyancy:

$$b = \frac{\theta'}{\theta_0} g_{\text{grav}}, \quad (2)$$

with the gravitational acceleration  $-g_{\text{grav}}\hat{e}_3$  (pointing downwards). Neglecting diabatic heating, the energy conservation equation then becomes an advection–diffusion equation for buoyancy. Here,  $\theta_0$  is a reference temperature throughout the domain and  $\theta'$  is the local deviation from this temperature. For non-dimensionalization of the system, we use the geostrophic wind  $G$  (with  $\mathbf{G} = (G_1, G_2, 0)^T$ , and  $G = \sqrt{G_1^2 + G_2^2}$ ), the Rossby radius  $\Lambda_{Ro} = G/f$  with the Coriolis parameter  $f$ , and the buoyancy difference  $\Delta B = B_0 - 0$  between the bottom and top boundaries of the domain. With these scales, the non-dimensionalized governing equations for continuity, momentum and buoyancy become (hats over dimensionless variables are dropped for convenience):

$$\frac{\partial u_i}{\partial x_i} = 0, \quad (3a)$$

$$\frac{\partial u_i}{\partial t} + u_j \frac{\partial u_i}{\partial x_j} = -\frac{\partial \pi}{\partial x_i} + \frac{1}{Re_\Lambda} \frac{\partial^2 u_i}{\partial x_j^2} + \epsilon_{ik3}(u_k - g_k) + Ri_\Lambda b \delta_{i3}, \quad (3b)$$

$$\frac{\partial b}{\partial t} + u_j \frac{\partial b}{\partial x_j} = \frac{1}{Re_\Lambda Pr} \frac{\partial^2 b}{\partial x_j^2}, \quad (3c)$$

with boundary conditions corresponding to Ekman flow:

$$\begin{pmatrix} u_i|_{z=0} \\ u_i|_{z=z_{\text{top}}} \end{pmatrix} = \begin{pmatrix} 0 \\ g_i \end{pmatrix} \quad \text{and}, \quad (3d)$$

$$\begin{pmatrix} b|_{z=0} \\ b|_{z=z_{\text{top}}} \end{pmatrix} = \begin{pmatrix} 0 \\ B_0 \end{pmatrix}. \quad (3e)$$

Here,  $t$  is the time,  $x_i$  the Cartesian coordinates with  $x_i = (x, y, z)^T$ , where  $x, y$  are the streamwise, spanwise directions and  $z$  the wall-normal coordinate (pointing upwards from the ground). The corresponding velocity vector is  $\mathbf{u} = (u, v, w)^T = (u_1, u_2, u_3)^T$ . The ageostrophic non-hydrostatic pressure is  $\pi$  and the non-dimensional geostrophic wind vector is  $\mathbf{g} = (g_1, g_2, 0)$ .

In case of  $Ri_\Lambda = 0$  (no buoyancy), the buoyancy equation (3c) reduces to an equation for a passive scalar  $s$  (non-dimensionalized with  $\Delta S$ , the scalar difference between bottom and top boundaries), without feedback on the momentum equations, since the buoyancy term in (3b) is dropped.

## 2.2 Dimensionless Parameters

The system of Eqs. (3a–3c) is governed by three dimensionless parameters,

$$Re_\Lambda = \frac{G \Lambda_{Ro}}{\nu}, \quad (4a)$$

$$Pr = \frac{\nu}{\kappa_d}, \quad (4b)$$

$$Ri_\Lambda = \frac{\Delta B \Lambda_{Ro}}{G^2}, \quad (4c)$$

the external Reynolds number  $Re_\Lambda$ , the molecular Prandtl number  $Pr$  and the bulk Richardson number  $Ri_\Lambda$  with the constant kinematic fluid viscosity  $\nu$  and constant molecular diffusivity  $\kappa_d$ . The Reynolds number  $Re_D = GD/\nu = \sqrt{2}Re_\Lambda$ , the Richardson number  $Ri_D = \Delta BD/G^2 = Fr^{-2}$  ( $Fr$  being the Froude number), based on the laminar thickness of the Ekman layer  $D = \sqrt{2\nu/f}$  and the Richardson bulk number  $Ri_B = \Delta B \delta_N/G^2$ , with the turbulent boundary thickness  $\delta_N$  for a neutral flow, are given for comparison with other studies. Whereas the ratios of  $Re_D/Re_\Lambda$  and  $Ri_D/Ri_\Lambda$  reduce to the length scale ratio of the system of  $D/\Lambda_{Ro}$ .

The study of the turbulent problem requires a mapping from the non-dimensionalization with external parameters to the classical inner  $(\cdot)^+$  and outer  $(\cdot)^-$  normalization for velocities and length scales (KA24):



$$x_i^+ = x_i u_\star Re_\Lambda, \quad (5a)$$

$$u_i^+ = \frac{u_i}{u_\star}, \quad (5b)$$

$$x_i^- = \frac{x_i}{u_\star}, \quad (5c)$$

$$u_i^- = u_i. \quad (5d)$$

The inner and outer scales are mapped by  $x_i^+ = Re_\tau x_i^-$  and  $u_i^- = u_\star u_i^+$ . Here,  $x_i^+ = x_i \Lambda_{Ro} u_\tau / \nu$ , with the dimensional coordinate  $x_i \Lambda_{Ro}$  and the viscous unit  $\nu / u_\tau$ . The non-dimensional friction velocity  $u_\star = u_\tau / G$ , where  $u_\tau$  is corresponding dimensional quantity and is derived from an integration procedure described in KA24, which is linked to the non-dimensional boundary layer depth scale  $\delta_{\star N} = u_{\tau N} (\Lambda_{Ro} f)^{-1} = u_{\star N}$  for neutral conditions (subscript  $(\cdot)_N$ ). Further, we define the non-dimensional boundary layer depth scale  $\delta_{\star,95}$  (cf. their Eq. 30, here without extrapolation, Kosović and Curry 2000), of relevance for stable stratification, defined as:

$$\delta_{\star,95} = z \left( \frac{\sqrt{\langle u'w' \rangle^2 + \langle v'w' \rangle^2}}{u_\star^2} = 0.05 \right), \quad (6)$$

the height, where the total vertical momentum stress is 5 % of the total stress. In the following, the temporal averaging of the flow variables is denoted by  $\overline{(\cdot)}$  and spatial averaging in the horizontal by  $\langle (\cdot) \rangle$ .

In stratified flow, the Obukhov length  $L_O$  (Obukhov 1971; Nieuwstadt 2005; Flores and Riley 2011) is commonly used to describe the relative impact of stratification. Here, for the choice of Dirichlet boundary conditions for buoyancy, the evolution of  $L_O$  is part of the solution, i.e. unknown *a priori*. As such we diagnose it from the simulations. When expressed in viscous units,  $L_O^+ = Re_L$  is a Reynolds number, sometimes termed the buoyancy Reynolds number, and it can be interpreted as the inverse of the gradient-Richardson number  $Ri_G$  evaluated at the surface (Ansoerge and Mellado 2014) (commensurate with a flux-Richardson number  $Ri_F$  evaluated at the bottom of the constant flux layer):

$$L_O^+ = L_O \frac{u_\tau}{\nu} = \left( \frac{u_\star^3}{u_\star b_\star} \right)^+, \quad (7a)$$

$$Ri_G = \frac{1}{L_O^+}. \quad (7b)$$

The buoyancy friction value  $b_\star$  is derived with an integration procedure described in KA24 (similar procedure to  $s_\star$ , the friction value of the passive scalar). In contrast to Obukhov (1971), we follow the definition of Nieuwstadt (2005) and skip the von Kármán constant  $\kappa$ . Therefore, the mapping is according to  $L_O^{O71} = \kappa^{-1} L_O$ , where  $L_O^{O71}$  is the Obukhov length including the von Kármán constant as introduced by Obukhov (1971).

### 2.3 Algorithm

For the simulation and analysis of turbulent flow we use the highly scalable and MPI-parallel tool-suite `tLab`,<sup>1</sup> which is open-source and contains an extensive documentation, validation routines and examples. `tLab` is based on a factorization of the pressure-Poisson equation, as

<sup>1</sup> <https://github.com/turbulencia/tlab>.

discussed by Mellado and Anson (2012), where details on the numerics and validation of the code can be found. The horizontally periodic flow problem is discretized and solved in a finite-size cuboidal domain  $[L_x, L_y, L_z]$  using compact Padé schemes of sixth order in the interior of the domain (Lele 1992) and a fourth-order five-stage low-storage Runge–Kutta scheme (Williamson 1980).

## 2.4 Surface Roughness

Roughness is represented via an immersed boundary method (IBM). Here, we use the alternating direction reconstruction IBM (ADR IBM, based on Giannenas and Laizet 2021) with cubic splines to fully resolve obstacles in the flow. The implementation of the ADR IBM in the DNS code is discussed in Sect. 2.4 in KA24.

As roughness setup in the whole study we choose the case r3 (cf. KA24, Fig. 3), with  $56^2$  square blocks located at the lower domain boundary. To introduce a certain degree of randomness, the blocks are slightly displaced from a regular grid and heights, widths of the elements are uniformly distributed within  $\Delta H^+ = 13.8$ ,  $\Delta W^+ = 27.6$  and therefore:

$$H \in \left[ H^+ - \frac{\Delta H^+}{2}, H^+ + \frac{\Delta H^+}{2} \right], \quad (8a)$$

$$W \in \left[ W^+ - \frac{\Delta W^+}{2}, W^+ + \frac{\Delta W^+}{2} \right]. \quad (8b)$$

The mean height is  $H^+ = 40.8$  and the mean width is  $W^+ = 55.2$ . The roughness morphology is characterized by the plan area density of  $\lambda_p = A_P/A_T \approx 10\%$  and frontal solidity of  $\lambda_f = A_F/A_T \approx 7\%$ , with the total surface area  $A_T$ , the frontal area  $A_F$  and the plan area  $A_P$  occupied by all roughness elements (cf. Figure 2 in Grimmond and Oke 1999, ). This particular choice is considered as small-scale surface roughness, since the scale separation measured in  $Re_\tau = 2688$  is large from the DNS perspective and thus results in a small blocking ratio of  $H/\delta \approx 1.5\%$  for relevance of the ABL. Case r3 is on the verge of the transition to the fully rough regime, with a diagnosed apparent roughness length of  $z_{0m}^+ \approx 2$ . This roughness setup is at the limit of what is possible with the available computational resources.

## 2.5 Stratification

For progression to the regimes of stronger stability, we use a constant-in-time Dirichlet boundary condition for the buoyancy (Eq. 3e). This allows us to analyze the quasi-steady state that is reached once the SBL is in equilibrium with the stratification imposed. Provided the perturbation is not too large, the expected duration for this equilibrium to be reached is on the order of the eddy-turnover time  $f^{-1}$ . (Where the eddy-turnover time emerges as the ratio of the boundary layer depth scale and the turbulent velocity scale.) For the first stratified case, which is well within the weakly stratified regime, we use the flow fields from the neutrally stratified precursor simulations as initial condition in combination with the initial temperature profile described in Fig. 1, where the entire gradient is located above the highest roughness elements, since mixing is strong here.

The subsequent cases with higher stratification use the turbulent fields of buoyancy and momentum from its respective precursors as initial condition (vertical connections in Fig. 2). The increase in stratification is represented by a change in the Richardson number, which corresponds to a ramp-up in stratification across the boundary layer. The presence of realistic

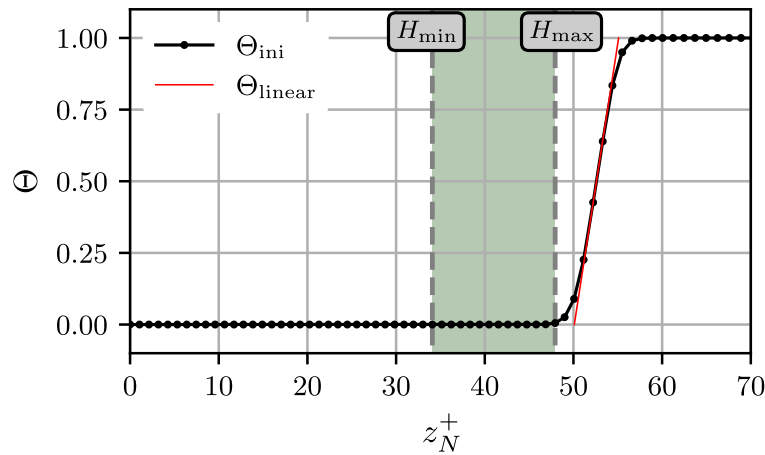


**Fig. 1** Temperature profile used for initialization of the first stratified case S001 in black. The linear temperature profile (gradient corresponding to  $L_O^+ \approx 1000$ ) in red is smoothed to the boundary values. The gradient is concentrated at the highest roughness elements  $z_N^+ > H_{\max}$  (green shaded area relates to the range of roughness element heights). The subscript  $(\cdot)_N$ , relates to the viscous units of the neutral case. The numerical values of  $\Theta_{\text{ini}}$  can be found in the available data in Kostelecky and Ansgore (2024b) (10.17169/refubium-45292)

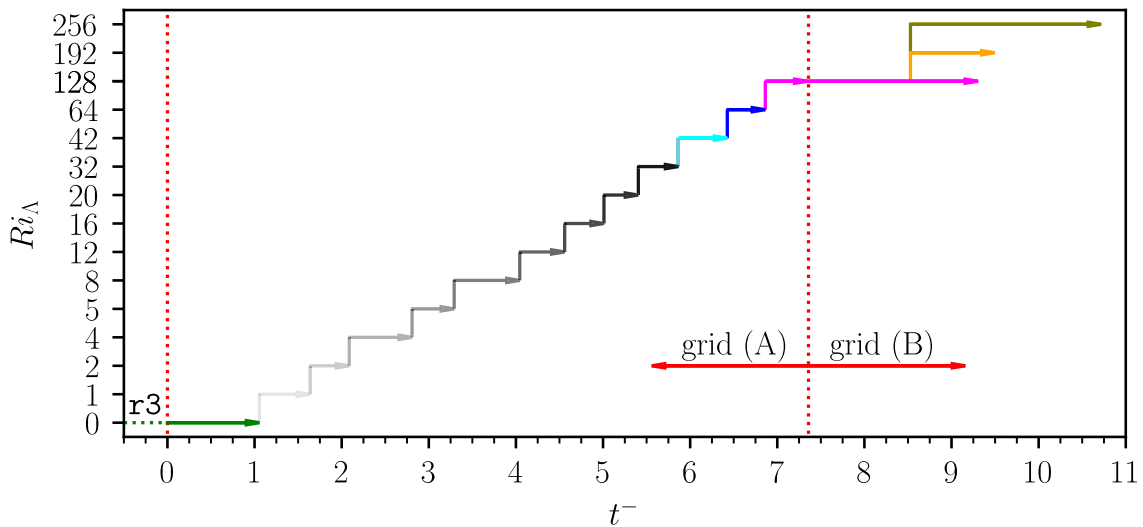


**Fig. 2** Temporal evolution of  $Ri_\Delta$  for the sequence of stratified simulation (cf. Table 2). The neutral precursor simulation r3 is shown as a green arrow ( $t^- > 0$ ) and dashed line ( $t^- < 0$ ). Further, the computational grid is changed in favour of a lower one to resolve less of the laminar fluid aloft the PBL from (A) to (B) at  $t^- \approx 7.3$ , where  $t^-$  is the eddy turnover time  $f^{-1}$

turbulent perturbations in the initial fields (i) avoids a potential complete laminarization of the flow, which leads on the one hand in a slow recovery and on the other to strong turbulent bursts, which are numerically challenging (large gradients), and (ii) is a viable approach to present the build-up of stable density stratification following the evening transition. At the same time, however, each case reaches a quasi-steady state that can be analyzed in accordance with surface-layer similarity. The aim of this procedure is not to exactly mimic a realistic transition of the boundary layer but to enable a fast transition of the simulations into the quasi-steady state where we can analyze the data in accordance with surface-layer similarity.

**Table 1** (a) Dimensionless numbers, grid and domain parameters for all cases

$Re_A$	$Re_D$	$Pr$	$N_{xy} \times N_z$	$(L_{xy} \times L_z) / \delta_N^3$	$\Delta x_N^+ \times \Delta z_{N,\min}^+$
$5 \cdot 10^5$	$10^3$	1.0	$3840^2 \times 704$ (A)	$3.7^2 \times 3.5$ (A)	$2.6^2 \times 1.0$
			$3840^2 \times 576$ (B)	$3.7^2 \times 1.5$ (B)	

Grids (A) and (B) are used in this study, with the latter (B) being cropped from the top. The domain size normalized with the Rossby radius is (A)  $(L_{xy} \times L_z) / \Lambda_{Ro}^3 = 0.27^2 \times 0.26$  and (B)  $(L_{xy} \times L_z) / \Lambda_{Ro}^3 = 0.27^2 \times 0.11$

## 2.6 Simulations

Tables 1 and 2 list the simulations used here. All cases share the same heterogeneity pattern corresponding to case r3 in KA24, consisting of  $56 \times 56$  roughness elements in quasi-random arrangement. The molecular Prandtl number is  $Pr = 1$ , and the external Reynolds is fixed at  $Re_A = 5 \cdot 10^5$ , corresponding to  $Re_D = 1000$ . As initial condition, we use three-dimensional fields of momentum and buoyancy of case r3 in KA24. These data reside on a grid of  $N_{xy} \times N_z = 3072^2 \times 656$  collocation points and are interpolated to grid (A) (cf. Table 1), i.e. a slightly increased resolution. This is necessary as stronger gradients in stratified flow (causing higher velocities in vicinity of roughness elements) pose numerical challenges at the vertical walls of roughness elements. As a consequence of interpolating the fields, the surface roughness of case N is not identical with case r3, but it features identical statistical properties (mean height, width and distributions). Case N is run without stratification to equilibrate the new roughness configuration on grid (A) before stratification is added to the problem.

Starting from the neutral case N, stratification is sequentially increased in 12 steps from the weak to the very strong stability (cf. Table 2 and Fig. 2). In the very stable regime, three cases (S128P, S192P, S256P) are run in parallel on the new grid (B). Grid (B) is similar to (A) but cropped on top to decrease computational cost, since the boundary layer thickness is substantially decreased compared to the weakly stable cases.

















Numerical integration is accomplished with the algorithm suite `tLab` on the high-performance computing system `hawk` at HLRS Stuttgart. Simulations were run for 86.5 days of wall-clock time on 128 nodes (16,384 physical CPUs). The total simulation period covers a time span  $\Delta t_{\text{total}}^- = \sum_{i=1}^{N=16} \Delta t_{\text{sim},i}^- = 12.37$ , which corresponds to one week of wall-clock time or 21,500 Node-hours per eddy turnover period ( $1/f$ ). Processed results are available for download in Kostecky and Ansgor (2024b) (doi:10.17169/refubium-45292).

## 3 Bulk Statistics and Turbulence Regimes

### 3.1 Surface Friction and Boundary-Layer Depth

We commence by analyzing the statistics that form once the boundary layer has reached a quasi-steady state in equilibrium with the surface state. Each increment in stratification, viz.  $Ri_A$ , is followed by an adaptation period on the order of an eddy-turnover time (this initial transient is depicted by dotted lines in Figs. 3, 5). During this initial transient, surface-layer similarity is not expected to hold, and it is consequently excluded from subsequent analysis.

**Table 2** Overview of the simulation cases of this study, with the corresponding stratification level (Richardson numbers), grid type and the total simulation time in eddy-turnover times  $f^{-1}$  for each case

Case (ID)	$Ri_A$	$Ri_B$	Grid	$\Delta t_{sim}^- [1/f]$	(ID)
N	0	0.000	A	1.06	
S001	1	0.073	A	0.58	
S002	2	0.147	A	0.44	
S004	4	0.293	A	0.71	
S005	5	0.367	A	0.48	
S008	8	0.587	A	0.74	
S012	12	0.880	A	0.51	
S016	16	1.174	A	0.44	
S020	20	1.467	A	0.39	
S032	32	2.348	A	0.45	
S042	42	3.081	A	0.55	
S064	64	4.695	A	0.43	
S128	128	9.390	A	0.48	
S128P	128	9.390	B	1.95	
S192P	192	14.086	B	0.97	
S256P	256	18.781	B	2.19	

Notation of case ID: N for neutral, S for stable, P for concurrent runs and numbering according to the value of  $Ri_A$

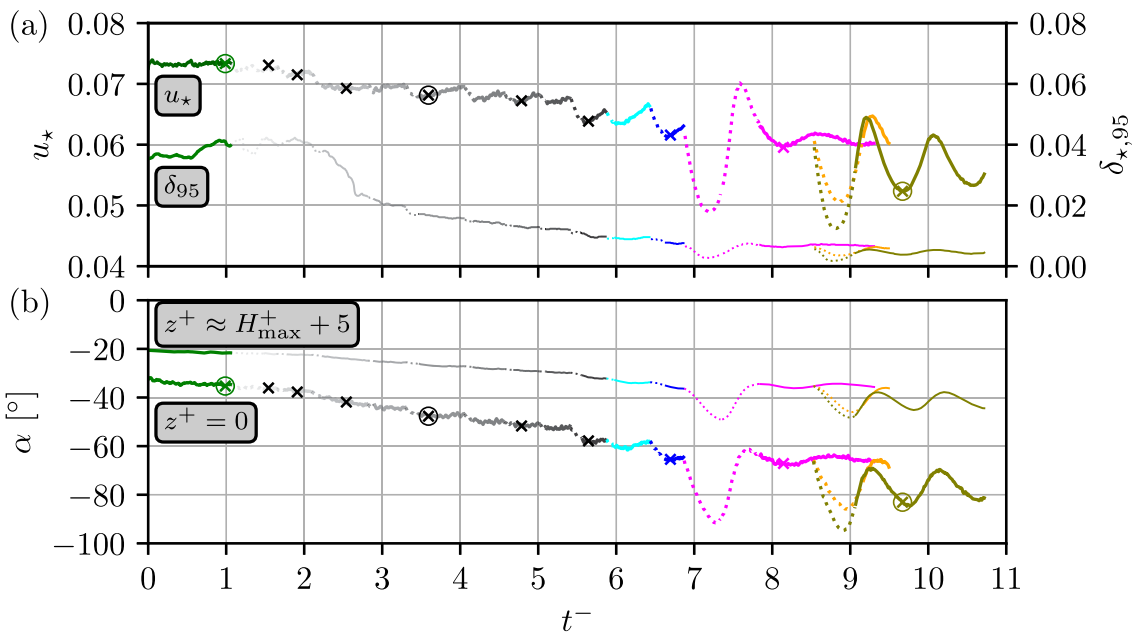


**Fig. 3** **a** Temporal evolution of the friction velocity  $u_*(t^-)$  (thick lines) and boundary layer thickness  $\delta_{*,95}(t^-)$  (6, thin lines). **b** Wind veer  $\alpha(t^-)$  at the surface  $z^+ = 0$  (thick lines) and above the roughness elements  $z^+ \approx H_{max}^+ + 5$  (thin lines). Markers for the analysis in Sect. 3.5. The coordinate system is aligned with the geostrophic wind for estimating the wind veer. Dotted lines are excluded from the analysis, since these parts are identified as initial transients. Case S128 ( $6.8 \leq t^- \leq 7.8$ ) is out of equilibrium and therefore excluded from subsequent analysis

If stratification is weak, the buoyancy term in the momentum equations is small in comparison to the dominant balance in the ASL. In such conditions, the downward buoyancy flux is limited by small temperature gradients, and no substantial changes in the bulk statistics (Fig. 3) are found. This is the case for our simulations S001–S002 ( $t^- \leq 2.1$ ) where buoyancy acts as a passive scalar. From case S004 onward, buoyancy starts to act on the flow fields, and the thickness of the boundary layer, measured in terms of  $\delta_{*,95}$ , decreases by about 50 % (Fig. 3a). With increasing stratification,  $\delta_{*,95}$  decreases to approximately one fifth of its neutral value for case S064 ( $5.8 \leq t^- \leq 6.8$ ). In contrast, the friction velocity decreases only slightly so that the ratio  $\delta_{*,95}/\delta_*$  (not shown) drops from its neutral value 0.5–0.6 to approximately 0.1 for the most stable cases. This indicates that shear production ( $u_*$ ) is no longer the single appropriate scaling variable in the surface layer. Indeed, the Obukhov length  $L_O$ , in dimensional terms: the buoyancy flux, enters. The bulk statistics of the flow indicate a regime transition from WSBL to VSBL around  $t^- > 6.8$  (cases S128–S256P): instead of a rather steady and smooth evolution for each case ( $t^- \leq 6.8$ ), we now find sizeable oscillation in the bulk quantities. This is in agreement with previous findings in Ansonge and Mellado (2014): if strong stability is abruptly imposed on the flow, turbulence vanishes in vicinity of the wall (in the viscous sublayer, located next to the ground and around roughness elements), where mixing is attributed to viscous diffusion. The rapid change is followed by a somewhat slower recovery and an overshoot (at  $t^- \approx 7.6$  for case S128P and  $t^- \approx [9.2, 9.3]$  for cases S192P, S256P).

### 3.2 Wind Veer and Pressure-Driven Channeling

An over-veering of the surface wind, a rotation of more than  $45^\circ$ , is sometimes observed in particular under stably stratified conditions or for strongly anisotropic orography. With increasing stability, the turbulence intensity decreases along with buoyant destruction of turbulence and the velocity profile shifts to a more *laminar-like* profile with reduced velocity in the vicinity of the ground and an enhanced velocity in the upper part of the SBL. Hence, velocity gradients close to the ground and within the roughness are reduced and  $u_*(t)$  decreases (by approximately 15 %, cf. Figure 3a). Such reduced mixing comes with an increased surface wind veer  $\alpha_*(t)$  in Ekman flow which is known from both theoretical (Rossby and Montgomery 1935; Spalart 1989) and numerical (Coleman et al. 1992; Deusebio et al. 2014; Shah and Bou-Zeid 2014; Ansonge and Mellado 2014) consideration of the problem, see also KA24 (their Eq. 7). We evaluate the veering both throughout the domain ( $\alpha(z, t)$ ) and at the surface ( $\alpha_*(t)$ ) as:

$$\alpha(z, t) \triangleleft (\langle \mathbf{u}(z) \rangle, \mathbf{g}), \quad (9a)$$

$$\text{and } \alpha_*(t) \triangleleft (-\boldsymbol{\tau}_*(t), \mathbf{g}), \quad (9b)$$

where  $\boldsymbol{\tau}_*(t)$  is the non-dimensional instantaneous, domain-averaged surface shear stress. Stability further increases the turning, measured in terms of  $\alpha_*$ , that is already increased due to roughness in neutral conditions (cf. Sect. 4.4 in KA24):  $\alpha_*$  grows from  $\approx 35^\circ$  (case N) to  $65^\circ$  (S064, cf. Figure 3b). If we consider the SBL above  $z^+ = H_{\max}^+ + 5$ , in other words above the roughness, the veering angle approaches approximately  $40^\circ$ , close to the laminar limit of  $45^\circ$ . A large portion of the increase in veering is concentrated within the roughness, where  $\Delta\alpha$  (here, specified in the range of  $0 \leq z^+ \leq H_{\max}^+ + 5$ ) triples from  $\approx 10^\circ$  to  $\approx 30^\circ$ .

For homogeneous, smooth surface conditions under stable stratification one would expect turning angles that are smaller than the laminar limit, viz.  $\alpha_* < 45^\circ$ . However, observations under certain orographic conditions indicate otherwise: In extended valleys (e.g. Upper Rhine



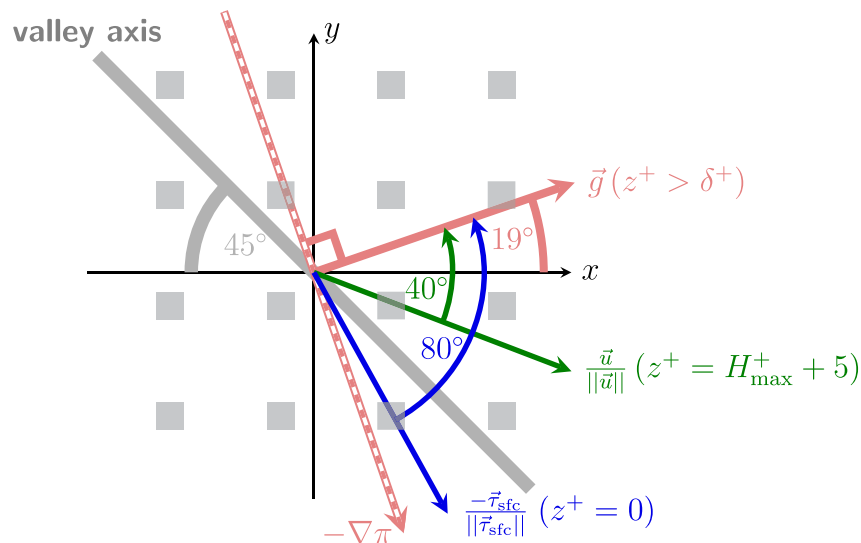


**Fig. 4** Schematic of the channeling mechanism for the case S256P, with the angles of the geostrophic wind ( $z^+ > \delta^+$ , red), the orthogonal pressure gradient (red dashed line), the horizontal velocity in the vicinity of the crests of the roughness elements ( $z^+ = H_{\max}^+ + 5$ , green) and the angle of the surface shear stress on the lower wall of the domain ( $z^+ = 0$ , blue). Gray squares in the background depict the surface roughness

valley in Germany (Wippermann and Gross 1981), Tennessee valley in the USA (Whiteman and Doran 1993), region of the MISTRAL campaign (Weber and Kaufmann 1998)), the near-surface wind may turn by more than  $90^\circ$  with respect to the large-scale geostrophic wind (e.g. Wippermann and Gross 1981; Kalthoff and Vogel 1992). This phenomenon is termed *pressure-driven channeling* and was first described by Fiedler (1983), where the near-surface wind is observed to be preferably aligned with the valley axis in stable and low-wind conditions. Fiedler (1983) relates the cause of this mechanism to the valley-aligned component of the pressure gradient and friction on the side walls of the valley, while the Coriolis force was assumed to be negligible in this context. In our rough setup, three principal axes (‘valleys’) for the channeling mechanism exist: (i) the streamwise  $x$ -direction, (ii) the spanwise  $y$ -direction and (iii) the transverse direction, inclined by  $45^\circ$  to the roughness grid. The wind can flow through these ‘valleys’ more or less unimpeded by the surface roughness.

Our results indicate that option (iii) is relevant (cf. Figure 7c). The present results suggest an explanation of the channeling mechanism based on the momentum balance (cf. Figure 4): As stability increases, the wind speed within the roughness layer is substantially reduced (here, by approximately half, leading to a more *laminar-like* velocity profile, compare cases N vs. S256P) and, hence, the Coriolis and friction forces reduce. This results in a stronger turning of the wind in favour of the pressure gradient, which is the remaining large-scale forcing of the system. In our particular case, the large-scale forcing is shear-aligned for the smooth surface case, i.e. has an angle of  $\alpha \approx 19^\circ$  (KA24). Hence, the angle of the pressure gradient with respect to the  $45^\circ$ -axis is only  $\approx 26^\circ$ , i.e. the projection of  $\nabla\pi$  onto this  $45^\circ$ -axis is large. Therefore, we conclude that the triadic balance of the pressure gradient, friction and Coriolis forces determine the observed strong turning of the wind within the roughness, where the main mechanism for the super-rotation in the case of pressure-driven channeling is a reduction of the Coriolis force due to the reduced wind speed. We conclude that frictional effects alone do not explain the turning of the wind, and the balance of forces is only closed and consistent if the Coriolis force is considered—also within the roughness layer.

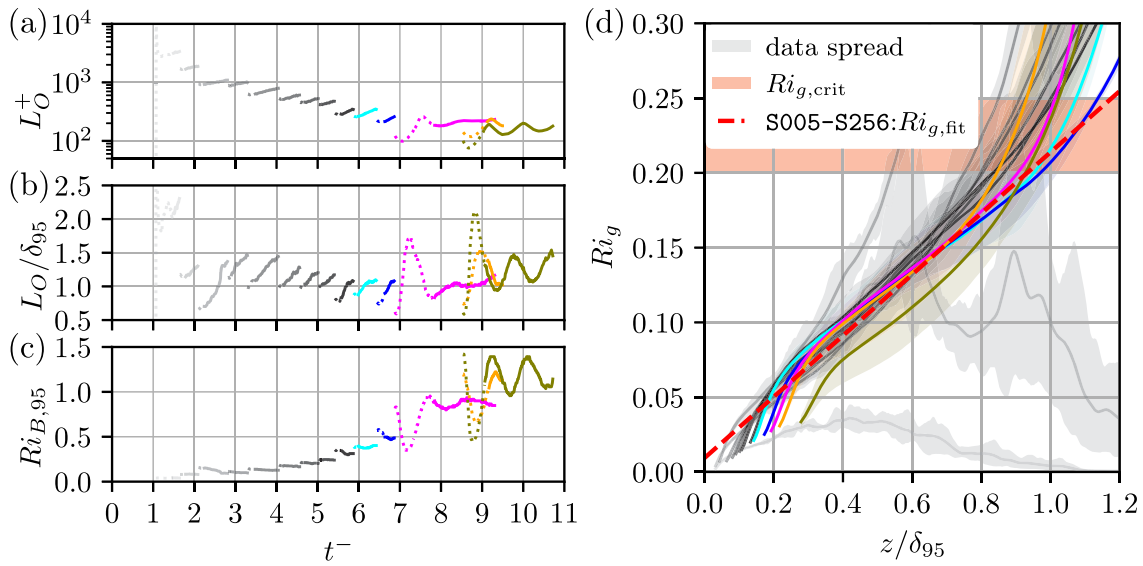


**Fig. 5** **a** Temporal evolution of the Obukhov length in viscous units  $L_O^+(t^-)$  and **b** scaled in outer units with  $L_O(t^-)/\delta_{95}(t^-)$ . **c** Temporal evolution of the bulk Richardson number  $Ri_{B,95} = B\delta_{95}/G^2 = Ri_\Lambda\delta_{95}/\Lambda R_O$ . Dotted lines are excluded from the analysis, since these parts are identified as initial transients. **d** Time-averaged gradient Richardson number  $Ri_g = (\partial_z \langle \bar{b} \rangle) / [(\partial_z \langle \bar{u} \rangle)^2 + (\partial_z \langle \bar{v} \rangle)^2]$ , plotted as a function of the mean non-dimensional height  $z/\delta_{95} > H_{\max}/\delta_{95}$  of the stable cases. The red dashed line indicates the linear fit for the cases S005–S256P for  $0.35 < z/\delta_{95} < 0.7$  with  $Ri_{g,fit} = 0.01 + 0.2z/\delta_{95}$ , the red shaded area depicts the range of the critical Richardson number  $Ri_{g,crit} = 0.2 - 0.25$  according to the literature, and the shaded regions corresponds to the spread of the data

### 3.3 Obukhov Length

At a height  $z = L_O$  (cf. 7a), the buoyant destruction of TKE equals its mechanical shear generation, under the prerequisite that fluxes are truly constant; for the boundary layers studied here, this is an approximation that is commonly used when interpreting data in the context of ASL similarity. Hence, absent pressure redistribution and transport effects, the shear generation dominates for  $z \lesssim L_O$ . Alternatively,  $L_O$  is the largest wall-attached eddy for which the kinetic energy is sufficient to overcome stratification (Van de Wiel et al. 2008).

Flores and Riley (2011) propose the buoyancy Reynolds number  $Re_L \equiv L_O^+$  as scaling parameter to indicate turbulence collapse in a hydraulically smooth SBL. They find that the flow laminarizes for  $Re_L < Re_{L,crit} \approx 40$  which implies  $L_{O,crit}^+ = Re_{L,crit}/\kappa \approx 100$ . In the case of rough walls, they suggest  $L_{O,crit}/h_r \approx 1$  as an appropriate criterion, where  $h_r$  is a characteristic roughness length scale. Here, the roughness length  $h_r \hat{=} H$  is the mean height of the roughness elements, in viscous units  $H^+ \approx 30 - 40$  (with the range of  $u_\star(t)$  in Fig. 3a). By coincidence, both suggested criteria are equivalent given our setup. In the current study, we do not observe a complete laminarization of the flow since the most stable cases at  $t^- \approx 8.7$  drop to  $L_O^+ \approx 75$  (Fig. 5a). These cases are close to laminarization and hence, it is a strong indicator of the intermittent regime, where turbulent and laminar regions coexists in the flow. As previously discussed, the flow is effected by buoyancy for  $t^- > 2.1$ , where the ratio  $L_O/\delta_{95} < 1$  for the first time (Fig. 5b). Here, buoyancy is the dominating process, since  $L_O \lesssim \delta_{95}$ . Interestingly, for the very stable case S128P at  $t^- > 8$  the ratio  $L_O/\delta_{95} \approx 1$ , whereas cases S192P, S256P oscillate with a damped amplitude (observable for case 256P) around the value  $L_O/\delta_{95} \approx 1.1 - 1.2$ .

### 3.4 Richardson Number

An important indicator for the collapse of turbulence in stably stratified flow is the local gradient Richardson number, defined as:

$$Ri_g = \frac{\partial \langle b \rangle / \partial z}{(\partial \langle u \rangle / \partial z)^2 + (\partial \langle v \rangle / \partial z)^2}, \quad (10)$$

with a ‘critical’ range of  $Ri_{g,\text{crit}} \approx 0.2 - 0.25$  (Garratt 1992), where the precise value and nature of the threshold is still a matter of debate (cf. extensive discussion in Sect. 4.2, Grachev et al. 2013). The flow regime we find for the stable cases S005–S256P (Fig. 5d) is in accordance with previous findings regarding their Richardson number. The cases pass the range of 0.2–0.25 for  $0.8 < z/\delta_{95} < 1.1$ . Above the boundary layer thickness  $\delta_{95}$ , the flow is mostly laminar. Within the boundary layer  $Ri_g$  approximately follows a linear relation (cf. red dashed line in Fig. 5d). The cases S001–S002 do not reach  $Ri_{g,\text{crit}}$  and are therefore slightly effected by buoyancy. With respect to both field observation and numerical bulk models of the SBL, the bulk Richardson number is a key parameter. We use here  $Ri_{B,95}$  based on  $\delta_{95}$  (Fig. 5c). While  $Ri_B \ll 1$  for near-neutral cases where buoyancy acts as a passive scalar, it reaches 1 for the most stable cases indicating that (i) our study spans the full range of stability regimes *and* (ii) the criticality of stability is well reproduced in our rough setup, also in terms of the bulk Richardson number.

### 3.5 Synopsis of the Turbulent Flow

Visual inspection of instantaneous snapshots of enstrophy  $\xi(x_i)$  for the neutral case N at  $t^- \approx 1.1$ , weakly stable case S008 at  $t^- \approx 3.5$  and very stable case S256P at  $t^- \approx 8.8$  (Figs. 6, 7) reveal the antagonistic interplay of static stability and small-scale surface roughness despite the small blocking ratio ( $H/\delta_N \approx 0.015$  for case N).

Immediately above the roughness elements, strong vortical activity is observable (Fig. 6a, b), indicative of the buffer-layer (for homogeneous surfaces at  $5 < z^+ < 30$ , according to Pope (2000); here, elevated by the roughness height). Here, turbulent production peaks and the fine turbulent structures move upwards while increasing in size until the boundary layer height is reached (blue bars in Fig. 6 for  $\delta$  and  $\delta_{95}$ ). Non-turbulent fluid from aloft is entrained deeply into the boundary layer (cf. light regions in Fig. 6a, e.g. at  $1 \lesssim t^- \lesssim 1.5$ ). Simultaneously, ejections of turbulent fluid penetrate into the upper part of the boundary layer. This phenomenon is inherent to boundary layer flow and related to the external intermittency of the turbulent Ekman flow (Ansoerge and Mellado 2014).

The suppression of turbulence by buoyancy reduces the boundary layer height of case S008 (Fig. 6b), measured in terms of  $\delta_{95}$ , by half in comparison to N, whereas  $\delta$  is reduced by approximately 10 %. It is distinctly recognizable that  $\delta_{95}$  rather than  $\delta$  is the appropriate scale of the boundary layer thickness in the presence of stable density stratification. Large-scale structures are still visible for S008 at  $z > \delta_{95}$  above the boundary layer, which is attributed to residual turbulence inherited from case N. A further increase in stability leads to a strong reduction in turbulence activity in the VSBL for case S256P (Fig. 6c) with a boundary layer thickness of  $\delta_{95} \approx 3H$ . In this case the boundary layer becomes very thin and there is a complex interplay between gravity waves, residual turbulence and large-scale intermittency which is probably not relevant at atmospheric scale due to the mismatch in scale separation vide the reduced Reynolds number of our setup.

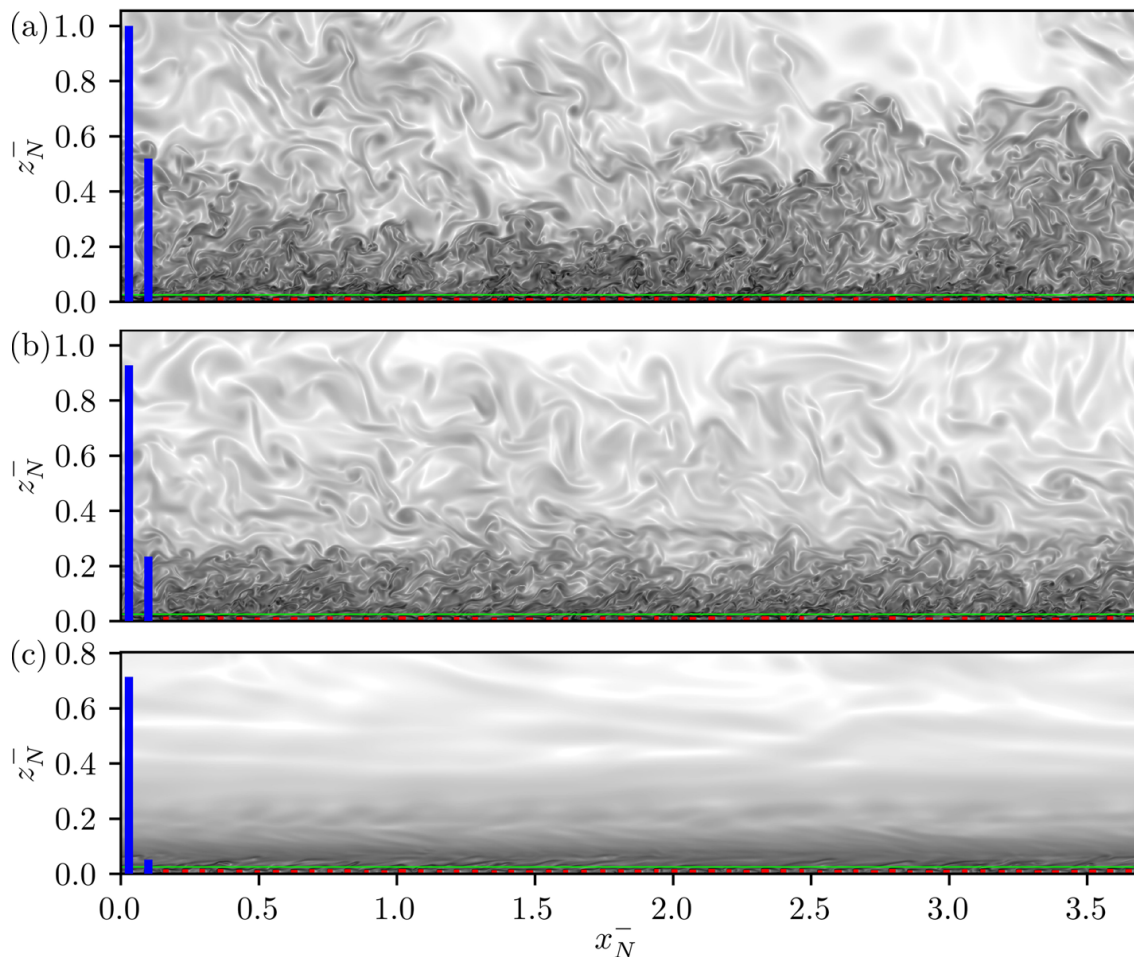


**Fig. 6** Streamwise-vertical, instantaneous intersection of the logarithm of the enstrophy  $\xi(x_i)$  with a linear colormap  $0 \leq \xi \leq 16$  of **a** case N, **b** case S008, and **c** case S256P; time corresponds to circles in Fig. 3. The axes are scaled with the neutral boundary layer thickness and blue bars depict the instantaneous boundary layer thickness  $\delta_*(t)$  and  $\delta_{*,95}(t)$ . The roughness elements on the ground are shown as red cuboid blocks. Green lines for the vertical position of Fig. 7d–f

Within the surface roughness (at half the height of the elements) and above the roughness, located at the lower bound of the surface e.g. logarithmic layer, no distinct differences are visible between the cases N and S008 (Fig. 7a, b, d, e). The flow is turbulent inside the roughness, due to the high Reynolds number of the flow and instabilities induced by the roughness elements (Fig. 7a,b). Above (Fig. 7d,e), the turbulence is homogeneous with the imprint of hairpin vortices seen as elongated enstrophy filaments. Hairpins originate from the buffer layer and are characteristic for wall-bounded flows in the logarithmic layer (Adrian 2007). In conclusion, the visual appearance of the turbulence in the close-wall region is comparable for the neutral and weakly stable regime, which is consistent with the literature (García-Villalba and del Álamo 2011; Watanabe et al. 2019; Atoufi et al. 2021), despite the reduction in  $\delta_{95}$  and the stronger turning angle  $\alpha$ . In case of very strong stability, heavy fluid is trapped inside the roughness and therefore, the surface layer is decoupled from the outer layer (Van de Wiel et al. 2012a). Weak turbulence activity is visible within the roughness, which is induced by the transverse flow ( $\approx 45^\circ$ ) of the objects with sharp edges (Fig. 7c). Above the roughness, the intermittent behaviour of the flow is clearly observable (Fig. 7f), where patches of turbulent fluid (regions with sharp transitions) are embedded in non-turbulent fluid (smeared regions). Global intermittency in the VSBL appears in space and time, and



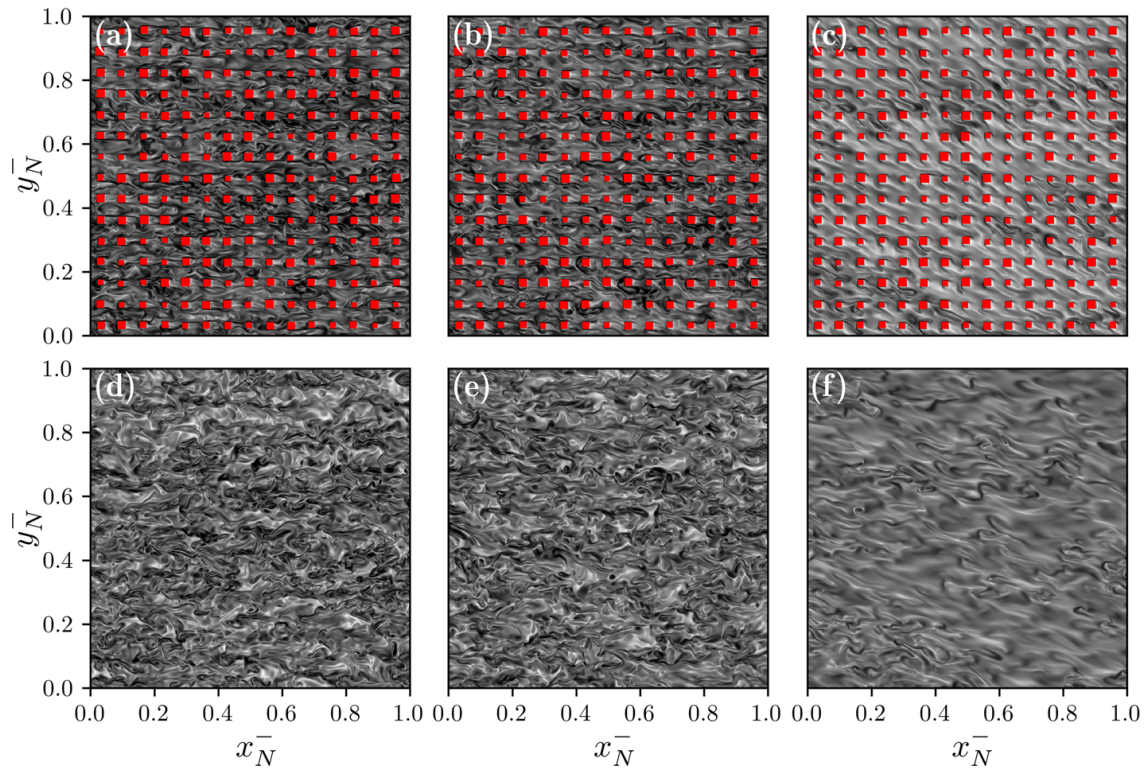


**Fig. 7** Horizontal (streamwise-spanwise) intersection of the size  $[\delta_N \times \delta_N]$ , corresponding to approximately 1/14 of the computational domain (time instances cf. circles in Fig. 3) with a linear colormap  $5 \leq \xi \leq 15$  (cf. explanations in Fig. 6, identical turbulent fields are chosen). Shown are the cases **a**, **d** N, **b**, **c** S008 and **c**, **f** S256P at half height of the roughness elements (**a–c**)  $z_N^+ \approx 20$  and in the surface layer at  $z_N^+ \approx 65$  [(**d–f**), cf. green lines in Fig. 6]

is not an on–off process (Mahrt 2014; Ansonge and Mellado 2014). In order to investigate this behaviour, computational domains of sufficient size are required that can accommodate these laminar-turbulent patterns (Deusebio et al. 2014), which is the case here.

### 3.6 Maximum Sustainable Heat Flux

The heat (buoyancy) flux  $\langle w'b' \rangle$  represents at the same time also the buoyant destruction (production) term in the TKE budget equation, and it is limited from two-sides given a large-scale forcing (De Bruin 1994). In the WSBL, the vertical mean temperature profile is nearly neutral with a small gradient, and turbulent mixing is strong. In these conditions, heat flux is limited due to lack of temperature contrast, i.e.  $\langle b'b' \rangle$ . The other extreme is the VSBL, where the restoration of buoyant forces is so strong that turbulent mixing in the boundary layer is inhibited and the heat flux is limited for lack of velocity fluctuations  $\langle w'w' \rangle$ . In between these two extrema, the heat flux assumes a maximum according to the concept of the *maximum sustainable heat flux* (MSHF) Van de Wiel et al. (2012a, b).

The core of the MSHF concept is confirmed by the current simulations (Fig. 8). However, we observe for the vertically integrated buoyancy term of the TKE budget a pronounced plateau over two orders of magnitude in  $Ri_\Delta$  rather than a distinct maximum, which differs from stable Ekman flow over smooth surfaces, where the plateau width is less than one order of magnitude in  $Ri_\Delta$  (cf. Fig. 6c, Ansonge and Mellado 2014).

This characteristic behaviour of  $\langle w'b' \rangle$  as a function of the stability, underpins the importance of roughness as a very efficient triggering mechanism of turbulence due to flow

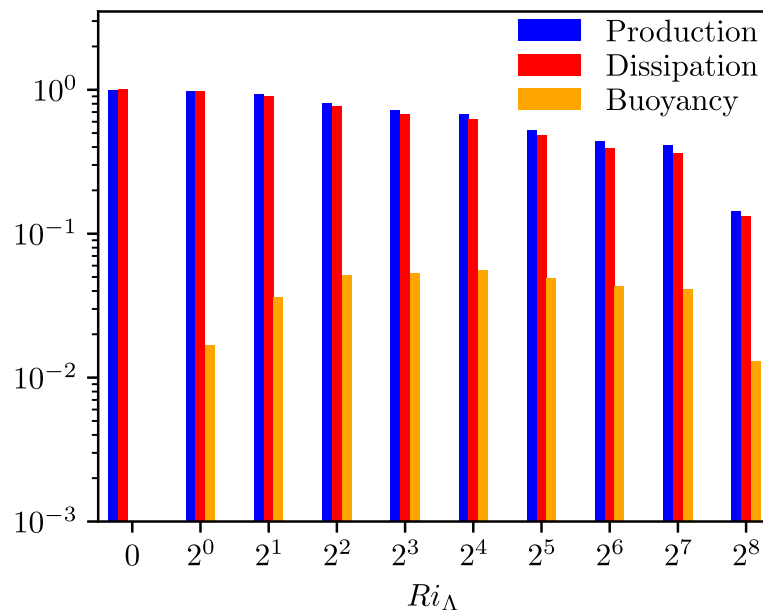


**Fig. 8** Domain-wise, vertically integrated contributions to the TKE budget (shear production, buoyancy destruction and dissipation of TKE). Bounds for vertical integration are  $H_{\max}$  to  $L_z$  as a function of the external Richardson number  $Ri_{\Delta}$ . Terms are normalized with the neutral production rate. The integration is shown for  $\Delta t^- \approx 0.1$  around the time instances depicted as  $\times$ -symbols in Fig. 3 (not all cases are considered)

instabilities on sharp edges (detached eddies), which counteracts efficiently buoyancy induced reduction of turbulence and is assumed to form the observed plateau. The remaining imbalance of the presented TKE terms (shear production, dissipation, buoyancy destruction) in Fig. 8, especially for the more stable cases, are the integrated temporal tendency and transport terms of the TKE budget (not shown). These terms are non-zero, as the more stable cases are out of equilibrium to a certain degree.

#### 4 Surface-Layer Similarity

For guidance in the subsequent gradient analysis, Fig. 9 present horizontal velocity and buoyancy profiles with increasing stratification. In contrast to non-rotating flow problems, the horizontal mean velocity profiles in Ekman layers exhibit a super-geostrophic velocity, referred to as the low-level jet (LLJ) (Fig. 9a). With increasing stability, the height of the LLJ maximum is reduced from  $z_N^- \approx 0.4$  for the neutral case N to  $z_N^- \approx 0.1$  for the most stable case S256P, with a velocity increase of  $\approx 4\%$  (N) up to  $\approx 20\%$  (S064) with respect to the geostrophic velocity. The reduction in the vertical LLJ position is accompanied by a reduced boundary layer thickness (cf. Figures 3a, 6), which also reduces the outer length scale relevant for the formation of turbulence. Due to the increased shear and turbulence triggering by roughness, also the inner length scale of the turbulent boundary layer is reduced, such that a turbulent boundary layer is maintained. While our data suggest the thickness of the surface layer is marginal for the most stable cases, this cannot be judged based on surface scales alone. Hence, the following discussion assumes existence of a surface layer, which is common when using surface layer similarity in an observational, operational, or modelling context. Within the roughness (indistinguishable in Fig. 9a) at  $z_N^- \lesssim H$ , the velocity reduces with increasing stability, whereas for  $z_N^- \gtrsim 2H$  the velocity enhances with increasing stability. Here, above the roughness ( $z_N^- \gtrsim 2H$ ), the velocity gradient increases due



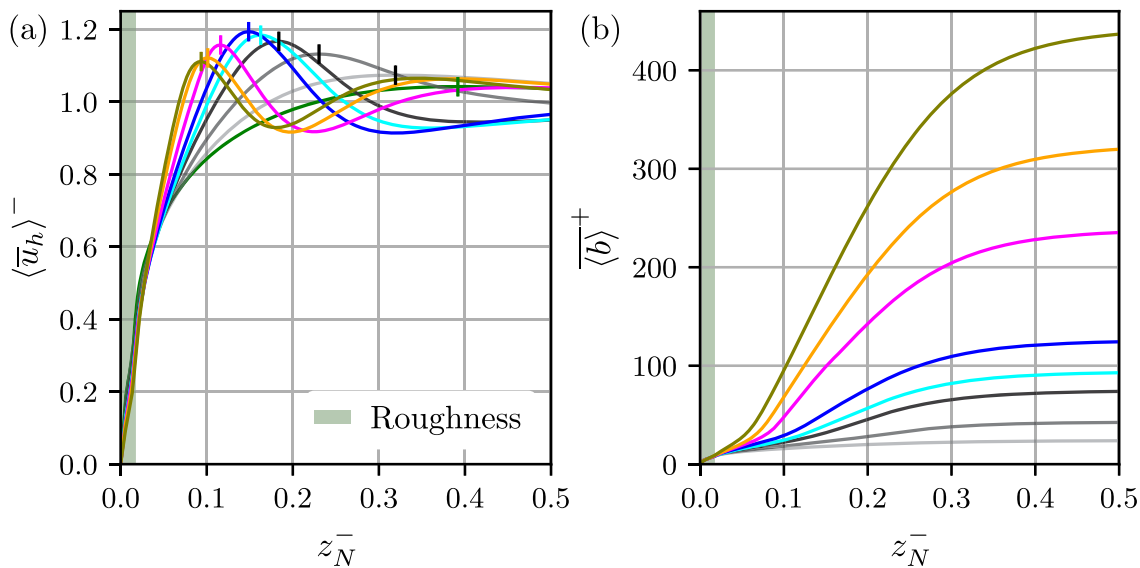


**Fig. 9** **a** Horizontal mean velocity and **b** buoyancy profiles (normalized with  $b_*(t)$ ) of the stable cases S004, S012, S032–S256P, case N only in **(a)** (green). The vertical strokes in **(a)** depict the position of the super-geostrophic velocity. Temporal averaging according to the intervals in Fig. 3. The vertical distance is normalized with the turbulent boundary layer thickness of the neutral case (N) as reference. The green shaded areas depict the maximum height of the surface roughness

to less vertical mixing. With increasing stratification ( $Ri_A$ ) the buoyancy profiles steepen, respectively the gradient increases. Above the boundary layer thickness, where diffusion dominates (approximately the position of the LLJ) buoyancy increases linearly and then flattens (Deusebio et al. 2014).

#### 4.1 ASL Similarity in Vicinity to the Rough Boundary

MOST, the corner stone of ASL similarity (Obukhov 1971; Foken 2006), is limited to horizontally homogeneous and statistically stationary conditions (ASL, Obukhov 1971; Ansorge 2019). It further precludes that the stability (e.g. measured in terms of  $Ri$ ) does not exceed a critical value  $Ri_{crit}$  and neglects the vertical flux divergence due to the Coriolis force, leading to the so-called *constant flux layer* (maximum of the total turbulent flux varies less than 10%, cf. Stull 1988) or *channel-flow analogy*. In KA24 we show that the neglect of the Coriolis force in the ASL is a strong assumption for intermediate  $Re$ , where the share of the Coriolis term in the total drag is up to 10% at the top of the roughness elements. Obviously, this assumption becomes even stronger in stratified conditions where the ABL height decreases in response to surface cooling. We intend here to also reach the regime of extreme stability where not only the scale separation shrinks and existence of a surface layer becomes questionable in general, but also the stability correction exceeds the order of one, which is a fundamental problem from the perspective of flux parameterization. Nonetheless, in the following, we stick to the common height range defined in terms of the friction thickness  $\delta_*$ , which requires caution when interpreting data for strongly stable cases at the larger end of the stability parameter ( $\zeta$ , defined below). In fact, ASL closures implied by MOST are ubiquitous in numerical models at all scales, and even if requirements are not fully met (e.g. for complex terrain, the non-stationarity of the ABL, etc.), observations confirm to the theory (Grachev et al. 2013; Stiperski and Calaf 2018).

Within the ASL, MOST implies that appropriately non-dimensionalized gradients of the horizontal wind speed,  $u_h(z) = \sqrt{\langle u \rangle^2 + \langle v \rangle^2}$ , and buoyancy,  $b(z)$ , depend on a non-dimensional height only, namely:

$$\zeta_i = \kappa_i(z - d_i)/L_O, \tag{11a}$$

(here the von Kármán constants are included, since  $L_O$  is formulated without). Based on the TKE equation,  $\zeta$  can be interpreted as a stability parameter representative of an eddy size beyond which stability effects exceed inertia. The index  $i$  corresponds to  $(\cdot)_m$  for momentum or  $(\cdot)_h$  for heat, reflecting the different von Kármán constants ( $\kappa_m = 0.42$ ,  $\kappa_h = 0.35$ ). KA24 found different displacement heights for momentum and heat, but an overall small dependence of the  $L_2$  error on the particular value. Here, we therefore stick to the common assumption  $d_h = d_m \equiv d$  and use  $d/H = 2/3$ . For the non-dimensionalized gradients  $\Phi_m(\zeta_m)$  and  $\Phi_h(\zeta_h)$  we obtain:

$$\frac{\kappa_m(z - d)}{u_\star} \sqrt{\left(\frac{\partial \langle u \rangle}{\partial z}\right)^2 + \left(\frac{\partial \langle v \rangle}{\partial z}\right)^2} = \Phi_m(\zeta_m), \tag{11b}$$

$$\frac{\kappa_h(z - d)}{b_\star} \frac{\partial \langle b \rangle}{\partial z} = \Phi_h(\zeta_h). \tag{11c}$$

The existence of such unique representations  $\Phi_i(\zeta_i)$  is understood to indicate the suitability of the assumptions of the constant-flux layer. The dependencies of  $\Phi_m$  and  $\Phi_h$  on  $\zeta_m$  and  $\zeta_h$ , respectively, describe the stability dependence of the velocity and scalar profiles. In neutrally stratified flow with  $\zeta_i = 0$  (since  $L_O \rightarrow \infty$ ), the logarithmic law of the velocity emerges with  $\Phi_m(\zeta_m = 0) = 1$ , whereas  $\zeta_i > 0$  for stably stratified flow. Based on observational studies, the Businger–Dyer relations (Businger et al. 1971; Dyer 1974; Garratt 1992):

$$\Phi_m(\zeta_m) = \alpha_m + \beta_m \zeta_m, \tag{12a}$$

$$\Phi_h(\zeta_h) = \alpha_h + \beta_h \zeta_h, \tag{12b}$$

are widely accepted for the weakly stable regime ( $\zeta_i \ll 1$ ). The empirical parameters are  $\alpha_m = 1$ ,  $\alpha_h = 0.74$  and  $\beta_m = \beta_h = 4.7$  (Högström 1988, 1996; commonly approximated with  $\beta_i \approx 5$ ).

We find reasonable agreement with these observational fits for stability corrections  $\zeta \lesssim 1$  (Fig. 11). As mentioned above, results for stronger stability should be interpreted with caution, which is in fact seen by an increased spread for higher stability and a systematic deviation from the ASL fits in Fig. 10.

This also agrees with previous DNS of Ekman flow over smooth surfaces (Ansorge and Mellado 2014; Shah and Bou-Zeid 2014; Ansorge 2019) and LES of Ekman flow with subsidence (Bon et al. 2024). The best fits for the non-dimensional gradients of wind speed and buoyancy are:

$$\Phi_m(\zeta_m) - \alpha_m = 5.3\zeta_m, \tag{13a}$$

$$\Phi_h(\zeta_h) - \alpha_h = 12.5\zeta_h, \tag{13b}$$

respectively, where we estimate  $\alpha_m = 0.89$  and  $\alpha_h = 0.72$  (cf. discussion in the Appendix 1). The analysis here is exempt from the exact value of the parameters  $\alpha_i$ . In terms of  $\zeta_m$ , we find  $\Phi_h(\zeta_m) - \alpha_h = 10.5\zeta_m$  for cases S001–S064. In many practical applications of ASL theory,  $\zeta_h$  is approximated by  $\zeta_m$  due to the lack of informative models for turbulent

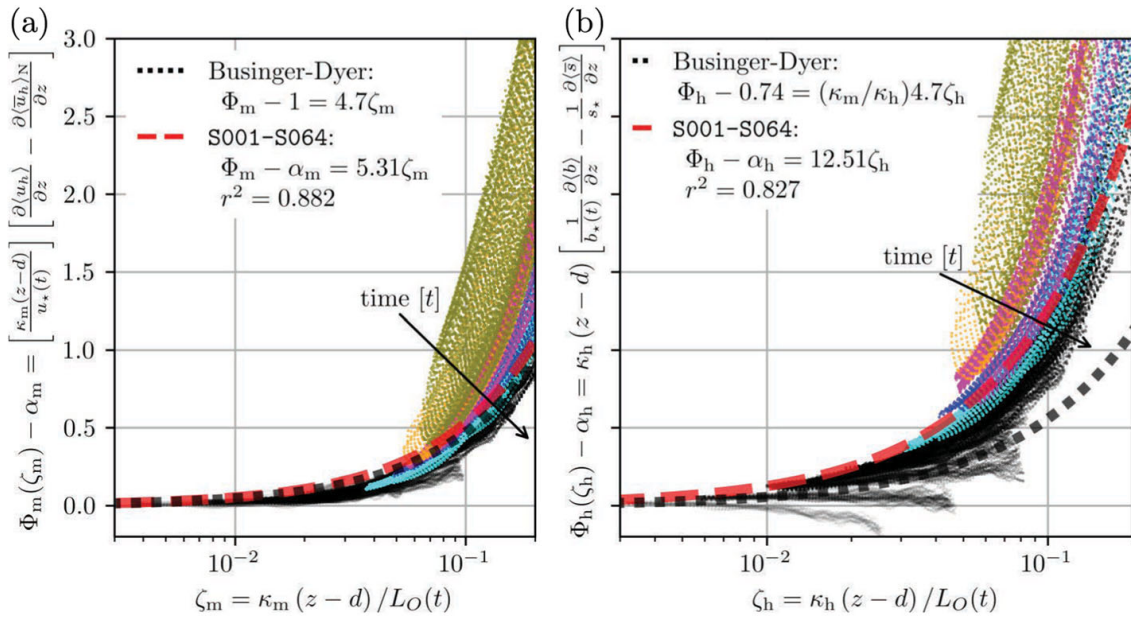


**Fig. 10** Non-dimensional gradients of the **a** horizontal velocity and **b** buoyancy, as a function of the stability parameter  $\zeta_m$ ,  $\zeta_h$ , according to (11). The data in the regime  $z_{\log,i}^+ \leq z^+ \leq 0.1Re_\tau$  is instantaneous and spatially averaged in the horizontal, while using the respective instantaneous friction values of  $u_*(t)$ ,  $b_*(t)$  (respectively  $s_*$  for the neutral case N) and the Obukhov length  $L_O(t)$ . The linear regression functions (red dashed lines, with the  $r^2$ -value, the coefficient of determination) are derived in consideration of the cases S001–S064 with a zero-plane displacement of  $d/H = 2/3$ . The arrows (*time*) depict the temporal evolution

diffusivity. We use  $d_h = d_m$ , which implies:

$$\Phi_h(\zeta_m) = \alpha_h + \frac{\kappa_h}{\kappa_m} \beta_h \zeta_m. \tag{14}$$

The data is fitted in the regime  $z_{\log,i}^+ \leq z^+ \leq 0.1Re_\tau$ , with the lower boundary of the logarithmic layer at  $z_{\log,i}^+ = 30 + d_i^+$  (KA24) and the commonly accepted limit of the upper boundary of the ASL with approximately 10 % of  $\delta_*$ .

Cases with stronger stability fall into the very stable regime where a linearization of the stability correction  $\Phi_m - \alpha_m$  (magenta, orange, olive coloured cases) is no longer appropriate (Mahrt 2014) for the limited extent of the ASL and large effects of stability. While outside the ASL in terms of strict criteria ( $\delta_{95}$ , cf. Fig. 6), the very stable data of the cases S128P–S256P show a distinct left curvature (cf. Anson 2019, Fig. 12). As the simulation time progresses, a tendency is observed to the right, closer to the linear fit, indicating that the left curvature for large values of the stability parameter ( $\zeta > 0.1$ ) is a transient effect reflecting the imbalance of the ABL with the surface boundary condition.

The linear fit of  $\Phi_m$  is very close to the widely-used Businger–Dyer relation, whereas  $\Phi_h$  does not agree. We attribute this disagreement to insufficient convergence, respectively, the nonequilibrium state of the data for large stratification, since the linear fit improves if only the weakly stable cases S001–S005 are considered ( $\beta_h = 4.9$ ). We further note that also Högström (1988) estimates  $\beta_h \approx 8$  after eliminating systematic errors from observational data.

For large stratification, the linear stability correction is known to deviate in the very stable regime, due to its highly non-stationarity (inertial oscillation, adaptation of the turbulent boundary layer to strongly modified surface boundary, intermittency) and strong turning of the wind within the substantially decreasing boundary layer thickness (Fig. 3). Moreover,

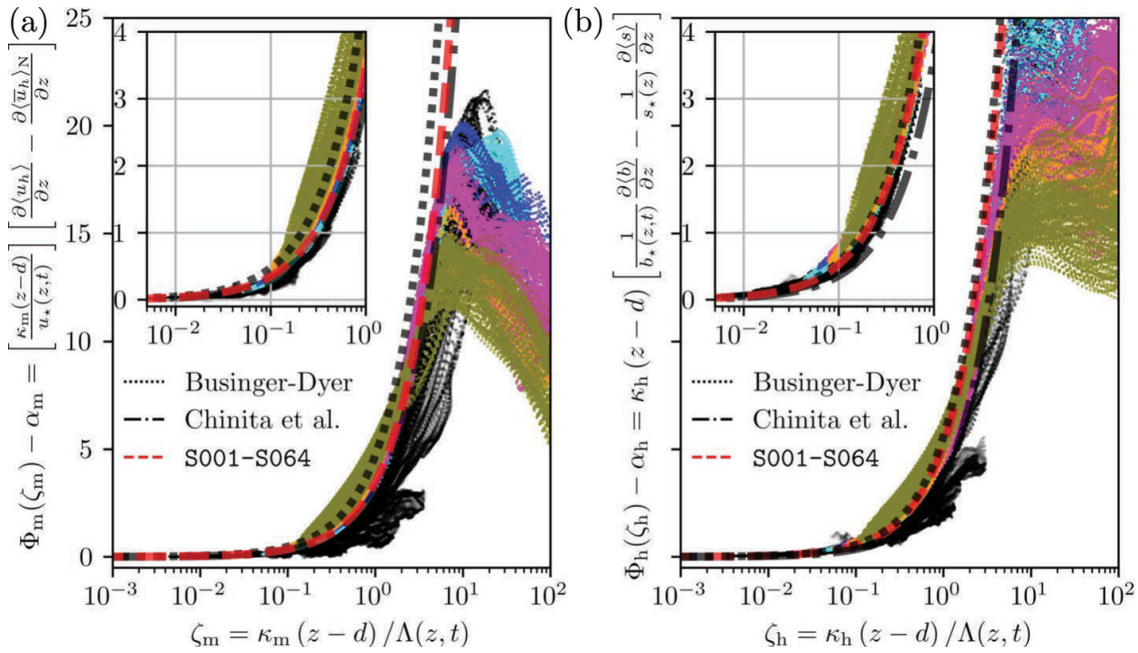


**Fig. 11** Similar to Fig. 10. Here, with the instantaneous and local (in the vertical) values of  $u_\star(z, t)$ ,  $b_\star(z, t)$ ,  $\Lambda(z, t)$ , according to the local theory of Nieuwstadt (1984). The close-up views and the similarity functions are fitted up to the height  $z^+ < 0.1\delta_\star$ , and data is plotted up to  $z^+ < 0.3\delta_\star$ . **a** Lines: Businger–Dyer relation,  $\Phi_m - 1 = 4.7\zeta_m$  (black dotted line); Chinita et al. (2022)  $\Phi_m - 1 = 3\zeta_m$  (black dot-dashed line); S001–S064,  $\Phi_m - \alpha_m = 3.45\zeta_m$  (red dashed line) with  $r^2 = 0.97$ . **b** Lines: Businger–Dyer relation,  $\Phi_h - 0.74 = 4.7\kappa_m\kappa_h^{-1}\zeta_h$  (black dotted line); Chinita et al. (2022),  $\Phi_h - 0.74 = 3\kappa_m\kappa_h^{-1}\zeta_h$  (black dot-dashed line); S001–S064  $\Phi_h - \alpha_h = 5.21\zeta_h$  (red dashed line) with  $r^2 = 0.981$

turbulence is observed to be highly anisotropic, respectively of non-Kolmogorov type (Stiperski and Calaf 2018). Then, the surface flux seems to be a relevant scaling parameter, and we follow the local scaling approach of Nieuwstadt (1984) (cf. Fig. 11), while using local values of the Obukhov length  $\Lambda(z, t)$  for the stability parameters  $\zeta_i$  and the local friction values  $u_\star(z, t)$ ,  $b_\star(z, t)$  for the stability functions  $\Phi_i$ . This approach yields a better collapse of the data compared to Fig. 10, since the scattering of data is significantly reduced. Chinita et al. (2022) proposes for the local MOST based on LES simulations the parameters  $\beta_i \approx 3$  (rather than  $\beta_i \approx 5$ ). Notably, the very stable cases do follow the proposed linear stability correction functions as well, even though, according to strict criteria, some values originate from above the ASL. Anyhow, the values of  $\beta_h$  in the weakly stable and moderately stable regimes are higher compared to the proposed value. Again, this is assumed to be related to limited simulation times and insufficient convergence.

In the context of the local scaling approach, the very stable cases indicate a right curvature of the data with respect to the linear fits, which is in accordance with observations (e.g. Cheng and Brutsaert 2005; Grachev et al. 2013, ). For  $\zeta_i \gg 1$  a *levelling-off* of  $\Phi_i$  (Fig. 11) is observed, while  $\Phi_m$  reaches a peak and continues with a negative slope and  $\Phi_h$  forms a plateau. Peak and plateau values of  $\Phi_i$  decrease with increasing stability of the cases. Mahrt (2007) links this characteristic with a simultaneous increasing stability and non-stationarity of the flow (wave-like, meandering motions) and thus an enhanced mixing efficiency. As a result, the slope  $\Phi_i$  decrease for large  $\zeta_i$ , whereas this behaviour is pronounced for momentum compared to buoyancy. However, the data are presented up to the upper bound  $0.3\delta_\star$ , which is outside the very stable boundary layer, measured in terms of  $\delta_{\star,95}$  (cf. Figure 6), and is thus associated with problems in LES and observations where the first model layer or the first



measurement point under strongly stable conditions could as well lie outside the boundary layer.

Surface roughness increases  $u_\star$  in comparison to a smooth surface with similar forcing of the flow. Hence, the scale separation measured in  $Re_\tau$  is enhanced, which results in a deeper logarithmic layer. As a consequence of the rise of  $Re_\tau$ , we observe a higher degree of consistency of our data for a wider range of stability in contrast to the smooth case at similar  $Re_D$  (cf. Ansorge 2019, Fig. 12). The induced growth in scale separation by roughness is counteracted by increasing stability, since it reduces the extent of the remaining logarithmic layer until a critical value, here  $Ri_A > 64$ , is reached from where measurements deviate from the theory.

## 4.2 Non-dimensional Gradients in the Roughness Region

The validity of MOST is limited to the inertial sublayer. Hence, classic surface-layer similarity only holds above the top of the roughness elements. This is in part for theoretical reasons, but also due to practical limitations, as in the field, it is virtually impossible to obtain data within small-scale roughness. Here, we briefly report on the scalings observed below the height of the roughness elements. In the lower part of the roughness region, i.e. below  $z^+ \approx 10$ , the velocity gradients appear to fall in a narrow band that grows linearly with distance from the wall (Fig. 12a). This suggests that the viscous law of the wall is appropriate here. The classical scaling  $u^+ = z^+$  would be re-covered if a truly wall-based velocity scale would be considered, i.e. if the friction velocity were calculated from the bottom shear alone. Near the top of roughness elements, the scaling is not universal and would need to include information on the velocity scale at the top of the roughness elements. Interestingly, the transition of the velocity profile to the different velocities in the outer region (higher for stronger stability) is mostly confined to the upper region of the roughness region, where a strong stability-dependence is observed. This dual behaviour suggests that it will not be possible to prescribe profiles in the roughness region by either a wall-based or a surface-layer-base scaling; instead, a complete description will need to resort to a mixed scaling incorporating information from the friction at the top of the roughness elements and the friction at the actual domain bottom. The partitioning of friction between the top of roughness elements and the actual domain bottom is hence a key parameter to determine the dynamics within the roughness region.

The scalar profiles show a similar duality suggesting wall-based scaling below  $z^+ \approx 10$  and profile-dependency above. Interestingly, there is a maximum in the scalar gradient around  $z^+ \approx 10$  and a plateau and collapse of data (cases S001–S064) for the non-dimensional buoyancy gradients (Fig. 12b). The plateau is located above the viscous sublayer  $z^+ > 5$  and below the lowest roughness elements, here limited to  $z^+ < 20$  with a value of 0.76, which is close to  $\alpha_h$ . This maximum of the gradient is related to a local minimum of turbulent scalar transport, and we suppose it is due the separation of the mixing at the roughness tops from the mixing at the domain bottom. Apparently, this separation is stronger for buoyancy (which shows a local maximum) than it is for momentum (which only shows a right curvature in the profile at the respective height). This difference underlines the critical role of pressure (blocking) effects in the roughness region which are the root cause for differences between scalar and momentum quantities and cause a stability and height-dependence of the turbulent Prandtl number (cf. Sect. 4.4).

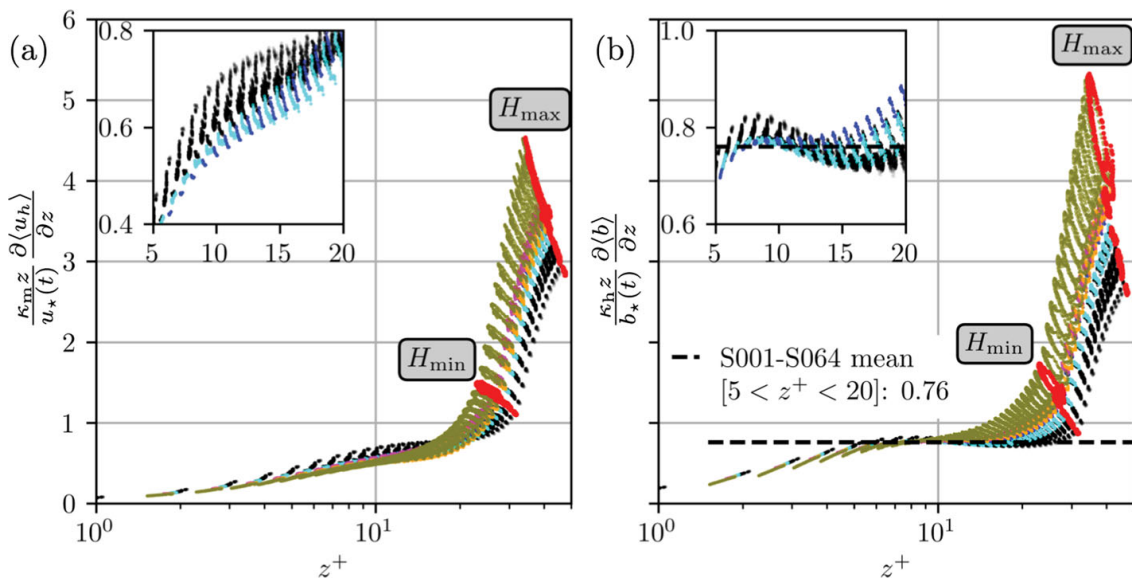


**Fig. 12** Non-dimensional gradients of the **a** horizontal velocity and the **b** buoyancy within the reach of the roughness elements ( $H_{min}$  and  $H_{max}$  depict the distribution of roughness element heights, red markers), plotted against the vertical distance in viscous units  $z^+$ . The presented data is instantaneous and horizontally averaged, while using the respective instantaneous values of  $u_*(t)$ ,  $b_*(t)$ . **b** The mean value is derived in consideration of the cases S001–S064 in the range  $5 < z^+ < 20$

### 4.3 Reynolds Number Effects on the ASL Similarity

ASL theory commonly neglects viscous effects for the very high Reynolds number encountered in geophysical problems. For typical scales of the neutral ABL, the magnitude of  $Re_{ABL}$ , indicative of the scale separation in a neutrally stratified atmosphere, is  $\mathcal{O}(10^8)$  (Mellado et al. 2018). With increasing stability and thus decreasing depth of the ABL (cf. Figure 3a), the relevant scale separation  $Re_{ABL}$  is reduced and viscous effects may matter, at least to some extent. For the intermediate Reynolds number of our setup ( $Re_\tau \approx 1800\text{--}2700$ ), we expect viscous stress to be non-negligible in the ASL theory at strong stability. While this is not necessarily the case in atmospheric conditions, we need to consider those viscous effects to allow for an uncontaminated formulation of the similarity theory with respect to the actual geophysical scale separation. We, however, note that close to the surface these effects also occur in the atmosphere which may be relevant for some very high-resolution LES studies with resolutions on the sub-metre scale. Further, this section makes use of the common assumption that it is the total stress, total vertical gradient and total horizontal velocity which scale in the context of surface-layer similarity. While this is certainly an increasingly strong assumption for stratified flow, it is consistent with the way in which surface-layer similarity is commonly applied.

The total stress  $\tau_{tot}$  in the boundary layer is composed of the viscous and turbulent stress, which in our non-dimensionalized formulation reads as:

$$\tau_{\star,tot} = \tau_{\star,visc} + \tau_{\star,turb} = \frac{1}{Re_\Delta} \frac{\partial \langle u_h \rangle}{\partial z} + \sqrt{\langle u'w' \rangle^2 + \langle v'w' \rangle^2}. \tag{15a}$$

Here, we consider the horizontal velocity and total vertical flux, since the veering of the wind within the surface layer is substantial. Commonly, the turbulent stress is modelled with the eddy viscosity approach introduced by Boussinesq (cf. Sect. 3.4.1 on p.171, Rotta 1972),



where the turbulent flux is related to the local vertical mean gradient, given by:

$$\tau_{\star, \text{turb}} = -K_{\star, m} \frac{\partial \langle u_h \rangle}{\partial z}, \tag{15b}$$

$$\text{with: } K_{\star, m} = l_{\star, m}^2 \frac{\partial \langle u_h \rangle}{\partial z}. \tag{15c}$$

The eddy viscosity  $K_{\star, m}$  is modelled with the mixing length  $l_{\star, m}$ , where the simple relation  $l_{\star, m} = \kappa_m z$  (Prandtl 1925) is used. Therefore,  $K_{\star, m}$  is the eddy viscosity non-dimensionalized by  $G \Lambda_{Ro}$ , and not constant but rather a function of time and space. The non-dimensionalized total shear stress  $\tau_{\star, \text{tot}}$  (15a) is given by:

$$\tau_{\star, \text{tot}} = \frac{\partial \langle u_h \rangle^+}{\partial z^+} + (\kappa z^+)^2 \left( \frac{\partial \langle u_h \rangle^+}{\partial z^+} \right)^2 = \frac{\partial \langle u_h \rangle^+}{\partial z^+} + [\Phi_{m, \text{cor}}(\zeta_m)]^2, \tag{15d}$$

whereas  $\Phi_{m, \text{cor}}$  is the stability function (11b) corrected by the viscous stress and hence,

$$\Phi_{m, \text{cor}}(\zeta_m) = \Phi_m(\zeta_m) - \sqrt{\frac{\partial \langle u_h \rangle^+}{\partial z^+}} = \alpha_m + \beta_{m, \text{cor}} \zeta_m. \tag{16a}$$

In this reading,  $\Phi_{m, \text{cor}}$  corresponds to the actual non-dimensional gradient in the context of similarity theory and  $\Phi_m$  corresponds to the classic estimate used above.

Hence, we expect that the corrected coefficient  $\beta_{m, \text{cor}}$  matches better field observations where viscous effects are smaller than in our DNS.

Analogously, the viscous correction approach is applied on the stability function  $\Phi_h$  (11c) for buoyancy, with:

$$\Phi_{h, \text{cor}}(\zeta_h) = \Phi_h(\zeta_h) - \sqrt{\frac{\partial \langle b \rangle^+}{\partial z^+}} = \alpha_m + \beta_{h, \text{cor}} \zeta_h. \tag{16b}$$

Our findings (Fig. 13) are in accordance with ( Chung and Matheou 2012, § 4.4); with decreasing Reynolds number and thus increasing stability (cf.  $u_\star$  in Fig. 3a), a shift of the data to the left is observed.

For decreasing Reynolds numbers, the stability parameters  $\beta_i$  are enhanced compared to the atmospheric value  $\beta_i = 4.7$  (similar characteristic is observed in the study of Shah and Bou-Zeid 2014, ). Here, we measure  $\beta_{m, \text{cor}} = 4.88$  instead of  $\beta_m = 5.31$  (Fig. 10a) and  $\beta_{h, \text{cor}} = 11.7$  instead of  $\beta_m = 12.51$  (Fig. 10b). The relative importance of the viscous correction term in the regime  $\zeta_i < 0.1$  is up to approximately 25%. Near surface data of the *corrected* stability functions  $\Phi_{i, \text{cor}}$  for the cases S064–S256P reveal a better collapse of data with the weakly stable cases (grey to black data points in Fig. 13), observable in the region  $0.04 \lesssim \zeta_i \lesssim 0.08$ .

Högström (1988) proposed a second-order regression for the weakly stable regime ( $\zeta_i \ll 1$ ) up to a threshold  $\zeta_i = \zeta_{i, 1}$  ( $\zeta_{m, 1} = 0.15$  and  $\zeta_{h, 1} = 0.2$ ), above which the common linear regression (12a) is valid. This approach improves the fit in the region  $\zeta_i < 0.1$ , since the linear regression systematically overestimates the data (Fig. 13). The best quadratic fits based on the cases S001–S064 in the region  $z_{\log, i}^+ \leq z^+ \leq 0.1 Re_\tau$  are:

$$\Phi_m(\zeta_m) - \alpha_m = 2.41 \zeta_m + 16.48 \zeta_m^2, \tag{17a}$$

$$\Phi_h(\zeta_h) - \alpha_h = 4.66 \zeta_h + 55.84 \zeta_h^2. \tag{17b}$$

We observe a larger scatter and stronger curvature of the data to the left for  $\Phi_h$  (cf. Figures 10b, 13b) compared to  $\Phi_m$  (Fig. 13b) and hence, estimate a large quadratic term which deviates

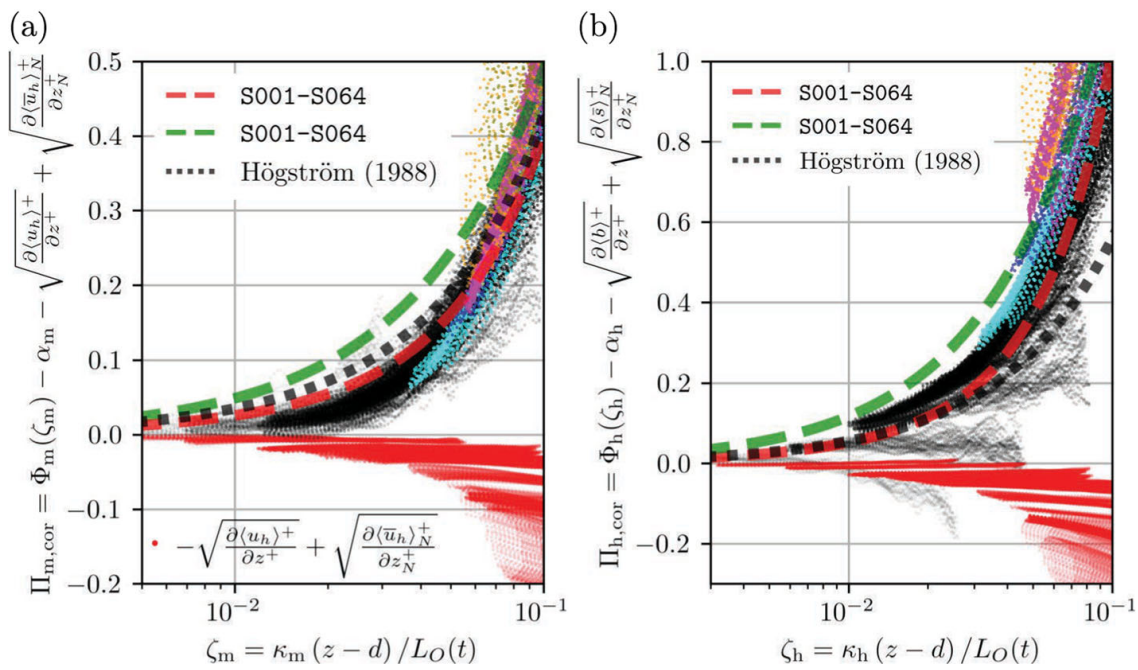


**Fig. 13** Similar to Fig. 10, with the viscous correction (magnitude of the correction depicted with red data points) with  $\Pi_{i,cor} = \Phi_{i,cor}(\zeta_i) - \alpha_i$ . Only the weakly stable regime is shown for  $\zeta_i < 0.1$ . Nevertheless, the regression lines (green and red dashed lines) are computed for  $z^+ < 0.1\delta_*$ . **a** Lines: S001-S064,  $\Phi_m - \alpha_m = 2.41\zeta_m + 16.48\zeta_m^2$  with  $r^2 = 0.948$  (red dashed line); S001-S064,  $\Phi_m - \alpha_m = 4.88\zeta_m$  with  $r^2 = 0.865$  (green dashed line); Högström (1988),  $\Phi_m - 1 = 3.43\zeta_m + 8.4\zeta_m^2$  (black dotted line). **b** Lines: S001-S064,  $\Phi_h - \alpha_h = 4.66\zeta_h + 55.84\zeta_h^2$  with  $r^2 = 0.929$  (red dashed line); S001-S064,  $\Phi_h - \alpha_h = 11.7\zeta_h$  with  $r^2 = 0.818$  (green dashed line); Högström (1988),  $\Phi_h - 0.95 = 5.24\zeta_h + 6.3\zeta_h^2$  (black dotted line)

from the fits in the literature. In comparison, the quadratic fits according to Högström (1988) are  $\Phi_m - (1 \pm 0.018) = (3.34 \pm 0.32)\zeta + (8.4 \pm 5.9)\zeta^2$  and  $\Phi_h - (0.95 \pm 0.039) = (5.24 \pm 0.64)\zeta + (6.3 \pm 11.8)\zeta^2$ , with standard error estimates (for  $\zeta_i \leq 0.1$ ). In their study, they claim that the data base for  $\Phi_h$  is also less clear.

#### 4.4 Dependence of the Richardson and Turbulent Prandtl Numbers on Stability

The Richardson flux and gradient numbers  $Ri_f$  and  $Ri_g$  (10) are, in addition to the Monin–Obukhov stability parameter  $\zeta_i$ , decisive measures of the flow stability and can be defined as (Stull 1988; Coleman et al. 1992):

$$Ri_f = \frac{\langle w'b' \rangle}{\langle u'w' \rangle (\partial \langle u \rangle / \partial z) + \langle v'w' \rangle (\partial \langle v \rangle / \partial z)} = \frac{\zeta_m}{\Phi_m}, \tag{18a}$$

$$Ri_g = \frac{\zeta_m \Phi_h}{\Phi_m^2}, \tag{18b}$$

where  $Ri_g = N^2/S^2$  is the ratio of the buoyancy, respectively the Brunt–Väi-sä-lä frequency  $N$  and the shear frequency  $S$ . The Richardson flux number is the ratio of the TKE destruction (production) by buoyancy to the TKE production by shear and is a key parameter for turbulence closure schemes (cf. Mellor and Yamada 1974, 1982, ). The ratio of Richardson

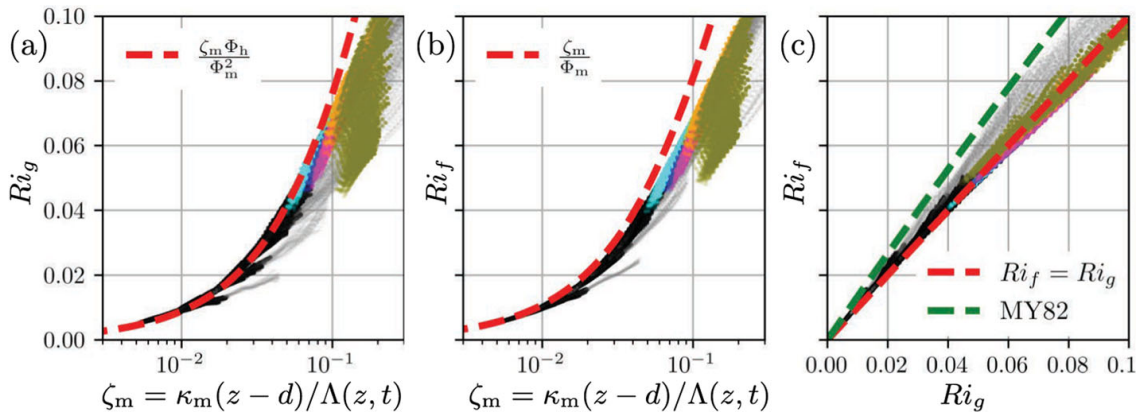


**Fig. 14** **a, b** The gradient and flux Richardson numbers  $Ri_g(\zeta_m)$ ,  $Ri_f(\zeta_m)$  as functions of the local stability parameter  $\zeta_m$  and **(c)** the Richardson flux number  $Ri_f(Ri_g)$ . The parameters of the stability functions  $\Phi_i$  in **(a, b)** from Fig. 11, the green curve in **(c)** after Mellor and Yamada (1974, 1982) (MY82) with  $Ri_f = 0.725 \left[ Ri_g + 0.186 - \left( Ri_g^2 - 0.316 Ri_g + 0.0346 \right)^{1/2} \right]$ . The coloured data is plotted within the constant-flux layer located in the region between the peak of the total turbulent flux  $\max\{\sqrt{\langle u'w' \rangle^2 + \langle v'w' \rangle^2}\}$  and where the flux is reduced by 10 % (Stull 1988). Light grey data in is plotted in the region  $z_{\log,i}^+ \leq z^+ \leq 0.1 Re_\tau$

numbers  $Ri_g/Ri_f$  forms the turbulent Prandtl number  $Pr_t$ , given by:

$$Pr_t = \frac{Ri_g}{Ri_f} = \frac{(\partial \langle b \rangle / \partial z) [\langle u'w' \rangle (\partial \langle u \rangle / \partial z) + \langle v'w' \rangle (\partial \langle v \rangle / \partial z)]}{\langle w'b' \rangle [(\partial \langle u \rangle / \partial z)^2 + (\partial \langle v \rangle / \partial z)^2]} = \frac{\Phi_h}{\Phi_m} = \frac{\tilde{K}_{\star,m}}{K_{\star,h}}. \quad (19)$$

The turbulent Prandtl number  $Pr_t$  describes the difference in eddy viscosity  $\tilde{K}_{\star,m}$  and diffusivity  $K_{\star,h}$ , i.e. the difference in turbulent mixing of momentum and heat (cf. review by Li 2019, ). In (19), we follow the approach of Coleman et al. (1992) for  $\tilde{K}_{\star,m}$  which differs from the previous definition of  $K_{\star,m}$  in (15c). We define the dimensionless numbers (18, 19) by considering the veering of the wind (coordinate system rotation) within the surface layer, since the lateral  $v$ -velocity component is nonzero for an Ekman flow.

The Richardson numbers in Fig. 14a, b increase with the stability parameter  $\zeta_m$  and follow the proposed scaling approaches (red dashed lines), while a systematic shift of the data to the right is observed at higher stabilities.

This overestimation of  $Ri_g$ ,  $Ri_f$  is assumed to originate from the deviation of the linear stability functions and data in Fig. 11 at large  $\zeta_i$ . Within the considered regime  $Ri_g \leq 0.1$ , the dependence of  $Ri_f(Ri_g)$  is linear ( $\mathcal{O}(Ri_f/Ri_g) = 1$ , cf. Figure 14c). The linear dependence of  $Ri_f(Ri_g)$  for small  $\zeta_m$  is in agreement with previous studies, e.g. Pardyjak et al. (2002) reports an increase of  $Ri_f$  with  $Ri_g$  until  $Ri_g \approx 1$  and subsequently a levelling-off of  $Ri_f$  with a maximum of approximately 0.4 – 0.5 (cf. also Fig. 9, in Grachev et al. 2013, ). This characteristic can not be approved with our data, since the scatter of data is large outside the ASL for MOST. We observe an overestimation of  $Ri_f$  by the parameterization of Mellor and Yamada (1974, 1982) of  $\approx 20\%$ .

The turbulent Prandtl number data as a function of the stability in the regime  $z_{\log,i}^+ \leq z^+ \leq 0.1 Re_\tau$  exhibits a large scatter (Fig. 15).

If the turbulent Prandtl number is considered in the constant-flux layer (validity region of MOST), or merely at the lower bound at  $z^+ = 50$  where the vertical turbulent flux tends to peak (red data points in Fig. 15),  $Pr_t$  increases with stability (similar for  $Pr_t(Ri_f)$ , not shown here) with a neutral value of  $Pr_{t,0} = Pr_t|_{Ri_g=0} \approx 0.94$  and hence, the surface-layer

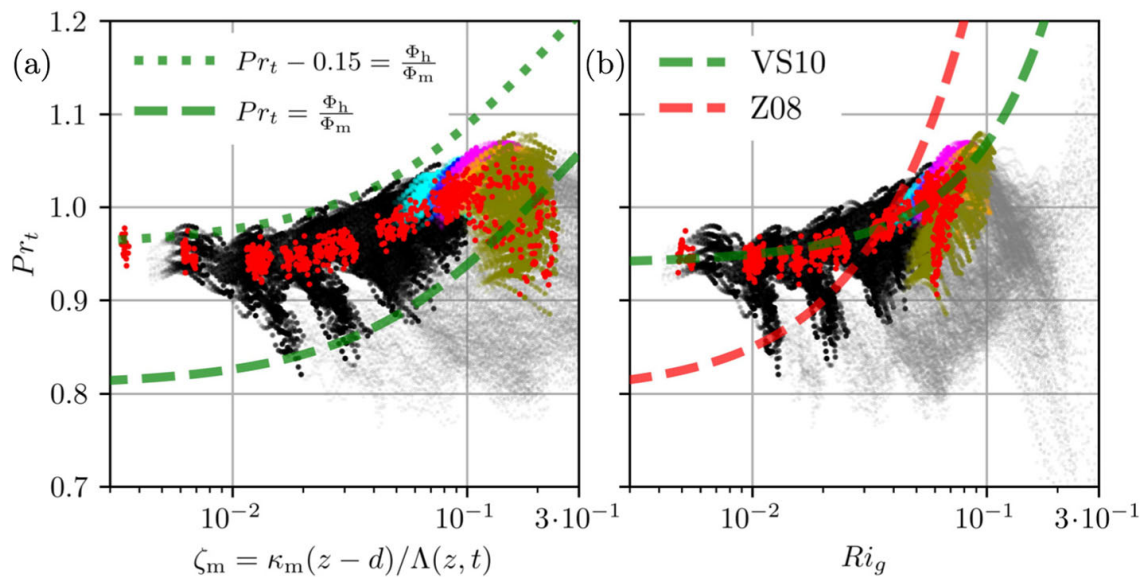


**Fig. 15** **a** Turbulent Prandtl number  $Pr_t(\zeta_m)$ , with the parameters of the stability functions  $\Phi_i$  from Fig. 11. **b**  $Pr_t(Ri_g)$  vs. stability ( $Ri_\Delta$ ), with the fit (green line) based on (20) (cf. Equation 3.6, Venayagamoorthy and Stretch 2010, (VS10)) and the fit (red line) based on (Zilitinkevich et al. (2008), (Z08)) with  $Pr_t = 0.8 + 5Ri_g$ . The data shown here is similar to Fig. 14 and red data points are located at  $z^+ = 50$

data is located between the envelopes  $Pr_t = \Phi_h/\Phi_m$  and  $Pr_t - 0.15 = \Phi_h/\Phi_m$  (Fig. 15a). The  $Pr_t(Ri_g)$  model of Venayagamoorthy and Stretch (2010) (their Eq. 3.6), which is refined from Schumann and Gerz (1995) (their Eq. 22), takes the form of:

$$Pr_t = Pr_{t,0} \exp\left(-\frac{Ri_g}{Pr_{t,0} Ri_{f,\infty}} + \frac{Ri_g}{Pr_{t,0}}\right) + \frac{Ri_g}{Ri_{f,\infty}}, \tag{20}$$

with  $Ri_{f,\infty} = Ri_f|_{Ri_g=\infty}$ . The model (20) shows surprisingly good agreement with our data (Fig. 15b), with  $Pr_{t,0} = \lim_{Ri_g \rightarrow 0} Pr_t(Ri_g) = 0.15 + \alpha_h/\alpha_m \approx 0.94$  and  $Ri_{f,\infty} = \lim_{Ri_g \rightarrow \infty} Ri_f(Ri_g) = \beta_m^{-1} \approx 0.29$ . Further, Zilitinkevich et al. (2008) propose the relation  $Pr_t \approx Pr_{t,0} + 5Ri_g$ , with the asymptote  $Pr_{t,0} \approx 0.8$ , based on measurement campaigns, experimental and modelling results. In contrast to the previous model (20) this overestimates our data for large  $Ri_g$ , and underestimates for small  $Ri_g$ . The increasing behaviour of  $Pr_t$  with increasing stability is supported by the findings of Mauritsen and Svensson (2007), where they find finite values of the momentum flux and zero values of the heat flux for  $Ri_g \gg 1$ . The asymptotical behaviour of  $Pr_t$  for small  $\zeta$  is  $Pr_{t,0} \sim \alpha_h/\alpha_m$  ( $z$ -less stratification, Wyngaard 1973) and therefore, 0.74 for Businger et al. (1971) and 1.0 for Dyer (1974). Townsend (1976); Yakhot and Orszag (1986) predict a neutral value of  $\approx 0.7$  and Schumann and Gerz (1995) expect values between 0.7 and 1.2. The asymptotical value of  $Ri_{f,\infty}$  is according to Nieuwstadt (1984) 0.2 and Schumann and Gerz (1995) 0.25 and hence, our values of  $Pr_{t,0}$ ,  $Ri_{f,\infty}$  fit well with those of the literature.

The dependence of the Prandtl number in the stable regime is controversial. A major challenge, apart from the large scatter of measurement data, is self-correlation of  $Pr_t$  with the stability measures, due to shared variables (e.g. velocity and buoyancy gradients are present in  $Pr_t$  and  $Ri_g$ , cf. discussions in Grachev et al. (2007); Mahrt (2007); Anderson (2009); Sorbjan and Grachev (2010). Mahrt (2007) points out the importance of non-stationarity in the VSBL, where non-turbulent motions (e.g. wave-like, meandering motions) transport

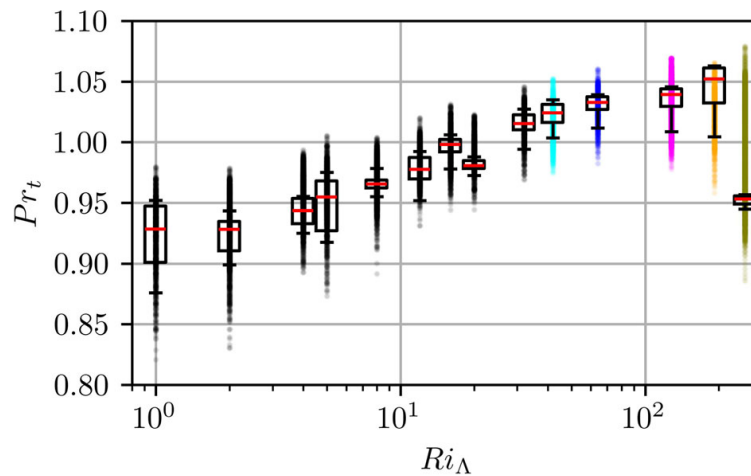


**Fig. 16** The turbulent Prandtl number  $Pr_t(Ri_A)$  as a function of the external stability parameter  $Ri_A$  (4c). The data points are in the constant-flux layer and the box plots are derived from the data shown here

momentum more efficiently than heat, suggesting an increase of the turbulent Prandtl number with stability. This behaviour is supported by the ratio  $Ri_g/Ri_f$ , since  $Ri_f$  is assumed to reach a constant, whereas  $Ri_g$  increases. Howell and Sun (1999) observed  $Pr_t(\zeta) \approx 1.0$  for  $10^{-2} < \zeta < 10^1$ , with a large scatter in the data similar to Yagüe et al. (2001), where an exact dependence of  $Pr_t$  on  $\zeta$  remains uncertain. Whereas Yagüe et al. (2001) reports an increase of  $Pr_t(Ri_g)$  at  $Ri_g \gtrsim 0.1$ . Sorbjan and Grachev (2010) found a neutral value  $Pr_{t,0} = 0.9$  and a slight decrease with  $Ri_g$  to 0.7, after neglecting outliers in  $Ri_g$  from the analysis.

To circumvent self-correlation, Grachev et al. (2007) considers the  $Pr_t$  as a function of the Richardson bulk number  $Ri_B$  (cf. their Eq. 6 for the bulk Richardson number  $Ri_B$ ) and finds a decrease with stability. Anderson (2009) proposed a self-correlation free method and observes an increase of the Prandtl number as a function of the gradient Richardson number  $Pr_t(Ri_g)$ . In our simulations, the turbulent Prandtl number  $Pr_t(Ri_A)$  in the surfaces layer increases as a function of the external Richardson number  $Ri_A$  (4c, Fig. 16), contrasting the results of Grachev et al. (2007).

While the data for  $Pr_t$  presented in this study (Figs. 15, 16) exhibit a substantial scatter, we find that  $Pr_t$  increases in the constant-flux layer with any of the stability measures  $Ri_g$ ,  $Ri_f$ ,  $\zeta_m$ ,  $Ri_A$ . The most stable, intermittently turbulent case S256P shows a different behaviour, which is related to the large imbalance in TKE; in fact, this case features such a thin boundary layer that it is not possible to identify a surface layer by strict criteria.

## 5 Discussion and Conclusions

We investigate the competing interaction of small-scale surface roughness and stable stratification on ASL similarity using idealized DNS of turbulent Ekman flow. The surface roughness is fully resolved with an immersed boundary method (ADR IBM) and the flow is driven with an identical large-scale forcing for all cases. On the lower boundary there are  $56 \times 56$  rectangular blocks with a certain degree of randomness in structure and layout, which leaves the setup under neutral stratification on the verge of the transitionally to fully rough regime, with  $z_0^+ \approx 2$ . The stability of the flow is incrementally increased in 12 steps to cover the full span of the stability regime, from the WSBL to the VSBL at meaningful scale separation (high



Reynolds number in DNS context,  $Re_{\tau,N} \approx 2700$ ,  $Re_D = 1000$ ). We now conclude with respect to the research questions posed in Sect. 1.

(1) *The presence of small-scale surface roughness extends the stability regime, where turbulence is in a continuous state.* Roughness is observed to be a very effective triggering mechanism of turbulence by inducing flow instabilities, since flow around objects with sharp edges creates detached eddies and turbulent mixing. This enhances the production of TKE in the ASL and counteracts the suppression of turbulence by buoyancy. The WSBL regime is extended, which is characterized by a decreasing boundary layer depth and a continuous state of turbulence. This gives rise to a pronounced plateau of the vertically integrated buoyancy flux (MSHF concept) over an extensive stability regime. The regime transition from the WSBL to the VSBL manifests itself in distinct oscillations of global flow properties with decaying amplitude in time, such as  $u_\star$  and  $L_O^+$ . At the transition to the VSBL, where a drastic decrease of turbulence is observable, buoyancy is dominating with  $L_O \lesssim \delta_{95}$ ,  $Ri_{B,95} \approx 1$  and where  $L_O^+$  gets close to  $Re_{L,crit}$ .

(2) *Global intermittency is an inherent characteristic of the rough VSBL.* In the presence of surface roughness, global intermittency in the VSBL is successfully simulated and observed to appear in space (across the boundary layer) and time (oscillating intensity). In this study, it was not possible to completely laminarize the flow at very strong stability. We therefore assume that the intermittency in the VSBL over heterogeneous surfaces lasts over a broader stability range than in the VSBL over smooth surfaces, where complete laminarization of the flow occurs for smaller values of stable stratification. This is supported by observation of intermittency in the real-world SBL, since the atmospheric Reynolds number is large, the Earth's surface is rough and hence, a complete laminarization is not observed. Here, further investigation would shed light on the intermittency phenomenon over rough surfaces.

(3) *Turning of the wind is enhanced in the rough VSBL and an appropriate boundary layer depth scale is  $\delta_{\star,95}$ .* The turning of the surface wind with respect to the geostrophic wind is enhanced by roughness. In the VSBL values of  $\alpha_\star > 90^\circ$  are observed for case S256P, which exceeds by far the laminar limit of  $\alpha_\star = 45^\circ$  for an Ekman flow. The proposed mechanism is based on the momentum balance within the surface roughness. With increasing stability, the velocity is reduced and so are the Coriolis and friction force. Eventually, the wind turns in favour of the pressure gradient force, resulting in a large  $\alpha_\star$ , which we suggest as the reason for pressure-driven channeling in more complex situations. With increasing stratification, the boundary layer thickness decreases: When comparing the neutral case N and the very stable case S256P,  $\delta_\star$  is reduced by approximately 30 %,  $\delta_{\star,95}$  by 90 %, which changes their ratio from  $\delta_{\star,95}/\delta_\star \approx 0.55$  in the neutral regime to  $\approx 0.08$  in the VSBL. Both visual inspection of the flow and scaling of global stability measures, such as  $Ri_{B,95}$ ,  $L_O/\delta_{95}$  suggest that the boundary layer depth  $\delta_{\star,95}$  is an appropriate scale in case of stable stratification rather than the scale  $\delta_\star$ .

(4) *Surface layer similarity holds in the known limits for the cases S001–S064.* With the displacement height  $d/H = 2/3$ , von Kármán constants of heat and momentum  $\kappa_m = 0.42$ ,  $\kappa_h = 0.35$ , we estimate the following parameters of the linear MOST correction functions:  $\alpha_m = 0.89$ ,  $\alpha_h = 0.72$  and  $\beta_m = 5.3$ ,  $\beta_h = 12.5$ . In contrast to classical MOST, local similarity theory results in a more accurate collapse of the data onto the linear fit, with slope parameters of  $\beta_m = 3.45$ ,  $\beta_h = 5.21$ . For large stability values, we observe a levelling-off of the stability correction, which is in accordance with observations. Viscous effects impact ASL theory, due to the present intermediate Reynolds number compared to the atmospheric one. Hence, we propose a viscous correction method for the MOST and reveal, that fitting parameters converge closer to the observational values. Furthermore, based on the current data, we observe that a linear stability correction function is overestimating for small and



underestimating for large stabilities ( $\zeta$ ). Here, a quadratic fit in the WSBL regime seems to improve the collapse of data, in agreement with the fits derived by Högström (1996) based on observational data.

Regarding the controversial discussion on the turbulent Prandtl number  $Pr_t$  and its dependence on stability (e.g.  $\zeta$ ,  $Ri_f$ ,  $Ri_g$ ), –despite substantial scatter–we observe an increase with stability and a neutral value of  $Pr_{t,0} \approx 0.94$ .

In summary, we provide a setup consistently treating outer dynamics in the boundary layer (i.e. the rotation, and associated triadic balance in Ekman flow), the turbulent mixing in the logarithmic layer and the immediate interaction with the surface through a roughness layer and viscous sublayer. While this requires substantial numerical resources on the largest supercomputers, it yields valuable insight to the boundary-layer dynamics. Based on an analysis of well-known surface-layer scaling relations, we show that roughness helps to maintain turbulence and shifts the stability regimes to higher stratification (cf. 1), that global intermittency is an intrinsic characteristic, also of the rough boundary layer (cf. 2), that stratification and roughness together can cause over-veering of the wind (cf. 3). The agreement of results from such a strongly idealized setup with MOST and the semi-empirical fits based on field observation demonstrates the consistency of our setup and its relevance for atmospheric conditions when the data is scaled properly. Indeed, the results underline the potential of such idealized setup to further address open questions regarding land–atmosphere interactions on the process-level, for the first time also including processes in the roughness sublayer.

## Appendix 1: Determination of the Stability Functions for Neutral Stratification

The linear stability correction functions (12a) reduce to  $\Phi_i|_{\zeta_i=0} = \alpha_i$  at neutral stratification. Based on theory, the empirical parameter for momentum  $\alpha_m$  is equal to unity in order to retain the logarithmic law of the wall for the mean velocity. For buoyancy, the parameter  $\alpha_h$  equals the ratio of the von Kármán constants of heat and momentum  $\alpha_h = \kappa_h/\kappa_m$  (Brutsaert 1982; Cheng and Brutsaert 2005), or it is interpreted as  $\alpha_h = \alpha_m/(K_h/K_m)$ , depending on the ratio of the eddy diffusivities  $K_h$ ,  $K_m$ . For momentum, the common value in the literature is  $\alpha_m = 1$ , while the picture is less clear for buoyancy. Cheng and Brutsaert (2005) proposed equal values for the von Kármán constants and therefore  $\alpha_h = 1$  (the so-called Reynolds analogy, namely equal transport properties for heat and momentum), Businger et al. (1971) give  $\alpha_h = 0.74$  and Högström (1988) gives  $\alpha_h = 0.95$ . However, Businger et al. (1971) corrected the value of the commonly accepted von Kármán constant  $\kappa_m = 0.4$  to  $\kappa_m = 0.35$  to obtain  $\alpha_m = 1$  instead of  $\alpha_m = 1.15$  and used  $\kappa_m = \kappa_h$  and argued that the eddy diffusivities are different for heat and momentum.

The empirical slope parameters  $\beta_i$  from Sect. 4.1 with  $\beta_m = 5.31$ ,  $\beta_h = 12.51$  are taken to estimate the parameters  $\alpha_i$  with a least squares fit within the constant-flux layer for the cases S001–S064, where MOST is valid (cf. Fig. 17).

With this approach, we estimate  $\alpha_h = 0.72$ , which is similar to the common literature value, and  $\alpha_m = 0.89$ , which does not fit the expected value of unity.

Here, we do not follow the approach by Businger et al. (1971) to correct the von Kármán constants to gain  $\alpha_m = 1$ . We take the carefully estimated values of the von Kármán constants from KA24 at neutral stratification, namely  $\kappa_m = 0.42$ ,  $\kappa_h = 0.35$  and assume that these are universal, since the flow type is unchanged between the current study and KA24. The

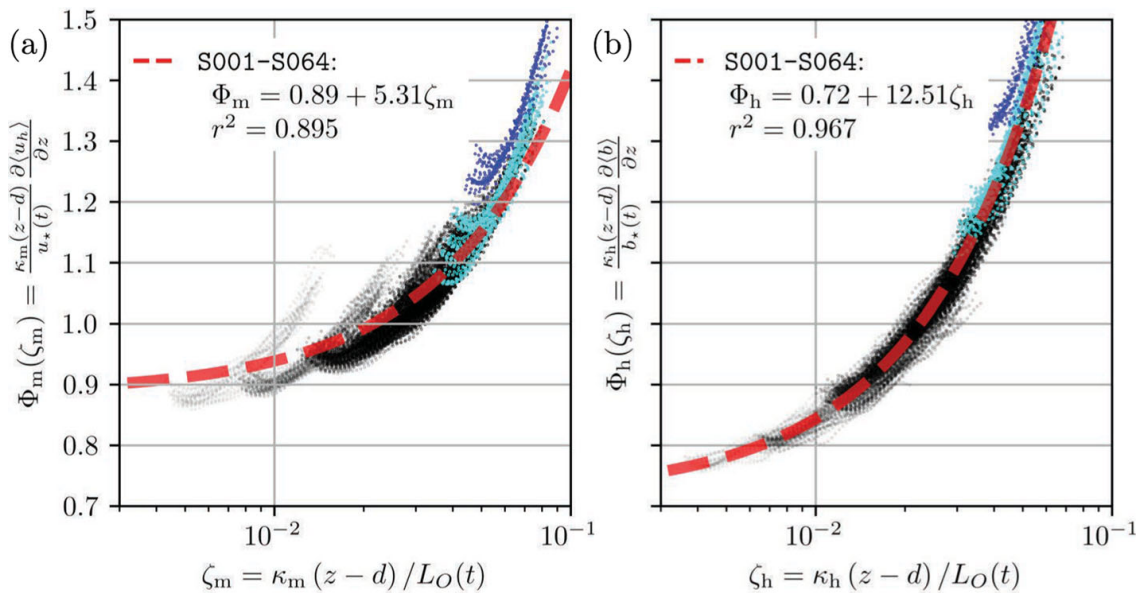


**Fig. 17** Stability correction functions  $\Phi_i(\zeta_i)$  for the cases S001–S064. The data is plotted within the constant-flux layer located in the region between the peak of the total turbulent flux  $\max\{\sqrt{\langle u'w' \rangle^2 + \langle v'w' \rangle^2}\}$  and where the flux is reduced by 10% (Stull 1988). The linear regression lines (red dashed lines) are derived with the slope parameters  $\beta_i$  from Sect. 4.1

analysis concerning the MOST in the current study is exempted from the precise values of  $\alpha_i$  through removing the neutral share of the dimensionless gradients.

**Acknowledgements** We are grateful for the invaluable insights provided by Prof. B. J. H. van de Wiel and two anonymous reviewers, which shaped and improved this article. Simulations were performed on the resources of the High-Performance Computing Center Stuttgart (HLRS) on the Hawk cluster, founded by the Baden-Württemberg Ministry of Science, Research, and the Arts and the German Federal Ministry of Education and Research through the Gauss Centre for Supercomputing. The computing time and storage facilities were provided by the project 'trainABL' (ACID44187). We further acknowledge the support of FU Berlin's refubium team in the process of data publication.

**Author Contributions** J.K. conducted the numerical simulations, performed the post-processing of the data, created the visualizations, interpreted the results and wrote the original draft. Both authors contributed to the conceptualization of the study. C.A. supervised the research, contributed with discussion and interpretation of results, reviewed and edited the original draft and was responsible for acquisition of funding.

**Funding** Open Access funding enabled and organized by Projekt DEAL. The authors acknowledge financial support through the ERC grant trainABL with the project number 851374; <https://doi.org/10.3030/851374>.

**Data availability** The data supporting the findings of this study is published under the F.A.I.R. paradigm (cf. *open access*) in Kostecky and Ansoerg (2024b).

## Declarations

**Conflict of interest** The authors declare no Conflict of interest.

**Open Access** The authors commit to the F.A.I.R. paradigms of open access regarding the contents of this article and their own related data. This article, including the images, is licensed under a Creative Commons Attribution 4.0 International License (CC-BY, <http://creativecommons.org/licenses/by/4.0/>). The CC-BY license permits re-use and sharing of the contents provided appropriate credit to the original authors and the source, a link to the licence are given and changes to the original content are indicated.

**Open Access** This article is licensed under a Creative Commons Attribution 4.0 International License, which permits use, sharing, adaptation, distribution and reproduction in any medium or format, as long as you give appropriate credit to the original author(s) and the source, provide a link to the Creative Commons licence, and indicate if changes were made. The images or other third party material in this article are included in the article's Creative Commons licence, unless indicated otherwise in a credit line to the material. If material is not included in the article's Creative Commons licence and your intended use is not permitted by statutory regulation or exceeds the permitted use, you will need to obtain permission directly from the copyright holder. To view a copy of this licence, visit <http://creativecommons.org/licenses/by/4.0/>.

## References

- Adrian RJ (2007) Hairpin vortex organization in wall turbulence. *Phys Fluids* 19(4):041301. <https://doi.org/10.1063/1.2717527>
- Anderson PS (2009) Measurement of Prandtl number as a function of Richardson number avoiding self-correlation. *Boundary-Layer Meteorol* 131(3):345–362. <https://doi.org/10.1007/s10546-009-9376-4>
- Ansonge C (2019) Scale dependence of atmosphere-surface coupling through similarity theory. *Boundary-Layer Meteorol* 170(1):1–27. <https://doi.org/10.1007/s10546-018-0386-y>
- Ansonge C, Mellado JP (2014) Global intermittency and collapsing turbulence in the stratified planetary boundary layer. *Boundary-Layer Meteorol* 153(1):89–116. <https://doi.org/10.1007/s10546-014-9941-3>
- Ansonge C, Mellado JP (2016) Analyses of external and global intermittency in the logarithmic layer of Ekman flow. *J Fluid Mech* 805:611–635. <https://doi.org/10.1017/jfm.2016.534>
- Atoufi A, Scott KA, Waite ML (2021) Kinetic energy cascade in stably stratified open-channel flows. *J Fluid Mech* 925:A25. <https://doi.org/10.1017/jfm.2021.665>
- Bhimireddy SR, Sun J, Wang J, Kristovich DAR, Hiscox AL (2024) Effect of small-scale topographical variations and fetch from roughness elements on the stable boundary layer turbulence statistics. *Boundary-Layer Meteorol* 190(1):1–19. <https://doi.org/10.1007/s10546-023-00855-5>
- Bon T, Cal RB, Meyers J (2024) Stable boundary layers with subsidence: scaling and similarity of the steady state. *Boundary-Layer Meteorol* 190(10):42. <https://doi.org/10.1007/s10546-024-00882-w>
- Boyko V, Vercauteren N (2024) Simulating the unsteady stable boundary layer with a stochastic stability equation. *J Geophys Res Atmos* 129(5):e2023JD039370. <https://doi.org/10.1029/2023JD039370>
- Brutsaert W (1982) *Evaporation into the atmosphere*. Springer, Netherlands. <https://doi.org/10.1007/978-94-017-1497-6>
- Businger JA (1973) *Turbulence transfer in the atmospheric surface layer*. American Meteorological Society, Workshop on Micrometeorology
- Businger JA, Wyngaard JC, Izumi Y, Bradley EF (1971) Flux-profile relationships in the atmospheric surface layer. *J Atmos Sci* 28(2):181–189. [https://doi.org/10.1175/1520-0469\(1971\)028%3C0181:FPRITA%3E2.0.CO;2](https://doi.org/10.1175/1520-0469(1971)028%3C0181:FPRITA%3E2.0.CO;2)
- Chenge Y, Brutsaert W (2005) Flux-profile relationships for wind speed and temperature in the stable atmospheric boundary layer. *Boundary-Layer Meteorol* 114(3):519–538. <https://doi.org/10.1007/s10546-004-1425-4>
- Chinita MJ, Matheou G, Miranda PMA (2022) Large-eddy simulation of very stable boundary layers. Part I: modeling methodology. *Q J R Meteorol Soc* 148(745):1805–1823. <https://doi.org/10.1002/qj.4279>
- Chung D, Matheou G (2012) Direct numerical simulation of stationary homogeneous stratified sheared turbulence. *J Fluid Mech* 696:434–467. <https://doi.org/10.1017/jfm.2012.59>
- Coleman GN (1999) Similarity statistics from a direct numerical simulation of the neutrally stratified planetary boundary layer. *J Atmos Sci* 56(6):891–900. [https://doi.org/10.1175/1520-0469\(1999\)056%3C0891:SSFADN%3E2.0.CO;2](https://doi.org/10.1175/1520-0469(1999)056%3C0891:SSFADN%3E2.0.CO;2)
- Coleman GN, Ferziger JH, Spalart PR (1990) A numerical study of the turbulent Ekman layer. *J Fluid Mech* 213:313–348. <https://doi.org/10.1017/S0022112090002348>
- Coleman GN, Ferziger JH, Spalart PR (1992) Direct simulation of the stably stratified turbulent Ekman layer. *J Fluid Mech* 244:677–712. <https://doi.org/10.1017/S0022112092003264>
- De Bruin HAR (1994) Analytic solutions of the equations governing the temperature fluctuation method. *Boundary-Layer Meteorol* 68(4):427–432. <https://doi.org/10.1007/BF00706800>
- Deusebio E, Brethouwer G, Schlatter P, Lindborg E (2014) A numerical study of the unstratified and stratified Ekman layer. *J Fluid Mech* 755:672–704. <https://doi.org/10.1017/jfm.2014.318>
- Deusebio E, Caulfield CP, Taylor JR (2015) The intermittency boundary in stratified plane Couette flow. *J Fluid Mech* 781:298–329. <https://doi.org/10.1017/jfm.2015.497>

- Donda JMM, van Hooijdonk IGS, Moene AF, Jonker HJJ, van Heijst GJF, Clercx HJH, van de Wiel BJH (2015) Collapse of turbulence in stably stratified channel flow: a transient phenomenon. *Q J R Meteorol Soc* 141(691):2137–2147. <https://doi.org/10.1002/qj.2511>
- Donda JMM, van Hooijdonk IGS, Moene AF, van Heijst GJF, Clercx HJH, van de Wiel BJH (2016) The maximum sustainable heat flux in stably stratified channel flows. *Q J R Meteorol Soc* 142(695):781–792. <https://doi.org/10.1002/qj.2680>
- Dyer AJ (1974) A review of flux-profile relationships. *Boundary-Layer Meteorol* 7(3):363–372. <https://doi.org/10.1007/BF00240838>
- Edwards JM, Beljaars ACM, Holtslag AAM, Lock AP (2020) Representation of boundary-layer processes in numerical weather prediction and climate models. *Boundary-Layer Meteorol* 177(2):511–539. <https://doi.org/10.1007/s10546-020-00530-z>
- Ekman VW (1905) On the influence of the earth's rotation on ocean-currents. *Arkiv for Matematik, Astronomi Och Fysik* 2:1–53
- Fiedler F (1983) Einige Charakteristika der Strömung im Oberrheingraben. *Wissenschaftliche Berichte des Instituts für Meteorologie und Klimaforschung der Universität Karlsruhe* 4:113–123
- Flores O, Riley JJ (2011) Analysis of turbulence collapse in the stably stratified surface layer using direct numerical simulation. *Boundary-Layer Meteorol* 139(2):241–259. <https://doi.org/10.1007/s10546-011-9588-2>
- Foken T (2006) 50 years of the Monin–Obukhov similarity theory. *Boundary-Layer Meteorol* 119(3):431–447. <https://doi.org/10.1007/s10546-006-9048-6>
- García-Villalba M, del Álamo JC (2011) Turbulence modification by stable stratification in channel flow. *Phys Fluids* 23(4):1–22. <https://doi.org/10.1063/1.3560359>
- Garg RP, Ferziger JH, Monismith SG, Koseff JR (2000) Stably stratified turbulent channel flows. I. Stratification regimes and turbulence suppression mechanism. *Phys Fluids* 12(10):2569–2594. <https://doi.org/10.1063/1.1288608>
- Garratt JR (1992) *The Atmospheric boundary layer*. Cambridge atmospheric and space science series, Cambridge University Press, Cambridge
- Giannenas AE, Laizet S (2021) A simple and scalable immersed boundary method for high-fidelity simulations of fixed and moving objects on a Cartesian mesh. *Appl Math Model* 99:606–627. <https://doi.org/10.1016/j.apm.2021.06.026>
- Grachev AA, Andreas EL, Fairall CW, Guest PS, Persson POG (2007) On the turbulent Prandtl number in the stable atmospheric boundary layer. *Boundary-Layer Meteorol* 125(2):329–341. <https://doi.org/10.1007/s10546-007-9192-7>
- Grachev AA, Andreas EL, Fairall CW, Guest PS, Persson POG (2013) The critical Richardson number and limits of applicability of local similarity theory in the stable boundary layer. *Boundary-Layer Meteorol* 147(1):51–82. <https://doi.org/10.1007/s10546-012-9771-0>
- Grimmond CSB, Oke TR (1999) Aerodynamic properties of urban areas derived from analysis of surface form. *J Appl Meteorol Climatol* 38(9):1262–1292. [https://doi.org/10.1175/1520-0450\(1999\)038%3C1262:APOUAD%3E2.0.CO;2](https://doi.org/10.1175/1520-0450(1999)038%3C1262:APOUAD%3E2.0.CO;2)
- Gucci F, Giovannini L, Stiperski I, Zardi D, Vercauteren N (2023) Sources of anisotropy in the Reynolds stress tensor in the stable boundary layer. *Q J R Meteorol Soc* 149(750):277–299. <https://doi.org/10.1002/qj.4407>
- Högström U (1988) Non-dimensional wind and temperature profiles in the atmospheric surface layer: a re-evaluation. *Boundary-Layer Meteorol* 42(1):55–78. <https://doi.org/10.1007/BF00119875>
- Högström U (1996) Review of some basic characteristics of the atmospheric surface layer. *Boundary-Layer Meteorol* 78(3):215–246. <https://doi.org/10.1007/BF00120937>
- Holtslag AAM, Svensson G, Baas P, Basu S, Beare B, Beljaars ACM, Bosveld FC, Cuxart J, Lindvall J, Steeneveld GJ, Tjernström M, Van de Wiel BJH (2013) Stable atmospheric boundary layers and diurnal cycles: challenges for weather and climate models. *Bull Am Meteor Soc* 94(11):1691–1706. <https://doi.org/10.1175/BAMS-D-11-00187.1>
- Howell JF, Sun J (1999) Surface-layer fluxes in stable conditions. *Boundary-Layer Meteorol* 90(3):495–520. <https://doi.org/10.1023/A:1001788515355>
- Jiménez MA, Cuxart J (2005) Large-eddy simulations of the stable boundary layer using the standard Kolmogorov theory: range of applicability. *Boundary-Layer Meteorol* 115(2):241–261. <https://doi.org/10.1007/s10546-004-3470-4>
- Kalthoff N, Vogel B (1992) Counter-current and channelling effect under stable stratification in the area of Karlsruhe. *Theoret Appl Climatol* 45(2):113–126. <https://doi.org/10.1007/BF00866400>
- Kosović B, Curry JA (2000) A large eddy simulation study of a quasi-steady, stably stratified atmospheric boundary layer. *J Atmos Sci* 57(8):1052–1068. [https://doi.org/10.1175/1520-0469\(2000\)057%3C1052:ALESSO%3E2.0.CO;2](https://doi.org/10.1175/1520-0469(2000)057%3C1052:ALESSO%3E2.0.CO;2)



- Kostelecky J, Ansonge C (2024a) Simulation and scaling analysis of periodic surfaces with small-scale roughness in turbulent Ekman flow. *J Fluid Mech* 992:A8. <https://doi.org/10.1017/jfm.2024.542>
- Kostelecky J, Ansonge C (2024b) Turbulent Ekman flow with cubic small-scale surface roughness under stable stratification ( $Re=1000$ ). <https://doi.org/10.17169/refubium-45292>
- Lee S, Gohari SMI, Sarkar S (2020) Direct numerical simulation of stratified Ekman layers over a periodic rough surface. *J Fluid Mech* 902:A25. <https://doi.org/10.1017/jfm.2020.590>
- Lele SK (1992) Compact finite difference schemes with spectral-like resolution. *J Comput Phys* 103(1):16–42. [https://doi.org/10.1016/0021-9991\(92\)90324-R](https://doi.org/10.1016/0021-9991(92)90324-R)
- LeMone MA, Angevine WM, Bretherton CS, Chen F, Dudhia J, Fedorovich E, Katsaros KB, Lenschow DH, Mahrt L, Patton EG, Sun J, Tjernström M, Weil J (2019) 100 years of progress in boundary layer meteorology. *Meteorol Monogr* 59(1):9.1–9.85. <https://doi.org/10.1175/AMSMONOGRAPHS-D-18-0013.1>
- Li D (2019) Turbulent Prandtl number in the atmospheric boundary layer—where are we now? *Atmos Res* 216:86–105. <https://doi.org/10.1016/j.atmosres.2018.09.015>
- Mahrt L (1998) Stratified atmospheric boundary layers and breakdown of models. *Theoret Comput Fluid Dyn* 11(3):263–279. <https://doi.org/10.1007/s001620050093>
- Mahrt L (1999) Stratified atmospheric boundary layers. *Boundary-Layer Meteorol* 90(3):375–396. <https://doi.org/10.1023/A:1001765727956>
- Mahrt L (2007) The influence of nonstationarity on the turbulent flux-gradient relationship for stable stratification. *Boundary-Layer Meteorol* 125(2):245–264. <https://doi.org/10.1007/s10546-007-9154-0>
- Mahrt L (2014) Stably stratified atmospheric boundary layers. *Annu Rev Fluid Mech* 46(1):23–45. <https://doi.org/10.1146/annurev-fluid-010313-141354>
- Marlatt S, Waggy S, Biringen S (2012) Direct numerical simulation of the turbulent Ekman layer: evaluation of closure models. *J Atmos Sci* 69(3):1106–1117. <https://doi.org/10.1175/JAS-D-11-0107.1>
- Maroneze R, Costa FD, Acevedo OC, Medeiros LE, Puhales FS, Anabor V, Mortarini L (2023) A new stable boundary layer parameterization for numerical weather prediction models: a heat flux budget approach. *Boundary-Layer Meteorol* 188(2):209–228. <https://doi.org/10.1007/s10546-023-00810-4>
- Mauritsen T, Svensson G (2007) Observations of stably stratified shear-driven atmospheric turbulence at low and High Richardson numbers. *J Atmos Sci* 64(2):645–655. <https://doi.org/10.1175/JAS3856.1>
- Mellado JP, Ansonge C (2012) Factorization of the Fourier transform of the pressure-Poisson equation using finite differences in colocated grids. *ZAMM-J Appl Math Mech/Zeitschrift für Angewandte Mathematik und Mechanik* 92(5):380–392. <https://doi.org/10.1002/zamm.201100078>
- Mellado JP, Bretherton CS, Stevens B, Wyant MC (2018) DNS and LES for simulating stratocumulus: better together. *J Adv Model Earth Syst* 10(7):1421–1438. <https://doi.org/10.1029/2018MS001312>
- Mellor GL, Yamada T (1974) A hierarchy of turbulence closure models for planetary boundary layers. *J Atmos Sci* 31(7):1791–1806. [https://doi.org/10.1175/1520-0469\(1974\)031%3C1791:AHOTCM%3E2.0.CO;2](https://doi.org/10.1175/1520-0469(1974)031%3C1791:AHOTCM%3E2.0.CO;2)
- Mellor GL, Yamada T (1982) Development of a turbulence closure model for geophysical fluid problems. *Rev Geophys* 20(4):851–875. <https://doi.org/10.1029/RG020i004p00851>
- Mironov DV, Sullivan PP (2023) Turbulence structure and mixing in strongly stable boundary-layer flows over thermally heterogeneous surfaces. *Boundary-Layer Meteorol* 187(1):371–393. <https://doi.org/10.1007/s10546-022-00766-x>
- Miyashita K, Iwamoto K, Kawamura H (2006) Direct numerical simulation of the neutrally stratified turbulent Ekman boundary layer. *J Earth Simul* 6:3–15
- Monin AS (1970) The atmospheric boundary layer. *Annu Rev Fluid Mech* 2(1):225–250. <https://doi.org/10.1146/annurev.fl.02.010170.001301>
- Nieuwstadt FTM (1984) The turbulent structure of the stable, nocturnal boundary layer. *J Atmos Sci* 41(14):2202–2216. [https://doi.org/10.1175/1520-0469\(1984\)041%3C2202:TTSOTS%3E2.0.CO;2](https://doi.org/10.1175/1520-0469(1984)041%3C2202:TTSOTS%3E2.0.CO;2)
- Nieuwstadt FTM (2005) Direct numerical simulation of stable channel flow at large stability. *Boundary-Layer Meteorol* 116(2):277–299. <https://doi.org/10.1007/s10546-004-2818-0>
- Obukhov AM (1971) Turbulence in an atmosphere with a non-uniform temperature. *Boundary-Layer Meteorol* 2(1):7–29. <https://doi.org/10.1007/BF00718085>
- Pardyjak ER, Monti P, Fernando HJS (2002) Flux Richardson number measurements in stable atmospheric shear flows. *J Fluid Mech* 459:307–316. <https://doi.org/10.1017/S0022112002008406>
- Pope SB (2000) *Turbulent flows*. Cambridge University Press, Cambridge
- Prandtl L (1925) 7. Bericht über Untersuchungen zur ausgebildeten Turbulenz. *ZAMM-J Appl Math Mech/Zeitschrift für Angewandte Mathematik und Mechanik* 5(2):136–139. <https://doi.org/10.1002/zamm.19250050212>
- Rossby CG, Montgomery RB (1935) *The layer of frictional influence in wind and ocean currents*. Massachusetts Institute of Technology and Woods Hole Oceanographic Institution, Cambridge and Woods. <https://doi.org/10.1575/1912/1157>

- Rotta JC (1972) Turbulente Strömungen: eine Einführung in die Theorie und ihre Anwendung. No. 15 in Leitfäden der angewandten Mathematik und Mechanik, Teubner, Stuttgart
- Sandu I, Beljaars A, Bechtold P, Mauritsen T, Balsamo G (2013) Why is it so difficult to represent stably stratified conditions in numerical weather prediction (NWP) models? *J Adv Model Earth Syst* 5(2):117–133. <https://doi.org/10.1002/jame.20013>
- Schumann U, Gerz T (1995) Turbulent mixing in stably stratified shear flows. *J Appl Meteorol Climatol* 34(1):33–48. <https://doi.org/10.1175/1520-0450-34.1.33>
- Shah SK, Bou-Zeid E (2014) Direct numerical simulations of turbulent Ekman layers with increasing static stability: modifications to the bulk structure and second-order statistics. *J Fluid Mech* 760:494–539. <https://doi.org/10.1017/jfm.2014.597>
- Shingai K, Kawamura H (2004) A study of turbulence structure and large-scale motion in the Ekman layer through direct numerical simulations. *J Turbul* 5(1):1–18. <https://doi.org/10.1088/1468-5248/5/1/013>
- Sorbjan Z, Grachev AA (2010) An evaluation of the flux-gradient relationship in the stable boundary layer. *Boundary-Layer Meteorol* 135(3):385–405. <https://doi.org/10.1007/s10546-010-9482-3>
- Spalart PR (1989) Theoretical and numerical study of a three-dimensional turbulent boundary layer. *J Fluid Mech* 205:319–340. <https://doi.org/10.1017/S0022112089002053>
- Spalart PR, Coleman GN, Johnstone R (2008) Direct numerical simulation of the Ekman layer: a step in Reynolds number, and cautious support for a log law with a shifted origin. *Phys Fluids* 20(10):101507. <https://doi.org/10.1063/1.3005858>
- Spalart PR, Coleman GN, Johnstone R (2009) Retraction: “Direct numerical simulation of the Ekman layer: a step in Reynolds number, and cautious support for a log law with a shifted origin” [*Phys. Fluids* 20, 101507 (2008)]. *Phys Fluids* 21(10):109901. <https://doi.org/10.1063/1.3247176>
- Steenefeld GJ (2014) Current challenges in understanding and forecasting stable boundary layers over land and ice. *Front Environ Sci* 2(41):1–6. <https://doi.org/10.3389/fenvs.2014.00041>
- Stefanello M, Frantz RAS, Acevedo O, Degrazia G, Silvestrini JH (2022) Horizontal meandering in direct numerical simulations of the stable boundary layer. *Q J R Meteorol Soc* 148(749):3604–3621. <https://doi.org/10.1002/qj.4376>
- Stiperski I, Calaf M (2018) Dependence of near-surface similarity scaling on the anisotropy of atmospheric turbulence. *Q J R Meteorol Soc* 144(712):641–657. <https://doi.org/10.1002/qj.3224>
- Stopa JE, Wang C, Vandemark D, Foster R, Mouche A, Chapron B (2022) Automated global classification of surface layer stratification using high-resolution sea surface roughness measurements by satellite synthetic aperture radar. *Geophys Res Lett* 49(12):1–11. <https://doi.org/10.1029/2022GL098686>
- Stull RB (1988) An introduction to boundary layer meteorology. Atmospheric Sciences Library, Kluwer Academic Publishers, Dordrecht, Boston
- Townsend AA (1976) The structure of turbulent shear flow, 2nd edn. Cambridge University Press, Cambridge
- Van de Wiel BJH, Moene AF, De Ronde WH, Jonker HJJ (2008) Local similarity in the stable boundary layer and mixing-length approaches: consistency of concepts. *Boundary-Layer Meteorol* 128(1):103–116. <https://doi.org/10.1007/s10546-008-9277-y>
- Van de Wiel BJH, Moene AF, Jonker HJJ (2012) The cessation of continuous turbulence as precursor of the very stable nocturnal boundary layer. *J Atmos Sci* 69(11):3097–3115. <https://doi.org/10.1175/JAS-D-12-064.1>
- Van de Wiel BJH, Moene AF, Jonker HJJ, Baas P, Basu S, Donda JMM, Sun J, AaM Holtslag (2012) The minimum wind speed for sustainable turbulence in the nocturnal boundary layer. *J Atmos Sci* 69(11):3116–3127. <https://doi.org/10.1175/JAS-D-12-0107.1>
- Van der Linden S, Van de Wiel BJH, Petenko I, Van Heerwaarden CC, Baas P, Jonker HJJ (2020) A Businger mechanism for intermittent bursting in the stable boundary layer. *J Atmos Sci* 77(10):3343–3360. <https://doi.org/10.1175/JAS-D-19-0309.1>
- Venayagamoorthy SK, Stretch DD (2010) On the turbulent Prandtl number in homogeneous stably stratified turbulence. *J Fluid Mech* 644:359–369. <https://doi.org/10.1017/S002211200999293X>
- Vercauteren N, Boyko V, Faranda D, Stiperski I (2019) Scale interactions and anisotropy in stable boundary layers. *Q J R Meteorol Soc* 145(722):1799–1813. <https://doi.org/10.1002/qj.3524>
- Watanabe T, Riley JJ, Nagata K, Matsuda K, Onishi R (2019) Hairpin vortices and highly elongated flow structures in a stably stratified shear layer. *J Fluid Mech* 878:37–61. <https://doi.org/10.1017/jfm.2019.577>
- Weber RO, Kaufmann P (1998) Relationship of synoptic winds and complex terrain flows during the MIS-TRAL field experiment. *J Appl Meteorol Climatol* 37(11):1486–1496. [https://doi.org/10.1175/1520-0450\(1998\)037%3C1486:ROSWAC%3E2.0.CO;2](https://doi.org/10.1175/1520-0450(1998)037%3C1486:ROSWAC%3E2.0.CO;2)
- Whiteman CD, Doran JC (1993) The relationship between overlying synoptic-scale flows and winds within a valley. *J Appl Meteorol Climatol* 32(11):1669–1682. [https://doi.org/10.1175/1520-0450\(1993\)032%3C1669:TRBOSS%3E2.0.CO;2](https://doi.org/10.1175/1520-0450(1993)032%3C1669:TRBOSS%3E2.0.CO;2)



- Williamson JH (1980) Low-storage Runge–Kutta schemes. *J Comput Phys* 35(1):48–56. [https://doi.org/10.1016/0021-9991\(80\)90033-9](https://doi.org/10.1016/0021-9991(80)90033-9)
- Wippermann F, Gross G (1981) Construction of orographically influenced wind roses for given distributions of the large-scale wind. *Contrib Atmos Phys (Germany, Federal Republic of)* 54:4
- Wyngaard JC (1973) On surface layer turbulence. In: Haugen DH (ed) *Workshop on Micrometeorology*, Ed., American Meteorological Society, p 392
- Yague C, Maqueda G, Rees JM (2001) Characteristics of turbulence in the lower atmosphere at Halley IV station, Antarctica. *Dyn Atmos Oceans* 34(2):205–223. [https://doi.org/10.1016/S0377-0265\(01\)00068-9](https://doi.org/10.1016/S0377-0265(01)00068-9)
- Yakhot V, Orszag SA (1986) Renormalization group analysis of turbulence. I. Basic theory. *J Sci Comput* 1(1):3–51. <https://doi.org/10.1007/BF01061452>
- Zilitinkevich SS, Elperin T, Kleerorin N, Rogachevskii I, Esau I, Mauritsen T, Miles MW (2008) Turbulence energetics in stably stratified geophysical flows: strong and weak mixing regimes. *Q J R Meteorol Soc* 134(633):793–799. <https://doi.org/10.1002/qj.264>
- Zilitinkevich SS, Tyuryakov SA, Troitskaya YuI, Mareev EA (2012) Theoretical models of the height of the atmospheric boundary layer and turbulent entrainment at its upper boundary. *Izv Atmos Ocean Phys* 48(1):133–142. <https://doi.org/10.1134/S0001433812010148>

**Publisher's Note** Springer Nature remains neutral with regard to jurisdictional claims in published maps and institutional affiliations.

## 6. Conclusions and Outlook

Surface roughness is an omnipresent and crucial feature of the atmospheric boundary layer. In the present dissertation, the effect of roughness on the bulk properties of the flow was first unveiled for neutral conditions (Study I, chapter 4). Stability was then introduced (Study II, chapter 5) to investigate the competing interplay of enhanced mixing due to roughness and suppression of turbulence by buoyant restoring forces and the implications on **ASL** theory.

In large-scale atmospheric models (e.g. **GCMs**, **NWP** models), the effect of unresolved surface roughness and turbulence in the **ABL** on resolved properties are parameterized since model grid resolutions are too coarse for an explicit representation. These parameterizations tend to fail to reproduce certain **ABL** characteristics in extreme regimes, especially under strong stability where global intermittency is observed. The main challenge for these models is the lack of a general framework ranging from the **WSBL** to the **VSBL**. With the aim of shedding light on the interactions of surface roughness with **ABL** dynamics, particularly in combination with stable density stratification, these complex processes were investigated through a simplified model: the canonical flow problem of rough, turbulent Ekman flow. Ekman flow is the flow over a flat plate with surface heterogeneity, driven by a large-scale pressure gradient and subjected to steady system rotation.

Concerning the conceptual simplicity, **DNS** is chosen as the simulation paradigm for the rough, turbulent Ekman flow, which brings the present analysis to the core problem of fluid dynamics, the numerical solution of the **NSE** (chapter 2). The three-dimensional surface roughness and turbulent motions are explicitly and fully resolved on the computational grid without relying on turbulence closure assumptions and surface models. The demand for an extremely fine grid resolution is accompanied by tremendous computational costs, which still limits **DNS** to a reduced scale separation, i.e. low to intermediate Reynolds numbers. The **DNS** approach is comparably new for analyzing geophysical wall-bounded flows, although it has already been used for some decades in engineering. The rise of **DNS** in the meteorological context has been favored in recent years by the advent of increasingly powerful supercomputers, enabling geophysically relevant scale separations, computational domain sizes and simulation durations. In the present dissertation, the **TIER-0 HPC** system **HAWK** in Stuttgart was employed for the simulations in studies I & II, whereby the **DNS** code ran massively parallel on up to 128 compute nodes with each 128 compute cores. Simulation data of both studies I & II is published and available to the public (Kostecky and Ansoerge, 2024a,c). The rough Ekman flow problem and **HPC** usage demand cutting-edge algorithms of high accuracy and scalability. With the intention of representing three-dimensional roughness elements in the simulation domain, the **ADR IBM**, based

on cubic splines for high accuracy, was implemented and successfully validated. Data from a combined wind tunnel and **LES** study and from another **DNS** code employing the **ADR IBM** was taken for the validation (chapter 3). Spurious pressure oscillations are avoided using a horizontal pressure grid staggering and a compact pressure filter in the vertical direction. The pressure grid is staggered with interpolatory compact schemes similar to the schemes for spatial discretization. As an initial finding from the computational standpoint, the numerical framework implemented into the **DNS** code enables—for the first time—**DNS** of Ekman flows with fully resolved, three-dimensional roughness elements with sharp edges. Utilization of **TIER-0 HPC** facilities allows **DNS** with large domain sizes and high Reynolds numbers  $Re_\tau \approx 2700$ .

## 6.1 Study I: The Neutrally Stratified Rough Ekman Layer

In Study I, the effect of a controlled and fully-resolved, small-scale surface roughness on bulk properties of the flow with neutral density stratification is investigated (temperature is treated as a passive scalar). The considered cases are driven with an identical large-scale forcing and differ only in their mean roughness height. The following conclusions are drawn concerning the research questions posed (section 1.4):

- The drag is measured with a newly introduced integration method of the momentum and scalar budgets and significantly increases if the surface is rough. Consequently, the friction values of the velocity  $u_*$ , scalar  $s_*$  and the friction Reynolds number  $Re_\tau$  are enhanced. In addition, a strong veering of the wind with height is observed, with a substantial share of the veering already within the roughness.
- An extended logarithmic layer is formed, favored by the increase in the scale separation ( $Re_\tau$ ). The velocity and scalar profiles of the rough cases collapse with high accuracy on the rough-wall scaling within the logarithmic layer. When estimating the log-law parameters, a strong correlation of the von Kármán constant  $\kappa$  and the offset parameter  $A$  is observed. Values of the zero-plane displacement thickness and scaling of log ratios of the aerodynamic roughness lengths are approved by known values from the literature. Furthermore, the simulated cases are transitionally rough and at the verge of the fully rough regime.
- Within the smooth and transitionally rough regime, scalar mixing outweighs momentum mixing. In contrast, momentum mixing is larger at the edge of the fully rough regime, highlighting the importance of pressure.

The findings of Study I have implications for **ABL** research. The observed increase in the wind veering with the mean roughness height is remarkable and far exceeds the known reduction of the veering angle with increasing Reynolds number. The scale separation in the **ABL** for the large eddies is governed by the reduced Reynolds number  $Re_\tau/Re_{z_0}$  (with the roughness Reynolds number  $Re_{z_0}$  based on the aerodynamic roughness length  $z_0$ ), rather than by  $Re_\tau$ . Consequently, from the view-point of the outer layer, this implies an effective atmospheric Reynolds number lower than the commonly assumed  $Re_{ABL} \sim 10^8$  (section 1.4), as the real-world **ABL** is located well within the fully rough regime.

Considering the turning of the wind within the roughness and surface layer is important for drag measurements. An estimation based only on the maximum turbulent stress would result in Study I in an underestimation of the drag of up to 10%. Therefore, the common constant flux layer assumption—neglecting the Coriolis force—might be problematic, particularly in conditions of reduced scale separation, viz., stable density stratification. The decisive dissimilarity between the momentum and scalar conservation equations is the pressure gradient term. In the fully rough regime, momentum is more efficiently mixed than the scalar with  $z_{0m} > z_{0h}$ , which underlines the important role of pressure (blocking) effects within the roughness.

## 6.2 Study II: The Stably Stratified Rough Ekman Layer

The rough Ekman layer in Study II is exposed to an incrementally increasing stable density stratification that spans the full range from the **WSBL** to the **VSBL**. The focus of this study is the counteracting interplay of surface roughness and stability as well as the impact on **ASL** theory (**MOST**). Concerning the research questions posed (section 1.4), the following conclusions are drawn:

- The stability regime, where turbulence is in a continuous state, is extended in the presence of surface roughness. Roughness enhances turbulent mixing by inducing flow instabilities and generating eddies detached from the bottom surface at the sharp edges of the roughness elements. This increased level of mixing counteracts buoyancy-induced suppression of turbulence efficiently.
- The phenomenon of global intermittency in the **VSBL** is an inherent feature of the rough **SBL**, and a complete laminarization of the flow was not achieved despite the strong stability in the **VSBL**.
- Surface layer similarity (**MOST**) holds in the **WSBL** and deviates from the classical linear scaling in the **VSBL**. Using a local-in-height approach increases the accuracy of the collapse onto semi-empirical fits. Further, a correction approach for viscous effects on the stability correction functions is proposed, which significantly improves the fits compared to observational values.

The findings of Study II indicate that the turning of the wind with height under stable conditions is even more pronounced than in Study I. An over-veering of the wind (with a turning angle of the wind  $\alpha_* > 90^\circ$ ) is observed with increasing stability that exceeds by far the laminar limit of  $45^\circ$ . The wind turns in favor of the pressure gradient force since Coriolis and friction forces are reduced with increasing stability (triadic force balance in Ekman flow). This has implications for the classical **ASL** theory (**MOST**), where the turning of the wind is neglected—a potentially strong assumption. However, the measured high level of agreement in the **ASL** scaling behavior with the known values from observations is encouraging despite the intermediate Reynolds number of the present simulations compared to the atmospheric Reynolds number. Owing to the relatively large roughness Reynolds number in many realistic **ABL** flows, the gap in Reynolds numbers of the present **DNS** and the atmosphere might not be as large as commonly assumed and underlines the relevance of the present findings for atmospheric conditions.

## 6.3 Outlook

In conclusion, turbulent Ekman flow with small-scale surface roughness is an appropriate model to study **ABL** processes in a well-defined setup at reduced complexity. The important dynamical features of the **ABL**—the triadic balance, consisting of the pressure gradient, Coriolis and friction forces—are adequately captured. While considering surface roughness in **DNS** of turbulent Ekman flow, the essential difference between these simulations and a real-world **ABL** is eliminated, owing to advanced numerical methods and available computational resources. This dissertation emphasizes the significance of roughness for the dynamics of the **ABL**, as the Earth’s surface is inherently rough and lays the foundation for promising future investigations into surface-atmosphere interactions.

The provided numerical framework, consisting of the **ADR IBM** and the pressure grid staggering, paves the way for future high-resolution studies of rough wall-bounded flows at the scale of geophysical interest. Studying flows subjected to surface roughness offers a vast parameter space (e.g. distribution of roughness elements, geometry, mean height, roughness density). In both studies I & II of the present work, the statistical properties of the surface roughness remained unchanged, apart from the varying mean height of the

roughness elements (in viscous units  $H^+ \approx 10 - 40$ , and blocking ratio  $H/\delta \approx 0.7 - 1.5\%$ , cf. chapter 4). This work focussed on the impact of small-scale surface roughness on **ABL** properties. However, further exploring the roughness parameter space at relevant scales with well-defined cases would be very interesting. Nonetheless, a comprehensive parameter study is not feasible with the available computational resources.

The present setup with the largest mean roughness height is on the verge of the fully rough regime (roughness parameter  $z^+$  in viscous units  $z^+ \approx 2$ ). Therefore, analyzing a case well within the fully rough regime would be enlightening since the real-world **ABL** is also located here (large atmospheric Reynolds number). Performing such a simulation case is an intricate task with huge computational cost, but it appears to be possible on the next-generation **HPC**-systems. Increasing the mean height implies a higher Reynolds number (finer grid resolution, smaller simulation time step) to maintain the small-scale character of the roughness. (This will be possible soon owing to the ever-increasing computing resources.) Furthermore, the roughness elements are still arranged slightly offset on a regular grid. Concerning the arrangement, future studies should elucidate how an increased degree of randomness in surface roughness and incorporating multiscale roughness can provide a higher degree of realism in the simulations. Concerning processes within the surface roughness, the advantage of the present high-resolution DNS data is the availability of data in this flow region compared to observations, where measurements within the surface roughness are challenging or even impossible. Future work could thus as well focus on the near-wall region within the roughness to unveil the turbulence structures.

In Study I (chapter 4), a method was proposed to determine the total drag of the rough surface based on mean statistics of the flow. However, this approach is limited to the total value and the contributions originating from momentum budget terms (Coriolis, viscous and turbulent stress contributions). Based on this method, a drag partitioning into pressure drag, skin friction drag of the ground and roughness surfaces is impossible. These partitions can be determined based on the existing three-dimensional data, which would contribute to evaluating drag models and isolating leading drag processes in the roughness regimes. In addition, this would contribute to a better understanding of the transitionally rough regime.

In Study II (chapter 5), in the **VSBL**, global intermittency is observed to be intrinsic to the **VSBL**, where turbulence ceases locally in time and space. The quantitative characterization of this phenomenon as an intermittency factor is still unexplored in the present work. Precisely measuring this factor is challenging in the vicinity of the surface roughness, as shear and, thus, gradients are large and vorticity-based threshold methods could misinterpret turbulent and non-turbulent regions. Hence, sophisticated methods are required (e.g. filtering approaches). Furthermore, it is observed that turbulence becomes increasingly anisotropic with stability. Considering both governing aspects of the **VSBL**—anisotropy of turbulence and global intermittency—for future development of general turbulence closures and unified **ASL** similarity theories, incorporating the **VSBL** and **VSBL**, seems to be very promising. This would significantly improve large-scale meteorological models that rely heavily on these parameterizations.

# Bibliography

- Adrian, R. J. (2007). Hairpin vortex organization in wall turbulence. *Physics of Fluids*, 19(4):041301. doi: [10.1063/1.2717527](https://doi.org/10.1063/1.2717527).
- Ahn, J., Lee, J. H., and Sung, H. J. (2013). Statistics of the turbulent boundary layers over 3D cube-roughened walls. *International Journal of Heat and Fluid Flow*, 44:394–402. doi: [10.1016/j.ijheatfluidflow.2013.07.010](https://doi.org/10.1016/j.ijheatfluidflow.2013.07.010).
- Almgren, A. S., Bell, J. B., and Szymczak, W. G. (1996). A Numerical Method for the Incompressible Navier-Stokes Equations Based on an Approximate Projection. *SIAM Journal on Scientific Computing*, 17(2):358–369. doi: [10.1137/S1064827593244213](https://doi.org/10.1137/S1064827593244213).
- Anderson, P. S. (2009). Measurement of Prandtl Number as a Function of Richardson Number Avoiding Self-Correlation. *Boundary-Layer Meteorology*, 131(3):345–362. doi: [10.1007/s10546-009-9376-4](https://doi.org/10.1007/s10546-009-9376-4).
- Andreas, E. L. (1987). A theory for the scalar roughness and the scalar transfer coefficients over snow and sea ice. *Boundary-Layer Meteorology*, 38(1):159–184. doi: [10.1007/BF00121562](https://doi.org/10.1007/BF00121562).
- Andreas, E. L., Claffey, K. J., Jordan, R. E., Fairall, C. W., Guest, P. S., Persson, P. O. G., and Grachev, A. A. (2006). Evaluations of the von Kármán constant in the atmospheric surface layer. *Journal of Fluid Mechanics*, 559:117–149. doi: [10.1017/S0022112006000164](https://doi.org/10.1017/S0022112006000164).
- Ansorge, C. (2017). *Analyses of Turbulence in the Neutrally and Stably Stratified Planetary Boundary Layer*. Springer Theses. Springer International Publishing, Cham. doi: [10.1007/978-3-319-45044-5](https://doi.org/10.1007/978-3-319-45044-5).
- Ansorge, C. (2019). Scale Dependence of Atmosphere–Surface Coupling Through Similarity Theory. *Boundary-Layer Meteorology*, 170(1):1–27. doi: [10.1007/s10546-018-0386-y](https://doi.org/10.1007/s10546-018-0386-y).
- Ansorge, C. and Mellado, J. P. (2014). Global Intermittency and Collapsing Turbulence in the Stratified Planetary Boundary Layer. *Boundary-Layer Meteorology*, 153(1):89–116. doi: [10.1007/s10546-014-9941-3](https://doi.org/10.1007/s10546-014-9941-3).
- Ansorge, C. and Mellado, J. P. (2016). Analyses of external and global intermittency in the logarithmic layer of Ekman flow. *Journal of Fluid Mechanics*, 805:611–635. doi: [10.1017/jfm.2016.534](https://doi.org/10.1017/jfm.2016.534).
- Ashrafian, A., Andersson, H. I., and Manhart, M. (2004). DNS of turbulent flow in a rod-roughened channel. *International Journal of Heat and Fluid Flow*, 25(3):373–383. doi: [10.1016/j.ijheatfluidflow.2004.02.004](https://doi.org/10.1016/j.ijheatfluidflow.2004.02.004).
- Atoufi, A., Scott, K. A., and Waite, M. L. (2021). Kinetic energy cascade in stably stratified open-channel flows. *Journal of Fluid Mechanics*, 925:A25. doi: [10.1017/jfm.2021.665](https://doi.org/10.1017/jfm.2021.665).
- Barenblatt, G. I. (1993). Scaling laws for fully developed turbulent shear flows. Part 1. Basic hypotheses and analysis. *Journal of Fluid Mechanics*, 248:513–520. doi: [10.1017/S0022112093000874](https://doi.org/10.1017/S0022112093000874).
- Batchelor, G. K. (1967). *An Introduction to Fluid Dynamics*. Cambridge University Press, Cambridge.
- Beare, R. J., Macvean, M. K., Holtslag, A. A. M., Cuxart, J., Esau, I., Golaz, J.-C., Jimenez, M. A., Khairoutdinov, M., Kosovic, B., Lewellen, D., Lund, T. S., Lundquist,



- J. K., McCabe, A., Moene, A. F., Noh, Y., Raasch, S., and Sullivan, P. (2006). An Intercomparison of Large-Eddy Simulations of the Stable Boundary Layer. *Boundary-Layer Meteorology*, 118(2):247–272. doi: [10.1007/s10546-004-2820-6](https://doi.org/10.1007/s10546-004-2820-6).
- Bhimireddy, S. R., Sun, J., Wang, J., Kristovich, D. A. R., and Hiscox, A. L. (2024). Effect of Small-Scale Topographical Variations and Fetch from Roughness Elements on the Stable Boundary Layer Turbulence Statistics. *Boundary-Layer Meteorology*, 190(1):1–19. doi: [10.1007/s10546-023-00855-5](https://doi.org/10.1007/s10546-023-00855-5).
- Bon, T., Broos, D., Cal, R. B., and Meyers, J. (2023). Secondary flows induced by two-dimensional surface temperature heterogeneity in stably stratified channel flow. *Journal of Fluid Mechanics*, 970:A20. doi: [10.1017/jfm.2023.619](https://doi.org/10.1017/jfm.2023.619).
- Bon, T., Cal, R. B., and Meyers, J. (2024). Stable Boundary Layers with Subsidence: Scaling and Similarity of the Steady State. *Boundary-Layer Meteorology*, 190(10):42. doi: [10.1007/s10546-024-00882-w](https://doi.org/10.1007/s10546-024-00882-w).
- Bon, T. and Meyers, J. (2022). Stable channel flow with spanwise heterogeneous surface temperature. *Journal of Fluid Mechanics*, 933. doi: [10.1017/jfm.2021.1113](https://doi.org/10.1017/jfm.2021.1113).
- Boyko, V. and Vercauteren, N. (2024). Simulating the Unsteady Stable Boundary Layer With a Stochastic Stability Equation. *Journal of Geophysical Research: Atmospheres*, 129(5):e2023JD039370. doi: [10.1029/2023JD039370](https://doi.org/10.1029/2023JD039370).
- Brethouwer, G., Duguet, Y., and Schlatter, P. (2012). Turbulent–laminar coexistence in wall flows with Coriolis, buoyancy or Lorentz forces. *Journal of Fluid Mechanics*, 704:137–172. doi: [10.1017/jfm.2012.224](https://doi.org/10.1017/jfm.2012.224).
- Brown, D. L., Cortez, R., and Minion, M. L. (2001). Accurate Projection Methods for the Incompressible Navier–Stokes Equations. *Journal of Computational Physics*, 168(2):464–499. doi: [10.1006/jcph.2001.6715](https://doi.org/10.1006/jcph.2001.6715).
- Brutsaert, W. (1975a). The Roughness Length for Water Vapor Sensible Heat, and Other Scalars. *Journal of the Atmospheric Sciences*, 32(10):2028–2031. doi: [10.1175/1520-0469\(1975\)032<2029:TRLFWV>2.0.CO;2](https://doi.org/10.1175/1520-0469(1975)032<2029:TRLFWV>2.0.CO;2).
- Brutsaert, W. (1975b). A theory for local evaporation (or heat transfer) from rough and smooth surfaces at ground level. *Water Resources Research*, 11(4):543–550. doi: [10.1029/WR011i004p00543](https://doi.org/10.1029/WR011i004p00543).
- Brutsaert, W. (1982). *Evaporation into the Atmosphere*. Springer Netherlands, Dordrecht. doi: [10.1007/978-94-017-1497-6](https://doi.org/10.1007/978-94-017-1497-6).
- Buckingham, E. (1914). On Physically Similar Systems; Illustrations of the Use of Dimensional Equations. *Physical Review*, 4(4):345–376. doi: [10.1103/PhysRev.4.345](https://doi.org/10.1103/PhysRev.4.345).
- Businger, J. A. (1973). *Turbulence Transfer in the Atmospheric Surface Layer*. Workshop on Micrometeorology. American Meteorological Society.
- Businger, J. A., Wyngaard, J. C., Izumi, Y., and Bradley, E. F. (1971). Flux-Profile Relationships in the Atmospheric Surface Layer. *Journal of the Atmospheric Sciences*, 28(2):181–189. doi: [10.1175/1520-0469\(1971\)028<0181:FPRITA>2.0.CO;2](https://doi.org/10.1175/1520-0469(1971)028<0181:FPRITA>2.0.CO;2).
- Carpenter, M. H., Gottlieb, D., and Abarbanel, S. (1993). The Stability of Numerical Boundary Treatments for Compact High-Order Finite-Difference Schemes. *Journal of Computational Physics*, 108(2):272–295. doi: [10.1006/jcph.1993.1182](https://doi.org/10.1006/jcph.1993.1182).
- Carpenter, M. H. and Kennedy, C. A. (1994). Fourth-order 2N-storage Runge-Kutta schemes. Technical Report NASA-TM-109112.
- Castro, I. P. (2007). Rough-wall boundary layers: Mean flow universality. *Journal of Fluid Mechanics*, 585:469–485. doi: [10.1017/S0022112007006921](https://doi.org/10.1017/S0022112007006921).
- Castro, I. P., Kim, J. W., Stroh, A., and Lim, H. C. (2021). Channel flow with large longitudinal ribs. *Journal of Fluid Mechanics*, 915:A92. doi: [10.1017/jfm.2021.110](https://doi.org/10.1017/jfm.2021.110).
- Castro, I. P. and Leonardi, S. (2010). Very-Rough-Wall Channel Flows: A DNS Study. In Nickels, T. B., editor, *IUTAM Symposium on The Physics of Wall-Bounded Tur-*

- bulent Flows on Rough Walls*, IUTAM Bookseries, pages 175–181, Dordrecht. Springer Netherlands. doi: [10.1007/978-90-481-9631-9\\_24](https://doi.org/10.1007/978-90-481-9631-9_24).
- Cebeci, T. and Bradshaw, P. (1984). *Physical and Computational Aspects of Convective Heat Transfer. H: Hauptband*. Springer, New York Berlin Heidelberg London Paris Tokyo.
- Chan-Braun, C., García-Villalba, M., and Uhlmann, M. (2011). Force and torque acting on particles in a transitionally rough open-channel flow. *Journal of Fluid Mechanics*, 684:441–474. doi: [10.1017/jfm.2011.311](https://doi.org/10.1017/jfm.2011.311).
- Chandramouli, P., Heitz, D., Laizet, S., and Mémin, E. (2018). Coarse large-eddy simulations in a transitional wake flow with flow models under location uncertainty. *Computers & Fluids*, 168:170–189. doi: [10.1016/j.compfluid.2018.04.001](https://doi.org/10.1016/j.compfluid.2018.04.001).
- Cheng, H., Hayden, P., Robins, A., and Castro, I. (2007). Flow over cube arrays of different packing densities. *Journal of Wind Engineering and Industrial Aerodynamics*, 95(8):715–740. doi: [10.1016/j.jweia.2007.01.004](https://doi.org/10.1016/j.jweia.2007.01.004).
- Cheng, W.-C. and Porté-Agel, F. (2015). Adjustment of Turbulent Boundary-Layer Flow to Idealized Urban Surfaces: A Large-Eddy Simulation Study. *Boundary-Layer Meteorology*, 155(2):249–270. doi: [10.1007/s10546-015-0004-1](https://doi.org/10.1007/s10546-015-0004-1).
- Chenge, Y. and Brutsaert, W. (2005). Flux-profile Relationships for Wind Speed and Temperature in the Stable Atmospheric Boundary Layer. *Boundary-Layer Meteorology*, 114(3):519–538. doi: [10.1007/s10546-004-1425-4](https://doi.org/10.1007/s10546-004-1425-4).
- Chinita, M. J., Matheou, G., and Miranda, P. M. A. (2022). Large-eddy simulation of very stable boundary layers. Part I: Modeling methodology. *Quarterly Journal of the Royal Meteorological Society*, 148(745):1805–1823. doi: [10.1002/qj.4279](https://doi.org/10.1002/qj.4279).
- Chorin, A. J. (1968). Numerical solution of the Navier-Stokes equations. *Mathematics of Computation*, 22(104):745–762. doi: [10.1090/S0025-5718-1968-0242392-2](https://doi.org/10.1090/S0025-5718-1968-0242392-2).
- Chung, D., Hutchins, N., Schultz, M. P., and Flack, K. A. (2021). Predicting the Drag of Rough Surfaces. *Annual Review of Fluid Mechanics*, 53(1):439–471. doi: [10.1146/annurev-fluid-062520-115127](https://doi.org/10.1146/annurev-fluid-062520-115127).
- Chung, D. and Matheou, G. (2012). Direct numerical simulation of stationary homogeneous stratified sheared turbulence. *Journal of Fluid Mechanics*, 696:434–467. doi: [10.1017/jfm.2012.59](https://doi.org/10.1017/jfm.2012.59).
- Clauser, F. H. (1954). Turbulent Boundary Layers in Adverse Pressure Gradients. *Journal of the Aeronautical Sciences*, 21(2):91–108. doi: [10.2514/8.2938](https://doi.org/10.2514/8.2938).
- Coccal, O., Thomas, T. G., Castro, I. P., and Belcher, S. E. (2006). Mean Flow and Turbulence Statistics Over Groups of Urban-like Cubical Obstacles. *Boundary-Layer Meteorology*, 121(3):491–519. doi: [10.1007/s10546-006-9076-2](https://doi.org/10.1007/s10546-006-9076-2).
- Coleman, G. and Sandberg, R. (2010). A Primer on Direct Numerical Simulation of Turbulence – Methods, Procedures and Guidelines. Technical Report AFM-09/01b, Aerodynamics & Flight Mechanics Research Group (School of Engineering Sciences, University of Southampton, SO17 1BJ UK), Southampton.
- Coleman, G. N. (1999). Similarity Statistics from a Direct Numerical Simulation of the Neutrally Stratified Planetary Boundary Layer. *Journal of the Atmospheric Sciences*, 56(6):891–900. doi: [10.1175/1520-0469\(1999\)056<0891:SSFADN>2.0.CO;2](https://doi.org/10.1175/1520-0469(1999)056<0891:SSFADN>2.0.CO;2).
- Coleman, G. N., Ferziger, J. H., and Spalart, P. R. (1990). A numerical study of the turbulent Ekman layer. *Journal of Fluid Mechanics*, 213:313–348. doi: [10.1017/S0022112090002348](https://doi.org/10.1017/S0022112090002348).
- Coleman, G. N., Ferziger, J. H., and Spalart, P. R. (1992). Direct simulation of the stably stratified turbulent Ekman layer. *Journal of Fluid Mechanics*, 244:677–712. doi: [10.1017/S0022112092003264](https://doi.org/10.1017/S0022112092003264).
- Courant, R., Friedrichs, K., and Lewy, H. (1928). Über die partiellen Differenzengle-

- ichungen der mathematischen Physik. *Mathematische Annalen*, 100(1):32–74. doi: [10.1007/BF01448839](https://doi.org/10.1007/BF01448839).
- Cushman-Roisin, B. and Beckers, J.-M. (2011). *Introduction to Geophysical Fluid Dynamics: Physical and Numerical Aspects*. Number v. 101 in International Geophysics Series. Academic Press, Waltham, MA, 2nd ed edition.
- De Bruin, H. A. R. (1994). Analytic solutions of the equations governing the temperature fluctuation method. *Boundary-Layer Meteorology*, 68(4):427–432. doi: [10.1007/BF00706800](https://doi.org/10.1007/BF00706800).
- Dean, R. B. (1978). Reynolds Number Dependence of Skin Friction and Other Bulk Flow Variables in Two-Dimensional Rectangular Duct Flow. *Journal of Fluids Engineering*, 100(2):215–223. doi: [10.1115/1.3448633](https://doi.org/10.1115/1.3448633).
- Derbyshire, S. H. (1999). Boundary-Layer Decoupling over Cold Surfaces as a Physical Boundary-Instability. *Boundary-Layer Meteorology*, 90(2):297–325. doi: [10.1023/A:1001710014316](https://doi.org/10.1023/A:1001710014316).
- Deusebio, E., Brethouwer, G., Schlatter, P., and Lindborg, E. (2014). A numerical study of the unstratified and stratified Ekman layer. *Journal of Fluid Mechanics*, 755:672–704. doi: [10.1017/jfm.2014.318](https://doi.org/10.1017/jfm.2014.318).
- Deusebio, E., Caulfield, C. P., and Taylor, J. R. (2015). The intermittency boundary in stratified plane Couette flow. *Journal of Fluid Mechanics*, 781:298–329. doi: [10.1017/jfm.2015.497](https://doi.org/10.1017/jfm.2015.497).
- Dimotakis, P. E. (2000). The mixing transition in turbulent flows. *Journal of Fluid Mechanics*, 409:69–98. doi: [10.1017/S0022112099007946](https://doi.org/10.1017/S0022112099007946).
- Dimotakis, P. E. (2005). Turbulent Mixing. *Annual Review of Fluid Mechanics*, 37(1):329–356. doi: [10.1146/annurev.fluid.36.050802.122015](https://doi.org/10.1146/annurev.fluid.36.050802.122015).
- Donda, J. M. M., van Hooijdonk, I. G. S., Moene, A. F., Jonker, H. J. J., van Heijst, G. J. F., Clercx, H. J. H., and van de Wiel, B. J. H. (2015). Collapse of turbulence in stably stratified channel flow: A transient phenomenon. *Quarterly Journal of the Royal Meteorological Society*, 141(691):2137–2147. doi: [10.1002/qj.2511](https://doi.org/10.1002/qj.2511).
- Donda, J. M. M., van Hooijdonk, I. G. S., Moene, A. F., van Heijst, G. J. F., Clercx, H. J. H., and van de Wiel, B. J. H. (2016). The maximum sustainable heat flux in stably stratified channel flows. *Quarterly Journal of the Royal Meteorological Society*, 142(695):781–792. doi: [10.1002/qj.2680](https://doi.org/10.1002/qj.2680).
- Dyer, A. J. (1974). A review of flux-profile relationships. *Boundary-Layer Meteorology*, 7(3):363–372. doi: [10.1007/BF00240838](https://doi.org/10.1007/BF00240838).
- ECMWF (2024). Newsletter No. 179 - Spring 2024. doi: [10.21957/LR71SF656J](https://doi.org/10.21957/LR71SF656J).
- Edwards, J. M., Beljaars, A. C. M., Holtslag, A. A. M., and Lock, A. P. (2020). Representation of Boundary-Layer Processes in Numerical Weather Prediction and Climate Models. *Boundary-Layer Meteorology*, 177(2):511–539. doi: [10.1007/s10546-020-00530-z](https://doi.org/10.1007/s10546-020-00530-z).
- Ekman, V. W. (1905). On the influence of the earth’s rotation on ocean-currents. *Arkiv for Matematik, Astronomi Och Fysik*, 2:1–53.
- Fadlun, E. A., Verzicco, R., Orlandi, P., and Mohd-Yusof, J. (2000). Combined Immersed-Boundary Finite-Difference Methods for Three-Dimensional Complex Flow Simulations. *Journal of Computational Physics*, 161(1):35–60. doi: [10.1006/jcph.2000.6484](https://doi.org/10.1006/jcph.2000.6484).
- Fang, J., Diebold, M., Higgins, C., and Parlange, M. B. (2011). Towards oscillation-free implementation of the immersed boundary method with spectral-like methods. *Journal of Computational Physics*, 230(22):8179–8191. doi: [10.1016/j.jcp.2011.07.017](https://doi.org/10.1016/j.jcp.2011.07.017).
- Ferziger, J. H., Perić, M., and Street, R. L. (2020). *Computational Methods for Fluid Dynamics*. Springer International Publishing, Cham. doi: [10.1007/978-3-319-99693-6](https://doi.org/10.1007/978-3-319-99693-6).
- Fiedler, F. (1983). Einige Charakteristika der Strömung im Oberrheingraben. *Wis-*

- senschaftliche Berichte des Instituts für Meteorologie und Klimaforschung der Universität Karlsruhe*, 4:113–123.
- Finnigan, J. (2000). Turbulence in Plant Canopies. *Annual Review of Fluid Mechanics*, 32(1):519–571. doi: [10.1146/annurev.fluid.32.1.519](https://doi.org/10.1146/annurev.fluid.32.1.519).
- Flack, K. A. and Schultz, M. P. (2010). Review of Hydraulic Roughness Scales in the Fully Rough Regime. *Journal of Fluids Engineering*, 132(4):041203. doi: [10.1115/1.4001492](https://doi.org/10.1115/1.4001492).
- Flores, O. and Riley, J. J. (2011). Analysis of Turbulence Collapse in the Stably Stratified Surface Layer Using Direct Numerical Simulation. *Boundary-Layer Meteorology*, 139(2):241–259. doi: [10.1007/s10546-011-9588-2](https://doi.org/10.1007/s10546-011-9588-2).
- Foken, T. (2006). 50 Years of the Monin–Obukhov Similarity Theory. *Boundary-Layer Meteorology*, 119(3):431–447. doi: [10.1007/s10546-006-9048-6](https://doi.org/10.1007/s10546-006-9048-6).
- Fornberg, B. (1996). *A Practical Guide to Pseudospectral Methods*. Cambridge Monographs on Applied and Computational Mathematics. Cambridge University Press, Cambridge. doi: [10.1017/CBO9780511626357](https://doi.org/10.1017/CBO9780511626357).
- Fortin, M., Peyret, R., and Temam, R. (1971). Calcul des Ecoulements d’un Fluide Visqueux Incompressible. In Holt, M., editor, *Proceedings of the Second International Conference on Numerical Methods in Fluid Dynamics*, volume 8, pages 336–342. Springer Berlin Heidelberg, Berlin, Heidelberg. doi: [10.1007/3-540-05407-3\\_48](https://doi.org/10.1007/3-540-05407-3_48).
- Frenzen, P. and Vogel, C. A. (1995a). A further note “on the magnitude and apparent range of variation of the von karman constant”. *Boundary-Layer Meteorology*, 75(3):315–317. doi: [10.1007/BF00712700](https://doi.org/10.1007/BF00712700).
- Frenzen, P. and Vogel, C. A. (1995b). On the magnitude and apparent range of variation of the von Karman constant in the atmospheric surface layer. *Boundary-Layer Meteorology*, 72(4):371–392. doi: [10.1007/BF00709000](https://doi.org/10.1007/BF00709000).
- García-Villalba, M. and del Álamo, J. C. (2011). Turbulence modification by stable stratification in channel flow. *Physics of Fluids*, 23(4):1–22. doi: [10.1063/1.3560359](https://doi.org/10.1063/1.3560359).
- Garg, R. P., Ferziger, J. H., Monismith, S. G., and Koseff, J. R. (2000). Stably stratified turbulent channel flows. I. Stratification regimes and turbulence suppression mechanism. *Physics of Fluids*, 12(10):2569–2594. doi: [10.1063/1.1288608](https://doi.org/10.1063/1.1288608).
- Garratt, J. R. (1992). *The Atmospheric Boundary Layer*. Cambridge Atmospheric and Space Science Series. Cambridge University Press, Cambridge; New York.
- Gautier, R., Biau, D., and Lamballais, E. (2013). A reference solution of the flow over a circular cylinder at  $Re=40$ . *Computers & Fluids*, 75:103–111. doi: [10.1016/j.compfluid.2012.12.017](https://doi.org/10.1016/j.compfluid.2012.12.017).
- Gautier, R., Laizet, S., and Lamballais, E. (2014). A DNS study of jet control with microjets using an immersed boundary method. *International Journal of Computational Fluid Dynamics*, 28(6-10):393–410. doi: [10.1080/10618562.2014.950046](https://doi.org/10.1080/10618562.2014.950046).
- Gayen, B. and Sarkar, S. (2011). Direct and large-eddy simulations of internal tide generation at a near-critical slope. *Journal of Fluid Mechanics*, 681:48–79. doi: [10.1017/jfm.2011.170](https://doi.org/10.1017/jfm.2011.170).
- George, A., Huang, L. C., Tang, W.-P., and Wu, Y. D. (2000). Numerical Simulation of Unsteady Incompressible Flow ( $Re < 9500$ ) on the Curvilinear Half-Staggered Mesh. *SIAM Journal on Scientific Computing*, 21(6):2331–2351. doi: [10.1137/S1064827598337099](https://doi.org/10.1137/S1064827598337099).
- Giannenas, A. E. and Laizet, S. (2021). A simple and scalable immersed boundary method for high-fidelity simulations of fixed and moving objects on a Cartesian mesh. *Applied Mathematical Modelling*, 99:606–627. doi: [10.1016/j.apm.2021.06.026](https://doi.org/10.1016/j.apm.2021.06.026).
- Goldstein, D., Handler, R., and Sirovich, L. (1993). Modeling a No-Slip Flow Boundary with an External Force Field. *Journal of Computational Physics*, 105(2):354–366. doi: [10.1006/jcph.1993.1081](https://doi.org/10.1006/jcph.1993.1081).
- Grachev, A. A., Andreas, E. L., Fairall, C. W., Guest, P. S., and Persson, P. O. G. (2007).



- On the turbulent Prandtl number in the stable atmospheric boundary layer. *Boundary-Layer Meteorology*, 125(2):329–341. doi: [10.1007/s10546-007-9192-7](https://doi.org/10.1007/s10546-007-9192-7).
- Grachev, A. A., Andreas, E. L., Fairall, C. W., Guest, P. S., and Persson, P. O. G. (2012). Outlier Problem in Evaluating Similarity Functions in the Stable Atmospheric Boundary Layer. *Boundary-Layer Meteorology*, 144(2):137–155. doi: [10.1007/s10546-012-9714-9](https://doi.org/10.1007/s10546-012-9714-9).
- Grachev, A. A., Andreas, E. L., Fairall, C. W., Guest, P. S., and Persson, P. O. G. (2013). The Critical Richardson Number and Limits of Applicability of Local Similarity Theory in the Stable Boundary Layer. *Boundary-Layer Meteorology*, 147(1):51–82. doi: [10.1007/s10546-012-9771-0](https://doi.org/10.1007/s10546-012-9771-0).
- Grimmond, C. S. B. and Oke, T. R. (1999). Aerodynamic Properties of Urban Areas Derived from Analysis of Surface Form. *Journal of Applied Meteorology and Climatology*, 38(9):1262–1292. doi: [10.1175/1520-0450\(1999\)038<1262:APOUAD>2.0.CO;2](https://doi.org/10.1175/1520-0450(1999)038<1262:APOUAD>2.0.CO;2).
- Ha, K.-J., Hyun, Y.-K., Oh, H.-M., Kim, K.-E., and Mahrt, L. (2007). Evaluation of Boundary Layer Similarity Theory for Stable Conditions in CASES-99. *Monthly Weather Review*, 135(10):3474–3483. doi: [10.1175/MWR3488.1](https://doi.org/10.1175/MWR3488.1).
- Haiden, T., Janousek, M., Vitart, F., Ben-Bouallegue, Z., Ferranti, L., and Prates, F. (2021). Evaluation of ECMWF forecasts, including the 2021 upgrade. doi: [10.21957/90PGICJK4](https://doi.org/10.21957/90PGICJK4).
- Hama, F. R. (1954). Boundary Layer characteristics for smooth and rough surfaces. volume 62, pages 333–358. *Trans. Soc. Nav. Archit. Mar. Engrs.*
- He, P. (2016). A high order finite difference solver for massively parallel simulations of stably stratified turbulent channel flows. *Computers & Fluids*, 127:161–173. doi: [10.1016/j.compfluid.2015.12.012](https://doi.org/10.1016/j.compfluid.2015.12.012).
- Högström, U. (1988). Non-dimensional wind and temperature profiles in the atmospheric surface layer: A re-evaluation. *Boundary-Layer Meteorology*, 42(1):55–78. doi: [10.1007/BF00119875](https://doi.org/10.1007/BF00119875).
- Högström, U. (1996). Review of some basic characteristics of the atmospheric surface layer. *Boundary-Layer Meteorology*, 78(3):215–246. doi: [10.1007/BF00120937](https://doi.org/10.1007/BF00120937).
- Holton, J. R. (2004). *An Introduction to Dynamic Meteorology*. Number v. 88 in International Geophysics Series. Elsevier Academic Press, Burlington, MA, 4th ed edition.
- Holtslag, A. A. M. (2014). Introduction to the Third GEWEX Atmospheric Boundary Layer Study (GABLS3). *Boundary-Layer Meteorology*, 152(2):127–132. doi: [10.1007/s10546-014-9931-5](https://doi.org/10.1007/s10546-014-9931-5).
- Holtslag, A. A. M., Svensson, G., Baas, P., Basu, S., Beare, B., Beljaars, A. C. M., Bosveld, F. C., Cuxart, J., Lindvall, J., Steeneveld, G. J., Tjernström, M., and Van de Wiel, B. J. H. (2013). Stable Atmospheric Boundary Layers and Diurnal Cycles: Challenges for Weather and Climate Models. *Bulletin of the American Meteorological Society*, 94(11):1691–1706. doi: [10.1175/BAMS-D-11-00187.1](https://doi.org/10.1175/BAMS-D-11-00187.1).
- Howell, J. F. and Sun, J. (1999). Surface-Layer Fluxes in Stable Conditions. *Boundary-Layer Meteorology*, 90(3):495–520. doi: [10.1023/A:1001788515355](https://doi.org/10.1023/A:1001788515355).
- Hu, F. Q. (1996). On Absorbing Boundary Conditions for Linearized Euler Equations by a Perfectly Matched Layer. *Journal of Computational Physics*, 129(1):201–219. doi: [10.1006/jcph.1996.0244](https://doi.org/10.1006/jcph.1996.0244).
- Huang, J. and Bou-Zeid, E. (2013). Turbulence and Vertical Fluxes in the Stable Atmospheric Boundary Layer. Part I: A Large-Eddy Simulation Study. *Journal of the Atmospheric Sciences*, 70(6):1513–1527. doi: [10.1175/JAS-D-12-0167.1](https://doi.org/10.1175/JAS-D-12-0167.1).
- Hwang, H. G. and Lee, J. H. (2018). Secondary flows in turbulent boundary layers over longitudinal surface roughness. *Physical Review Fluids*, 3(1):014608. doi: [10.1103/PhysRevFluids.3.014608](https://doi.org/10.1103/PhysRevFluids.3.014608).
- Jayaraman, B. and Khan, S. (2020). Direct numerical simulation of turbulence over two-

- dimensional waves. *AIP Advances*, 10(2):025034. doi: [10.1063/1.5140000](https://doi.org/10.1063/1.5140000).
- Jelly, T. O., Ramani, A., Nugroho, B., Hutchins, N., and Busse, A. (2022). Impact of spanwise effective slope upon rough-wall turbulent channel flow. *Journal of Fluid Mechanics*, 951:A1. doi: [10.1017/jfm.2022.823](https://doi.org/10.1017/jfm.2022.823).
- Jiménez, J. (2004). Turbulent Flows Over Rough Walls. *Annual Review of Fluid Mechanics*, 36(1):173–196. doi: [10.1146/annurev.fluid.36.050802.122103](https://doi.org/10.1146/annurev.fluid.36.050802.122103).
- Jiménez, M. A. and Cuxart, J. (2005). Large-Eddy Simulations of the Stable Boundary Layer Using the Standard Kolmogorov Theory: Range of Applicability. *Boundary-Layer Meteorology*, 115(2):241–261. doi: [10.1007/s10546-004-3470-4](https://doi.org/10.1007/s10546-004-3470-4).
- Johansson, A. V. and Wikström, P. M. (2000). DNS and Modelling of Passive Scalar Transport in Turbulent Channel Flow with a Focus on Scalar Dissipation Rate Modelling. *Flow, Turbulence and Combustion*, 63(1):223–245. doi: [10.1023/A:1009948606944](https://doi.org/10.1023/A:1009948606944).
- Kader, B. A. (1981). Temperature and concentration profiles in fully turbulent boundary layers. *International Journal of Heat and Mass Transfer*, 24(9):1541–1544. doi: [10.1016/0017-9310\(81\)90220-9](https://doi.org/10.1016/0017-9310(81)90220-9).
- Kader, B. A. and Yaglom, A. M. (1972). Heat and mass transfer laws for fully turbulent wall flows. *International Journal of Heat and Mass Transfer*, 15(12):2329–2351. doi: [10.1016/0017-9310\(72\)90131-7](https://doi.org/10.1016/0017-9310(72)90131-7).
- Kadivar, M., Tormey, D., and McGranaghan, G. (2021). A review on turbulent flow over rough surfaces: Fundamentals and theories. *International Journal of Thermofluids*, 10:100077. doi: [10.1016/j.ijft.2021.100077](https://doi.org/10.1016/j.ijft.2021.100077).
- Kanda, M., Inagaki, A., Miyamoto, T., Gryschka, M., and Raasch, S. (2013). A New Aerodynamic Parametrization for Real Urban Surfaces. *Boundary-Layer Meteorology*, 148(2):357–377. doi: [10.1007/s10546-013-9818-x](https://doi.org/10.1007/s10546-013-9818-x).
- Kanda, M., Kanega, M., Kawai, T., Moriwaki, R., and Sugawara, H. (2007). Roughness Lengths for Momentum and Heat Derived from Outdoor Urban Scale Models. *Journal of Applied Meteorology and Climatology*, 46(7):1067–1079. doi: [10.1175/JAM2500.1](https://doi.org/10.1175/JAM2500.1).
- Kanda, M., Moriwaki, R., and Kasamatsu, F. (2004). Large-Eddy Simulation of Turbulent Organized Structures within and above Explicitly Resolved Cube Arrays. *Boundary-Layer Meteorology*, 112(2):343–368. doi: [10.1023/B:BOUN.0000027909.40439.7c](https://doi.org/10.1023/B:BOUN.0000027909.40439.7c).
- Kasagi, N., Tomita, Y., and Kuroda, A. (1992). Direct Numerical Simulation of Passive Scalar Field in a Turbulent Channel Flow. *Journal of Heat Transfer*, 114(3):598–606. doi: [10.1115/1.2911323](https://doi.org/10.1115/1.2911323).
- Kawamura, H., Abe, H., and Matsuo, Y. (1999). DNS of turbulent heat transfer in channel flow with respect to Reynolds and Prandtl number effects. *International Journal of Heat and Fluid Flow*, 20(3):196–207. doi: [10.1016/S0142-727X\(99\)00014-4](https://doi.org/10.1016/S0142-727X(99)00014-4).
- Kawamura, H., Abe, H., and Shingai, K. (2000). DNS of turbulence and heat transport in a channel flow with different Reynolds and Prandtl numbers and boundary conditions. *Proceedings of the 3rd International Symposium on Turbulence, Heat and Mass Transfer*.
- Khan, S. and Jayaraman, B. (2019). Statistical Structure and Deviations from Equilibrium in Wavy Channel Turbulence. *Fluids*, 4(3):161. doi: [10.3390/fluids4030161](https://doi.org/10.3390/fluids4030161).
- Kim, J., Kim, D., and Choi, H. (2001). An Immersed-Boundary Finite-Volume Method for Simulations of Flow in Complex Geometries. *Journal of Computational Physics*, 171(1):132–150. doi: [10.1006/jcph.2001.6778](https://doi.org/10.1006/jcph.2001.6778).
- Kim, J. and Moin, P. (1985). Application of a fractional-step method to incompressible Navier-Stokes equations. *Journal of Computational Physics*, 59(2):308–323. doi: [10.1016/0021-9991\(85\)90148-2](https://doi.org/10.1016/0021-9991(85)90148-2).
- Kim, J. and Moin, P. (1987). Transport of passive scalars in a turbulent channel flow. Technical Report NASA-TM-89463, NASA.
- Kim, J., Moin, P., and Moser, R. (1987). The Turbulence Statistics in Fully Developed



- Channel Flow at Low Reynolds Number. *Journal of Fluid Mechanics*, 177:133–166. doi: [10.1017/S0022112087000892](https://doi.org/10.1017/S0022112087000892).
- Kolmogorov, A. N. (1941). Dissipation of energy in the locally isotropic turbulence. *Dokl. Akad. Nauk. SSSR*, 32:15–17.
- Kosović, B. and Curry, J. A. (2000). A Large Eddy Simulation Study of a Quasi-Steady, Stably Stratified Atmospheric Boundary Layer. *Journal of the Atmospheric Sciences*, 57(8):1052–1068. doi: [10.1175/1520-0469\(2000\)057<1052:ALESSO>2.0.CO;2](https://doi.org/10.1175/1520-0469(2000)057<1052:ALESSO>2.0.CO;2).
- Kostelecky, J. and Ansorge, C. (2024a). Direct numerical simulation of turbulent Ekman flow with cubic small-scale surface roughness (Re=1000). doi: [10.17169/refubium-43215](https://doi.org/10.17169/refubium-43215).
- Kostelecky, J. and Ansorge, C. (2024b). Simulation and scaling analysis of periodic surfaces with small-scale roughness in turbulent Ekman flow. *Journal of Fluid Mechanics*, 992:A8. doi: [10.1017/jfm.2024.542](https://doi.org/10.1017/jfm.2024.542).
- Kostelecky, J. and Ansorge, C. (2024c). Turbulent Ekman flow with cubic small-scale surface roughness under stable stratification (Re=1000). doi: [10.17169/refubium-45292](https://doi.org/10.17169/refubium-45292).
- Kostelecky, J. and Ansorge, C. (2025). Surface Roughness in Stratified Turbulent Ekman Flow. *Boundary-Layer Meteorology*, 191(1):5. doi: [10.1007/s10546-024-00895-5](https://doi.org/10.1007/s10546-024-00895-5).
- Kundu, P., Cohen, I., and Dowling, D. (2015). *Fluid Mechanics*. Academic Press.
- Laizet, S. and Lamballais, É. (2009). High-order compact schemes for incompressible flows: A simple and efficient method with quasi-spectral accuracy. *Journal of Computational Physics*, 228(16):5989–6015. doi: [10.1016/j.jcp.2009.05.010](https://doi.org/10.1016/j.jcp.2009.05.010).
- Lamballais, É. and Silvestrini, J. (2002). Direct Numerical Simulation of Interactions Between a Mixing Layer and a Wake Around a Cylinder. *Journal of Turbulence*, 3:28. doi: [10.1088/1468-5248/3/1/028](https://doi.org/10.1088/1468-5248/3/1/028).
- Lee, J., Kim, J., Choi, H., and Yang, K.-S. (2011a). Sources of spurious force oscillations from an immersed boundary method for moving-body problems. *Journal of Computational Physics*, 230(7):2677–2695. doi: [10.1016/j.jcp.2011.01.004](https://doi.org/10.1016/j.jcp.2011.01.004).
- Lee, J. H., Sung, H. J., and Krogstad, P.-Å. (2011b). Direct numerical simulation of the turbulent boundary layer over a cube-roughened wall. *Journal of Fluid Mechanics*, 669:397–431. doi: [10.1017/S0022112010005082](https://doi.org/10.1017/S0022112010005082).
- Lee, M., Malaya, N., and Moser, R. (2013). Petascale direct numerical simulation of turbulent channel flow on up to 786K cores. In *International Conference for High Performance Computing, Networking, Storage and Analysis, SC*. doi: [10.1145/2503210.2503298](https://doi.org/10.1145/2503210.2503298).
- Lee, M. and Moser, R. D. (2015). Direct numerical simulation of turbulent channel flow up to  $Re\tau \approx 5200$ . *Journal of Fluid Mechanics*, 774:395–415. doi: [10.1017/jfm.2015.268](https://doi.org/10.1017/jfm.2015.268).
- Lee, S., Gohari, S. M. I., and Sarkar, S. (2020). Direct numerical simulation of stratified Ekman layers over a periodic rough surface. *Journal of Fluid Mechanics*, 902:A25. doi: [10.1017/jfm.2020.590](https://doi.org/10.1017/jfm.2020.590).
- Lele, S. K. (1992). Compact finite difference schemes with spectral-like resolution. *Journal of Computational Physics*, 103(1):16–42. doi: [10.1016/0021-9991\(92\)90324-R](https://doi.org/10.1016/0021-9991(92)90324-R).
- LeMone, M. A., Angevine, W. M., Bretherton, C. S., Chen, F., Dudhia, J., Fedorovich, E., Katsaros, K. B., Lenschow, D. H., Mahrt, L., Patton, E. G., Sun, J., Tjernström, M., and Weil, J. (2019). 100 Years of Progress in Boundary Layer Meteorology. *Meteorological Monographs*, 59(1):9.1–9.85. doi: [10.1175/AMSMONOGRAPHS-D-18-0013.1](https://doi.org/10.1175/AMSMONOGRAPHS-D-18-0013.1).
- Leonardi, S. and Castro, I. P. (2010). Channel flow over large cube roughness: A direct numerical simulation study. *Journal of Fluid Mechanics*, 651:519–539. doi: [10.1017/S002211200999423X](https://doi.org/10.1017/S002211200999423X).
- Leonardi, S., Orlandi, P., Smalley, R. J., Djenidi, L., and Antonia, R. A. (2003). Direct numerical simulations of turbulent channel flow with transverse square bars on one wall. *Journal of Fluid Mechanics*, 491:229–238. doi: [10.1017/S0022112003005500](https://doi.org/10.1017/S0022112003005500).
- Li, D. (2019). Turbulent Prandtl number in the atmospheric boundary layer - where are

- we now? *Atmospheric Research*, 216:86–105. doi: [10.1016/j.atmosres.2018.09.015](https://doi.org/10.1016/j.atmosres.2018.09.015).
- Li, D., Rigden, A., Salvucci, G., and Liu, H. (2017). Reconciling the Reynolds number dependence of scalar roughness length and laminar resistance. *Geophysical Research Letters*, 44(7):3193–3200. doi: [10.1002/2017GL072864](https://doi.org/10.1002/2017GL072864).
- Li, Q. and Bou-Zeid, E. (2019). Contrasts between momentum and scalar transport over very rough surfaces. *Journal of Fluid Mechanics*, 880:32–58. doi: [10.1017/jfm.2019.687](https://doi.org/10.1017/jfm.2019.687).
- Li, Q., Bou-Zeid, E., and Anderson, W. (2016). The impact and treatment of the Gibbs phenomenon in immersed boundary method simulations of momentum and scalar transport. *Journal of Computational Physics*, 310:237–251. doi: [10.1016/j.jcp.2016.01.013](https://doi.org/10.1016/j.jcp.2016.01.013).
- Li, Q., Bou-Zeid, E., Grimmond, S., Zilitinkevich, S., and Katul, G. (2020). Revisiting the relation between momentum and scalar roughness lengths of urban surfaces. *Quarterly Journal of the Royal Meteorological Society*, 146(732):3144–3164. doi: [10.1002/qj.3839](https://doi.org/10.1002/qj.3839).
- Lilly, D. K. (1966). On the Instability of Ekman Boundary Flow. *Journal of the Atmospheric Sciences*, 23(5):481–494. doi: [10.1175/1520-0469\(1966\)023<0481:OTIOEB>2.0.CO;2](https://doi.org/10.1175/1520-0469(1966)023<0481:OTIOEB>2.0.CO;2).
- Llaguno-Munitxa, M., Bou-Zeid, E., and Hultmark, M. (2017). The influence of building geometry on street canyon air flow: Validation of large eddy simulations against wind tunnel experiments. *Journal of Wind Engineering and Industrial Aerodynamics*, 165:115–130. doi: [10.1016/j.jweia.2017.03.007](https://doi.org/10.1016/j.jweia.2017.03.007).
- Lorenz, E. N. (1963). Deterministic nonperiodic flow. *Journal of atmospheric sciences*, 20(2):130–141.
- Lorenz, E. N. (1969). The predictability of a flow which possesses many scales of motion. *Tellus*, 21(3):289–307. doi: [10.3402/tellusa.v21i3.10086](https://doi.org/10.3402/tellusa.v21i3.10086).
- Ma, R., Alamé, K., and Mahesh, K. (2021). Direct numerical simulation of turbulent channel flow over random rough surfaces. *Journal of Fluid Mechanics*, 908:A40. doi: [10.1017/jfm.2020.874](https://doi.org/10.1017/jfm.2020.874).
- Mahrt, L. (1998). Stratified Atmospheric Boundary Layers and Breakdown of Models. *Theoretical and Computational Fluid Dynamics*, 11(3):263–279. doi: [10.1007/s001620050093](https://doi.org/10.1007/s001620050093).
- Mahrt, L. (1999). Stratified Atmospheric Boundary Layers. *Boundary-Layer Meteorology*, 90(3):375–396. doi: [10.1023/A:1001765727956](https://doi.org/10.1023/A:1001765727956).
- Mahrt, L. (2007). The influence of nonstationarity on the turbulent flux–gradient relationship for stable stratification. *Boundary-Layer Meteorology*, 125(2):245–264. doi: [10.1007/s10546-007-9154-0](https://doi.org/10.1007/s10546-007-9154-0).
- Mahrt, L. (2014). Stably Stratified Atmospheric Boundary Layers. *Annual Review of Fluid Mechanics*, 46(1):23–45. doi: [10.1146/annurev-fluid-010313-141354](https://doi.org/10.1146/annurev-fluid-010313-141354).
- Marlatt, S., Waggy, S., and Biringen, S. (2012). Direct Numerical Simulation of the Turbulent Ekman Layer: Evaluation of Closure Models. *Journal of the Atmospheric Sciences*, 69(3):1106–1117. doi: [10.1175/JAS-D-11-0107.1](https://doi.org/10.1175/JAS-D-11-0107.1).
- Maroneze, R., Costa, F. D., Acevedo, O. C., Medeiros, L. E., Puhales, F. S., Anabor, V., and Mortarini, L. (2023). A New Stable Boundary Layer Parameterization for Numerical Weather Prediction Models: A Heat Flux Budget Approach. *Boundary-Layer Meteorology*, 188(2):209–228. doi: [10.1007/s10546-023-00810-4](https://doi.org/10.1007/s10546-023-00810-4).
- Marusic, I., Monty, J. P., Hultmark, M., and Smits, A. J. (2013). On the logarithmic region in wall turbulence. *Journal of Fluid Mechanics*, 716:R3. doi: [10.1017/jfm.2012.511](https://doi.org/10.1017/jfm.2012.511).
- Mauritsen, T. and Svensson, G. (2007). Observations of Stably Stratified Shear-Driven Atmospheric Turbulence at Low and High Richardson Numbers. *Journal of the Atmospheric Sciences*, 64(2):645–655. doi: [10.1175/JAS3856.1](https://doi.org/10.1175/JAS3856.1).
- Mellado, J. P. and Anson, C. (2012). Factorization of the Fourier transform of the pressure-Poisson equation using finite differences in colocated grids. *ZAMM - Journal*

- of *Applied Mathematics and Mechanics / Zeitschrift für Angewandte Mathematik und Mechanik*, 92(5):380–392. doi: [10.1002/zamm.201100078](https://doi.org/10.1002/zamm.201100078).
- Mellado, J. P., Bretherton, C. S., Stevens, B., and Wyant, M. C. (2018). DNS and LES for Simulating Stratocumulus: Better Together. *Journal of Advances in Modeling Earth Systems*, 10(7):1421–1438. doi: [10.1029/2018MS001312](https://doi.org/10.1029/2018MS001312).
- Mellor, G. L. and Yamada, T. (1974). A Hierarchy of Turbulence Closure Models for Planetary Boundary Layers. *Journal of the Atmospheric Sciences*, 31(7):1791–1806. doi: [10.1175/1520-0469\(1974\)031<1791:AHOTCM>2.0.CO;2](https://doi.org/10.1175/1520-0469(1974)031<1791:AHOTCM>2.0.CO;2).
- Mellor, G. L. and Yamada, T. (1982). Development of a turbulence closure model for geophysical fluid problems. *Reviews of Geophysics*, 20(4):851–875. doi: [10.1029/RG020i004p00851](https://doi.org/10.1029/RG020i004p00851).
- Mironov, D. V. and Sullivan, P. P. (2023). Turbulence Structure and Mixing in Strongly Stable Boundary-Layer Flows over Thermally Heterogeneous Surfaces. *Boundary-Layer Meteorology*, 187(1):371–393. doi: [10.1007/s10546-022-00766-x](https://doi.org/10.1007/s10546-022-00766-x).
- Mittal, R. and Iaccarino, G. (2005). Immersed Boundary Methods. *Annual Review of Fluid Mechanics*, 37(1):239–261. doi: [10.1146/annurev.fluid.37.061903.175743](https://doi.org/10.1146/annurev.fluid.37.061903.175743).
- Miyashita, K., Iwamoto, K., and Kawamura, H. (2006). Direct Numerical Simulation of the Neutrally Stratified Turbulent Ekman Boundary Layer. *Journal of the Earth Simulator*, 6:3–15.
- Mohd-Yusof, J. (1997). Combined Immersed Boundaries/B-Splines Methods for Simulations of Flows in Complex Geometries. *Center for Turbulence Research*, pages 317–327.
- Moin, P. and Mahesh, K. (1998). DIRECT NUMERICAL SIMULATION: A Tool in Turbulence Research. *Annual Review of Fluid Mechanics*, 30(1):539–578. doi: [10.1146/annurev.fluid.30.1.539](https://doi.org/10.1146/annurev.fluid.30.1.539).
- Monin, A. S. (1970). The Atmospheric Boundary Layer. *Annual Review of Fluid Mechanics*, 2(1):225–250. doi: [10.1146/annurev.fl.02.010170.001301](https://doi.org/10.1146/annurev.fl.02.010170.001301).
- Monin, A. S. and Obukhov, A. M. (1954). Basic laws of turbulent mixing in the surface layer of the atmosphere. *Contrib. Geophys. Inst. Acad. Sci. USSR*, 151(163):e187.
- Monin, A. S. and Yaglom, A. M. (1971). *Statistical fluid mechanics: mechanics of turbulence*. MIT Press, Cambridge, Mass, english ed. updated, augmented and rev edition.
- Nagano, Y., Hattori, H., and Houra, T. (2004). DNS of velocity and thermal fields in turbulent channel flow with transverse-rib roughness. *International Journal of Heat and Fluid Flow*, 25(3):393–403. doi: [10.1016/j.ijheatfluidflow.2004.02.011](https://doi.org/10.1016/j.ijheatfluidflow.2004.02.011).
- Nagib, H. M. and Chauhan, K. A. (2008). Variations of von Kármán coefficient in canonical flows. *Physics of Fluids*, 20(10):101518. doi: [10.1063/1.3006423](https://doi.org/10.1063/1.3006423).
- Nieuwstadt, F. T. M. (1984). The Turbulent Structure of the Stable, Nocturnal Boundary Layer. *Journal of the Atmospheric Sciences*, 41(14):2202–2216. doi: [10.1175/1520-0469\(1984\)041<2202:TTSOTS>2.0.CO;2](https://doi.org/10.1175/1520-0469(1984)041<2202:TTSOTS>2.0.CO;2).
- Nieuwstadt, F. T. M. (2005). Direct Numerical Simulation of Stable Channel Flow at Large Stability. *Boundary-Layer Meteorology*, 116(2):277–299. doi: [10.1007/s10546-004-2818-0](https://doi.org/10.1007/s10546-004-2818-0).
- Nikuradse, J. (1932). *Gesetzmässigkeiten Der Turbulenten Strömung in Glatten Rohren*. VDI-Forschungsheft No. 356. VDI-Verlag.
- Nikuradse, J. (1933). Laws of Flow in Rough Pipes. *NACA Technical Memorandum 1295*.
- Obukhov, A. M. (1941). O Raspredelenie energii w spektre turbulentnowo potoka. *Izvestija Akademii Nauk SSSR*, 1941(4-5):453–466.
- Obukhov, A. M. (1946). Turbulence in an atmosphere with inhomogeneous temperature. *Tr. Inst. Teor. Geofis. Akad. Nauk. SSSR*, 1:95–115.
- Obukhov, A. M. (1971). Turbulence in an atmosphere with a non-uniform temperature.

- Boundary-Layer Meteorology*, 2(1):7–29. doi: [10.1007/BF00718085](https://doi.org/10.1007/BF00718085).
- Paeschke, W. (1937). Experimentelle Untersuchungen zum Rauigkeitsproblem in der bodennahen Luftschicht. *Zeitschrift für Geophysik*, 13:14–21.
- Pardyjak, E. R., Monti, P., and Fernando, H. J. S. (2002). Flux Richardson number measurements in stable atmospheric shear flows. *Journal of Fluid Mechanics*, 459:307–316. doi: [10.1017/S0022112002008406](https://doi.org/10.1017/S0022112002008406).
- Parnaudeau, P., Carlier, J., Heitz, D., and Lamballais, E. (2008). Experimental and numerical studies of the flow over a circular cylinder at Reynolds number 3900. *Physics of Fluids*, 20(8):085101. doi: [10.1063/1.2957018](https://doi.org/10.1063/1.2957018).
- Parnaudeau, P., Lamballais, E., Heitz, D., and Silvestrini, J. H. (2004). Combination of the Immersed Boundary Method with Compact Schemes for DNS of Flows in Complex Geometry. In Friedrich, R., Geurts, B. J., and Métais, O., editors, *Direct and Large-Eddy Simulation V*, ERCOFTAC Series, pages 581–590, Dordrecht. Springer Netherlands. doi: [10.1007/978-1-4020-2313-2\\_61](https://doi.org/10.1007/978-1-4020-2313-2_61).
- Perot, J. B. (1993). An Analysis of the Fractional Step Method. *Journal of Computational Physics*, 108(1):51–58. doi: [10.1006/jcph.1993.1162](https://doi.org/10.1006/jcph.1993.1162).
- Perret, L., Basley, J., Mathis, R., and Piquet, T. (2019). The Atmospheric Boundary Layer Over Urban-Like Terrain: Influence of the Plan Density on Roughness Sublayer Dynamics. *Boundary-Layer Meteorology*, 170(2):205–234. doi: [10.1007/s10546-018-0396-9](https://doi.org/10.1007/s10546-018-0396-9).
- Peskin, C. S. (1972). Flow patterns around heart valves: A numerical method. *Journal of Computational Physics*, 10(2):252–271. doi: [10.1016/0021-9991\(72\)90065-4](https://doi.org/10.1016/0021-9991(72)90065-4).
- Peskin, C. S. (1977). Numerical analysis of blood flow in the heart. *Journal of Computational Physics*, 25(3):220–252. doi: [10.1016/0021-9991\(77\)90100-0](https://doi.org/10.1016/0021-9991(77)90100-0).
- Peskin, C. S. (2002). The immersed boundary method. *Acta Numerica*, 11:479–517. doi: [10.1017/S0962492902000077](https://doi.org/10.1017/S0962492902000077).
- Petenko, I., Argentini, S., Casasanta, G., Genthon, C., and Kallistratova, M. (2019). Stable Surface-Based Turbulent Layer During the Polar Winter at Dome C, Antarctica: Sodar and In Situ Observations. *Boundary-Layer Meteorology*, 171(1):101–128. doi: [10.1007/s10546-018-0419-6](https://doi.org/10.1007/s10546-018-0419-6).
- Piomelli, U. (2019). Recent advances in the numerical simulation of rough-wall boundary layers. *Physics and Chemistry of the Earth, Parts A/B/C*, 113:63–72. doi: [10.1016/j.pce.2018.10.005](https://doi.org/10.1016/j.pce.2018.10.005).
- Pirozzoli, S., Bernardini, M., and Orlandi, P. (2016). Passive scalars in turbulent channel flow at high Reynolds number. *Journal of Fluid Mechanics*, 788:614–639. doi: [10.1017/jfm.2015.711](https://doi.org/10.1017/jfm.2015.711).
- Pirozzoli, S., Romero, J., Fatica, M., Verzicco, R., and Orlandi, P. (2022). DNS of passive scalars in turbulent pipe flow. *Journal of Fluid Mechanics*, 940:A45. doi: [10.1017/jfm.2022.265](https://doi.org/10.1017/jfm.2022.265).
- Placidi, M. and Ganapathisubramani, B. (2015). Effects of frontal and plan solidities on aerodynamic parameters and the roughness sublayer in turbulent boundary layers. *Journal of Fluid Mechanics*, 782:541–566. doi: [10.1017/jfm.2015.552](https://doi.org/10.1017/jfm.2015.552).
- Pope, S. B. (2000). *Turbulent Flows*. Cambridge University Press, Cambridge; New York.
- Prandtl, L. (1925). 7. Bericht über Untersuchungen zur ausgebildeten Turbulenz. *ZAMM - Journal of Applied Mathematics and Mechanics / Zeitschrift für Angewandte Mathematik und Mechanik*, 5(2):136–139. doi: [10.1002/zamm.19250050212](https://doi.org/10.1002/zamm.19250050212).
- Prandtl, L. (1932). Zur turbulenten Strömung in Rohren und längs Platten. In *Ergebnisse der aerodynamischen Versuchsanstalt zu Göttingen Lfg. 4*, pages 18–29. De Gruyter. doi: [10.1007/978-3-662-11836-8](https://doi.org/10.1007/978-3-662-11836-8).
- Prandtl, L. (1952). Essentials of fluid dynamics. *Blackie and Son*, 79:570.



- Quadrio, M., Frohnapfel, B., and Hasegawa, Y. (2016). Does the choice of the forcing term affect flow statistics in DNS of turbulent channel flow? *European Journal of Mechanics - B/Fluids*, 55:286–293. doi: [10.1016/j.euromechflu.2015.09.005](https://doi.org/10.1016/j.euromechflu.2015.09.005).
- Raupach, M. R., Antonia, R. A., and Rajagopalan, S. (1991). Rough-Wall Turbulent Boundary Layers. *Applied Mechanics Reviews*, 44(1):1–25. doi: [10.1115/1.3119492](https://doi.org/10.1115/1.3119492).
- Resseguier, V., Mémin, E., Heitz, D., and Chapron, B. (2017). Stochastic modelling and diffusion modes for proper orthogonal decomposition models and small-scale flow analysis. *Journal of Fluid Mechanics*, 826:888–917. doi: [10.1017/jfm.2017.467](https://doi.org/10.1017/jfm.2017.467).
- Reynolds, O. (1895). On the dynamical theory of incompressible viscous fluids and the determination of the criterion. *Philosophical Transactions of the Royal Society of London. (A.)*, 186:123–164.
- Rossby, C.-G. and Montgomery, R. B. (1935). *The Layer of Frictional Influence in Wind and Ocean Currents*. Massachusetts Institute of Technology and Woods Hole Oceanographic Institution, Cambridge and Woods Hole, MA. doi: [10.1575/1912/1157](https://doi.org/10.1575/1912/1157).
- Rotta, J. C. (1972). *Turbulente Strömungen: eine Einführung in die Theorie und ihre Anwendung*. Number 15 in Leitfäden der angewandten Mathematik und Mechanik. Teubner, Stuttgart.
- Roy, S., De, A., and Balaras, E., editors (2020). *Immersed Boundary Method : Development and Applications*. Computational Methods in Engineering & the Sciences. Springer Singapore. doi: [10.1007/978-981-15-3940-4](https://doi.org/10.1007/978-981-15-3940-4).
- Runge, C. (1901). Über empirische Funktionen und die Interpolation zwischen äquidistanten Ordinaten. *Zeitschrift für Mathematik und Physik*, 46:224–243.
- Saiki, E. M. and Biringen, S. (1996). Numerical Simulation of a Cylinder in Uniform Flow: Application of a Virtual Boundary Method. *Journal of Computational Physics*, 123(2):450–465. doi: [10.1006/jeph.1996.0036](https://doi.org/10.1006/jeph.1996.0036).
- Sandu, I., Beljaars, A., Bechtold, P., Mauritsen, T., and Balsamo, G. (2013). Why is it so difficult to represent stably stratified conditions in numerical weather prediction (NWP) models? *Journal of Advances in Modeling Earth Systems*, 5(2):117–133. doi: [10.1002/jame.20013](https://doi.org/10.1002/jame.20013).
- Schäfer, K., Forooghi, P., Straub, S., Frohnapfel, B., and Stroh, A. (2020). Direct Numerical Simulations of a Turbulent Flow over Wall-Mounted Obstacles—A Comparison of Different Numerical Approaches. In García-Villalba, M., Kuerten, H., and Salvetti, M. V., editors, *Direct and Large Eddy Simulation XII*, volume 27, pages 91–96. Springer International Publishing, Cham. doi: [10.1007/978-3-030-42822-8\\_12](https://doi.org/10.1007/978-3-030-42822-8_12).
- Schäfer, K., Frohnapfel, B., and Mellado, J. P. (2022a). The effect of spanwise heterogeneous surfaces on mixed convection in turbulent channels. *Journal of Fluid Mechanics*, 950:A22. doi: [10.1017/jfm.2022.773](https://doi.org/10.1017/jfm.2022.773).
- Schäfer, K., Stroh, A., Forooghi, P., and Frohnapfel, B. (2022b). Modelling spanwise heterogeneous roughness through a parametric forcing approach. *Journal of Fluid Mechanics*, 930:A7. doi: [10.1017/jfm.2021.850](https://doi.org/10.1017/jfm.2021.850).
- Schäfer, K., Stroh, A., Frohnapfel, B., and Gatti, D. (2019). Investigation of turbulent budgets in channels with secondary motions induced by streamwise-aligned ridges. In *11th International Symposium on Turbulence and Shear Flow Phenomena (TSFP11)*, Southampton, UK, July 30 - August 2, 2019.
- Schlichting, H. (1936). Experimentelle Untersuchungen zum Rauigkeitsproblem. *Ingenieur-Archiv*, 7(1):1–34. doi: [10.1007/BF02084166](https://doi.org/10.1007/BF02084166).
- Schumann, U. and Gerz, T. (1995). Turbulent Mixing in Stably Stratified Shear Flows. *Journal of Applied Meteorology and Climatology*, 34(1):33–48. doi: [10.1175/1520-0450-34.1.33](https://doi.org/10.1175/1520-0450-34.1.33).
- Shah, S. K. and Bou-Zeid, E. (2014). Direct numerical simulations of turbulent Ekman

- layers with increasing static stability: Modifications to the bulk structure and second-order statistics. *Journal of Fluid Mechanics*, 760:494–539. doi: [10.1017/jfm.2014.597](https://doi.org/10.1017/jfm.2014.597).
- Shao, Y. and Yang, Y. (2008). A theory for drag partition over rough surfaces. *Journal of Geophysical Research*, 113(F2):F02S05. doi: [10.1029/2007JF000791](https://doi.org/10.1029/2007JF000791).
- Shingai, K. and Kawamura, H. (2004). A study of turbulence structure and large-scale motion in the Ekman layer through direct numerical simulations. *Journal of Turbulence*, 5(1):1–18. doi: [10.1088/1468-5248/5/1/013](https://doi.org/10.1088/1468-5248/5/1/013).
- Shukla, R. K. and Zhong, X. (2005). Derivation of high-order compact finite difference schemes for non-uniform grid using polynomial interpolation. *Journal of Computational Physics*, 204(2):404–429. doi: [10.1016/j.jcp.2004.10.014](https://doi.org/10.1016/j.jcp.2004.10.014).
- Soleimani, S. and Eckels, S. (2021). A review of drag reduction and heat transfer enhancement by riblet surfaces in closed and open channel flow. *International Journal of Thermofluids*, 9:100053. doi: [10.1016/j.ijft.2020.100053](https://doi.org/10.1016/j.ijft.2020.100053).
- Sorbjan, Z. and Grachev, A. A. (2010). An Evaluation of the Flux–Gradient Relationship in the Stable Boundary Layer. *Boundary-Layer Meteorology*, 135(3):385–405. doi: [10.1007/s10546-010-9482-3](https://doi.org/10.1007/s10546-010-9482-3).
- Spalart, P. R. (1989). Theoretical and numerical study of a three-dimensional turbulent boundary layer. *Journal of Fluid Mechanics*, 205:319–340. doi: [10.1017/S0022112089002053](https://doi.org/10.1017/S0022112089002053).
- Spalart, P. R., Coleman, G. N., and Johnstone, R. (2008). Direct numerical simulation of the Ekman layer: A step in Reynolds number, and cautious support for a log law with a shifted origin. *Physics of Fluids*, 20(10):101507. doi: [10.1063/1.3005858](https://doi.org/10.1063/1.3005858).
- Spalart, P. R., Coleman, G. N., and Johnstone, R. (2009). Retraction: “Direct numerical simulation of the Ekman layer: A step in Reynolds number, and cautious support for a log law with a shifted origin” [Phys. Fluids 20, 101507 (2008)]. *Physics of Fluids*, 21(10):109901. doi: [10.1063/1.3247176](https://doi.org/10.1063/1.3247176).
- Spiegel, E. A. and Veronis, G. (1960). On the Boussinesq Approximation for a Compressible Fluid. *The Astrophysical Journal*, 131:442. doi: [10.1086/146849](https://doi.org/10.1086/146849).
- Spurk, J. and Aksel, N. (2010). *Strömungslehre*. Springer-Lehrbuch. Springer Berlin Heidelberg, Berlin, Heidelberg. doi: [10.1007/978-3-642-13143-1](https://doi.org/10.1007/978-3-642-13143-1).
- Squire, D. T., Morrill-Winter, C., Hutchins, N., Schultz, M. P., Klewicki, J. C., and Marusic, I. (2016). Comparison of turbulent boundary layers over smooth and rough surfaces up to high Reynolds numbers. *Journal of Fluid Mechanics*, 795:210–240. doi: [10.1017/jfm.2016.196](https://doi.org/10.1017/jfm.2016.196).
- Steenefeld, G.-J. (2014). Current challenges in understanding and forecasting stable boundary layers over land and ice. *Frontiers in Environmental Science*, 2(41):1–6. doi: [10.3389/fenvs.2014.00041](https://doi.org/10.3389/fenvs.2014.00041).
- Stefanello, M., Frantz, R. A. S., Acevedo, O., Degrazia, G., and Silvestrini, J. H. (2022). Horizontal meandering in direct numerical simulations of the stable boundary layer. *Quarterly Journal of the Royal Meteorological Society*, 148(749):3604–3621. doi: [10.1002/qj.4376](https://doi.org/10.1002/qj.4376).
- Stiperski, I. and Calaf, M. (2018). Dependence of near-surface similarity scaling on the anisotropy of atmospheric turbulence. *Quarterly Journal of the Royal Meteorological Society*, 144(712):641–657. doi: [10.1002/qj.3224](https://doi.org/10.1002/qj.3224).
- Stopa, J. E., Wang, C., Vandemark, D., Foster, R., Mouche, A., and Chapron, B. (2022). Automated Global Classification of Surface Layer Stratification Using High-Resolution Sea Surface Roughness Measurements by Satellite Synthetic Aperture Radar. *Geophysical Research Letters*, 49(12):1–11. doi: [10.1029/2022GL098686](https://doi.org/10.1029/2022GL098686).
- Stroh, A., Hasegawa, Y., Kriegseis, J., and Frohnapfel, B. (2016). Secondary vortices over surfaces with spanwise varying drag. *Journal of Turbulence*, 17(12):1142–1158. doi: [10.1017/jfm.2016.196](https://doi.org/10.1017/jfm.2016.196).



- 10.1080/14685248.2016.1235277.
- Stroh, A., Schäfer, K., Forooghi, P., and Frohnapfel, B. (2020a). Secondary flow and heat transfer in turbulent flow over streamwise ridges. *International Journal of Heat and Fluid Flow*, 81:108518. doi: 10.1016/j.ijheatfluidflow.2019.108518.
- Stroh, A., Schäfer, K., Frohnapfel, B., and Forooghi, P. (2020b). Rearrangement of secondary flow over spanwise heterogeneous roughness. *Journal of Fluid Mechanics*, 885:R5. doi: 10.1017/jfm.2019.1030.
- Stull, R. B. (1988). *An Introduction to Boundary Layer Meteorology*. Atmospheric Sciences Library. Kluwer Academic Publishers, Dordrecht ; Boston.
- Subramanian, C. S. and Antonia, R. A. (1981). Effect of Reynolds number on a slightly heated turbulent boundary layer. *International Journal of Heat and Mass Transfer*, 24(11):1833–1846. doi: 10.1016/0017-9310(81)90149-6.
- Sun, J., Mahrt, L., Banta, R. M., and Pichugina, Y. L. (2012). Turbulence Regimes and Turbulence Intermittency in the Stable Boundary Layer during CASES-99. *Journal of the Atmospheric Sciences*, 69(1):338–351. doi: 10.1175/JAS-D-11-082.1.
- Svensson, G., Holtslag, A. A. M., Kumar, V., Mauritsen, T., Steeneveld, G. J., Angevine, W. M., Bazile, E., Beljaars, A., de Bruijn, E. I. F., Cheng, A., Conangla, L., Cuxart, J., Ek, M., Falk, M. J., Freedman, F., Kitagawa, H., Larson, V. E., Lock, A., Mailhot, J., Masson, V., Park, S., Pleim, J., Söderberg, S., Weng, W., and Zampieri, M. (2011). Evaluation of the Diurnal Cycle in the Atmospheric Boundary Layer Over Land as Represented by a Variety of Single-Column Models: The Second GABLS Experiment. *Boundary-Layer Meteorology*, 140(2):177–206. doi: 10.1007/s10546-011-9611-7.
- Témam, R. (1969). Sur l’approximation de la solution des équations de Navier-Stokes par la méthode des pas fractionnaires (II). *Archive for Rational Mechanics and Analysis*, 33(5):377–385. doi: 10.1007/BF00247696.
- Tennekes, H. and Lumley, J. L. (1972). *A First Course in Turbulence*. MIT Press, Cambridge, Mass.
- Theobald, F., Schäfer, K., Yang, J., Frohnapfel, B., Stripf, M., Forooghi, P., and Stroh, A. (2021). Comparison of Different Solvers and Geometry Representation Strategies for Dns of Rough Wall Channel Flow. In *14th WCCM-ECCOMAS Congress*. CIMNE. doi: 10.23967/wccm-eccomas.2020.089.
- Thomas, L. H. (1949). Elliptic problems in linear difference equations over a network. Watson Sci. Comput. Lab. Rept., Columbia University, New York 1.
- Townsend, A. A. (1961). Equilibrium layers and wall turbulence. *Journal of Fluid Mechanics*, 11(1):97–120. doi: 10.1017/S0022112061000883.
- Townsend, A. A. (1976). *The Structure of Turbulent Shear Flow*. Cambridge University Press, Cambridge, 2nd ed edition.
- Tritton, D. J. (1977). *Physical Fluid Dynamics*. Springer Netherlands, Dordrecht. doi: 10.1007/978-94-009-9992-3.
- Tseng, Y.-H., Meneveau, C., and Parlange, M. B. (2006). Modeling Flow around Bluff Bodies and Predicting Urban Dispersion Using Large Eddy Simulation. *Environmental Science & Technology*, 40(8):2653–2662. doi: 10.1021/es051708m.
- Vallis, G. K. (2017). *Atmospheric and Oceanic Fluid Dynamics: Fundamentals and Large-Scale Circulation*. Cambridge University Press, Cambridge, 2 edition. doi: 10.1017/9781107588417.
- Van de Wiel, B. J. H., Moene, A. F., De Ronde, W. H., and Jonker, H. J. J. (2008). Local Similarity in the Stable Boundary Layer and Mixing-Length Approaches: Consistency of Concepts. *Boundary-Layer Meteorology*, 128(1):103–116. doi: 10.1007/s10546-008-9277-y.
- Van de Wiel, B. J. H., Moene, A. F., and Jonker, H. J. J. (2012a). The Cessation of

- Continuous Turbulence as Precursor of the Very Stable Nocturnal Boundary Layer. *Journal of the Atmospheric Sciences*, 69(11):3097–3115. doi: [10.1175/JAS-D-12-064.1](https://doi.org/10.1175/JAS-D-12-064.1).
- Van de Wiel, B. J. H., Moene, A. F., Jonker, H. J. J., Baas, P., Basu, S., Donda, J. M. M., Sun, J., and Holtslag, A. a. M. (2012b). The Minimum Wind Speed for Sustainable Turbulence in the Nocturnal Boundary Layer. *Journal of the Atmospheric Sciences*, 69(11):3116–3127. doi: [10.1175/JAS-D-12-0107.1](https://doi.org/10.1175/JAS-D-12-0107.1).
- Van de Wiel, B. J. H., Moene, A. F., Ronda, R. J., Bruin, H. A. R. D., and Holtslag, A. a. M. (2002). Intermittent Turbulence and Oscillations in the Stable Boundary Layer over Land. Part II: A System Dynamics Approach. *Journal of the Atmospheric Sciences*, 59(17):2567–2581. doi: [10.1175/1520-0469\(2002\)059<2567:ITAOIT>2.0.CO;2](https://doi.org/10.1175/1520-0469(2002)059<2567:ITAOIT>2.0.CO;2).
- Van der Linden, S., Van de Wiel, B. J. H., Petenko, I., Van Heerwaarden, C. C., Baas, P., and Jonker, H. J. J. (2020). A Businger Mechanism for Intermittent Bursting in the Stable Boundary Layer. *Journal of the Atmospheric Sciences*, 77(10):3343–3360. doi: [10.1175/JAS-D-19-0309.1](https://doi.org/10.1175/JAS-D-19-0309.1).
- Van Hooijdonk, I. G. S., Clercx, H. J. H., Ansorge, C., Moene, A. F., and Van de Wiel, B. J. H. (2018). Parameters for the Collapse of Turbulence in the Stratified Plane Couette Flow. *Journal of the Atmospheric Sciences*, 75(9):3211–3231. doi: [10.1175/JAS-D-17-0335.1](https://doi.org/10.1175/JAS-D-17-0335.1).
- Vanderwel, C., Stroh, A., Kriegseis, J., Frohnapfel, B., and Ganapathisubramani, B. (2019). The instantaneous structure of secondary flows in turbulent boundary layers. *Journal of Fluid Mechanics*, 862:845–870. doi: [10.1017/jfm.2018.955](https://doi.org/10.1017/jfm.2018.955).
- Venayagamoorthy, S. K. and Stretch, D. D. (2010). On the turbulent Prandtl number in homogeneous stably stratified turbulence. *Journal of Fluid Mechanics*, 644:359–369. doi: [10.1017/S002211200999293X](https://doi.org/10.1017/S002211200999293X).
- Vercauteren, N., Boyko, V., Faranda, D., and Stiperski, I. (2019). Scale interactions and anisotropy in stable boundary layers. *Quarterly Journal of the Royal Meteorological Society*, 145(722):1799–1813. doi: [10.1002/qj.3524](https://doi.org/10.1002/qj.3524).
- Vignon, E., Van de Wiel, B. J. H., Van, I. G. S., Genthon, C., Van der Linden, S. J. A., Van Hooft, J. A., Baas, P., Maurel, W., Traullé, O., and Casasanta, G. (2017). Stable boundary-layer regimes at Dome C, Antarctica: Observation and analysis. *Quarterly Journal of the Royal Meteorological Society*, 143(704):1241–1253. doi: [10.1002/qj.2998](https://doi.org/10.1002/qj.2998).
- Vitart, F. (2014). Evolution of ECMWF sub-seasonal forecast skill scores: Evolution of the ECMWF Sub-Seasonal Forecast Skill. *Quarterly Journal of the Royal Meteorological Society*, 140(683):1889–1899. doi: [10.1002/qj.2256](https://doi.org/10.1002/qj.2256).
- Von Kármán, T. (1930). Mechanische Ähnlichkeit und turbulenz. *Nachrichten von der Gesellschaft der Wissenschaften zu Göttingen, Mathematisch-Physikalische Klasse*, 1930:58–76.
- Vreman, A. W. and Kuerten, J. G. M. (2014). Comparison of direct numerical simulation databases of turbulent channel flow at  $Re\tau = 180$ . *Physics of Fluids*, 26(1):015102. doi: [10.1063/1.4861064](https://doi.org/10.1063/1.4861064).
- Watanabe, T. and Nagata, K. (2021). Large-scale characteristics of a stably stratified turbulent shear layer. *Journal of Fluid Mechanics*, 927:A27. doi: [10.1017/jfm.2021.773](https://doi.org/10.1017/jfm.2021.773).
- Watanabe, T., Riley, J. J., Nagata, K., Matsuda, K., and Onishi, R. (2019). Hairpin vortices and highly elongated flow structures in a stably stratified shear layer. *Journal of Fluid Mechanics*, 878:37–61. doi: [10.1017/jfm.2019.577](https://doi.org/10.1017/jfm.2019.577).
- Weber, R. O. and Kaufmann, P. (1998). Relationship of Synoptic Winds and Complex Terrain Flows during the MISTRAL Field Experiment. *Journal of Applied Meteorology and Climatology*, 37(11):1486–1496. doi: [10.1175/1520-0450\(1998\)037<1486:ROSWAC>2.0.CO;2](https://doi.org/10.1175/1520-0450(1998)037<1486:ROSWAC>2.0.CO;2).
- Whiteman, C. D. and Doran, J. C. (1993). The Relationship between Overlying Synoptic-

- Scale Flows and Winds within a Valley. *Journal of Applied Meteorology and Climatology*, 32(11):1669–1682. doi: [10.1175/1520-0450\(1993\)032<1669:TRBOSS>2.0.CO;2](https://doi.org/10.1175/1520-0450(1993)032<1669:TRBOSS>2.0.CO;2).
- Williamson, J. H. (1980). Low-storage Runge-Kutta schemes. *Journal of Computational Physics*, 35(1):48–56. doi: [10.1016/0021-9991\(80\)90033-9](https://doi.org/10.1016/0021-9991(80)90033-9).
- Wilson, R. V., Demuren, A. O., and Carpenter, M. (1998). Higher-Order Compact Schemes for Numerical Simulation of Incompressible Flows. Technical Report NAS 1.26:206922.
- Wippermann, F. and Gross, G. (1981). Construction of orographically influenced wind roses for given distributions of the large-scale wind. *Contrib. Atmos. Phys.; (Germany, Federal Republic of)*, 54:4.
- Wyngaard, J. C. (1973). On surface layer turbulence. In Haugen, D. H., editor, *Workshop on Micrometeorology, Ed.*, page 392. American Meteorological Society.
- Wyngaard, J. C. (2010). *Turbulence in the Atmosphere*. Cambridge University Press, Cambridge. doi: [10.1017/CBO9780511840524](https://doi.org/10.1017/CBO9780511840524).
- Xiao, H., Wu, J.-L., Laizet, S., and Duan, L. (2020). Flows over periodic hills of parameterized geometries: A dataset for data-driven turbulence modeling from direct simulations. *Computers & Fluids*, 200:104431. doi: [10.1016/j.compfluid.2020.104431](https://doi.org/10.1016/j.compfluid.2020.104431).
- Xie, Z.-T., Coceal, O., and Castro, I. P. (2008). Large-Eddy Simulation of Flows over Random Urban-like Obstacles. *Boundary-Layer Meteorology*, 129(1):1–23. doi: [10.1007/s10546-008-9290-1](https://doi.org/10.1007/s10546-008-9290-1).
- Yagüe, C., Maqueda, G., and Rees, J. M. (2001). Characteristics of turbulence in the lower atmosphere at Halley IV station, Antarctica. *Dynamics of Atmospheres and Oceans*, 34(2):205–223. doi: [10.1016/S0377-0265\(01\)00068-9](https://doi.org/10.1016/S0377-0265(01)00068-9).
- Yakhot, V. and Orszag, S. A. (1986). Renormalization group analysis of turbulence. I. Basic theory. *Journal of Scientific Computing*, 1(1):3–51. doi: [10.1007/BF01061452](https://doi.org/10.1007/BF01061452).
- Yang, X. I. A., Sadique, J., Mittal, R., and Meneveau, C. (2016). Exponential roughness layer and analytical model for turbulent boundary layer flow over rectangular-prism roughness elements. *Journal of Fluid Mechanics*, 789:127–165. doi: [10.1017/jfm.2015.687](https://doi.org/10.1017/jfm.2015.687).
- Zanoun, E.-S., Durst, F., and Nagib, H. (2003). Evaluating the law of the wall in two-dimensional fully developed turbulent channel flows. *Physics of Fluids*, 15(10):3079–3089. doi: [10.1063/1.1608010](https://doi.org/10.1063/1.1608010).
- Zilitinkevich, S. (1995). Non-local Turbulent Transport: Pollution Dispersion Aspects Of Coherent Structure Of Connective Flows. In *Air Pollution 1995*, pages 53–60, Porto Carras, Greece. doi: [10.2495/AIR950071](https://doi.org/10.2495/AIR950071).
- Zilitinkevich, S. S., Elperin, T., Kleorin, N., Rogachevskii, I., Esau, I., Mauritsen, T., and Miles, M. W. (2008). Turbulence energetics in stably stratified geophysical flows: Strong and weak mixing regimes. *Quarterly Journal of the Royal Meteorological Society*, 134(633):793–799. doi: [10.1002/qj.264](https://doi.org/10.1002/qj.264).
- Zilitinkevich, S. S., Tyuryakov, S. A., Troitskaya, Yu. I., and Mareev, E. A. (2012). Theoretical models of the height of the atmospheric boundary layer and turbulent entrainment at its upper boundary. *Izvestiya, Atmospheric and Oceanic Physics*, 48(1):133–142. doi: [10.1134/S0001433812010148](https://doi.org/10.1134/S0001433812010148).
- Zonta, F. and Soldati, A. (2018). Stably Stratified Wall-Bounded Turbulence. *Applied Mechanics Reviews*, 70(4):040801. doi: [10.1115/1.4040838](https://doi.org/10.1115/1.4040838).

# Nomenclature

## Abbreviations

Acronym	Description
<b>ABL</b>	Atmospheric boundary layer
<b>ADR</b>	Alternating direction reconstruction
<b>ASL</b>	Atmospheric surface layer
<b>CFD</b>	Computational fluid dynamics
<b>CFL</b>	Courant–Friedrichs–Lewy number
<b>CFR</b>	Constant flow rate
<b>CPG</b>	Constant pressure gradient
<b>CPI</b>	Constant power input
<b>DNS</b>	Direct numerical simulation
<b>GCM</b>	General circulation model
<b>HPC</b>	High-performance computing
<b>IBM</b>	Immersed boundary method
<b>LES</b>	Large-eddy simulation
<b>LHS</b>	Left-hand side
<b>ML</b>	Mixed layer
<b>MOST</b>	Monin–Obukhov Similarity Theory
<b>MSHF</b>	Maximum sustainable heat flux
<b>NSE</b>	Navier–Stokes equations
<b>NWP</b>	Numerical weather prediction
<b>PDE</b>	Partial differential equation
<b>RHS</b>	Right-hand side
<b>RAM</b>	Random-access memory
<b>RANS</b>	Reynolds-averaged Navier–Stokes equations
<b>RK</b>	Runge–Kutta scheme
<b>rms</b>	Root-mean-square
<b>SBL</b>	Stably stratified planetary boundary layer
<b>SFOs</b>	Spurious force oscillations
<b>TIER</b>	Categorization of European HPC facilities in 3 tiers
<b>TKE</b>	Turbulent kinetic energy
<b>VSBL</b>	Very stable boundary layer
<b>WSBL</b>	Weakly stable boundary layer

## List of Greek Symbols and Variables

Symbol	Description
$\alpha_*$	angle between wall shear stress and geostrophic wind
$\beta_1, \beta_2$	parameters of the feedback forcing IBM
$\beta_{\text{buf}}$	buffer parameter
$\gamma$	volume fraction
$\Gamma_{\mathbb{F}}$	interface of the fluid region
$\Gamma_{\mathbb{S}}$	interface of the solid region (immersed object)
$\delta$	turbulent boundary layer thickness (in chapter 3, half-channel height)
$\delta_{\text{eff}}$	effective half-channel height
$\delta_{\text{melt}}$	meltdown height of the surface roughness
$\delta_{ij}$	Kronecker delta
$\delta_v$	viscous length scale
$\delta_*$	non-dimensional turbulent boundary layer thickness
$\Delta x, \Delta y, \Delta z$	spacing between two neighboring grid points, grid resolution
$\Delta B$	constant buoyancy difference between upper and lower wall
$\Delta S$	constant passive scalar difference between upper and lower wall
$\Delta U$	roughness function of the log-law
$\epsilon$	indicator function of the roughness geometry (velocity grid)
$\epsilon_p$	indicator function of the roughness geometry (pressure grid)
$\epsilon_{\text{dis}}$	energy dissipation rate
$\epsilon_{ijk}$	Levi–Civita symbol
$\zeta$	non-dimensional stability parameter
$\eta$	Kolmogorov length scale
$\Theta$	potential temperature
$\Theta_{\text{sfc}}$	potential temperature of the surface layer
$\kappa$	von Kármán constant
$\kappa_d$	thermal diffusivity
$\Lambda_{Ro}$	Rossby radius
$\mu$	dynamic viscosity
$\nu$	kinematic viscosity
$\nu_{\text{eff}}$	effective kinematic viscosity
$\xi$	enstrophy
$\pi$	modified non-hydrostatic pressure
$\rho$	fluid density
$\sigma$	buffer coefficient
$\tau$	time increment of Runge–Kutta scheme
$\tau_w$	wall shear stress
$\tau_*$	non-dimensional wall shear stress
$\phi$	latitude
$\phi_n$	discrete pressure from the Poisson solver
$\Phi$	stability correction function
$\varphi$	flow variable (e.g. velocity, temperature, buoyancy)
$\psi$	integrated universal function of the log-law
$\Psi, \Psi_I, \Psi_R, \Psi_W$	universal functions of the log-law
$\omega_j$	vorticity vector
$\Omega_i$	rotation vector

## List of Latin Symbols and Variables

Symbol	Description
$a_{ij}, b_j, c_j$	Runge–Kutta parameters
$\mathbf{A}_x, \mathbf{B}_x, \mathbf{C}_x, \mathbf{D}_x$	narrow banded matrices (compact schemes)
$A, A_R, \tilde{A}_R, B$	universal constants for the smooth (rough) log-law
$b$	buoyancy
$b_\star$	friction buoyancy
$\mathcal{B}_i$	Burgers operator in $i$ -direction
$c_{ij}$	prefactors for numerical discretization schemes
$c_s$	speed of sound
$c_u$	fluid velocity
$c_p$	specific heat capacity at constant pressure
$c_v$	specific heat capacity at constant volume
$CFL_a, CFL_d$	advection (diffusion) Courant–Friedrichs–Lewy number
$C_f$	skin friction coefficient
$D'_i, D''_i$	descrete first/second derivatives in $i$ -direction (Burgers operator)
$\mathbb{D}$	computational domain
$\mathbb{D}_F$	fluid region of the computational domain
$\mathbb{D}_S$	solid region of the computational domain
$d_R$	displacement thickness (rough log-law)
$D$	laminar Ekman layer thickness
$e_{ij}$	rate-of-strain tensor
$Ek_\Lambda$	Ekman number
$Eu_\Lambda$	Euler number
$E_{\varphi\varphi}$	spectral Energy densities
$f$	Coriolis parameter
$\mathbf{f}^{\text{IBM}}$	IBM volume force added to RHS of the NSE
$F$	RHS terms of NSE
$\tilde{F}$	RHS terms of NSE without pressure gradient term
$Fr_\Lambda$	Froude number based on Rossby radius
$g_{\text{grav}}$	gravity
$\mathbf{g}$	non-dimensional geostrophic wind vector
$\mathbf{G}$	geostrophic wind vector
$h_R$	characteristic roughness length scale
$H$	height of bars (housing blocks)
$k_s$	grain diameter of sand grain roughness
$k_i$	wavenumber in $i$ -direction
$k_{\text{rel}}$	relative wavenumber
$k'_i, k''_i$	modified wavenumbers for first and second derivatives
$L_x, L_y, L_z$	computational domain size
$L_O$	Obukhov length
$l_{\text{cut}}$	spectral filter parameter
$Ma$	Mach number
$n_x, n_y, n_z$	number of grid points
$n_{\text{obj}}$	number of objects
$n_p$	number of phases
$n_t$	number of samples
$Nu$	Nusselt number
$p$	pressure
$p_{\text{ref}}$	reference pressure (standard pressure $10^5$ Pa )



$Pr$	Prandtl number
$q_*$	buoyancy surface flux
$R$	specific gas constant
$\mathcal{R}e$	unspecific Reynolds number for the channel flow configuration
$Re_{ABL}$	Reynolds number of the <b>ABL</b>
$Re_b$	bulk Reynolds number
$Re_{cl}$	centerline Reynolds number
$Re_{crit}$	critical Reynolds number
$Re_D$	Reynolds number based on the laminar Ekman layer thickness
$Re_\Lambda$	Reynolds number based on the Rossby radius
$Re_L$	buoyancy Reynolds number
$Re_\tau$	friction Reynolds number
$Ri_\Lambda$	Richardson number based on the Rossby radius
$Ro_\Lambda$	Rossby number based on the Rossby radius
$s$	passive scalar
$s_*$	friction value of the passive scalar
$S$	spacing of bars (housing blocks)
$Sc$	Schmidt number
$t$	time
$T$	Temperature
$T^{cf}, T^{sf}$	transfer function of compact (spectral) filter
$u$	streamwise velocity component
$\mathbf{u}^*$	intermediate velocity
$u_b$	bulk velocity
$\tilde{u}_b$	time-varying bulk velocity
$\mathbf{u}_S$	velocity vector for a moving body
$u_{buf}$	streamwise buffer velocity
$u_{cl}$	centerline velocity
$u_h$	horizontal velocity
$u_i$	fluid velocity vector $\mathbf{u} = (u, v, w)^T$
$u_{tr}$	transition velocity for the buffer
$u_\tau$	friction velocity
$u_*$	non-dimensional friction velocity
$v$	spanwise velocity component
$V_{obj}$	volume of the objects
$w$	wall-normal velocity component
$W$	width of bars (housing blocks)
$x$	Cartesian coordinate, streamwise direction
$x_j$	Cartesian coordinate vector $x_i = (x, y, z)^T$
$y$	Cartesian coordinate, spanwise direction
$y_{tr}$	transition height for buffer velocity
$z$	Cartesian coordinate, wall-normal direction
$z_0$	aerodynamic roughness length
$D(\cdot)/Dt$	total (material) derivative in time
$\partial(\cdot)/\partial t$	partial derivative in time (in short: $\partial_t(\cdot)$ )
$\partial(\cdot)/\partial x_i$	partial derivative in $x_i$ direction (in short: $\partial_{x_i}(\cdot)$ )
$(\cdot)'$	instantaneous fluctuation (Reynolds decomposition)
$(\cdot)_0$	reference value
$(\cdot)_{eff}$	effective value, based on the effective half-channel height
$(\cdot)_{buf}$	value associated with the buffer region in the domain
$(\cdot)$	time average
$\langle(\cdot)\rangle$	spatial average in the horizontal directions

---

$\overline{(\cdot)}$	phase-average
$(\dots)^+$	scaled in inner (viscous) units
$(\dots)^-$	scaled in outer units
$(\dots)^{ex}$	extrinsic average
$(\dots)^{\mathbf{0}}$	conditional averaged on fluid region
$(\dots)^{\mathbf{1}}$	conditional averaged on solid region



# Appendix

## Channel Flow – Description and Forcing

<sup>1</sup>**Characteristics.** The canonical channel flow problem describes a flow between two infinitely extended plates in the horizontal directions. The height  $H$  of the closed channel is twice the half-channel height  $\delta$  with  $H = 2\delta$ , and  $H = \delta$  in case of an open channel flow. The insertion of roughness elements in the flow domain results in a reduced cross-sectional area of the channel, and hence in an effective half-channel height  $\delta_{\text{eff}} \leq \delta$ . The effective value is  $\delta_{\text{eff}} = \delta - \delta_{\text{melt}}$  (in the absence of obstacles  $\delta_{\text{eff}} = \delta$ ), with the meltdown height  $\delta_{\text{melt}}$  (equation 3.6). A single non-dimensional parameter, the Reynolds number of the flow, characterizes the flow problem itself. Depending on the characteristic velocity and length scale choice, several formulations are common (Pope, 2000). The following formulations are adapted to the rough channel with streamwise aligned roughness elements and are defined as

$$Re_{b,\text{eff}} = \frac{2\delta_{\text{eff}}u_{b,\text{eff}}}{\nu}, \quad u_{b,\text{eff}} = \frac{1}{2\delta_{\text{eff}}L_xL_z} \int_0^{L_x} \int_0^{L_z} \int_{h_{\text{bottom}}(z)}^{h_{\text{top}}(z)} \bar{u} \, dy \, dz \, dx, \quad (\text{A.1a,b})$$

$$Re_{cl,\text{eff}} = \frac{\delta_{\text{eff}}u_{cl,\text{eff}}}{\nu}, \quad u_{cl,\text{eff}} = \langle \bar{u} \rangle|_{y=\delta}, \quad (\text{A.1c,d})$$

$$Re_{\tau,\text{eff}} = \frac{\delta_{\text{eff}}u_{\tau,\text{eff}}}{\nu}, \quad u_{\tau,\text{eff}} = \sqrt{\frac{\tau_{w,\text{eff}}}{\rho}} = \sqrt{\nu \left. \frac{d\langle \bar{u} \rangle}{dy} \right|_{y=y_0}}, \quad (\text{A.1e,f})$$

the bulk, centerline, and friction velocities and Reynolds numbers. The surface profile on the bottom and the top boundary is depicted by  $h_{\text{bottom}}(z)$  and  $h_{\text{top}}(z)$ . The wall shear stress is  $\tau_w$ , and in the case of a rough channel flow,  $\tau_w$  is evaluated at the virtual height  $y_0 = \delta_{\text{melt}}$  (Chan-Braun et al., 2011). All properties with the subscript  $(\cdot)_{\text{eff}}$  are related to rough channel flow. When a smooth channel flow is considered, similar formulations apply with  $\delta_{\text{eff}} = \delta$  and  $y_0 = 0$ .

---

<sup>1</sup>Note the change of the coordinate system in this section following chapter 3 (cf. footnote 2). Furthermore, the governing equations (3.4) are used in the dimensional formulation.

**Laminar relations and turbulent approximations for a smooth channel flow.** The laminar parabolic mean velocity profile and wall shear stress with a known centerline velocity is given by

$$\langle \bar{u} \rangle (y) = -\frac{u_{cl}}{\delta^2} (y - \delta)^2 + u_{cl}, \quad \tau_w = \mu \left. \frac{d\langle \bar{u} \rangle}{dy} \right|_{y=0} = \rho\nu \frac{2u_{cl}}{\delta}. \quad (\text{A.2a,b})$$

Integrating the vertical mean velocity profile  $\langle \bar{u} \rangle$  over the full channel height leads to the following laminar relations

$$u_b = \frac{2}{3}u_{cl}, \quad Re_b = \frac{4}{3}Re_{cl}, \quad (\text{A.3a,b})$$

$$\frac{u_\tau}{u_{cl}} = \sqrt{\frac{2}{Re_{cl}}}, \quad Re_\tau = \sqrt{2Re_{cl}} = \sqrt{3Re_b}. \quad (\text{A.3c,d})$$

Considering turbulent channel flow, an excellent empirical approximation of the relation between friction, bulk, and centerline velocity is given by the simple power law (Dean, 1978; Pope, 2000):

$$Re_\tau \approx 0.09Re_b^{0.88} \approx 0.116Re_{cl}^{0.88}. \quad (\text{A.4})$$

**Mean momentum balances for smooth channel flow.** Applying the Reynolds decomposition for velocities and pressure to the governing equations (3.4a,3.4b) and averaging in time and space lead to the Reynolds-averaged Navier–Stokes equations (RANS) (Spurk and Aksel, 2010) and read as

$$\frac{\partial \langle \bar{u}_j \rangle}{\partial x_j} = 0 \quad (\text{A.5a})$$

$$\frac{\partial \langle \bar{u}_j \rangle}{\partial t} + \langle \bar{u}_j \rangle \frac{\partial \langle \bar{u}_i \rangle}{\partial x_i} = -\frac{1}{\rho} \frac{\partial \langle \bar{p} \rangle}{\partial x_j} + \frac{\partial}{\partial x_i} \left( \nu \frac{\partial \langle \bar{u}_j \rangle}{\partial x_i} - \langle u'_i u'_j \rangle \right). \quad (\text{A.5b})$$

The following assumptions are considered for the mean flow equations (A.5): (i) statistical homogeneity in the horizontal directions  $\partial_x \langle \bar{\cdot} \rangle = \partial_z \langle \bar{\cdot} \rangle = 0$ , (ii) statistical stationarity  $\partial_t \langle \bar{\cdot} \rangle = 0$  and (iii) a statistical plane flow  $\langle \bar{w} \rangle = 0$ . With these assumptions and the vertical integration of the continuum equation (A.5a) with regard to the impermeability of the wall result in a zero mean vertical velocity  $\bar{v} = 0$ . The RANS equations can be simplified to the following mean momentum balances:

$$\text{in } x: \quad 0 = -\frac{1}{\rho} \frac{d\langle \bar{p} \rangle}{dx} - \frac{d}{dy} \langle \overline{u'v'} \rangle + \nu \frac{\partial^2 \langle \bar{u} \rangle}{dy^2}, \quad (\text{A.6a})$$

$$\text{in } y: \quad 0 = -\frac{1}{\rho} \frac{d\langle \bar{p} \rangle}{dy} - \frac{d}{dy} \langle \overline{v'v'} \rangle, \quad (\text{A.6b})$$

$$\text{in } z: \quad 0 = -\frac{d}{dy} \langle \overline{v'w'} \rangle. \quad (\text{A.6c})$$

Integrating the spanwise balance (equation A.6c) in the vertical direction yields a zero mean Reynolds stress  $\langle \overline{v'w'} \rangle$ . Similar vertical integration of the vertical balance (equation A.6b) gives a constant pressure gradient  $d_x \langle \bar{p} \rangle = \text{const.}$  in the vertical direction. Inserting the streamwise pressure gradient in the mean streamwise momentum balance (equation A.6a) and a subsequent integration over the full channel height leads to

$$\frac{d\langle \bar{p} \rangle}{dx} = \frac{d}{dy} \left( \mu \frac{d\langle \bar{u} \rangle}{dy} - \rho \langle \overline{u'v'} \rangle \right) = \frac{d\tau}{dy}, \quad (\text{A.7a})$$

$$\int_0^{2\delta} \frac{d\langle \bar{p} \rangle}{dx} dy = \int_0^{2\delta} \frac{d\tau}{dy} dy, \quad (\text{A.7b})$$

$$\frac{d\langle \bar{p} \rangle}{dx} = -\frac{\tau_w}{\delta}. \quad (\text{A.7c})$$

Wall-bounded flows are constantly losing energy due to friction. Without adding a forcing term  $F_1$  to the RHS of the NSE (equation 3.4b), the flow would decelerate and come to rest. Therefore, a continuous forcing is needed to drive the turbulent channel flow at a constant Reynolds number.

**Rough channel flow forcing with a constant pressure gradient.** The following options are conceivable to force a channel flow (Quadrio et al., 2016): (i) a constant pressure gradient (CPG) in the streamwise direction, (ii) a constant flow rate (CFR) (constant mass flow per unit area), and (iii) a mixture of both approaches, a constant power input (CPI). Here, the CPG approach is used since Quadrio et al. (2016) showed in their study that the choice of forcing has no statistical significance. The CPG balances the wall shear stress (equation A.7a) and results in a time-dependent bulk velocity of the flow. For turbulent and laminar flows, the forcing term is defined as

$$F_{1,\text{turb}} = \left( \frac{Re_\tau}{Re_{cl}} \right)^2, \quad F_{1,\text{lam}} = \frac{2}{Re_{cl}}. \quad (\text{A.8a,b})$$

With the forcing term  $F_{1,\text{turb}}$  and the power-law (equation A.4) it is possible to precisely aim for a desired Reynolds number of a smooth turbulent channel flow.

The insertion of obstacles in the flow reduces the cross-sectional area of the channel. Ignoring this would result in a rough channel flow with a reduced Reynolds number compared to a smooth channel flow with a similar forcing. With the necessity for comparing rough and smooth channel flow statistics at similar Reynolds numbers, namely  $Re_{\tau,\text{rough}} = Re_{\tau,\text{smooth}}$ , the correction factor for the streamwise pressure gradient is according to (Stroh et al., 2020b) introduced with

$$\frac{d_x p_{\text{rough}}}{d_x p_{\text{smooth}}} = \frac{\tau_{w,\text{eff}}}{\tau_w} \frac{\delta}{\delta_{\text{eff}}}, \quad (\text{A.9a})$$

$$= \frac{\rho u_{\tau,\text{eff}}^2}{\rho u_\tau^2} \frac{\delta}{\delta_{\text{eff}}}, \quad (\text{A.9b})$$

$$= \left( \frac{\nu Re_{\tau,\text{rough}}}{\delta_{\text{eff}}} \right)^2 \left( \frac{\delta}{\nu Re_{\tau,\text{smooth}}} \right)^2 \frac{\delta}{\delta_{\text{eff}}}, \quad (\text{A.9c})$$

$$= \left( \frac{\delta}{\delta_{\text{eff}}} \right)^3. \quad (\text{A.9d})$$





# Acknowledgements

First of all, I am incredibly grateful to my supervisor Cedrick Ansorge for his unwavering guidance during the turbulent last four years, be it during the Covid lockdown when I started at the University of Cologne or later from the Freie Universität Berlin. Our innumerable exciting discussions and his patience in sharing his enormous knowledge with me gave me invaluable feedback and shaped the work into what it is now. I am also grateful for the freedom to pursue my ideas, without which I would not have stayed motivated all these years. Many thanks also to my supervisors, Prof. Roel Neggers and Prof. Yaping Shao, for our fruitful discussions and the uncomplicated way I was accepted into their working groups and for always offering me the opportunity to discuss my research. I would also like to thank Prof. Nikki Vercauteren for examining my dissertation, and I would like to thank Prof. Juan Pedro Mellado for providing me with the very well-maintained `DNS` code `t1ab` and for supporting me with all related questions that arise during the last years.

Many thanks also to my colleagues, Shreyas Deshpande and Sally Issa, at the Institute of Meteorology at the Freie Universität Berlin, for the enlightening and thrilling group meetings, conferences and Berlin visits we had. Furthermore, I would like to thank my colleagues at the Institute of Geophysics and Meteorology of the University of Cologne for the last few years. Thanks for the enjoyable moments, uplifting atmosphere, lunch breaks, and the daily compassionate support you have provided throughout my journey in the past years. Special thanks also to Ann-Kristin for the great mentoring program in which I was privileged to participate. Moreover, I thank all my proofreaders for their valuable comments on this thesis.

I am particularly grateful for my colleagues, friends, and flatmates: Leonie, Lukas, Yannick, Federica, Katharina, Alex, Christina, Nils, Anke, and Vincent, who kept an eye on my work-life balance and went climbing with me every week. Thanks also for all the cooking evenings, board games, and parties we celebrated.

Finally, I would like to express my deep gratitude to the most important people in my life, Lisa, my family and friends, for their unconditional support throughout the past years in Cologne. Without you, I would not have written these lines and completed my work.

Financial support is acknowledged through the European Research Council Starting Grant (ERC-STG) “*Turbulence-Resolving Approaches to the Intermittently Turbulent Atmospheric Boundary Layer*” (`trainABL`) with the project number 851374 lead by Dr. Cedrick Ansorge. The computational part of this work was performed on the resources of the High-Performance Computing Center Stuttgart (HLRS) on the `HAWK` cluster—a `TIER-0` supercomputer—founded by the Baden–Württemberg Ministry for Science, Research, and the Arts and the German Federal Ministry of Education and Research through the Gauss Centre for Supercomputing. The project `trainABL` provided computing time and storage facilities with project number 44187.



# Erklärung zur Dissertation

Hiermit versichere ich an Eides statt, dass ich die vorliegende Dissertation selbstständig und ohne die Benutzung anderer als der angegebenen Hilfsmittel und Literatur angefertigt habe. Alle Stellen, die wörtlich oder sinngemäß aus veröffentlichten und nicht veröffentlichten Werken dem Wortlaut oder dem Sinn nach entnommen wurden, sind als solche kenntlich gemacht. Ich versichere an Eides statt, dass diese Dissertation noch keiner anderen Fakultät oder Universität zur Prüfung vorgelegen hat; dass sie – abgesehen von unten angegebenen Teilpublikationen und eingebundenen Artikeln und Manuskripten – noch nicht veröffentlicht worden ist sowie, dass ich eine Veröffentlichung der Dissertation vor Abschluss der Promotion nicht ohne Genehmigung des Promotionsausschusses vornehmen werde. Die Bestimmungen dieser Ordnung sind mir bekannt. Darüber hinaus erkläre ich hiermit, dass ich die Ordnung zur Sicherung guter wissenschaftlicher Praxis und zum Umgang mit wissenschaftlichem Fehlverhalten der Universität zu Köln gelesen und sie bei der Durchführung der Dissertation zugrundeliegenden Arbeiten und der schriftlich verfassten Dissertation beachtet habe und verpflichte mich hiermit, die dort genannten Vorgaben bei allen wissenschaftlichen Tätigkeiten zu beachten und umzusetzen. Ich versichere, dass die eingereichte elektronische Fassung der eingereichten Druckfassung vollständig entspricht.

## TEILPUBLIKATIONEN

### First author publications:

**Kostelecky J., Ansorge C. (2024): Simulation and scaling analysis of periodic surfaces with small-scale roughness in turbulent Ekman flow**, *Journal of Fluid Mechanics*, 992, pp. A8, <https://doi.org/10.1017/jfm.2024.542>.

**Kostelecky J., Ansorge C. (2025): Surface Roughness in Stratified Turbulent Ekman Flow**, *Boundary-Layer Meteorology*, 191, pp. 5, <https://doi.org/10.1007/s10546-024-00895-5>.

### Second author publication:

**Ansorge C., Kostelecky J. (2022): Closing the Scale Gap for Resolved-Turbulence Simulations in Meteorology**, In Nagel W. E., Kröner D. H., Resch M. M., editors, *High Performance Computing in Science and Engineering '22*, p.315–335, Springer Nature Switzerland, Cham, <https://doi.org/10.1007/978-3-031-46870-4>.

**Ansorge C., Kostelecky J. (2023), in print: Direct Representation of Roughness in the Atmospheric Boundary Layer**, *High Performance Computing in Science and Engineering '23*.

Köln, 02.12.2024

(Jonathan Kostelecky)

## LIST OF PRESENTATIONS

### **Oral presentations:**

- European Meteorological Society (EMS) Annual Meeting 2022, September 2022, Bonn, Germany.
- European Geosciences Union (EGU) General Assembly 2022, May 2022, Vienna, Germany.
- American Meteorological Society (AMS) 24th Symposium on Boundary Layers and Turbulence (BLT), January 2023, Denver, CO, USA.
- American Physical Society (APS) 76th Annual Meeting of the Division of Fluid Dynamics (DFD), November 2023, Washington, DC, USA.
- European Geosciences Union (EGU) General Assembly 2024, April 2024, Vienna, Germany.
- 1st European Fluid Dynamics Conference (EFDC1), September 2024, Aachen, Germany.

### **Poster presentations:**

- Buijs Ballot Research School (BBOS) Autumn Symposium 2021, October 2021, Soesterberg, The Netherlands.
- American Physical Society (APS) 74th Annual Meeting of the Division of Fluid Dynamics (DFD), November 2021, Phoenix, AZ, USA.
- Graduate School of Geosciences (GSGS) Research Conference 2022, February 2022, Cologne, Germany.
- John von Neumann Institute for Computing (NIC) Symposium 2022, September 2022, Jülich, Germany.
- American Physical Society (APS) 76th Annual Meeting of the Division of Fluid Dynamics (DFD), Gallery of Fluid Motion, November 2023, Washington, DC, USA.

# Data and Code Availability

Data and code were created as part of this doctoral project. The implementations in the DNS code `t1ab`, i.e. the horizontal pressure grid staggering, the ADR IBM, and the data supporting the findings of Study I and Study II are made available to the public.

## Code Availability:

The DNS code `t1ab` is available under the GNU General Public License v3.0 in the GitHub repository: <https://github.com/turbulencia/t1ab>

The code is constantly under development by other users. However, care is taken to ensure the current implementation remains compatible and usable, as it is now an integral part of the code. The precise technical implementation in the code can be tracked with the author's GitHub Commits and the user manual.

## Data Availability – Study I & II:

The data of Study I & II (neutrally and stably stratified rough Ekman flow) is available to the public under the Creative Commons Attribution 4.0 International (CC-BY-4.0) at the Refubium, data repository of the Freie Universität of Berlin, and contains netCDF files for each simulation case with time-series of statistical data for the flow and scalar variables in the vertical direction (Kostelecky and Ansoerge, 2024a,c). Furthermore, the dataset contains a file describing the dataset and a list of parameters for the code to run the respective cases. The data can be accessed under the following links:

<http://dx.doi.org/10.17169/refubium-43215> (Study I)

<http://dx.doi.org/10.17169/refubium-45292> (Study II)